On recovering distributed induced polarization information from time-domain electromagnetic data

by

Seogi Kang

Geosystem Engineering, Hanyang University, 2010

Geophysics, Hanyang University, 2012

A THESIS SUBMITTED IN PARTIAL FULFILLMENT
OF THE REQUIREMENTS FOR THE DEGREE OF

Doctor of Philosophy

in

THE FACULTY OF GRADUATE AND POST DOCTORAL STUDIES

(Geophysics)

The University of British Columbia

(Vancouver)

March 2018

Abstract

The electrical conductivity of earth materials is frequency-dependent. This is due to a phenomenon known as induced polarization (IP), wherein electrical charges build-up under the application of an electric field. Macroscopically, rocks may be considered chargeable, as they act like electric capacitors. The goal of this thesis is to show how IP data can be extracted from time-domain electromagnetic (TEM) data, then inverted to recover information about chargeable targets. Although both frequency and time-domain electromagnetic (EM) surveys measure IP signals, this dissertation will focus solely on TEM. To recover chargeability information, the following TEM-IP inversion workflow is developed. (1) Extract a background conductivity model that is assumed free of IP signals. (2) Decouple the TEM and IP signals by subtracting the fundamental responses estimated using the background conductivity. (3) Invert the resultant IP data to recover pseudo-chargeabilities at multiple times for a set of 3D volumes. This is used to infer the location and dimensions of chargeable targets. (4) Carry out further analyses of pseudo-chargeabilities at multiple times to estimate intrinsic parameters such as Cole-Cole chargeability and its associated time constant. For grounded sources, the workflow is implemented for a synthetic gradient array example. Results show that the early time signals, which are often discarded, can be used to estimate the background conductivity. Applying the workflow to inductive sources such as airborne EM (AEM) is more challenging, as steady-state electric fields are not produced. This was overcome by developing an IP function which (1) accurately characterizes how electric fields from inductive sources behave in the earth and (2) allows the recovery of a 3D chargeability by solving a linear inverse problem. The efficacy of the aforementioned approach is validated using field AEM surveys over the Mt.

Milligan porphyry deposit in British Columbia and Tli Kwi Cho kimberlite deposit in the Northwestern Territories. For the kimberlite deposit, the recovered chargeability information is able to distinguish two distinct kimberlite units. To validate the approach, a 3D rock model for Tli Kiw Cho is constructed using the recovered chargeability and background conductivity. This model is compared against geological models obtained through drilling and shows good agreement.

Lay Summary

When materials are excited by electromagnetic (EM) sources, they may exhibit significant capapcitive properties due to the buildup of electrical charges; a phenomenon known as induced polarization (IP). Rocks exhibiting IP are said to be chargeable. Signals measured during EM geophysical surveys can include IP effects from chargeable rocks. This has been observed in mining, oil and gas, and groundwater applications. The strength of the IP effects, and their impact on field-collected data, depends upon the concentration and distribution of chageable materials below the surface. In this thesis, I develop a workflow capable of recovering a 3D chargeability distribution from EM geophysical data. The workflow is validated using both synthetic and field examples. In particular, I focus on the Tli Kwi Cho kimberlite complex in NWT, Canada.

Preface

The following document presents original research I completed at the Geophysical Inversion Facility (GIF) in the Department of Earth, Ocean and Atmospheric Sciences at the University of British Columbia (UBC), Vancouver, Canada. Significant portions of this research was used to produce three peer-reviewed journal articles and five expanded conference proceedings. Work as part of this dissertation has also been presented at seven conferences.

Chapters 2 and 3 contain the text and figures from the published paper by Kang and Oldenburg [2016] in *Geophysical Journal International*. The development of a TEM-IP inversion workflow which linearizes inductive source IP (ISIP) and accounts for inductive responses was originally proposed by Dr. Douglas Oldenburg. Under the supervision of Dr. Douglas Oldenburg, I produced all subsequent derivations, numerical modeling codes, numerical tests and manuscript preparations. Numerical modeling codes were completed under the supervision of Dr. Elded Haber. These codes were written within the framework of an open-source geophysical simulation and inversion package known as SIMPEG [Cockett et al., 2015]. Successful integration of original coding into this framework was done with the assistance of Mr. Rowan Cockett and Ms. Lindsey Heagy. Original numerical modeling codes developed for this dissertation were validated against the EMTDIP code developed by Dr. David Marchant [Marchant et al., 2014].

The workflow I developed from Dr. Douglas Oldenburg's original concept is applied to airborne IP data in Chapter 4. This chapter is divided into three sections. Section 4.1 summarizes content presented in the SEG expanded abstract [Kang and Oldenburg, 2015]. Section 4.2summarizes content presented in the SEG expanded abstract [Kang et al., 2014]. Here, the conductivity inversion is based upon PhD

work by Dr. Dikun Yang [Yang et al., 2014]. Additional numerical experiments were done using pre-existing SimPEG modeling packages. Sections 4.1 and 4.2 were edited with the help of Dr. Douglas Oldenburg. Original work summarized in Sections 4.1 and 4.2 are currently in preparation to be submitted as a journal article. Section 4.3 contains text and figures from the published paper by Kang et al. [2017] in *Interpretation*. This work was done in collaboration with several members of the UBC Geophysical Inversion Facility (UBC-GIF) group, most notably, Mr. Dominique Fournier. Mr. Dominique Fournier made significant contributions to the conductivity inversion code which was used; see Fournier et al. [2017] in *Interpretation*. All other numerical experiments are original work. Manuscript with editing was done with the help of Mr. Dominique Fournier and Dr. Douglas Oldenburg.

Chapter 5 is a revised version of the journal paper by Kang and Oldenburg [2017], which was published in *Geophysical Prospecting*. The idea was initiated from Dr. Douglas Oldenburg's suggestion to apply the workflow to DC-IP data. I performed numerical experiments with SIMPEG EM and DC-IP packages, and I wrote the journal paper with editing help from Dr. Douglas Oldenburg.

Appendices A, B, C contain materials relevant to Chapters 2 and 3.

This thesis manuscript is entirely original work. The manuscript was completed with editing help from Dr. Douglas Oldenburg, Dr. Eldad Haber and Dr. Randolph Enkin.

Table of Contents

Abstract . . . . . **ii**

Lay Summary . . . . . **iv**

Preface . . . . . **v**

Table of Contents . . . . . **vii**

List of Tables . . . . . **xi**

List of Figures . . . . . **xii**

Acknowledgments . . . . . **xxix**

Dedication . . . . . **xxxi**

1 Introduction **1**

1.1 Research Motivation 1

1.2 Polarization mechanisms 8

1.3 Complex Resistivity and Conductivity 15

1.4 Lab-scale IP Measurements 16

1.5 Modelling Maxwell's Equations 20

1.6 TEM-IP Inversion Workflow 32

1.7 Thesis Outline 35

2 Linearization **37**

2.1 Pseudo-chargeability 38
2.2 Linear IP Function 42
2.3 Numerical Experiments 48
2.3.1 IP Data 48
2.3.2 Polarization Currents 53
2.3.3 IP Currents 57
2.3.4 Validations of Linearization 63
2.4 Effective Pseudo-chargeability 65
2.5 Positivity on Time History of Electric Field 67
2.6 Conclusions 77

3 3D IP Inversion 79
3.1 Introduction 79
3.2 3D IP Inversion with a Linear Equation 79
3.3 Numerical Experiments 81
3.3.1 Incorrect Conductivity 82
3.3.2 Extracting Intrinsic IP Parameters 88
3.4 Conclusions 89

4 Airborne Examples 92
4.1 Synthetic Example 99
4.1.1 Setup 99
4.1.2 Data 101
4.1.3 Conductivity Inversion 105
4.1.4 EM-decoupling 107
4.1.5 IP Inversion 112
4.1.6 Conclusions 116
4.2 Field Example: Mt Milligan 117
4.2.1 Setup 117
4.2.2 Data 121
4.2.3 Conductivity Inversion 124
4.2.4 EM-decoupling 125
4.2.5 IP Inversion 128

4.2.6 Interpretation . . . 131
4.2.7 Conclusions . . . 135
4.3 Field Example: DO-27/18 kimberlites . . . 136
4.3.1 Setup . . . 136
4.3.2 Data . . . 139
4.3.3 Conductivity Inversion . . . 143
4.3.4 EM-decoupling . . . 146
4.3.5 IP Inversion . . . 149
4.3.6 Interpretation . . . 155
4.3.7 Synthesis . . . 158
4.3.8 Conclusions . . . 160

5 Grounded Source Example . . . 162
5.1 Introduction . . . 162
5.2 TEM-IP Inversion Workflow for Grounded Source . . . 166
5.3 Data . . . 168
5.4 Conductivity Inversion . . . 172
5.5 EM-decoupling . . . 174
5.6 IP Inversion . . . 176
5.7 Discussion . . . 178
5.8 Conclusions . . . 180

6 Conclusions . . . 181
6.1 Development of the TEM-IP Inversion Workflow . . . 182
6.2 Application to Airborne IP Data . . . 183
6.3 Application to DC-IP Data . . . 185
6.4 Future Research . . . 186
6.5 Concluding comments . . . 188

Bibliography . . . 191

A Handling Multiple Sources for AEM Surveys . . . 199

B Extracting Intrinsic IP Parameters . . . 205

C Discretization 207
C.1 Steady-state Maxwell's Equations 207
C.2 Linearized Kernel for IP Responses 208

List of Tables

Table 1.1 Cole-Cole parameters from different rocks (obtained from Pelton et al. [1978]). 7

Table 2.1 Amplitudes of decomposed IP currents at two marked points (white stars) shown in Fig. 2.10(b). Units in A/m^2 58

Table 4.1 Cole-Cole parameters of four anomalous bodies (A1-A4). . . . 100
Table 4.2 Parameters of conductivity inversion. 105
Table 4.3 Parameters of IP inversion. 113
Table 4.4 Recovered Cole-Cole parameters of four chargeable blocks (A1-A4). Values in parenthesis indicates true values. 114
Table 4.5 Expected physical property contrast for kimberlite deposits in the Lac de Gras region [Power and Hildes, 2007]. 138
Table 4.6 Mean and standard deviation of estimated τ (μs) and η for A1-A4. Used values of c for fitting are given. 153
Table 4.7 Petrophysical domains built from inversions of airborne EM data sets. Here σ, $\tilde{\eta}_E$, and $\tilde{\eta}_L$ correspondingly conductivity, and pseudo-chargeability at 130 and 410μs. 156

Table 5.1 Conductivity (σ_∞) and resistivity (ρ_∞) at infinite frequency, and Cole-Cole chargeability (η) values for five units: A1-A4 and half-space. 169
Table 5.2 Parameters for the TEM and DC inversions. See Section 3.2 for explanation of parameters. σ_{half} indicates conductivity of the homogeneous half-space, which has a value of 0.01 S/m. . . 172

List of Figures

Figure 1.1 Cole-Cole resistivity as a function of frequency [Pelton et al., 1978]. Black and red lines indicate real and imaginary part of the Cole-Cole resistivity. Used Cole-Cole parameters are: ρ_0=1.25 Ωm, η=0.2, τ=0.1 s, and c=0.5. 6

Figure 1.2 Conceptual diagram of (a) half-cycle input current waveform and (b) measured IP responses at surface electrodes. 6

Figure 1.3 Polarization phenomenon at a pore throat: (a) Initial state, (b) While electric field is applied, and (c) Right after removal of the electric field. (d) Input current. (e) Overvoltage at on-time. (f) Overvoltage at off-time. 9

Figure 1.4 Microscope images of rocks. (a) Illite (a clay mineral) with surface area-to-volume ratio of 100 m^2/g(1000 times greater than sandstone). (b) Quartz overgrowths in sandstone with surface area-to-volume ratio of 0.1 m^2/g. Modified from [GPG, 2018]. 10

Figure 1.5 Electrode polarization: (a) Initial state, (b) While electric field is applied, and (c) Right after removal of the electric field. Modified from Revil et al. [2015]. 12

Figure 1.6 Electrical double layer at the surface of insulating minerals. X^- indicates active sites at mineral surface, which attracts metallic cations M^+. M^+ is attached to the active sites, and bounded by the Outer Helmholtz Plane (OHP). The OHP separates the stern layer from the diffuse layer. A- indicates anion. Obtained from Revil [2013] 13
Figure 1.7 Polarization mechanisms related to Electrical Double Layer (EDL): (a) Initial state, (b) While electric field is applied, and (c) Right after removal of the electric field. Modified from Revil [2013]. 13
Figure 1.8 Maxwell-Wagner polarization: (a) Initial state. For a rock containing three different phases: solid, water, and air that have different conductivity and dielectric permittivity. (b) Polarization charge can be built when an electric field is applied. (c) Charges diffuse away when the electric field is removed, generating opposite direction of the current flow to the applied electric field. Modified from Chen and Or [2006]. 14
Figure 1.9 Lab scale IP measurement system in Geological Survey of Canada (GSC). The photo is taken from Cowan [2015]. 18
Figure 1.10 Complex impedance measurements using the Geological Survey of Canada system [Enkin et al.]. 19
Figure 1.11 Cole-Cole response in frequency domain (a) and time (b) domain. The Cole-Cole parameters are $\sigma_\infty = 10^{-2}$ S/m, $\eta = 0.5$, $\tau = 0.1$ s, and c=1. The arrow indicates a Dirac-delta function ($\sigma_\infty \delta(t)$). 24
Figure 1.12 3D chargeability model. (a) Plan and (b) Section views. White solid line on (a) shows the wire path, and the arrow indicates the direction of current in the wire when current is turned on. THe half-space conductivity is 0.05 S/m. 25

Figure 1.13 Time curves of the normalized potential difference at a receiver location (marked as black solid line with dots in Fig. 1.12(a)). Black, blue and red lines correspondingly indicate observed, fundamental and IP data. Solid and dashed lines distinguish positive and negative values. Black vertical dashed lines at three time channels indicate times at which the electric field distributions in Fig. 1.14 are provided. The halfspace conductivity is 0.05 S/m. 26
Figure 1.14 3D electric field distributions at three different times in the on-time. Top, middle and bottom panel correspondingly show the electric fields at 6 ms, 77 ms, and 1717 ms. (a) Plan view at the surface and (b) Section view at Northing 0 m. The halfspace conductivity is 0.05 S/m. 27
Figure 1.15 Time decaying curves of the normalized potential difference when the current is turned off. Black, blue, and red lines respectively indicate observed, fundamental and IP data. Dotted and solid lines distinguish positive and negative values. Halfspace conductivity is 0.05 S/m. 28
Figure 1.16 3D electric field distribution at three different times when the current is turned off. Top, middle and bottom panel correspondingly show the electric fields at 6 ms, 715 ms, and 2116 ms. (a) Plan view at the surface and (b) Section view at Northing 0 m. The halfspace conductivity is 0.05 S/m. 29
Figure 1.17 Observed potential difference at three different off times. (a) 6 ms, (b) 77 ms, and (c) 1717 ms. Halfspace conductivity is 0.05 S/m. 30
Figure 1.18 Time curves of the normalized potential difference at a receiver location (marked as black solid line with dots in Fig. 1.12(a)). Halfspace conductivity is 0.5 S/m. 30
Figure 1.19 Time decaying curves of the normalized potential difference when current is turned off. Halfspace conductivity is 0.5 S/m. 31

Figure 1.20 Observed potential difference at three different off times. (a) 6 ms, (b) 77 ms, and (c) 1717 ms. Halfspace conductivity is 0.5 S/m. 31

Figure 2.1 Cole-Cole response in frequency domain (a) and time (b) domain. The Cole-Cole parameters are $\sigma_\infty = 10^{-2}$ S/m, $\eta = 0.5$, $\tau = 0.01$ s, and c=1. The arrow shown in Fig. 2.1b indicates a delta function ($\sigma_\infty \delta(t)$). 42

Figure 2.2 Convolution of $\triangle\sigma$ and $\vec{e}$ resulting in polarization current, $\vec{j}^{pol}$. (a) DC source. (b) Inductive source. $\triangle\sigma$ and $\tilde{\eta}^I$ are respectively defined in eqs. (2.8) and (2.7). 43

Figure 2.3 Conceptual diagram for the amplitude of the fundamental electric fields. (a) DC source. (b) Inductive source. 43

Figure 2.4 Plan (a) and section (b) views of the IP model. The solid line in (a) delineates the boundary of the IP body. Solid circles in (a) denote the sounding locations. In (b) the conductivity σ_2 is variable so that canonical, conductive and resistive blocks can be examined 50

Figure 2.5 Time decaying curves of the observations (d; black line), fundamental (d^F; blue line) and IP (d^{IP}; red line) responses. All three cases: (a) canonical, (b) conductive and (c) resistive are presented. Right and left panels show b_z and $-\frac{\partial b_z}{\partial t}$. The vertical black dotted line indicates the time at which the polarization field reaches its maximum value. The flight height of the collocated transmitting and receiving loop is 30 m above the surface. 51

Figure 2.6 Interpolated maps of observed (left panel), fundamental (middle panel) and IP (right panel) responses. Two time channels at (a) 0.86 ms and (b) 6.7 ms are presented. The white line contours a zero-crossing in the observed response. 52

Figure 2.7 Maps of reference currents: (a) canonical and (b) conductive models. Left and right panels show plan and section views at -125 m-depth and 0 m-easting, respectively. A source is located at (-200 m, 0 m, 30 m). Black arrows and colored background respectively indicate the direction and amplitude of the current. Black solid lines outline the boundary of the chargeable body. 54

Figure 2.8 Maps of polarization currents: (a) canonical and (b) conductive models at 0.86 ms. Left and right panels show plan and section views at -125 m-depth and 0 m-easting, respectively. A source is located at (-200 m, 0 m, 30 m). Black arrows and shaded values respectively indicate the direction and amplitude of the current. Black solid lines outlin boundary of the surface or the chargeable body. 55

Figure 2.9 Maps of polarization currents: (a) canonical and (b) conductive models at 6.7 ms. Left and right panels show plan and section views at -125 m-depth and 0 m-easting, respectively. A source is located at (-200 m, 0 m, 30 m). Black arrows and shaded values indicate the direction and amplitude of the current, respectively. Black solid outlines boundary of the surface or the chargeable body. 56

Figure 2.10 Decomposition of the IP currents as $\vec{j}^{pol}$ (left panel), $-\sigma_\infty \vec{\nabla}\phi^{IP}$ (middle panel), and $-\sigma_\infty \vec{a}^{IP}$ (right panel) at 0.86 ms. Plan view maps of the currents at -125 m-depth are shown: (a) canonical, (b) conductive, and (c) resistive cases. 59

Figure 2.11 Comparisons of contributions of $\vec{j}^{pol}$, $-\sigma_\infty \vec{\nabla}\phi^{IP}$, and $-\sigma_\infty \vec{a}^{IP}$ to the observed IP magnetic field. Solid line indicates true b_z^{IP} responses. Stars, rectangles, and circles correspondingly indicate each IP response generated by applying the Biot-Savart law to $\vec{j}^{pol}$, $-\sigma_\infty \vec{\nabla}\phi^{IP}$, and $-\sigma_\infty \vec{a}^{IP}$. Empty and solid markers represent positive and negative values, respectively. 60

Figure 2.12 Interpolated maps of (a) true and (b) approximate IP currents at 0.86 ms. Left and right columns respectively show plan and section view maps at -125 m-depth and 0 m-easting. 61

Figure 2.13 Interpolated maps of (a) true and (b) approximate IP currents at 6.7 ms. Left and right columns respectively show plan and section view maps at -125 m-depth and 0 m-easting. 62

Figure 2.14 Comparison of true and approximate IP responses (b_z^{IP}). Black, blue, and red colors respectively indicate canonical, conductive, and resistive cases. Solid lines indicate true b_z^{IP}, computed by subtracting the fundamental response from the observation. The stars are the application of Biot-Savart to true IP current and generate $b_{z\,BS}^{IP}$. Empty circles show our approximate $b_{z\,approx}^{IP}$ response. 64

Figure 2.15 Conceptual diagram of EM induction process from a loop transmitter when a vertical conductor is embedded in a homogeneous half-space. After the transmitter current is turned-off from the loop, currents are induced in the subsurface and diffuse away like a smoke ring. This smoke ring currents will be channeled into the vertical conductor (dashed lines), and there will be vortex currents rotating (red dashed circle) in the conductor due to the time-varying magnetic field. In the conductor, at the top voxel (yellow) the half-space channeled current and the vortex current are in the same direction (in to the page), whereas at the bottom voxel they are in the opposite direction. 70

Figure 2.16 Plan and section views of a 3D conductivity model is shown in right and left panels, respectively. A vertical conductor (0.005 S/m) is embedded in a homogeneous half-space (0.001 S/m). Green solid circle indicates the horizontal location of the transmitter loop having 13 m-radius, and located 30 m above the surface. 71

Figure 2.17 The current densities at three different times due to a 13 m-radius loop located 30 m above the surface (marked as green solid circle) with a conductivity model having a vertical conductor shown in Fig. 2.16. Plan and section views of the current density at three different times after the current is off: (a) 0.01 ms, (b) 0.07 ms, and (c) 1.17 ms. The time history of the electric field at the top and bottom voxels in the conductor (yellow and green crosses, respectively) are presented in Fig. 2.19. 72

Figure 2.18 The peak current (or reference current) selected from the time history of the current density shown in Fig. 2.17. Plan and sections views are shown in right and left panels, respectively. The time history of the electric field at the top and bottom voxels in the conductor (yellow and green crosses, respectively) are presented in Fig. 2.19. 73

Figure 2.19 The time history of the electric field, w^{ref}, at the two voxels shown in Figs. 2.17 and 2.18. Yellow and green distinguish w^{ref} for the top and bottom voxels, respectively. (a) w^{ref} at the both voxels in semi-log scale ($log(t) - w^{ref}$). (b) w^{ref} at the top voxel only showing later times after 0.1 ms with linear scale in time. The negative values of w^{ref} exist at the very late-time for the bottom voxel (green) as shown in (b). 74

Figure 2.20 (a) Intrinsic pseudo-chargeability, $\tilde{\eta}^I$ as a function of time. Used Cole-Cole parameters are denoted in (a). (b) Pseudo-chargeability, $\tilde{\eta}$, calculated by convolving $\tilde{\eta}^I$ and w^{ref} at the bottom voxel shown in Fig. 2.19. Solid line and cross marks distinguish $\tilde{\eta}$ computed with and without positive projection on w^{ref}, $P_0[w^{ref}]$. 75

Figure 2.21 Computed IP data, d^{IP}, using linear IP function. IP data are computed with and without positive projection on w^{ref} and denoted as d^{IP} and d_0^{IP}, respectively; red dashed line and red crosses are distinguishing d^{IP} and d_0^{IP}, respectively. 76

Figure 3.1 Effect of depth weighting in 3D IP inversion. (a) True pseudo-chargeability model on vertical section at 0 m-northing. Recovered pseudo-chargeability models (b) without depth weighting and (c) with depth weighting. 83

Figure 3.2 IP responses on a profile line at 0 m-northing. IP responses are computed from perturbed σ_∞ models. Halfspace conductivity (σ_1) is perturbed: $2\times\sigma_1$ and $0.5\times\sigma_1$, which respectively resulting in overestimated (dotted line) and underestimated (dashed line) IP responses. The solid line shows the true IP response. 85

Figure 3.3 Recovered pseudo-chargeability sections from 3D IP inversions at 0 m-northing. (a) d^{IP} with true σ_1. (b) d^{IP} with $2\times\sigma_1$. (c) d^{IP} with $0.5\times\sigma_1$. (d) d^{IP} with $0.5\times\sigma_1$ and the positivity constraint on the pseudo-chargeability. White dashed lines contour zero-crossing lines. 86

Figure 3.4 Recovered pseudo-chargeability sections from the 3D IP inversions at 0 m-northing. (a) True and (b) incorrect σ_∞ is used to compute sensitivity function. For the incorrect sensitivity I used a halfspace conductivity σ_1. 87

Figure 3.5 Section views of recovered: (a) time constant and (b) chargeability. Any region where the pseudo-chargeability shown in Fig. 3.4a is smaller that 0.001 is ignored in this analysis, and blanked. 89

Figure 3.6 Comparisons of the observed pseudo-chargeability at a single pixel in a chargeable body from the 14 inversions at 14 time channels, and the predicted pseudo-chargeability. The empty circles and solid line respectively indicate predicted and observed pseudo-chargeability. The estimated time constant and chargeability are respectively expressed as τ_{est} and η_{est}. The true values for τ and η are respectively 0.005 s and 0.2. 90

Figure 4.1 Geometry of the VTEM system (Geotech). 95

Figure 4.2 Observed VTEM data over the Mt Milligan porphyry deposit, BC, Canada. (a) Profile line at Northing 6109000 m, which crosses Harris fault and Rainbow faults. (b) Time decay at Northing 6109000 m and Easting 433800 m. Here black and red lines distinguish positive and negative values. 96
Figure 4.3 Section of a chargeable cylinder embedded in a halfspace. Conductivity of the halfspace is σ_1=0.001 S/m. The conductive chargeable cylinder is parameterized with a Cole-Cole model and has higher conductivity than that of halfspace: σ_∞=0.01 S/m. Other parameters are given in the diagram. 97
Figure 4.4 Propagation of electric fields in time: 0.1 ms (left), 0.5 ms (middle), and 7.9 ms (right). e_y is plotted in the x-z plane, and fundamental electric field is rotating in counter-clock-wise-direction. In the late-time, the reversed direction of e_y is observed due to strong polarization effects. Boundaries of the air-earth interface and chargeable cylinder are shown as black lines. 97
Figure 4.5 Time decays of observed (d), fundamental (d^F), and IP (d^{IP}) voltages over a chargeable cylinder. Solid and dashed lines distinguish positive and negative values. (a) Only observed voltage. (b) All three voltages with distinction of early, intermediate, and late times. Vertical grey lines indicate three times (0.1, 0.5, and 7.9 ms) when electric fields are plotted in Fig. 4.4. 98
Figure 4.6 Sectional views of $\sigma_\infty(x,y,z)$ model. Solid lines delineate boundaries of four IP blocks. 99
Figure 4.7 2D map of the simulated data including both EM and IP effects (d). A1-A4 indicate corresponding anomalies due to four IP bodies. Black dotted lines indicate boundaries of the four IP bodies. Negative responses are shaded as white regions. Black dots are locations of Fig. 4.9. Black dots are locations of Fig. 4.9. 102

Figure 4.8 Profile line of the observed data, d at Northing (a) 630 m and (b) -630 m. Black and red lines distinguish positive and negative data. 103
Figure 4.9 Time decays of the observed data, d at four sounding locations close to A1-A4. Here solid and dashed lines distinguish positive and negative data. Error bars are shown from 0.1 to 1 ms, which indicate the uncertainty used in conductivity inversion. Three grey vertical liens indicate time channels shown in Fig. 4.7. 104
Figure 4.10 Sectional views of the recovered conductivity model (σ_{est}). Solid lines delineate boundaries of the four IP blocks. 106
Figure 4.11 Comparison of true and estimated fundamental responses at 0.2, 1.8 and 5.6 ms. (a) true fundamental response: $F[\sigma_\infty]$ and (b) estimated fundamental response: $F[\sigma_{est}]$. 108
Figure 4.12 Time decays of the d, $F[\sigma_\infty]$, and $F[\sigma_{est}]$ at four sounding locations close to A1-A4. Here solid and dashed lines distinguish positive and negative datum. Error bars are shown from 0.1 to 1 ms, which indicate uncertainty used in conductivity inversion. 109
Figure 4.13 Comparison of true and estimated IP responses at 0.2, 1.8 and 5.6 ms. (a) true IP response: $d^{IP}[\sigma_\infty]$ and (b) estimated IP response: $d^{IP}[\sigma_{est}]$. 110
Figure 4.14 Time decays of the d, $d^{IP}[\sigma_\infty]$, and $d^{IP}[\sigma_{est}]$ at four sounding locations close to A1-A4. Here solid and dashed lines or solid and empty circles distinguish positive and negative datum. . . 111
Figure 4.15 Regional removal procedure. Left, middle and right panels correspondingly indicate before removal, estimated regional fields, and after removal of $d^{IP}[\sigma_{est}]$ at 1.8 ms. Black dots and empty white circles indicate all stations and selected stations to estimate regional field. 111
Figure 4.16 Sectional views of the recovered $-d\tilde{\eta}/dt$ models at 1.8 ms. (a) Without regional removal. (b) With regional removal. . . . 114

Figure 4.17 Comparison of observed and predicted pseudo-chargeability for four chargeable anomalies: A1-A4. Solid lines and empty circles distinguish observed and predicted pseudo-chargeability. 115
Figure 4.18 Location of Mt Milligan and QUEST survey area. 118
Figure 4.19 Geology and VTEM survey at Mt Milligan porphyry deposit in British Columbia, Canada [Yang and Oldenburg, 2012]. . . 119
Figure 4.20 Normalized current waveform of the VTEM survey (2007) at Mt Milligan deposit. 119
Figure 4.21 Topography of the VTEM survey of the Mt Milligan region. Geology indicated with white lines. 120
Figure 4.22 2D map of the observed VTEM data at eight different times ranging from 4.6-7.1 ms. Solid white lines show boundaries of different gelogical units and the white areas indicate where the response has gone negative. 122
Figure 4.23 2D map of the VTEM data at 2.7 ms (left panel) and time decays at three stations close the negative anomalies at A1-A3 (right panel). Solid white lines on the right panel show boundaries of different geological units, and white dashed lines indicate the approximate locations of where there are. 123
Figure 4.24 3D Conductivity model of Mt Milligan porphyry deposit obtained by Yang et al. [2014]. 124
Figure 4.25 EM-decoupling of the VTEM data over Mt Milligan region. 2D maps of d, $F[\sigma_{est}]$, $d^{IP}[\sigma_{est}]$ are shown at (a) 2.7, (b) 0.7 and (c) 0.2 ms. $F[\sigma_{est}]$ is subtracted from d to obtain $d^{IP}[\sigma_{est}]$. A4-A5 are IP anomalies recognized by EM-decoupling, whereas A1-A3 were shown as negatives in d. A1-A3 and A4-A5 are marked as grey and black dashed circles, respectively. 126
Figure 4.26 Time decays of d, $F[\sigma_{est}]$, $d^{IP}[\sigma_{est}]$ at the five IP anomalies: A1-A5. Top left panel showed 2D map of $d^{IP}[\sigma_{est}]$ at 2.7 ms. 127

Figure 4.27 Plan and section views of the recovered pseudo-chargeability: (a) 2.7, (b) 0.7, and (c) 0.2 ms. Five anomalies recognized from $d^{IP}[\sigma_{est}]$ are marked as dashed circles on plan view (left panels). 129
Figure 4.28 Comparison of observed and predicted IP data for the IP inversion at three time channels: 2.7, 0.7 and 0.2 ms. 130
Figure 4.29 Plan and section views of 3D conductivity and pseudo-chargeability over Mt Milligan area. 132
Figure 4.30 The 3D rock model obtained from both conductivity and pseudo-chargeability models. Red and black dots indicates fault structures, and three mineralized zones, respectively. R3 shows the rock units obtained from the airborne IP data. 133
Figure 4.31 The 3D rock model obtained from both conductivity and pseudo-chargeability models. Red and black dots indicates fault structures, and three mineralized zones, respectively. R2 shows the rock units obtained from the airborne IP data. 134
Figure 4.32 Location map for the Tli Kwi Cho (TKC) kimberlites, NWT. DO-18 and DO-27 are two main kimberlite pipes at TKC region. PK, VK, and HK correspondingly indicate pyroclastic kimberlite (PK), volcaniclastic kimberlite (VK), and hypabyssal kimberlite (HK). 137
Figure 4.33 Schematic diagram of a kimberlite pipe in the Lac de Gras region (Modified from Devriese et al. [2017]). A lake may be present after glaciation and is often used as a first indicator of a possible kimberlite. Transverse lines are from the DIGHEM survey (1992). 138

Figure 4.34 Plan maps of four EM data sets at TKC: (a) DIGHEM (56000 Hz), (b) NanoTEM (77 μs), (c) AeroTEM II (26 μs), (d) VTEM (90 μs). For TEM data sets, a smaller region (red box) close to DO-18 and -27 is presented. The black line is a contour line of the negative anomaly (-8 nT/s) from AeroTEM data at 26 μs. The white line shows the boundary of the lakes. Negative anomalies: A1-A4 are correspondingly marked as purple, yellow, red, and green solid circles; A1-A3 showed strong negatives for all TEM data at an early-time as shown in Fig. 4.35. 140

Figure 4.35 Plan maps of four EM data sets at TKC: (a) DIGHEM (7200 Hz), (b) NanoTEM (603 μs), (c) AeroTEM II (534 μs), (d) VTEM (680 μs). For TEM data sets, a smaller region (red box) close to DO-18 and -27 is presented. The black line is a contour line of the negative anomaly (-8 nT/s) from AeroTEM data at 26 μs. The white line shows the boundary of the lakes. Negative anomalies: A1-A4 are correspondingly marked as purple, yellow, red, and green solid circles; A1-A3 showed strong negatives for all TEM data at an early-time as shown in Fig. 4.35. 141

Figure 4.36 Transient curves of NanoTEM and VTEM data. (a) NanoTEM soundings away from the pipe and representative of background (blue lines) and over the DO-18 pipe (black lines). They are marked as blue and black solid circles in Fig. 4.34(b). (b) VTEM soundings at A1-A4 (correspondingly purple, yellow, red, and green lines). They are marked as purple, yellow, red, and green solid circles in Fig. 4.34 (d) and Fig. 4.35(d). Solid and dashed lines distinguish positive and negative observations. 142

Figure 4.37 Plan and section views of the recovered conductivity model from the cooperative inversion of the VTEM and DIGHEM data sets: (a) VTEM and (b) DIGHEM. The white outlines delineate boundaries of the lake. The green outlines show the extent of DO-27 and DO-18 at the surface, based on drilling. . 144

Figure 4.38 Observed and estimated fundamental responses at TKC. Four sounding locations at A1-A4 are marked as solid circles. Regions having negative values are shown as white. 145
Figure 4.39 Time decaying curves of the d (black line), $F[\sigma_{est}]$ (blue line), and $d^{IP}[\sigma_{est}]$ (red line) data at (a) A1, (b) A2, (c) A3, and (d) A4. Solid and dashed lines distinguish positive and negative values. Vertical black dashed line indicate 130 and 410 μs, respectively. 147
Figure 4.40 Plan maps of d, $F[\sigma_{est}]$ and $d^{IP}[\sigma_{est}]$ at (a) 130 and (b) 410 μs. Left, middle, and right panels correspondingly show the d, $F[\sigma_{est}]$ and $d^{IP}[\sigma_{est}]$. 148
Figure 4.41 Plan and section views of the recovered pseudo-chargeability model from the 3D IP inversion of the raw IP at (a) 130 μs and (b) 410 μs, respectively. Left panel shows plan map at 99 m below surface. Top and bottom of right panels show A-A' and B-B' sections, respectively. Solid and dashed red lines delineate contours of the recovered pseudo-chargeability at 50 s^{-1} (130 μs) and 10 s^{-1} (410 μs). The black outlines delineate boundaries of the lake. The green outlines show the extent of DO-27 and DO-18 at the surface, based on drilling. 150
Figure 4.42 Cole-Cole conductivity as a function of frequency [Pelton et al., 1978]. Black and red lines indicate real and imaginary part of the Cole-Cole conductivity. Used Cole-Cole parameters are: σ_∞=1 S/m, η=0.2, and c=0.5; two τ values are considered: 10^{-3} s and 10^{-4} s. Solid and dashed line indicates complex conductivity generated with $\tau = 10^{-3}$ s and $\tau = 10^{-4}$ s, respectively. 152
Figure 4.43 Comparison of the observed (lines) and predicted (solid circles) pseudo-chargeability at cells close to A1-A4 (correspondingly purple, yellow, red, and green colors). (a) All time decaying curves of the observed and predicted pseudo-chargeability. (b) Median values of the observed and predicted pseudo-chargeability at each time. 153

Figure 4.44 A cross plot between the estimated time constant (τ) and chargeability (η) at cells close to A1-A4. Solid circles shaded as purple, yellow, red, and green colors correspondingly indicate A1-A4. 154
Figure 4.45 Comparative sections through the TKC kimberlites. (a) Overlaid anomalies of three physical property models: conductivity (dark grey), pseudo-chargeability at 130 (red), and 410 μs (green). (b) Generated rock model from three anomalies. The white outlines delineate boundaries of the lake. The green outlines show the extent of DO-27 and DO-18 at the surface, based on drilling. 157
Figure 4.46 Comparison of 3D geology and rock model. (a) 3D geologic model obtained from the known geology and drilling results at the TKC area (b) 3D petrophysical model obtained from airborne EM. The black outlines delineate boundaries of the lake. The green outlines show the extent of DO-27 and DO-18 at the surface, based on drilling. 159

Figure 5.1 Conceptual diagram of a ground-based grounded source with half-duty cycle current waveform. 164
Figure 5.2 A typical example of overvoltage effects in electric IP data. . . 164
Figure 5.3 Observed voltage with EM induction effects. EM effects dominate the early on and off-time data. Inset figure shows the enlarged off-time voltage and it demonstrates early EM induction effects (negative) and late-time IP effects (positive). Dashed and solid lines distinguish positive and negative voltages. . . . 165
Figure 5.4 Plan and section views of the 3D mesh. Black solid lines show the boundaries of four blocks (A1-A4). Only A2 and A3 (red labels) are chargeable. Arrows indicate a wire path for the grounded source. Black dots indicate potential electrodes. . . 169
Figure 5.5 Plan maps of the observed DC data: (a) Voltage and (b) Apparent resistivity. 170

Figure 5.6 Plan maps of the observed TEM data at (a) 5 ms, (b) 80 ms (c) 130, and (d) 500 ms. Dashed and solid contours differentiate negative and positive data. 170
Figure 5.7 Time decaying curves of the observed (d) and fundamental (d^F) data. Four sounding locations close to (a) A1, (b) A2, (c) A3, and (d) A4 are presented. Blue and black color indicates d and d^F. 171
Figure 5.8 Recovered conductivity models from: (a) TEM and (b) DC inversions by inverting off-time (EM) and on-time data (DC), respectively. 173
Figure 5.9 Plan maps for 80 ms. (a) observed data, (b) estimated fundamental using σ_{est}^{EM}, and (c) IP. 175
Figure 5.10 True and estimated fundamental responses at 80 ms. (a) True fundamental response; (b), (c), and (d) correspondingly indicate estimated fundamental responses using σ_{est}^{EM}, σ_{est}^{DC}, and σ_{est}^{half}. 175
Figure 5.11 True and estimated IP responses at 80 ms. (a) True d^{IP}; (b), (c), and (d) correspondingly indicate estimated IP responses using σ_{est}^{EM}, σ_{est}^{DC}, and σ_{est}^{half}. 175
Figure 5.12 Recovered chargeability models from IP inversions. IP data computed using an estimated conductivity model from (a) TEM and (b) DC inversions, respectively. 177
Figure 5.13 True and estimated IP responses at 130 ms. (a) True d^{IP}; (b), (c), and (d) correspondingly indicate estimated IP responses with use of EM, DC, and half-space conductivity. 179
Figure 5.14 Decay curves of the observed, fundamental and IP data at A3. (a) True and estimated fundamental responses with the observed data. (b) True and IP responses with the observed data. 179

Figure A.1 Normalized weights for the conductive case for all source locations. A single pixel located at (0 m, 0 m, -75 m) is used. . 202

Figure A.2 Time decays of $w^e(t)$ and $\hat{w}(t)$ for the conductive case. A single pixel located at (0 m, 0 m, -75 m) is used. Solid line and dashed lines correspond to $w^e(t)$ and $\hat{w}_k(t)$ for all sources ($k = 1, \ldots, nTx$); $\hat{w}_k$ at the center source located at (0 m, 0 m, 30 m) is marked as solid circles. A number of $w^e(t)$ curves are overlaid due to the symmetric position of source locations to the conductive block. 203

Figure A.3 Comparison of true and approximate b_z^{IP} responses at 0.86 ms on a plan view map. 204

Acknowledgments

This thesis work has built upon a number of people's previous efforts, and would have not been completed without the guidance and support from a large group of individualstod. So, I would to take this as an opportunity to express my gratitude to them.

First of all, I would like to express my deepest gratitude to my supervisor Prof. Doug Oldenburg for his academical, emotional, and financial supports for the past five and half years. When I first came to Vancouver, Canada from South Korea, I was eager to see and experience how electromagnetic geophysics has been used in the bigger world, and learn the state-of-art technology. Doug not only taught me about academic knowledge about the applied geophysics, but also opened up the doors that I can be connected to people from various disciplines which allowed me to experience how I can help solve real world problems. Further, his moral support was a fuel for me whenever I was down.

Next, I would like to thank my committee members, Prof. Eldad Haber and Dr. Randy Enkin. The foundation in computational electromagnetics that I have learned from Eldad was the basis for most of computational aspects in the thesis. Randy's guidance on understanding mechanisms of induced polarization effects made significant impact for me to interpret the field examples shown in the thesis. In addition, I would like thank my external examiner Prof. Richard Smith for his critical comments suggestions on my thesis.

The funding of this work was generously provided from a variety of sources. Thanks to University of British Columbia, the Department of Earth and Ocean Sciences, the Mathematics of Information Technology and Complex Systems, and the Canadian Exploration Geophysical Society for their support.

Many thanks to all of my friends and colleagues at Geophysical Inversion Facility, Simulation and Parameter Estimation in Geophysics community, and University of British Columbia that I have shared time with over the years. Thanks to David Marchant, Dikun Yang, Rowan Cockett, Lindsey Heagy, Mike Mitchell, Dominique Fournier, Sarah Deveriese, Kris Davis, Mike McMillan, Gudni Rosenkjar, Luz Angelica, Thibaut Astic, Devin Cowan, Patrick Belliveau, Daniel Bild-Enkin, Roman Shekhtman, Gesa Myer, Mike Wathen, Julie Nutini, and Jilmarie Stephens for making my Canadian life delightful.

Finally, I would like to show my love and gratitude to Angela, for all of the support and love that she provided rain or shine and being my lifetime companion.

Dedication

To my parents and in the loving memory of my mother.

Chapter 1

Introduction

1.1 Research Motivation

The electrical conductivity of earth materials is usually frequency dependent with the effective conductivity decreasing with decreasing frequency. The change in conductivity is due to the buildup of electric charges that occur under the application of an electric field. The rock is electrically polarized and thus it can be said that the rock is chargeable. This charge build-up phenomenon is called induced polarization (IP). At a microscopic level the causes of the IP depends upon the very fine scale structure of the rocks.

Rocks can have different polarization mechanisms and this will result in different IP characteristics as a function of frequency. There are many ways to parameterize the complex behavior but a commonly used one is the Cole-Cole model [Pelton et al., 1978]:

$$\rho(\omega) = \rho_0 \Big[1 - \eta \Big(1 - \frac{1}{1 + (\imath\omega\tau)^c} \Big) \Big], \tag{1.1}$$

where ρ_0 is resistivity at zero frequency, η is chargeability, τ is a time constant, c is a frequency exponent. Fig. 1.1 shows real and imaginary part of complex resistivity as a function of frequency. Using eq. (1.1), Pelton et al. [1978] fitted measured complex impedances of different rock samples and provided a range of Cole-Cole parameters. These are summarized in Table 1.1. IP surveys have been

successfully conducted in various geoscience applications. For mining applications, IP surveys are recognized as a principal geophysical technique for finding disseminated sulfide or porphyry deposits. This is mainly because of the metallic polarization effects arising from metallic minerals such as pyrite. On the other hand, non-metallic polarization effects (e.g. membrane polarization) can also generate IP signals in various geological settings. IP surveys have been used in a broad spectrum of environmental problems including hydraulic conductivity estimation [Hördt et al., 2007] and hydrocarbon contaminant mapping [Kemna et al., 2012]. In addition, Veeken et al. [2009a,b] has used IP surveys to find offshore hydrocarbons
.

A common type of IP survey is an electrical IP (EIP) survey (or often called DC-IP survey) where current electrodes, connected to a generator, are used to inject currents into the earth (grounded or galvanic source) and voltages as a function of time are measured at potential electrodes. For time-domain measurements, the input current waveform has an on- and off-time as shown in Fig. 1.2. Typically, the on-time is of the order of 0.1-10 seconds. At the potential electrodes on the surface, an electric potential difference is measured while input currents are switched on and off. Fig. 1.2 shows measured voltage, and here V_s indicates the secondary voltage (off-time), V_0 and V_∞ are potential differences at zero and infinite frequency, respectively. Assuming there are no electromagnetic (EM) induction effects, any signal in the off-time is the result of IP phenomena. Hence, any datum that captures some aspect of this secondary voltage is considered to be an IP datum. A commonly used form of the time-domain IP data, d^{IP} can be written as

$$d^{IP} = \frac{1}{V_0} \int_{t_1}^{t_2} V_s(t) \tag{1.2}$$

Here t_1 and t_2 are arbitrary times included in the off-time with $t_1 < t_2$. This measure correspond to to the area of the shaded region in Fig. 1.2, and when t is measured in milliseconds (ms), then its unit is ms. However, each time channel of secondary potential can be considered as an IP datum, then the units of d^{IP} can be mV/V. In the frequency domain, since measured voltage is complex-valued, both amplitude and phase are considered as IP data. Assuming that the voltage is measured at two different frequencies, percentage frequency effect (PFE), and phase difference

(mrad), are also commonly used as IP data. When only one frequency is used, phase is considered as IP data, as when there is no chargeability, the phase is zero.

Interpretation of the IP data is most commonly carried out by taking one of the many definitions of IP data, assume that the ground chargeability is small, linearize the problem [Seigel, 1959], and invert to find 2D or 3D volumes of a chargeability [Oldenburg and Li, 1994]. This IP inversion is commonly carried out using a two-stage inversion procedure: (a) first recover a resistivity distribution at zero frequency from DC data (in practical terms, the latest on-time data or the lowest frequency), then (b) recover a chargeability distribution by inverting d^{IP} data using a sensitivity function from the previous DC inversion.

Not all chargeable volumes are the economic resources sought and it is desirable to distinguish between the different chargeable units. Determining different IP characteristics by interpreting multiple time and frequency channels has thus been a long term goal. The generic term for this study is spectral IP (SIP). For instance, one may want to differentiate between a porphyry and a magnetite embedded in the earth. Both of them have significant chargeability, but different time constants as shown in Table 1.1. By inverting SIP data, and recovering both chargeability and time constants, these two different rocks can possibly be distinguished.

For extracting spectral IP information from IP data, I consider two main approaches. The first approach is simple and most often used. I invert each time or frequency IP data separately, and then interpret the recovered models to distinguish different IP sources using a complex resistivity model [Yuval and Oldenburg, 1997, Kemna et al., 2004, Hördt et al., 2006]. The second is more sophisticated, and this inverts multiple time or frequency IP data simultaneously by parameterizing the complex resistivity model with a few parameters, e.g. Cole-Cole [Kemna et al., 2004, Fiandaca et al., 2012, 2013]. Either approach can provide distributed IP information that is insightful. A principal challenge for inverting SIP data in 3D space is the increased dimensionality due to frequency- or time-dependent resistivity. For instance, in the frequency domain, the output of the inversion can be $\rho(x,y,z;\omega)$. This is four-dimensional function. Even if I chose a parameterization such as Cole-Cole [Pelton et al., 1978], which reduces the dimensionality from the number of frequencies to four representative values, I still have four times the number of parameters in the model that must be solved. With the first approach

where each time or frequency is inverted separately, this dimensionality issue may not be a critical problem. However, for the second approach where all parameters are found at once, one needs an effective strategy to handle the increased dimensionality to obtain a successful 3D inversion. Considering this generic challenge for inverting SIP data, I chose the first approach to recover 3D distribution of IP parameters.

A significant assumption behind the interpretation of DC-IP data is that EM induction effects can be ignored. EM induction effects arise from the time varying magnetic fields generated by the transmitter. These general electric fields are superposed on our desired IP signal. Depending on both the resistivity of the earth and measured times or frequencies, there can be situations where this assumption is not reasonable. For several decades, this issue has been treated using EM-decoupling techniques; that is, use a method to remove EM induction effects from the observations and thereby extract IP signals. There have been various EM-decoupling techniques suggested based on approximate representations of EM induction effects using a halfspace or layered-earth resistivity model [Wynn and Zonge, 1975, Routh and Oldenburg, 2001]. Although they have been effective for some case histories, I believe that the EM-decoupling issue has to be revisited using the latest 3D EM forward modelling and inversion capabilities.

On the other hand, whenever an electric field is applied to the earth, IP signals can be generated from a chargeable body [Macnae, 1988]. Thus, not only grounded sources, but also inductive sources such as airborne loop sources can excite chargeable bodies. However, the electric field generated by an inductive source is solely based on EM induction, and hence it is fundamentally different from the grounded source excitation. This difference needs to be considered in order to proceed to the interpretations of inductive source IP (ISIP) data. The airborne IP problem in time-domain is important in geophysics research. Negative transients measured in various time-domain airborne EM (AEM) systems are commonly observed [Smith and Klein, 1996, Jansen and Witherly, 2004, Kang et al., 2017, Kaminski and Viezzoli, 2017]. In theory, a chargeable earth is required to explain such negatives [Weidelt, 1982] particularly from a coincident loop system. I call either AEM survey or data including IP effects as an airborne IP. Inverting these airborne IP data, and recovering IP parameters, may yield information about

near surface structure that is relevant to mineral exploration and/or environmental problems such as permafrost [Smith and Klein, 1996, Kang et al., 2017]. These airborne IP data have typically been inverted by invoking a halfspace or layered-earth assumption [Kratzer and Macnae, 2012, Viezzoli et al., 2017]. However, IP signals are small and 3D analysis is likely necessary for many problems. Carrying out this analysis for airborne IP data is an important topic.

In this thesis I consider three open questions in the area of inductive source (particularly airborne IP) and grounded source (DC-IP).

1. How can we understand the fundamentals of inductive source IP, and can the time-domain airborne IP data be linearized similar to DC-IP data?

2. Can distributed IP information be recovered from the airborne IP data?

3. Can EM effects in DC-IP data be effectively removed to generate high quality IP data?

I develop an effective workflow that can separate EM and IP portions in the observation, and recover distributed IP information in 3D space. To apply the workflow to airborne IP data, the first question needs to be answered, and this is treated in Chapter 2. Based upon this linearization of IP data, 3D IP inversion code is developed in Chapter 3; this provides a complete workflow that can be applied to both airborne IP and DC-IP data. Chapter 4 considers the second question. Here, the workflow is applied to both synthetic and field examples of airborne IP data. In Chapter 5, the third and last question is treated by applying the workflow to a synthetic DC-IP example.

In this introductory Chapter 1, I will present mechanisms of IP phenomenon, a simple mathematical model for IP, how the IP effect can be simulated in TEM data with Maxwell's equations, and the workflow to restore polarization information from EM data including IP effects.

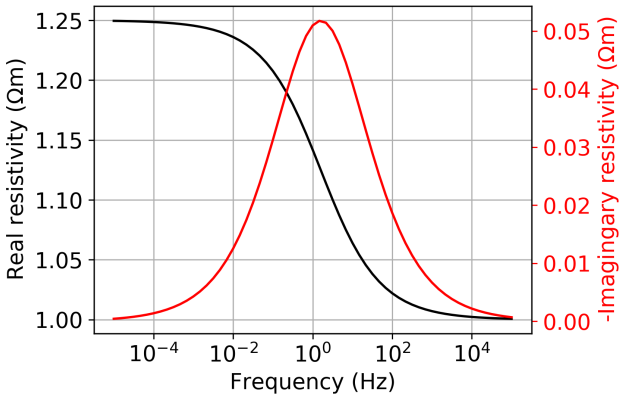

Figure 1.1: Cole-Cole resistivity as a function of frequency [Pelton et al., 1978]. Black and red lines indicate real and imaginary part of the Cole-Cole resistivity. Used Cole-Cole parameters are: ρ_0=1.25 Ωm, η=0.2, τ=0.1 s, and c=0.5.

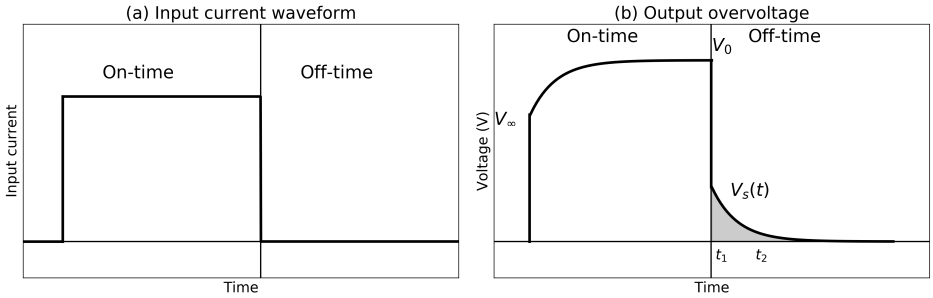

Figure 1.2: Conceptual diagram of (a) half-cycle input current waveform and (b) measured IP responses at surface electrodes.

Table 1.1: Cole-Cole parameters from different rocks (obtained from Pelton et al. [1978]).

	$\rho_0(\Omega m)$	η	τ (s)	c ($0< c <1$)
Porphyry (dry)	1×10^1 - 1×10^3	0.1 - 0.5	1×10^{-5} - 1×10^0	0.1 - 0.6
Porphyry (wet)	1×10^0 - 1×10^4	0.1 - 0.8	1×10^{-2} - 7×10^4	0.1 - 0.5
Magnetite	1×10^1 - 1×10^3	0.1 - 1.0	8×10^{-4} - 3×10^0	0.1 - 0.6
Pyrrhotite	1×10^0 - 1×10^3	0.3 - 0.8	3×10^0 - 1×10^5	0.1 - 0.5
Massive sulfide	1×10^{-2} - 1×10^3	0.6 - 0.95	8×10^{-4} - 2×10^0	0.1 - 0.4
Graphite	1×10^{-2} - 1×10^3	0.75 - 0.98	3×10^1 - 8×10^3	0.1 - 0.5

1.2 Polarization mechanisms

In this section, I want to provide some insight about polarization mechanisms since this thesis is devoted to recovering distributed polarization parameters of the ground from various TEM data. Polarization mechanisms are complex and I will not investigate them in detail nor do the specific details of mechanisms really matter to my thesis.

Induced polarization (IP) is caused by the transport and accumulation of charge carriers (ions and electrons) in earth materials (e.g. solid rock or unconsolidated soils) due to an applied electrical field. From an abstract point of view, the accumulation of charge carriers will oppose the current flow in the material. This creates an electric dipole that results in an overvoltage in potential measured at the surface and is also associated with a reversed current (in the opposite direction to the applied electric field). Fig. 1.3(e) illustrates this induced polarization phenomenon. Consider a pore throat with an ionic fluid. At the initial state, the system (rocks and fluids) is electrically neutral. When an electrical field is applied (in the case by a battery or a generator), ions will move through the rock, and accumulate at the pore throat, these charges accumulate and oppose the current flow in the rock. If voltage is measured as a function of time, it will increase in time, and reach to the steady state as shown in Fig. 1.3 (d). After the applied electric field is removed, polarized ions will revert back to the initial state, and this current flow is in the reversed direction of the applied electric field (see how the positive charges move). This effectively generates a decaying voltage as shown in Fig. 1.3. At the microscopic level, intuition can come from thinking about the surface area-to-volume ratio of pore material. As the surface area-to-volume ratio increases, so does the number of microscopic pores that can accumulate charges. This results in stronger induced polarization effects. Fig. 1.4 (a) and (b) show microscope images of clay mineral and sandstone. The surface area-to-volume ratio of the clay minerals is much bigger than that of the sandstone; this will results in much stronger polarization effects for the clay minerals when an electric field is applied.

Having a simple intuition is good; however, recognizing various polarization mechanisms are still important because this will allow us to identify potential applications of IP. Thus, I provide a brief overview of some important IP mechanisms

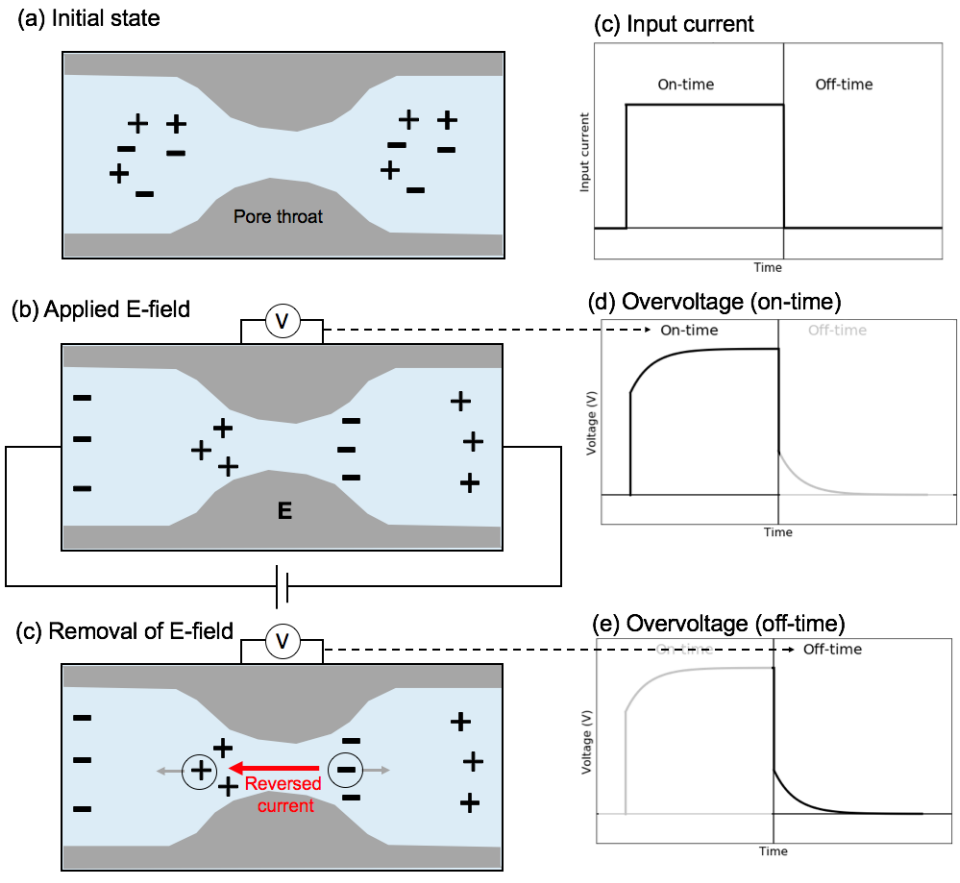

Figure 1.3: Polarization phenomenon at a pore throat: (a) Initial state, (b) While electric field is applied, and (c) Right after removal of the electric field. (d) Input current. (e) Overvoltage at on-time. (f) Overvoltage at off-time.

below 1 MHz. These can be classified as five different categories:

1. Electrode polarization
2. Stern layer polarization
3. Diffuse layer polarization
4. Membrane polarization

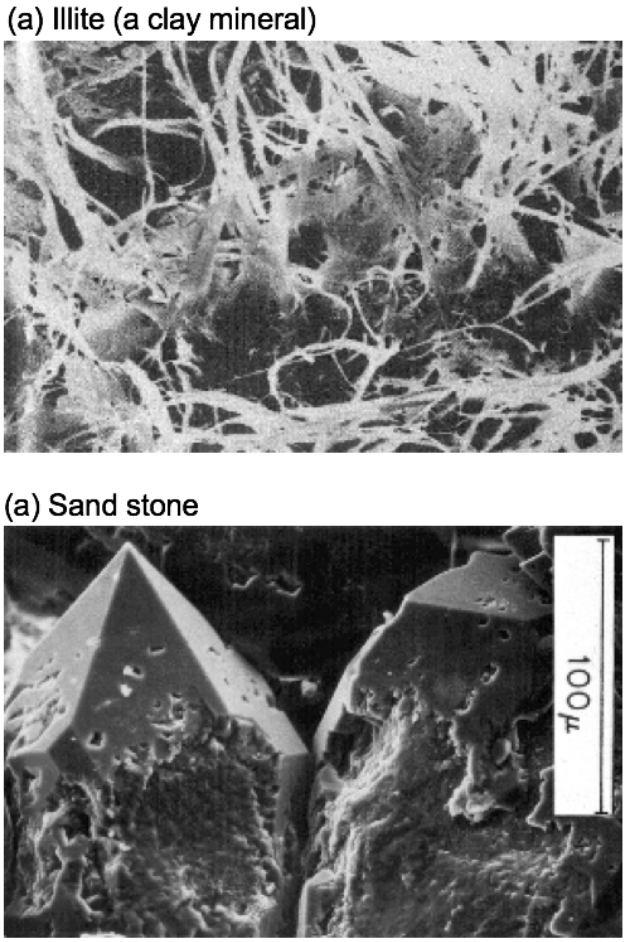

Figure 1.4: Microscope images of rocks. (a) Illite (a clay mineral) with surface area-to-volume ratio of 100 m^2/g(1000 times greater than sandstone). (b) Quartz overgrowths in sandstone with surface area-to-volume ratio of 0.1 m^2/g. Modified from [GPG, 2018].

5. Maxwell-Wagner polarization

Electrode polarization can be observed in the presence of disseminated conductive minerals such as pyrite, chalcopyrite, pyrrhotite, and magnetite [Pelton et al., 1978, Wong, 1979, Revil et al., 2015]. This has been very useful model for mining applications such as finding porphyry deposits. Fig. 1.5 illustrates before and

after the electric field is applied to a metallic particle in a solution. The electrode polarization will mainly depends upon type, volume and geometry (e.g. diameter and shape) of the metallic particle, and it can explain both low and high frequency polarization effects [Pelton et al., 1978, Wong, 1979, Revil et al., 2015]. In most mining applications, low frequency polarization effects are observed in DC-IP data (< 10 Hz).

Stern (2)[Reference], Diffuse layer (3)[Reference], and Membrane (4)[Reference] polarization are related to the electrical double layer (EDL) structure; they explain polarization mechanisms of porous media, but in particular for clays. Fig. 1.6 shows the EDL composed of Stern layer (fixed) and Diffuse layer. An insulating grain is in the the electrolyte containing a dissolved salt and hence both cations and anions exist in the solution. Cations are bounded in the Stern layer, whereas both cations and anions can move in the Diffuse layer. Fig. 1.7 illustrates the three polarization mechanisms:(2)-(4). Both the Stern and the Diffuse layer can be polarized with the applied electric field, and after removal of the electric field, polarized charges diffuse [Marshall and Madden, 1959, Revil, 2013]. These three mechanisms can contribute to low frequency polarization effect (< 10 Hz; Revil [2013]). In Fig. 1.7(b) due to greater mobility of cations than anions, they can be accumulated on the right hand side as a consequence of the applied electric field. After removal of the electric field, accumulated charges diffuse backward. These two phenomenon acting together is sometimes called membrane polarization, and this can contribute to both low and high frequency polarization effects [Bücker and Hördt, 2013]. All three mechanisms will depends upon structure of the pore, and how cations can be exchanged on the surface of the grain. Hence, both cation exchange capacity (CEC) and the surface area-to-volume ratio will be key parameters for these mechanisms.

The Maxwell-Wagner polarization [Chen and Or, 2006] is an interfacial polarization due to the discontinuity of displacement currents in a multiphase system with discontinuities of the dielectric permittivity and/or electrical conductivity at the interface between the different phases [Kemna et al., 2012]. Fig. 1.8 illustrates the Maxwell-Wagner polarization. When an electric field is applied to a medium having three different phases: solid (rock), water, and air. This mechanism is controlled by the tortuosity of the different phases, their volume fractions, and the

conductivity and permittivity of the different phases. The Maxwell-Wagner polarization is mainly responsible for polarization phenomena at frequencies above 10 Hz [Chen and Or, 2006].

To summarize, from a conceptual view point, the polarization effect is explained as buildup of polarization charge which disturbs flow of the electrical current. When the applied electric field is removed, the accumulated polarization charges diffuse backward, which generates a current that has opposite direction to the electric field. Five different mechanisms of IP are introduced here: (1) Electrode polarization, (2) Stern layer polarization, (3) Diffuse layer polarization, (4) Membrane polarization, and (5) Maxwell-Wagner polarization. (1)-(4) were related to electromigration of ions or electrons, whereas (5) was mainly due to interfacial discontinuities in both conductivity and dielectric permittivity. (1)-(4) can contribute to low frequency polarization effects ($<$ 10 Hz), whereas (5) mostly contribute to high frequency polarization effect ($>$ 10 Hz). (1) and (4) can also cause high frequency polarization effects.

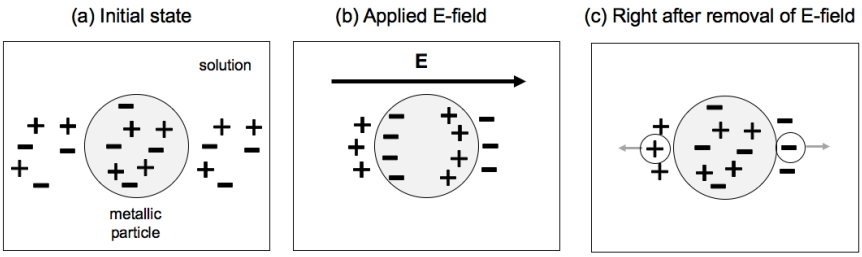

Figure 1.5: Electrode polarization: (a) Initial state, (b) While electric field is applied, and (c) Right after removal of the electric field. Modified from Revil et al. [2015].

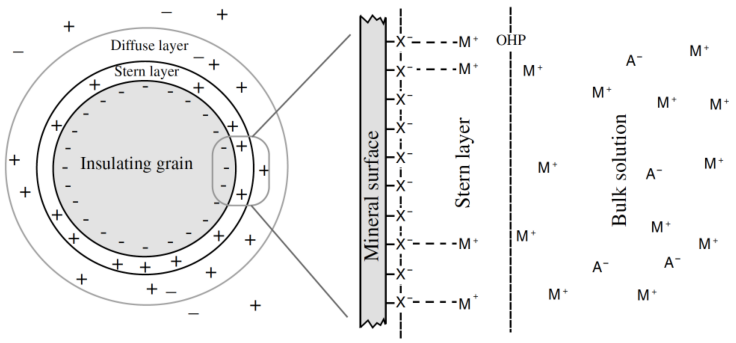

Figure 1.6: Electrical double layer at the surface of insulating minerals. X^- indicates active sites at mineral surface, which attracts metallic cations M^+. M^+ is attached to the active sites, and bounded by the Outer Helmholtz Plane (OHP). The OHP separates the stern layer from the diffuse layer. A- indicates anion. Obtained from Revil [2013]

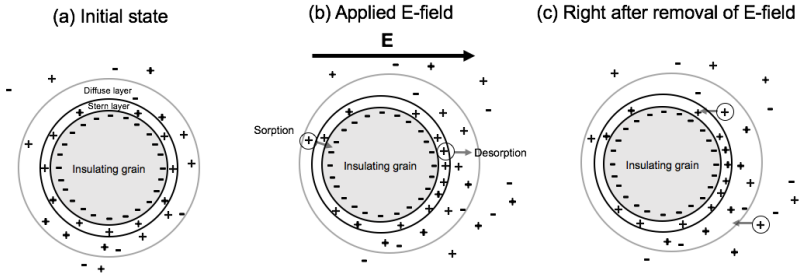

Figure 1.7: Polarization mechanisms related to Electrical Double Layer (EDL): (a) Initial state, (b) While electric field is applied, and (c) Right after removal of the electric field. Modified from Revil [2013].

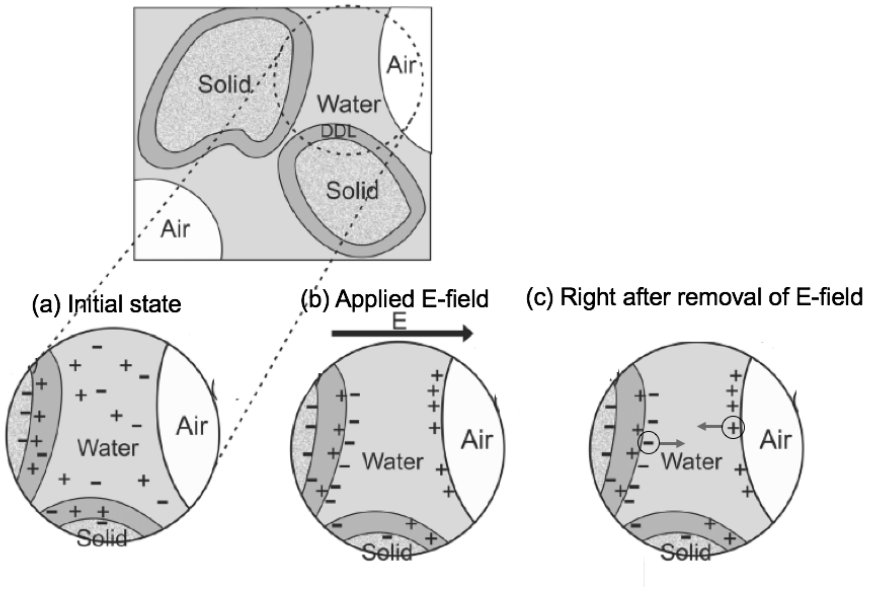

Figure 1.8: Maxwell-Wagner polarization: (a) Initial state. For a rock containing three different phases: solid, water, and air that have different conductivity and dielectric permittivity. (b) Polarization charge can be built when an electric field is applied. (c) Charges diffuse away when the electric field is removed, generating opposite direction of the current flow to the applied electric field. Modified from Chen and Or [2006].

1.3 Complex Resistivity and Conductivity

Mathematical representations of IP effects are often defined in the frequency domain with the resistivity represented as a complex function. An extremely simple, but a most used model, is the Cole-Cole model. One representation due to Pelton et al. [1978] can be expressed as

$$Z(\omega) = R_0\Big[1 - \eta\Big(1 - \frac{1}{1+(\imath\omega\tau)^c}\Big)\Big], \tag{1.3}$$

where R_0 is the resistance at zero frequency, η is the chargeability, τ is the time constant, c is the frequency exponent. As frequency goes to infinity, the above complex impedance value ($Z(\omega)$) asymptotes to $R_\infty = \frac{R_0}{1-\eta}$. This yields an expression of the chargeability as

$$\eta = \frac{R_0 - R_\infty}{R_0}. \tag{1.4}$$

For a sample rock with area A (m^2) and length l (m), the complex resistivity, $\rho(\omega)$ can be simply obtained by

$$\rho(\omega) = Z(\omega)\frac{A}{l}. \tag{1.5}$$

Pelton's Cole-Cole model can also be expressed in resistivity form:

$$\rho(\omega) = \rho_0\Big[1 - \eta\Big(1 - \frac{1}{1+(\imath\omega\tau)^c}\Big)\Big], \tag{1.6}$$

and the same equation can be written in conductivity form:

$$\sigma(\omega) = \rho(\omega)^{-1} = \sigma_\infty - \sigma_\infty\frac{\eta}{1+(1-\eta)(\imath\omega\tau)^c}, \tag{1.7}$$

where subscripts 0 and ∞ respectively stands for a value at zero and inifinte frequency. Here, the chargeability can be defined as either using either resistivity and conductivity:

$$\eta = \frac{\rho_0 - \rho_\infty}{\rho_0} = \frac{\sigma_\infty - \sigma_0}{\sigma_\infty}. \tag{1.8}$$

Note that eqs. (1.6) and (1.7) is essentially the same as the equation for resistivity when the dielectric permittivity is complex [Cole and Cole, 1941]. For

conductivity, the original Cole-Cole model can be written as:

$$\begin{aligned}\sigma_{cc}(\omega) &= \sigma_\infty + \frac{\sigma_0 - \sigma_\infty}{1 + (\imath\omega\tau_{cc})^{c_{cc}}} \\ &= \sigma_\infty - \sigma_\infty \frac{\eta}{1 + (\imath\omega\tau_{cc})^{c_{cc}}}. \end{aligned} \tag{1.9}$$

I shall refer to eq. (1.7) a Pelton's model (PM) and eq. (1.9) a Cole-Cole model (CCM) following Tarasov and Titov [2013]. Here, τ_{cc} and c_{cc} differ from τ and c of PM. Noticeable difference lies in the denominator: PM includes $(1-\eta)$, but CCM do not. There are some preferences among different researchers for CCM and PM, and Tarasov and Titov [2013] throughly investigated pros and cons of each model. However, it is not the focus of my PhD research, and I choose Pelton's model, which extensively used in mining applications, throughout my thesis. Hence when I am referring to the 'Cole-Cole model', that indicates PM.

1.4 Lab-scale IP Measurements

To understand how IP effects can be measured, I consider a lab-scale IP measurement system used in Geological Survey of Canada [Enkin et al.] as shown in Fig. 1.9. A core sample cut in a standardized size and shape is located between two cylinder-shaped copper electrodes. To prevent possible charge build-up on the contacts of electrodes and rock, two paper membranes, soaked with copper sulphate, are attached between the rock sample and copper electrodes. A source and a volt-meter are attached to the copper electrodes. The source generates a sinusoidal current ranging from 0.025Hz -1MHz, and the volt-meter measures the complex impedance at each transmitting frequency.

Fig. 1.10(a) shows the measured complex impedance from a core sample obtained from a Highland Valley region at British Columbia, Canada. This is a porphyry-copper deposit. The black solid lines show the observed amplitude and phase of the measured impedance. The observations are assumed to be the sum of a complex impedance associated with the rock as well as other instrument effects such as capacitive effects associated with the copper electrodes and electrode effects associated with the contacts between the copper sulfate paper and rock. The black dots are the predicted data associated with all of these effects. The contribu-

tion to the complex impedance that arises from the rock is marked as stars. This is the response of a Cole-Cole model, with parameters shown on the plot. For further details about extracting the impedance of the rock from the observations, the reader is referred to Enkin et al.. The Cole-Cole impedance reproduces the lower and mid-frequency parts of the observations. The chargeability of the porphyry is estimated to be $\eta = 0.16$ and the time constant $\tau = 2.6 \times 10^{-3}$s.

As a second example, I present the complex impedance of a core sample obtained from the DO-27/18 kimberlites. It is shown in Fig. 1.10b. This sample shows significantly different Cole-Cole parameters especially for the time constant (τ). For the kimberlite $\tau \simeq 4 \times 10^{-5}$s which is very small compared to that from the porphyry deposit. This difference may be due to different polarization mechanisms. The first sample from a porphyry deposit contains significant amount of pyrites which are possibly more related to metallic polarization. On the other hand, the sample from the kimberlite deposit (crater facies) contains a considerable amount of clay minerals with high porosity, and might be filled with water; more relevant to the membrane polarization and Maxwell-Wagner polarization. Nevertheless, the exact understanding for the cause of the IP response is not crucial for my research. An important point is that at the hand-specimen scale, these two rocks are associated with different IP parameters, and a geophysical experiment measured distinctly different Cole-Cole parameters may thus allow us to distinguish between them.

con

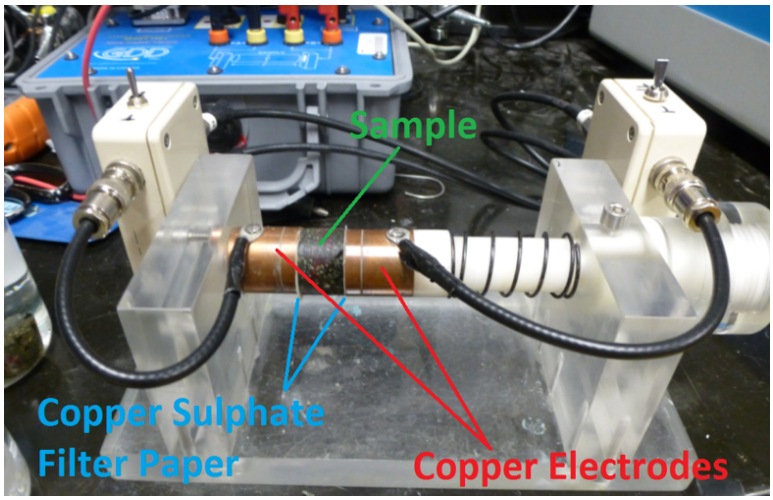

Figure 1.9: Lab scale IP measurement system in Geological Survey of Canada (GSC). The photo is taken from Cowan [2015].

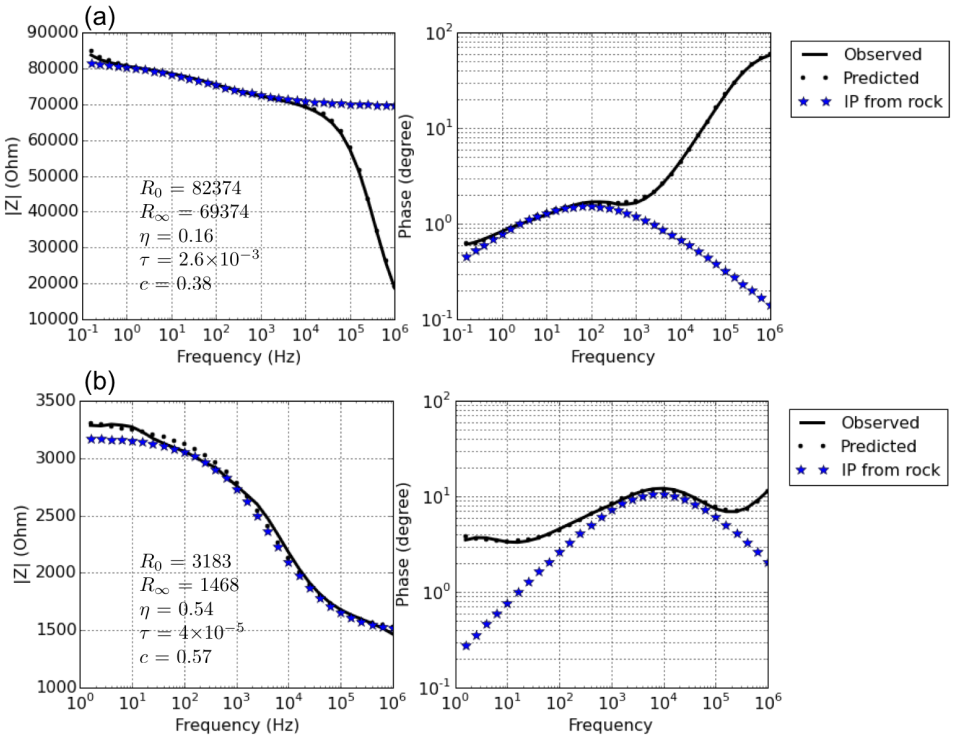

Figure 1.10: Complex impedance measurements using the Geological Survey of Canada system [Enkin et al.].

1.5 Modelling Maxwell's Equations

IP responses in various types of time-domain electromagnetic (TEM) surveys are governed by Maxwell's equations. When the electrical conductivity of the earth is frequency-dependent, then current density, $\vec{J}(\omega)$, in the frequency domain is

$$\vec{J} = \sigma(\omega)\vec{E}, \tag{1.10}$$

where $\vec{E}$ is the electric field (V/m) and $\sigma(\omega)$ is the frequency-dependent conductivity (S/m), which is complex-valued. The complex conductivity is plotted in Fig. 1.11(a) as a function of frequency. In the time-domain, eq. (1.10) can be written as

$$\vec{j} = \sigma(t) \otimes \vec{e}, \tag{1.11}$$

where $\otimes$ indicates a causal convolution, and $\vec{e}$ is the electric field. To compute TEM signals including IP effects, this convolution between $\sigma(t)$ and $\vec{e}$ needs to be taken account when solving Maxwell's equations. I first illustrate complex conductivity. For problems in the time-domain, it is convenient to work in the Laplace domain. The complex conductivity model in the Laplace domain can be expressed as

$$\sigma(s) = \sigma_\infty + \triangle\sigma(s), \tag{1.12}$$

where $s = \imath\omega$ is Laplace transform parameter and σ_∞ is the conductivity at infinite frequency. The inverse Laplace transform of this yields:

$$\sigma(t) = \mathscr{L}^{-1}[\sigma(s)] = \sigma_\infty\delta(t) + \triangle\sigma(t), \tag{1.13}$$

where $\mathscr{L}[\cdot]$ is a Laplace transform, $\delta(t)$ is a Dirac-delta function, and $\triangle\sigma(t) = \mathscr{L}^{-1}[\triangle\sigma(s)]$, which look like Fig. 1.11(b). Note that $\sigma(t)$ includes a delta function at t=0, and a decaying function after t=0 with negative amplitude. Its convolution with $\vec{e}$ is well-defined. Consider a special case for a Cole-Cole model (eq. 1.9) with c=1, $\triangle\sigma(s)$ can be expressed as

$$\triangle\sigma(\omega) = -\sigma_\infty \frac{\eta}{1 + (1-\eta)(s\tau)}, \tag{1.14}$$

In the time-domain, $\triangle\sigma(t)$ can be expressed as

$$\triangle\sigma(t) = -\sigma_\infty \frac{\eta}{(1-\eta)\tau} e^{-\frac{t}{(1-\eta)\tau}}. \tag{1.15}$$

Now I turn our attention to Maxwell's equations. Here I first define EM fields without and with IP effects, then introduce how IP data can be defined. The electromagnetic (EM) fields without IP effects are referred to as fundamental fields [Smith and West, 1989], and the corresponding Maxwell's equations can be written as

$$\vec{\nabla} \times \vec{e}^F = -\frac{\partial \vec{b}^F}{\partial t}, \tag{1.16}$$

$$\vec{\nabla} \times \frac{1}{\mu}\vec{b}^F - \sigma_\infty \vec{e}^F = \vec{j}_s. \tag{1.17}$$

Here the superscript F on EM fields in the above equations refers to fundamental fields, $\vec{b}$ is the magnetic flux density (Wb/m^2), $\vec{j}_s$ is the current source (A/m^2) and μ is the magnetic permeability (H/m). Observed data will include both EM and IP effects, and corresponding Maxwells equations can be written as

$$\vec{\nabla} \times \vec{e} = -\frac{\partial \vec{b}}{\partial t}, \tag{1.18}$$

$$\vec{\nabla} \times \frac{1}{\mu}\vec{b} - \vec{j} = \vec{j}_s, \tag{1.19}$$

Again, the total current $\vec{j}$ is a convolution of $\sigma(t)$ and $\vec{e}(t)$:

$$\vec{j}(t) = \mathscr{L}^{-1}[\sigma(s)\vec{E}(s)] = \sigma(t) \otimes \vec{e}(t) = \int_0^t \sigma(t-u)\vec{e}(u)du, \tag{1.20}$$

where $\vec{E}(s)$ is an electric field in the Laplace domain. Observed fields including both EM and IP effects can be defined as $\vec{e} = \vec{e}^F + \vec{e}^{IP}$, $\vec{b} = \vec{b}^F + \vec{b}^{IP}$ and $\vec{j} = \vec{j}^F + \vec{j}^{IP}$, where the superscript IP is induced polarization.

The IP response, d^{IP}, can be computed by subtracting the fundamental response d^F from the observation d:

$$d^{IP} = F[\sigma(s)] - F[\sigma_\infty] = d - d^F \tag{1.21}$$

where $F[\cdot]$ is Maxwell's operator. For example, $F[\sigma_\infty]$ outputs EM fields using a conductivity model σ_∞. Observed and fundamental responses correspond to $d = F[\sigma(s)]$ and $d^F = F[\sigma_\infty]$, respectively. By solving both Maxwells equations, I can evaluate both the observed and the fundamental responses, which allows me to compute d^{IP}. The subtraction in eq. (1.21) correspond to the EM-decoupling [Pelton et al., 1978, Routh and Oldenburg, 2001]. Note that when chargeability is zero, $\sigma(s) = \sigma_\infty$ and $d^{IP} = 0$. For these simulations I use EMTDIP code developed by Marchant et al. [2014]. This code is capable of solving the full Maxwell equations and hence of simulating both inductive current flow and galvanic current flow.

To understand how both fundamental and IP fields behave in a TEM survey, a simple grounded DC-IP survey, using a single source, is considered. The current waveform includes 2100 ms on- and off-time, in the transmitter wire, current flows in counter-clockwise direction. Fig. 1.12 shows a source wire path and the chargeability distribution in the core region of the 3D mesh (that is, padding cells are omitted). Chargeability of the chargeable block is 0.1. The conductivity model at the infinite frequency is a half-space conductivity, σ_{half} = 0.05 S/m. Two forward simulations are performed to compute observed ($d = F[\sigma(s)]$) and fundamental ($d^F = F[\sigma_\infty]$) responses. By subtracting d^F from d, the IP response (d^{IP}) is obtained. Computed potential difference at a receiver location (where the two electrodes are marked as black dots in Fig. 1.12(a) is shown in Fig. 1.13. Immediately after the current is switched on, significant EM induction arises due to Faraday's law, then as time proceeds the EM induction effect decays and the observed response converges to the steady-state. Similarly after the current switch-off, significant EM induction rises, and this decays as time passes. Here, the normalized potential difference is provided, which means $V(t)/V_0$, where $V(t)$ is the observed potential difference and V_0 is the potential at the DC limit.

Although only decay curves at a single receiver locations are provided in Fig. 1.13, electric field exists everywhere in the domain and seeing that in higher dimension can promote understanding of both EM and IP effects in this time-domain DC-IP survey. Figs. 1.14(a) and (b) respectively show plan and section views of the electric fields at 6 ms (the top panel), 715 ms (the middle panel), and 2116 ms (the bottom panel). These three times are marked as the black dashed lines in Fig. 1.13. At 6 ms, I can clearly recognize the induced EM signals from the current

wire path; those then disappear as at later when the voltage asymptotes to the DC limit. In the on-time, the IP response (red line) is much smaller than the fundamental response (blue line), whereas in the off-time the IP responses are large enough to be identified at late times. Fig. 1.15 show only off-time signals in the form of log-scaled normalized potential. Note that "off-time" indicates a time after current is turned off, and this time is set to zero (0 ms) when presenting off-time data. Dashed and solid lines differentiate the sign of responses, negative and positive respectively. At early times ($\sim$ 10 ms), observed and fundamental responses are almost coincident because EM induction is dominant at this time. At later time, the relative strength of the IP increases, and is dominant at 500 ms. Fig 1.16 shows the electric fields at three off-times (6, 77, and 1717 ms). Significant EM induction effects are observed at 6 ms near the current wires. At 77 ms, this EM induction effect smoothly diffuses away except for the chargeable region, where polarization charges have been been built. At 1717 ms EM induction is decayed significantly and hence IP is dominant. Here the chargeable block acts as a current dipole, which has opposite direction to the DC currents shown in Fig. 1.14, and this is consistent with the conceptual model described in Fig. 1.3(c). Grid of electrodes are deployed on the surface, and the potential differences of the shortest dipole in x-direction are shown as a map in Fig. 1.17. Three time channels at (a) 6 ms, (b) 715 ms, and (c) 2116 ms are shown here, and the plotted potential differences can be considered as electric fields in x-direction ($\vec{e} = -\nabla\phi$, where ϕ is the potential).

Conversely, most of time-domain DC-IP surveys assume that IP-dominant times are measured. However, when earth medium is highly conductive this assumption could be invalid. For instance, consider a simple case where the halfspace conductivity σ_{half} is increased to 0.5 S/m (previous one was 0.05 S/m). Fig 1.18 shows the normalized potential at both on- and off-time channels. Compared to the previous example, EM induction decays much slowly resulting in slower converges to the steady-state in on-time. In off-time, as shown in Fig. 1.19, d and d^F are almost coincident indicating EM is always dominant at all times. Fig 1.20 shows the measured potential difference at the off times.

To summarize, in observation d, which includes both EM and IP effects, natural separation of EM and IP responses in time exists as shown in Fig. 1.15:

- Early-time: EM-dominant
- Intermediate time: Both EM and IP are considerable
- Late-time: IP-dominant

At the EM-dominant time, the observation includes minor IP effect hence this can be used to recover conductivity distribution. Conversely at the IP-dominant time, EM induction effects in the observation are minor, thus these data can be used to recover a chargeability distribution. At intermediate time, both EM and IP effects are significant and here removal of either the EM or IP response (often called EM- or IP-decoupling) is required; this depends upon which information (conductivity or chargeability) is desired. Although a simple time-domain DC-IP example is shown here, a physical concept that an observed TEM signal shows natural separation of EM and IP effects in time is general enough to be extended to various TEM surveys (e.g. airborne EM).

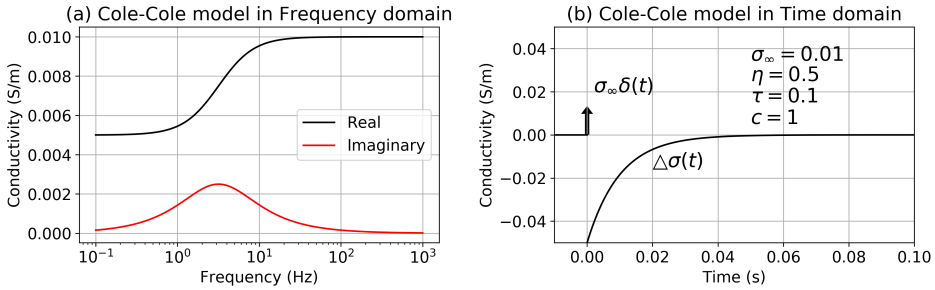

Figure 1.11: Cole-Cole response in frequency domain (a) and time (b) domain. The Cole-Cole parameters are $\sigma_\infty = 10^{-2}$ S/m, $\eta = 0.5$, $\tau = 0.1$ s, and c=1. The arrow indicates a Dirac-delta function ($\sigma_\infty \delta(t)$).

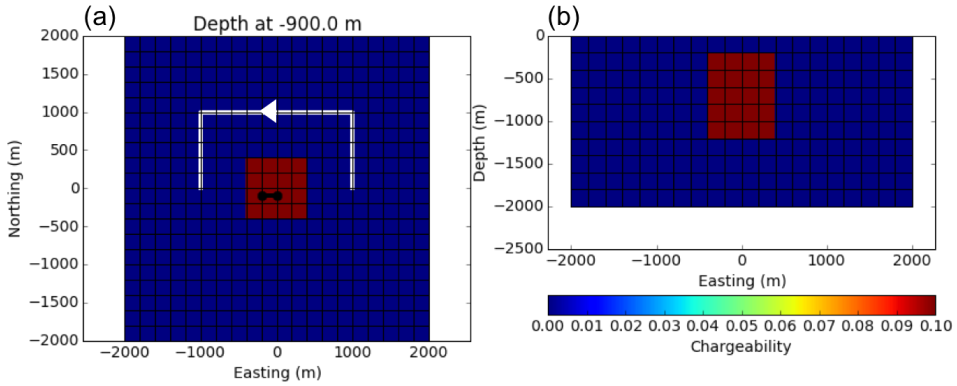

Figure 1.12: 3D chargeability model. (a) Plan and (b) Section views. White solid line on (a) shows the wire path, and the arrow indicates the direction of current in the wire when current is turned on. THe half-space conductivity is 0.05 S/m.

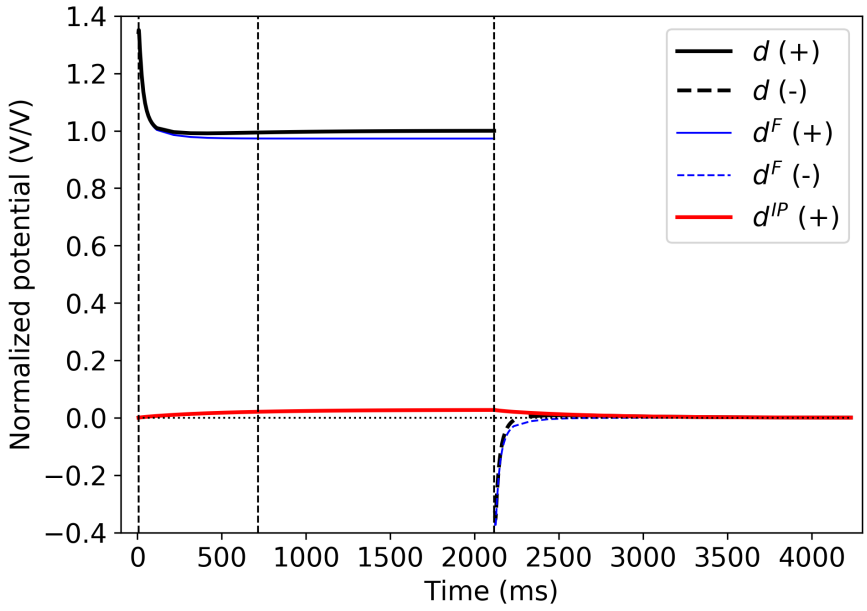

Figure 1.13: Time curves of the normalized potential difference at a receiver location (marked as black solid line with dots in Fig. 1.12(a)). Black, blue and red lines correspondingly indicate observed, fundamental and IP data. Solid and dashed lines distinguish positive and negative values. Black vertical dashed lines at three time channels indicate times at which the electric field distributions in Fig. 1.14 are provided. The halfspace conductivity is 0.05 S/m.

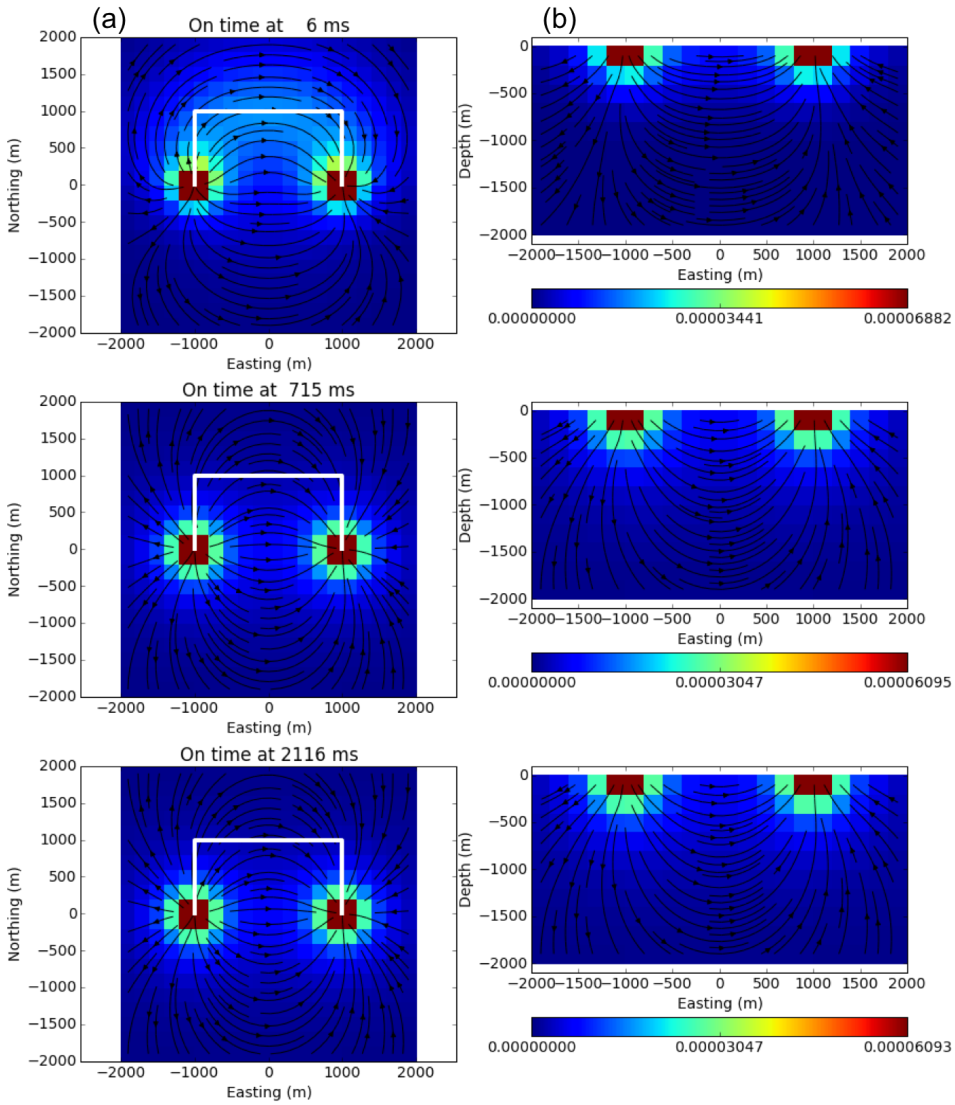

Figure 1.14: 3D electric field distributions at three different times in the on-time. Top, middle and bottom panel correspondingly show the electric fields at 6 ms, 77 ms, and 1717 ms. (a) Plan view at the surface and (b) Section view at Northing 0 m. The halfspace conductivity is 0.05 S/m.

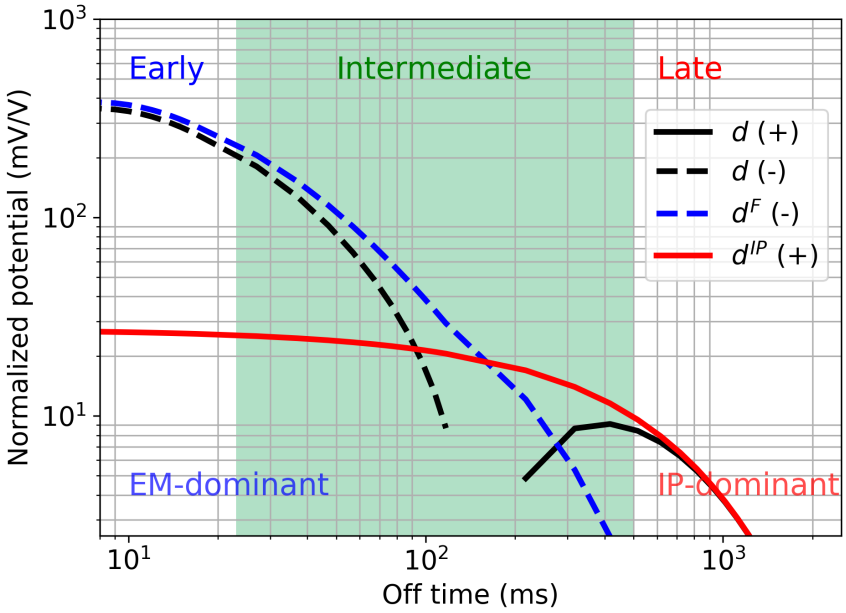

Figure 1.15: Time decaying curves of the normalized potential difference when the current is turned off. Black, blue, and red lines respectively indicate observed, fundamental and IP data. Dotted and solid lines distinguish positive and negative values. Halfspace conductivity is 0.05 S/m.

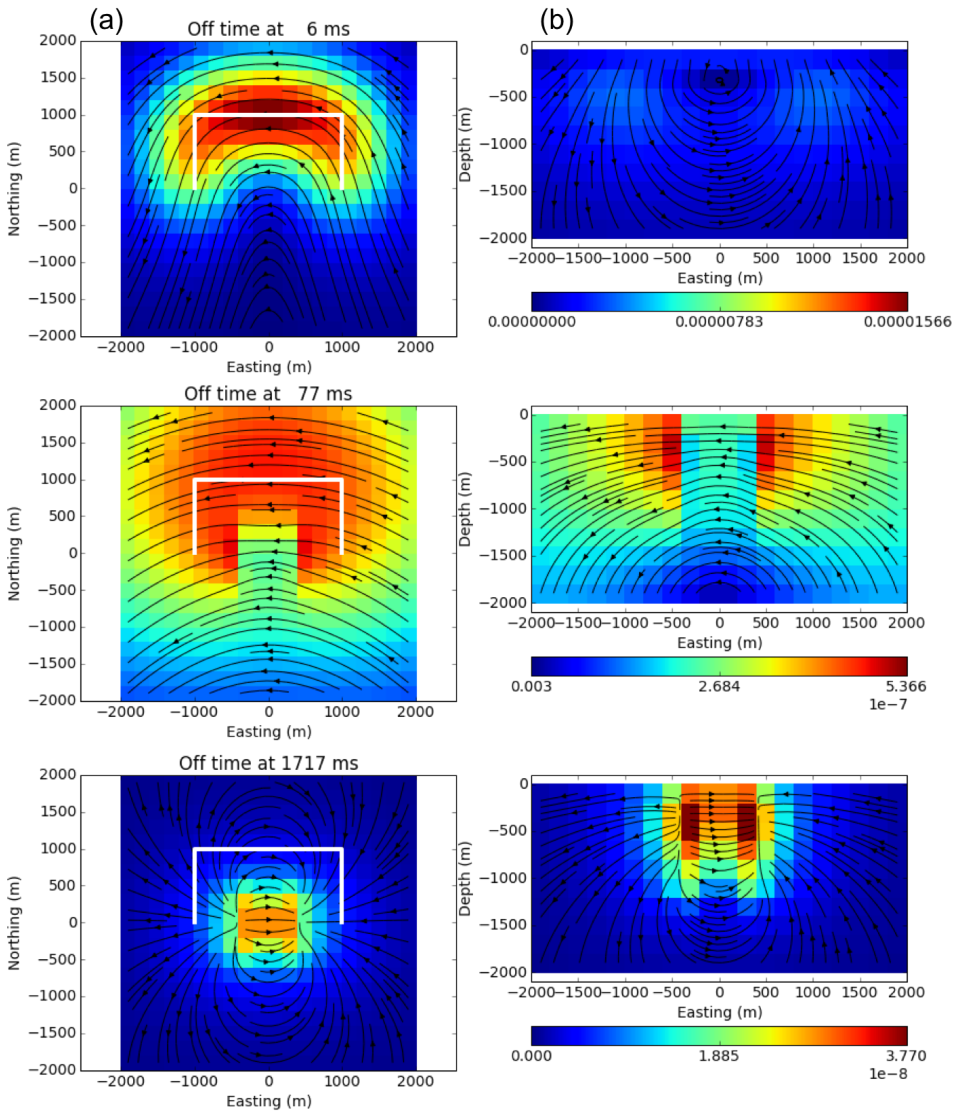

Figure 1.16: 3D electric field distribution at three different times when the current is turned off. Top, middle and bottom panel correspondingly show the electric fields at 6 ms, 715 ms, and 2116 ms. (a) Plan view at the surface and (b) Section view at Northing 0 m. The halfspace conductivity is 0.05 S/m.

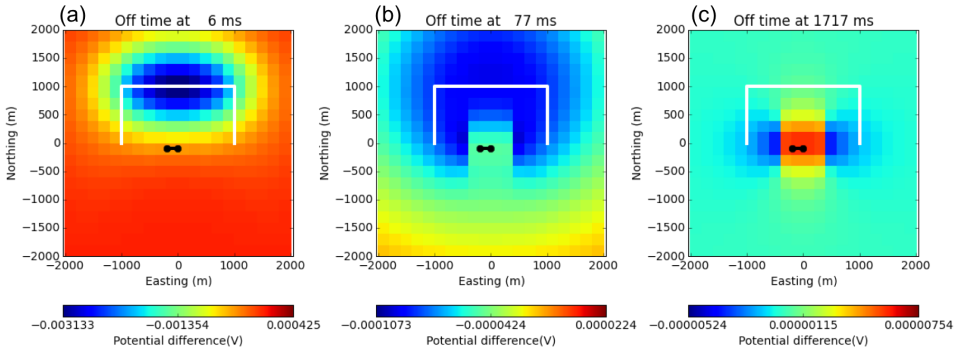

Figure 1.17: Observed potential difference at three different off times. (a) 6 ms, (b) 77 ms, and (c) 1717 ms. Halfspace conductivity is 0.05 S/m.

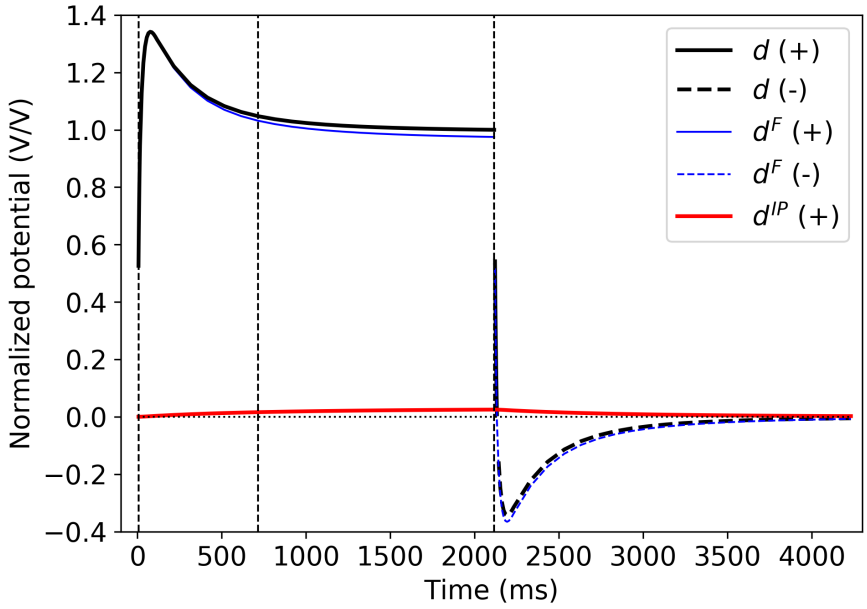

Figure 1.18: Time curves of the normalized potential difference at a receiver location (marked as black solid line with dots in Fig. 1.12(a)). Halfspace conductivity is 0.5 S/m.

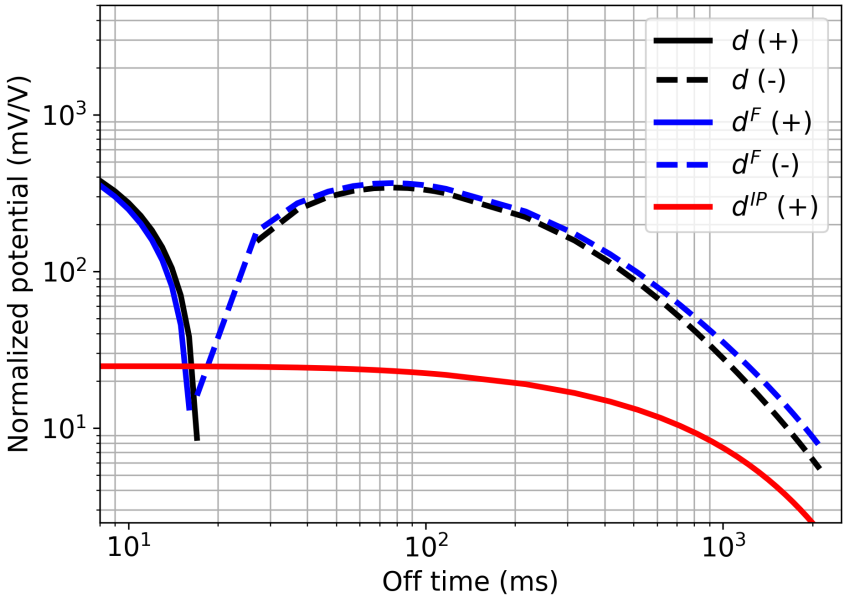

Figure 1.19: Time decaying curves of the normalized potential difference when current is turned off. Halfspace conductivity is 0.5 S/m.

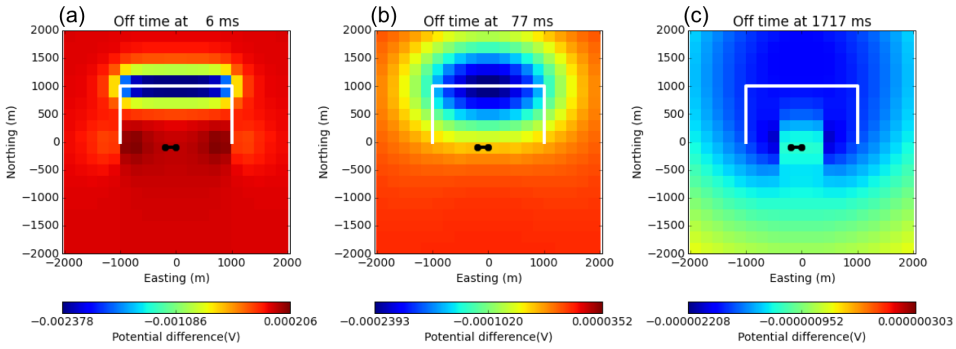

Figure 1.20: Observed potential difference at three different off times. (a) 6 ms, (b) 77 ms, and (c) 1717 ms. Halfspace conductivity is 0.5 S/m.

1.6 TEM-IP Inversion Workflow

The previous examples show how IP and EM induction phenomenon affect EM data. A primary goal of this thesis is to recover distributed IP information in 3D from observed TEM data, which include both EM and IP signals. An effective strategy is required to achieve this goal, and three main options can be considered:

- Formulate an inverse problem to find a complex conductivity: $\sigma(x, y, z; \omega)$. For instance, in frequency domain, each frequency can be inverted separately or simultaneously, and recover a complex conductivity distribution [Kemna et al., 2004, Commer et al., 2011].

- Parameterize complex conductivity as a few parameters (e.g. Cole-Cole: σ_∞, η, τ, and c), then measured data can jointly be inverted for those multiple parameters [Fiandaca et al., 2012, Marchant et al., 2013, Xu and Zhdanov, 2015].

- Realize that the signal has an early (EM) part, a late (IP) part and an intermediate zone of mixed signals as shown in Fig. 1.15. Isolate these by applying EM-decoupling or IP-decoupling, and work with each independently. This is what has been done with most routine applications Oldenburg and Li [1994]. For instance, a two-stage approach for DC-IP data inverts late on-time data (DC) to recover conductivity and uses that conductivity to invert early off-time data (IP) to recover a chargeability.

The first and second options are advantageous given that they are taking account both EM and IP effects simultaneously. However, in particular for a 3D inversion, those choices will increase both non-uniqueness and computational cost of the inversion dramatically, since model space is enlarged at least four times (e.g. Cole-Cole) and the computational cost of solving Maxwell's equations is increased due to time-dependent conductivity [Marchant et al., 2014]. The third option is robust and cost-effective, but this will have issues when earth medium includes conductive structures resulting in significant EM-coupling even at the latest time channel, or there are very early-time IP effects that make conductivity estimation difficult.

Each option has pros and cons, but basically depends on how observed data, d are represented. Here d can be any types of EM fields or fluxes that can be measured. Two choices are

$$d = F[\sigma(x,y,z;\omega)], \tag{1.22}$$

$$d = F[\sigma_\infty] + d^{IP}. \tag{1.23}$$

eq. (1.22) indicates that the observation can be simulated as a non-linear function, which takes a complex conductivity $\sigma(x,y,z;\omega)$; here both EM and IP effects are coupled into the observation. In contrast as described in eq. 1.23, the observation can also be separated as EM and IP, and treated separately. For this case, the IP datum, d^{IP} can be linearized as described in Seigel [1974], Oldenburg and Li [1994]: $d^{IP} = J\tilde{\eta}$, which yields

$$d = F[\sigma_\infty] + J\tilde{\eta}, \tag{1.24}$$

where J is a sensitivity function and $\tilde{\eta}$ is a pseudo-chargeability [1]; its definition will be described in Chapter 2. I prefer the second view point (eq. 1.24), which decomposes two different physical effects, and provides a way to linearize d^{IP}. From a learning point of view, separating EM and IP parts in the observation, investigating how each physical effect behaves, and even linearizing the IP part for various TEM surveys, promotes physical understanding of each phenomenon.

Therefore, I choose the third option and modify the two-stage approach so that it could handle EM-coupling in the observation. This new workflow is named the TEM-IP inversion workflow, and its procedures are as follows:

- The first step is to estimate a background conductivity. To achieve this, the late on-time or the early off-time data can be inverted by respectively using the DC or TEM inversion algorithms to recover conductivity, σ_{est}. Either way, a selection of data for inversion assumes that any IP effects in the data are insignificant.

- Using the estimated conductivity σ_{est}, a TEM response can be computed;

[1] I note that pseudo-chargeability, $\tilde{\eta}$ is different from Cole-Cole chargeability, $\eta = \frac{\sigma_\infty - \sigma_0}{\sigma_\infty}$

this is an approximate fundamental response: $F[\sigma_{est}]$. By subtracting this from the observation, the IP data can be defined:

$$d^{IP}[\sigma_{est}] = d - F[\sigma_{est}],$$

and this corresponds to EM-decoupling.

- Then develop a linearized function of d^{IP}:

$$d^{IP} = J\tilde{\eta}$$

and this linear equation is used to recover a pseudo-chargeability by inverting the obtained IP data, $d^{IP}[\sigma_{est}]$.

1.7 Thesis Outline

The main goals of this thesis are:

- Develop a methodology by which IP information about the 3D earth's subsurface can be extracted from inductive and grounded sources.
- Contend with important aspects of EM-coupling.
- Apply the technique to field data sets from TEM surveys.

As introduced in Section 1.6, the TEM-IP inversion workflow has three main steps: (a) Invert TEM data to recover conductivity distribution. (b) Subtract the predicted EM response (obtained by the recovered conductivity) from the observation, to obtain IP data. (c) Using a linearized IP function, invert the IP data to recover a distributed chargeability information. The application of the workflow is focused on two types of TEM surveys: (a) AEM and (b) DC-IP surveys. Chapters 2 and 3 presents how the IP signal from an inductive source is linearized as a function of a pseudo-chargeability, and how a 3D IP inversion is developed to recover 3D distribution of the pseudo-chargeability. The TEM-IP inversion workflow is applied to both the AEM and DC-IP surveys. In Chapter 4, I concentrate upon the inversion of synthetic and field AEM data sets. Here, one synthetic example (Section 4.1) and two field examples: the Mt. Milligan porphyry deposit (Section 4.2) and Tli Kwi Cho (TKC) kimberlites (Section 4.3) are presented. The workflow is general and hence it can also be applied to grounded sources. Chapter 5 presents the application of the workflow to the gradient array DC-IP survey, and emphasizes the use of early-time TEM data to recover a better conductivity model, and its use for the EM-decoupling for the late off-time IP data.

Collectively, my specific contribution to science includes:

1. Developing the TEM-IP inversion workflow to recover both conductivity and chargeability information in 3D from various TEM surveys.
2. Deriving and verifying a linear IP functional for inductive sources and in particular for AEM surveys.

3. Recovering both conductivity and chargeability information from AEM data that include negative transients. In particular, my work on a kimberlite deposit (TKC) shows how 3D conductivity and chargeability information can be an important component of generating a geophysical (and alternatively geologic) rock model from AEM data.

4. Removing EM-coupling in the DC-IP data to obtain better 3D chargeability by using early-time TEM signals, which are often discarded.

Chapter 2

Linearization

Earth materials are chargeable, hence polarization charges and currents can be generated whenever an electric field is applied. Hence any EM data set can include IP effects, and effectively interpreting these IP data has been an important issue. For a DC source (grounded source without EM-coupling), a linearized form of IP data is well-known [Seigel, 1959], and successfully used as a forward kernel for IP inversions [Oldenburg and Li, 1994, Li and Oldenburg, 2000]. Seigel's basic idea is that polarization effects can be considered as a small perturbation in conductivity, which can be written as

$$\sigma = \sigma_\infty(1-\tilde{\eta}). \tag{2.1}$$

Here σ includes polarization effects, but σ_∞ does not; recall, $\sigma(s) = \sigma_\infty$ (with $s = \imath\omega$) when $\eta = 0$. Here ω is the angular frequency. Pseudo-chargeability $\tilde{\eta}$ is often assumed to be small ($\tilde{\eta} \ll 1$). Note that the pseudo-chargeability is not the same as the chargeability ($\eta = \frac{\sigma_\infty - \sigma_0}{\sigma_\infty}$), but it is similar in the sense that both of them can be thought as a small fraction of conductivity change. Now based upon eq. (2.1) and following Seigel [1959], IP data can be linearized using Taylor's expansion

$$\begin{aligned} d^{IP} &= F_{dc}[\sigma_\infty(1-\tilde{\eta})] - F_{dc}[\sigma_\infty] \\ &\approx -\frac{d\, F_{dc}[\sigma_\infty]}{d\, log(\sigma_\infty)}\tilde{\eta} = J_{dc}[\sigma_\infty]\tilde{\eta}, \end{aligned} \tag{2.2}$$

where $F_{dc}[\cdot]$ is a DC operator, which takes conductivity and computes a DC response, and $J_{dc}[\sigma_\infty] = -\frac{d\ F_{dc}[\sigma_\infty]}{d\ log(\sigma_\infty)}$ is a sensitivity function.

Extension of this linearization to an inductive source is not available, and this limits the capability to apply the TEM-IP inversion workflow to inductive source IP (ISIP) data to restore polarizable information. The challenge posed by the use of inductive sources is that steady-state electric fields are not established inside the earth as they are for the DC source. At any location in the earth the electric field will increase to a maximum value and then decrease as the electromagnetic (EM) wave diffuses through. The EM fields at any position and time depending upon the convolution of the electric field with the time-dependent conductivity of the rock. Unraveling these complexities, and linearizing ISIP data are issues that I address in this Chapter. Systematic numerical verifications will support validity of the derivation, and these will be focused upon the airborne EM (AEM) geometry. Although the focus is linearizing the ISIP, the developed IP function will be general enough to handle IP data from various TEM surveys (e.g. AEM and DC-IP surveys).

2.1 Pseudo-chargeability

The goal of this chapter is to linearize ISIP data as a function of pseudo-chargeability. Here I define what the pseudo-chargeability is, and build a foundation for the following sections.

Polarization phenomenon is effectively described by a complex conductivity model, and its general form (with $s = \imath\omega$) is a good starting point:

$$\sigma(s) = \sigma_\infty + \triangle\sigma(s). \tag{2.3}$$

Here ω is the angular frequency. Depending upon the choice of a complex conductivity model, $\triangle\sigma(s)$ can be defined differently; for instance $\triangle\sigma(s)$ of Pelton's Cole-Cole model is:

$$\triangle\sigma(s) = -\frac{\sigma_\infty\eta}{1+(1-\eta)(s\tau)^c}. \tag{2.4}$$

Fig. 2.1(a) shows an example Cole-Cole model as a function of frequency. The time-domain form of complex conductivity can be obtained using inverse Laplace

transform:

$$\sigma(t) = \mathscr{L}^{-1}[\sigma(s)] = \sigma_\infty \delta(t) + \triangle\sigma(t), \tag{2.5}$$

where $\delta(t)$ is Dirac delta function, and $\mathscr{L}^{-1}[\cdot]$ is inverse Laplace transform operator. Note that only a causal function is considered here, which is only defined when $t \geq 0$.

The chargeability η is

$$\eta = -\frac{1}{\sigma_\infty} \lim_{t\to\infty} \mathscr{L}^{-1}[\frac{\triangle\sigma(s)}{s}] = \frac{\sigma_\infty - \sigma_0}{\sigma_\infty}. \tag{2.6}$$

Here $\triangle\sigma(s)$ is divided by s to obtain a step-function in time. It is convenient to define an time-dependent impulse reponse, $\tilde{\eta}^I(t)$, as

$$\tilde{\eta}^I(t) = -\frac{\triangle\sigma(t)}{\sigma_\infty}. \tag{2.7}$$

which transforms to

$$\triangle\sigma(t) = -\sigma_\infty \tilde{\eta}^I(t), \tag{2.8}$$

Note that the intrinsic chargeability, η, is not time-dependent but the impulse pseudo-chargeability, $\tilde{\eta}^I(t)$ is time-dependent. The Cole-Cole response in time-domain is shown in Fig. 2.1(b). The arrow at t=0 s indicates $\sigma_\infty\delta(t)$, which is a delta function, and after t=0 s, $\sigma(t) = \triangle\sigma(t)$. When $c = 1$, the inverse Laplace transform can be evaluated and the corresponding $\tilde{\eta}^I(t)$ is:

$$\tilde{\eta}^I(t) = \frac{\eta}{(1-\eta)\tau} e^{-\frac{t}{(1-\eta)\tau}}. \tag{2.9}$$

Ohm's law describes how currents are generated when an electric field is applied to a conductive medium, and in Laplace domain it can be written as

$$\vec{J}(s) = \sigma(s)\vec{E}(s) \tag{2.10}$$

The inverse Laplace transform of this yields

$$\vec{j}(t) = \mathscr{L}^{-1}[\vec{J}(s)] = \sigma(t) \otimes \vec{e}(t), \tag{2.11}$$

where $\otimes$ is a causal convolution.

I define the IP currents, $\vec{j}^{IP}$, as the total current ($\vec{j}$) minus the fundamental current ($\vec{j}^{F}$):

$$\vec{j}^{IP} = \vec{j} - \vec{j}^{F}. \tag{2.12}$$

Using eqs. (2.5) and (2.11) I obtain

$$\vec{j}^{IP} = \sigma_{\infty}\vec{e}^{\,IP} + \vec{j}^{pol}, \tag{2.13}$$

where the polarization current ($\vec{j}^{pol}$) is

$$\vec{j}^{pol}(t) = \triangle\sigma(t) \otimes \vec{e}(t). \tag{2.14}$$

If the electric field has different characteristics for inductive and grounded sources this will generate different features in the polarization current. Consider two cases: (1) a DC source with grounded electrodes and (2) an inductive source. The first case corresponds to the usual approache for interpreting DC-IP data [Seigel, 1959, Oldenburg and Li, 1994], and the second is associated with ISIP. The polarization current is a convolution between $\triangle\sigma$ and $\vec{e}$ (eq. 2.14), and Fig. 2.2(a) illustrates this process for case (1) with known $\vec{e}$. Here the electric field is instantaneously turned on then off, which emulates an electric field from case (1) without EM induction effects. This electric field is convolved with $\triangle\sigma$, and outputs the $\vec{j}^{pol}$, which has the opposite sign of the electric field (due to negative $\triangle\sigma$). As shown in Fig. 2.2(b), a similar process is applied for case (2), and here $\vec{e}$ has a different time behavior because case (2) excites the earth inductively. It starts from zero, increases to a peak then decays. The resultant $\vec{j}^{pol}$ shows a similar time behavior to the applied electric field. Comparison of $\vec{j}^{pol}$ due to cases (1) and (2) illustrates different polarization buildups when the earth's subsurface is excited differently. The main difference in between cases (1) and (2) is that the absence of steady-state electric field for case (2) resulting in a more dynamic polarization process for case (2).

To capture this difference in a linearized IP function, pseudo-chargeability,

$\tilde{\eta}(t)$ is defined as

$$\tilde{\eta}(t) = -\frac{\vec{j}^{pol}(t)}{\vec{j}^{ref}}, \tag{2.15}$$

where the reference current, $\vec{j}^{ref}$ is defined as

$$\vec{j}^{ref} = \sigma_\infty \vec{e}^{ref}. \tag{2.16}$$

Here $\vec{e}^{ref}$ is the reference electric field, and a choice of $\vec{e}^{ref}$ is described below. The pseudo-chargeability defined in eq. (2.15) is the ratio of the polarization current to the reference current. The pseudo-chargeability is a small quantity and this plays an essential role in our linearization. To evaluate the pseudo-chargeability, a reference current or reference electric field $\vec{e}^{ref}$ is required to be identified; in my definition (eq. 2.15) this is independent of time. For DC-IP, the value of the electric field achieved when there is no IP is chosen, that is the value shown in Fig. 2.3(a). For the inductive source the peak electric field is selected as shown in Fig. 2.3(b).

Each pixel in the earth has its own reference electric field and time that the peak value occurs thus both $\vec{e}^{ref}$ and t^{ref} have a 3D distribution. For both DC-IP and ISIP cases, the choice of the reference electric field can mathematically be presented as

$$\vec{e}^{ref} = \vec{e}^{F}(t) \otimes \delta(t - t^{ref}). \tag{2.17}$$

The reference time for the DC-IP case can be any time in the on-time. By rearranging eq. (2.15), I obtain

$$\vec{j}^{pol} = -\vec{j}^{ref}\tilde{\eta}(t). \tag{2.18}$$

This states that the polarization current has an opposite direction to the reference current, and is proportional to the pseudo-chargeability. This reversed direction of the current in a chargeable medium results from the negative values of the time-dependent conductivity when $t > 0$ as shown in Fig. 2.1(b). This conceptual model about the polarization current shown in eq. (2.18) is consistent with Seigel [1959]'s result. Note that for any pixel, even if $\vec{e}^{ref}$ attains the same value for an ISIP survey as for an DC-IP survey, the pseudo-chargeability resulting from an ISIP survey will be less than that from a DC-IP survey. To illustrate, let us assume e_0 and $\triangle\sigma$

shown in Fig. 2.2(a) and (b) are the same, but the area for the DC source will always be greater than the inductive source resulting in greater $\vec{j}^{pol}$; that is greater pseudo-chargeability. Considering the linearizations for DC-IP problems worked well when $\tilde{\eta}$ is small (< 1), I can infer from this that linearization techniques should be successful in ISIP problems, which have even smaller $\tilde{\eta}$ compared to DC-IP problems.

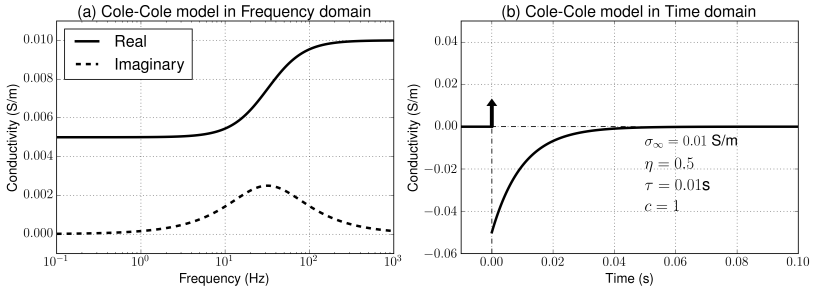

Figure 2.1: Cole-Cole response in frequency domain (a) and time (b) domain. The Cole-Cole parameters are $\sigma_\infty = 10^{-2}$ S/m, $\eta = 0.5$, $\tau = 0.01$ s, and c=1. The arrow shown in Fig. 2.1b indicates a delta function ($\sigma_\infty \delta(t)$).

2.2 Linear IP Function

Following from the methodologies in DC-IP, our goal is to express the IP response, d^{IP} as a linear function of the pseudo-chargeability, $\tilde{\eta}(t)$. That is I wish to write $d^{IP}(t) = J\tilde{\eta}(t)$, where J is a yet to be determined sensitivity function which is independent of time. In doing this first consider a general EM system which is applicable to grounded or inductive sources. For any volume pixel in the earth the amplitude and direction of the electric field can vary dramatically in time and thus the IP charging process can be complicated. However, if substantial polarization currents are developed, an assumption can be made that there was a sufficiently large electric field in a predominant direction to generate them. Although the direction of the electric field is constant the amplitude varies with time.

Let $\vec{e}(t)$ be approximated as

$$\vec{e}(t) \approx \vec{e}^{\,ref} \hat{w}(t), \tag{2.19}$$

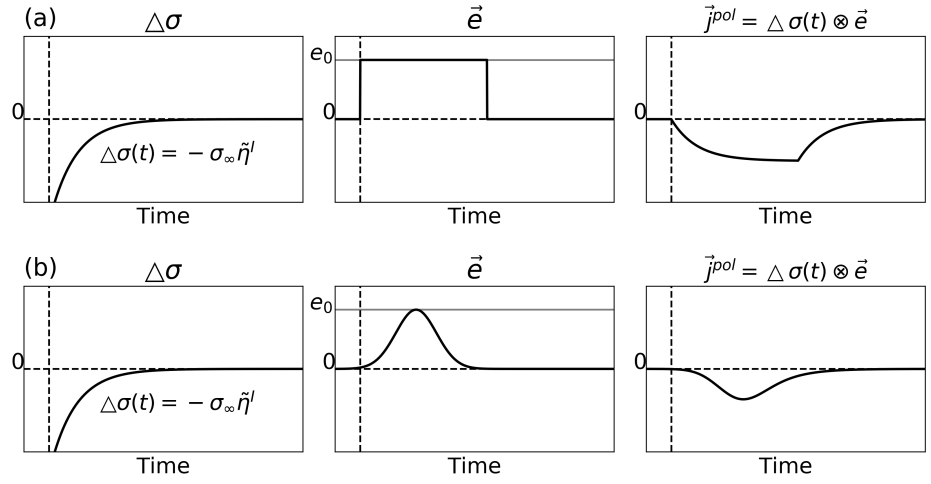

Figure 2.2: Convolution of $\triangle\sigma$ and $\vec{e}$ resulting in polarization current, $\vec{j}^{pol}$. (a) DC source. (b) Inductive source. $\triangle\sigma$ and $\tilde{\eta}^I$ are respectively defined in eqs. (2.8) and (2.7).

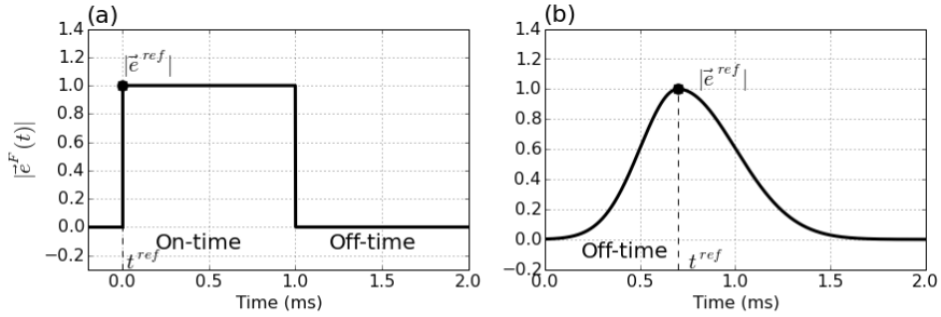

Figure 2.3: Conceptual diagram for the amplitude of the fundamental electric fields. (a) DC source. (b) Inductive source.

where $\hat{w}(t)$ is defined as:

$$\hat{w}(t) = P_0[w^{ref}(t)]. \tag{2.20}$$

Here a projection $P_0[\cdot]$ of an arbitrary time function, $f(t)$ is

$$P_0[f(t)] = \begin{cases} f(t) & f(t) \geq 0 \\ 0 & \text{if } f(t) < 0, \end{cases} \tag{2.21}$$

and

$$w^{ref}(t) = \frac{\vec{e}^{F}(t) \cdot \vec{e}^{\,ref}}{\vec{e}^{\,ref} \cdot \vec{e}^{\,ref}}. \tag{2.22}$$

$w^{ref}(t)$ is a dimensionless function that prescribes the time history of the electric field at each location along the direction of the chosen reference electric field, $\vec{e}^{\,ref}$. According to this definition, negative values of $w^{ref}(t)$ are set to zero in accordance with our conceptual model that polarization currents have an opposite direction to the reference current (eq. 2.18). The pseudo-chargeability is redefined as

$$\tilde{\eta}(t) = \tilde{\eta}^{I}(t) \otimes \hat{w}(t). \tag{2.23}$$

The polarization current, $\vec{j}^{pol}$ shown in eq. (2.14), can be approximated with eq. (2.7) as

$$\vec{j}^{pol}(t) \approx -\tilde{\eta}^{I}(t) \otimes \hat{w}(t)\vec{j}^{\,ref}. \tag{2.24}$$

Substituting into eq. (2.13) yields

$$\vec{j}^{IP}(t) \approx \sigma_{\infty}\vec{e}^{\,IP}(t) - \tilde{\eta}^{I}(t) \otimes \hat{w}(t)\vec{j}^{\,ref} \tag{2.25}$$

and this yields

$$\vec{j}^{IP}(t) \approx \sigma_{\infty}\vec{e}^{\,IP}(t) - \vec{j}^{\,ref}\tilde{\eta}(t). \tag{2.26}$$

The second term, $-\vec{j}^{\,ref}\tilde{\eta}(t)$ corresponds to polarization currents. In particular for ISIP, the first term, $\sigma_{\infty}\vec{e}^{\,IP}(t)$ is usually omitted [Smith et al., 1988]. This was because Smith et al. [1988] were mostly interested in chargeable targets that were significantly conductive compared to the background. However, if the conductivity of the chargeable target is similar to that of the background, the first term could be important. That first term is included here and the conditions in which it is important will be explored.

Because the reference current is static, any time-dependence in the polarization currents is encapsulated in the pseudo-chargeability. The buildup and decrease of polarization currents is a slow process and I assume therefore that this process does not produce induction effects ($\frac{\partial \vec{b}^{IP}}{\partial t} \approx 0$) and hence the IP electric field is assumed that it can be written as

$$\vec{e}^{\,IP} \approx \vec{e}^{\,IP}_{approx} = -\vec{\nabla}\phi^{IP}, \tag{2.27}$$

where ϕ^{IP} is the electrical potential for IP. By taking the divergence of eq. (2.26), I obtain

$$\nabla \cdot \vec{j}^{IP}(t) \approx \nabla \cdot \sigma_\infty \vec{e}^{\,IP}(t) - \nabla \cdot \vec{j}^{\,ref} \tilde{\eta}(t). \tag{2.28}$$

Here $\nabla \cdot \vec{j}^{IP} = 0$ because $\nabla \cdot \vec{j} = \nabla \cdot (\vec{j}^F + \vec{j}^{IP}) = -\nabla \cdot \vec{j}_s$, where $\nabla \cdot j^F = -\nabla \cdot \vec{j}_s$. Substituting $\vec{e}^{\,IP}$ with eq. (2.27) in eq. 2.28 and carrying out some linear algebra, I obtain

$$\phi^{IP}(t) \approx -[\nabla \cdot \sigma_\infty \vec{\nabla}]^{-1} \nabla \cdot \vec{j}^{\,ref} \tilde{\eta}(t). \tag{2.29}$$

By applying the gradient I obtain

$$\vec{e}^{\,IP}_{approx} = \vec{\nabla}\Big([\nabla \cdot \sigma_\infty \vec{\nabla}]^{-1} \nabla \cdot \vec{j}^{\,ref} \tilde{\eta}(t)\Big). \tag{2.30}$$

Thus, the electric field due to the IP effect can be expressed as a function of $\tilde{\eta}(t)$ in time. This form is also applicable to the DC-IP case, and the same form used for the conventional case (eq. 2.2) can be obtained from eq. (2.29):

$$\phi^{IP} \approx -\frac{d\ \phi_{\sigma_\infty}}{d\ log(\sigma_\infty)} \tilde{\eta}, \tag{2.31}$$

with $\frac{d\ \phi_{\sigma_\infty}}{d\ log(\sigma_\infty)} = -[\nabla \cdot \sigma_\infty \vec{\nabla}]^{-1}\Big(\nabla \cdot \sigma_\infty \vec{\nabla} \phi_{\sigma_\infty}\Big)$ and ϕ_{σ_∞} is a DC potential with σ_∞. Here the reference electric field $\vec{e}^{\,ref}$ is set to $-\vec{\nabla}\phi_{\sigma_\infty}$. For the DC case, the time history of the electric field is basically the same as the input current waveform. Hence, when a step-off function: $1 - u(t)$ is used for the current waveform, the pseudo-chargeability is

$$\tilde{\eta}(t) = \tilde{\eta}^I \otimes (1 - u(t)). \tag{2.32}$$

For a Cole-Cole model with c=1, this can be explicitly written as

$$sam\tilde{\eta}(t) = \eta e^{-\frac{t}{(1-\eta)\tau}}, \tag{2.33}$$

which is a similar result to Hördt et al. [2006] and Yuval and Oldenburg [1997].

For inductive sources, often data are either $\vec{b}$ or its time derivative and hence $\vec{b}^{IP}$ or its time derivative needs to be computed. For this, I first compute $\vec{j}^{IP}$ then use the Biot-Savart law. By substituting eq. (2.30) into eq. (2.26), the approximated

IP current density, $\vec{j}^{IP}_{approx}$ can be expressed as

$$\vec{j}^{IP}(t) \approx \vec{j}^{IP}_{approx} = \bar{S}\vec{j}^{\,ref}\tilde{\eta}(t), \tag{2.34}$$

where $\bar{S}$ is a matrix operator comprised of to terms:

$$\bar{S} = \sigma_\infty \vec{\nabla}[\nabla \cdot \sigma_\infty \vec{\nabla}]^{-1}\nabla \cdot -\bar{I} \tag{2.35}$$

and $\bar{I}$ is an identity tensor. Applying the Biot-Savart law I have:

$$\vec{b}^{IP}_{approx}(\vec{r};t) = \frac{\mu_0}{4\pi}\int_\Omega \frac{\bar{S}\vec{j}^{\,ref}(\vec{r}_s)\times\hat{r}}{|\vec{r}-\vec{r}_s|^2}\tilde{\eta}(t)d\vec{r}_s, \tag{2.36}$$

where $\vec{r}_s$ indicates a vector for a source location, and $\hat{r} = \frac{\vec{r}-\vec{r}_s}{|\vec{r}-\vec{r}_s|}$. If $\sigma_\infty \vec{e}^{\,IP}$ is omitted in $\vec{j}^{IP}$ then the tensor, $\bar{S}$, becomes $-\bar{I}$. In this situation, the IP current is the same as the polarization current, and it always has an opposite direction to the reference current. This reversed current, along with the Biot-Savart law, provides a physical understanding about the negative transients in AEM data when the earth is chargeable.

Observed data are often the time derivative of $\vec{b}$, hence by taking time derivative of eq. (2.36), I obtain

$$-\frac{\partial \vec{b}^{IP}_{approx}}{\partial t}(\vec{r};t) = \frac{\mu_0}{4\pi}\int_\Omega \frac{\bar{S}\vec{j}^{\,ref}(\vec{r}_s)\times\hat{r}}{|\vec{r}-\vec{r}_s|^2}\Big(-\frac{\partial\tilde{\eta}(t)}{\partial t}\Big)d\vec{r}_s. \tag{2.37}$$

Here I have chosen to keep the minus signs in eq. (2.37) so that $-\frac{\partial\tilde{\eta}(t)}{\partial t}$ is positive when $\tilde{\eta}(t)$ is decaying in time. Accordingly, the IP datum is given by $-\frac{\partial\vec{b}^{IP}}{\partial t}$. Note that for inductive sources the time history of the electric field $\hat{w}(t)$ is not the same as the input current waveform. Thus, $\tilde{\eta}$ defined in eq. (2.23) is dependent upon the time history of electric field diffused in the earth medium for ISIP, whereas it only depends polarization parameters and the current waveform for DC-IP as shown in eq. (2.32).

The IP fields shown in eqs (2.30), (2.36) and (2.37) are linear functionals of $\tilde{\eta}$

and the equations for a single time channel can be discretized in space as

$$\mathbf{d}^{IP} = \mathbf{J}\tilde{\eta}, \tag{2.38}$$

where $\mathbf{J}$ is the corresponding sensitivity matrix. In particular when the observed datum is the time derivative of $\vec{b}$, the linear relationship can be written as

$$\mathbf{d}^{IP} = \mathbf{J}(-\frac{\partial \tilde{\eta}}{\partial t}\Big). \tag{2.39}$$

A detailed description for the discretization of the linearized kernel is shown in Appendices C.1 and C.2. The representation in eq. (2.38) is valid for both grounded and inductive sources but the two assumptions: (a) $\vec{e} \approx \vec{e}^{\,ref}\hat{w}(t)$ and (b) $\vec{e}^{\,IP} \approx -\vec{\nabla}\phi^{IP}$ need to be tested numerically for the case of inductive sources.

2.3 Numerical Experiments

For numerical experiments I concentrate upon the AEM survey. This choice is made because of the observed negative transients that are direct indicators of polarization effects [Weidelt, 1982], and the extensive use of this survey by industry [Smith and Klein, 1996, Kratzer and Macnae, 2012, Kaminski and Viezzoli, 2017, Kang et al., 2017]. I begin with a simple IP model composed of a chargeable block in a halfspace as shown in Figure 2.4. Cole-Cole parameters of the block are η = 0.2, τ = 0.005 s and c = 1. The conductivity of the halfspace, σ_1, is 10^{-3} S/m, whereas the conductivity of the chargeable body, σ_2, will be assigned different values; σ_∞ is thus a 3D distribution. I consider three cases: (a) canonical ($\sigma_2 = \sigma_1$), (b) conductive ($\sigma_2 = 10^2 \times \sigma_1$) and (c) resistive models ($\sigma_2 = 10^{-2} \times \sigma_1$). The 3D space is discretized with $50 \times 50 \times 50$ m core cells and the number of cells in the domain is $41 \times 41 \times 40$. The size of the chargeable body is $250 \times 250 \times 200$ m and the top boundary is located 50 m below the surface. The EMTDIP code [Marchant et al., 2014] is used to simulate EM responses that include IP effects. The survey, consisting of 11 soundings along each of 11 lines, is shown in Fig. 2.4(a). Data are from a coincident-loop system and the flight height is 30 m above the surface; the radius of the loop is 10 m. A step-off source waveform is used and the range of the observed time channels is 0.01-60 ms. The observed responses can be the vertical component of $\vec{b}$ or $\frac{\partial \vec{b}}{\partial t}$. In these numerical experiments, first the observed responses and the total currents are decomposed into fundamental and IP portions to aid in the basic understanding of IP effects in AEM data. Then, the linearized IP function is systematically validated by computing the approximate IP currents and IP responses, and comparing these with the true values.

2.3.1 IP Data

Using the EMTDIP code and carrying out two simulations: $d = F[\sigma(s)]$ and $d^F = F[\sigma_\infty]$, d^{IP} is obtained by subtracting d^F from d. Fig. 2.5 shows the d, d^F, and d^{IP} at a sounding location above the center of the chargeable body for (a) canonical, (b) conductive and (c) resistive models. Both b_z and $-\frac{\partial b_z}{\partial t}$ data are shown. The IP effects are most noticeable for the conductive body and I turn attention to this example first. The IP response starts to significantly affect the observations near 0.6

ms and the observed responses show a sign reversal near 1 ms. Beyond that time the signal is dominated by the IP. The dashed line in Fig. 2.5(b) shows that after turning off the source current, the IP current increases (as inferred by the magnitude of the b_z field) until about 1 ms and then decreases. I interpret this in terms of charging and discharging phases for the chargeable body and a vertical dashed line in the figure defines the two phases. In the charging phase at early times the EM effects dominate and IP signals are not expected to be observed. In the discharging phase, which occurs at later time, the IP effects may eventually dominate the EM effects. The maximum of the b_z^{IP} corresponds to the zero crossing for $-\frac{\partial b_z^{IP}}{\partial t}$ but the times at which the IP signal becomes dominant are delayed compared to b_z^{IP}. By comparing the observations with the fundamental fields I see that the IP signal could be recognized in the b_z data near 0.7 ms and near 2.0 ms in the $-\frac{\partial b_z}{\partial t}$ data.

The plots for the canonical and resistive bodies show that the time that separates charging and discharging occurs earlier than that for the conductive body. This is a reflection that the fundamental currents reside for a longer time in a conductor. For the canonical body, a significant difference between the measured responses and the fundamental fields occur about 0.9 ms for b_z and about 2 ms for $-\frac{\partial b_z}{\partial t}$. The amplitudes of the IP responses are significantly smaller than those for the conductor. Lastly, there is little IP signal for the resistive body; the IP signal is much smaller than the fundamental response throughout the given time range. This is a consequence of the small fundamental currents in the resistor.

The decay curves from a sounding location provide insight about the IP response but more is gleaned by looking at data from all sounding locations in the AEM survey. I focus on b_z^{IP} for the conductive block at selected time channels. Fig. 2.6 shows interpolated maps of the d, d^F and d^{IP} at (a) 0.86 ms and (b) 6.7 ms which are respectively included in the charging and discharging times. For the conductive block, 0.86 ms is close to the peak time when the transition from charging to discharging occurs, but it is still included in the charging time. At this time, the d are dominated by the d^F and no negative values, which are the signature of the IP effect, are observed. Subtracting the d^F however, yields a residual d^{IP} data map that has a strong negative. This example shows that our EM-decoupling procedure can work satisfactorily for this simple model. At 6.7 ms, obtaining good IP data is easier because the d already show negative values. There is still a weak

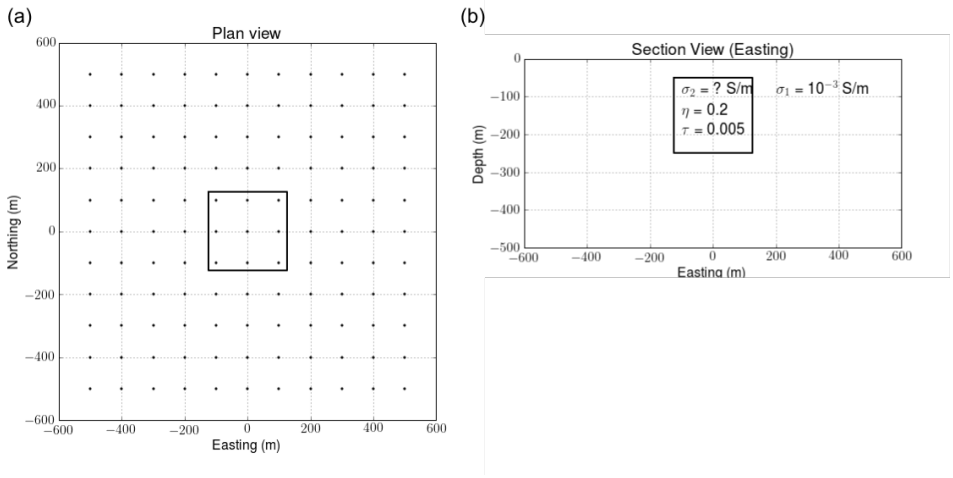

Figure 2.4: Plan (a) and section (b) views of the IP model. The solid line in (a) delineates the boundary of the IP body. Solid circles in (a) denote the sounding locations. In (b) the conductivity σ_2 is variable so that canonical, conductive and resistive blocks can be examined

fundamental field and the subtraction process improves the d^{IP} response. The d^{IP} data at 0.86 ms and 6.7 ms shown in Fig. 2.6 are of sufficient quality to be inverted.

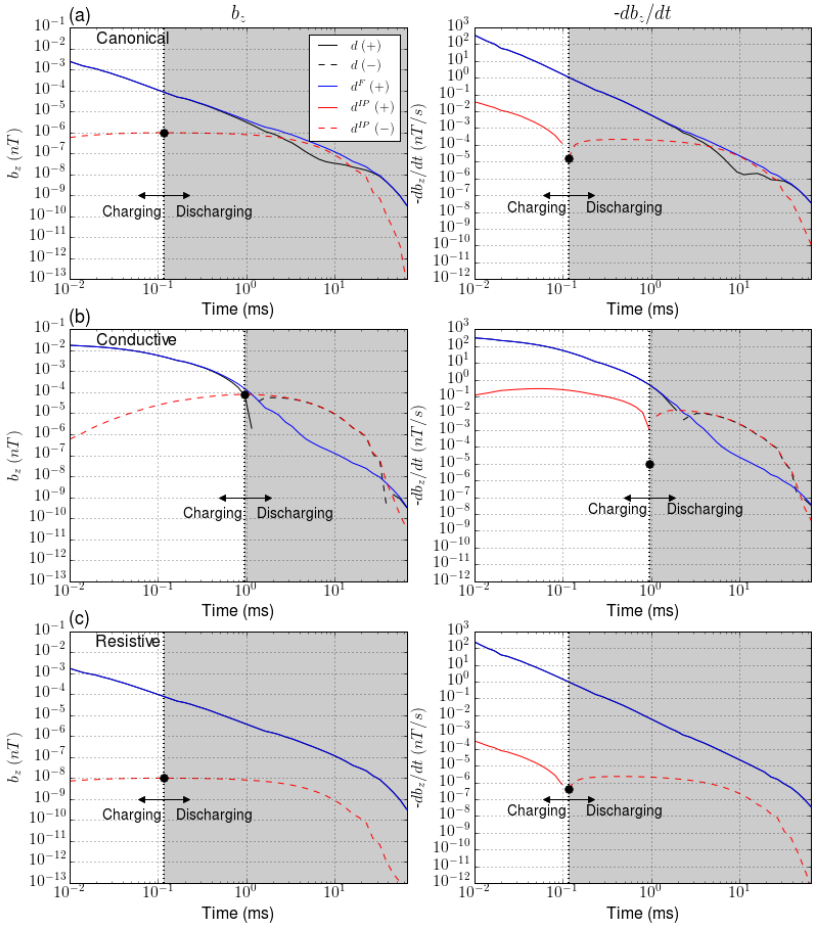

Figure 2.5: Time decaying curves of the observations (d; black line), fundamental (d^F; blue line) and IP (d^{IP}; red line) responses. All three cases: (a) canonical, (b) conductive and (c) resistive are presented. Right and left panels show b_z and $-\frac{\partial b_z}{\partial t}$. The vertical black dotted line indicates the time at which the polarization field reaches its maximum value. The flight height of the collocated transmitting and receiving loop is 30 m above the surface.

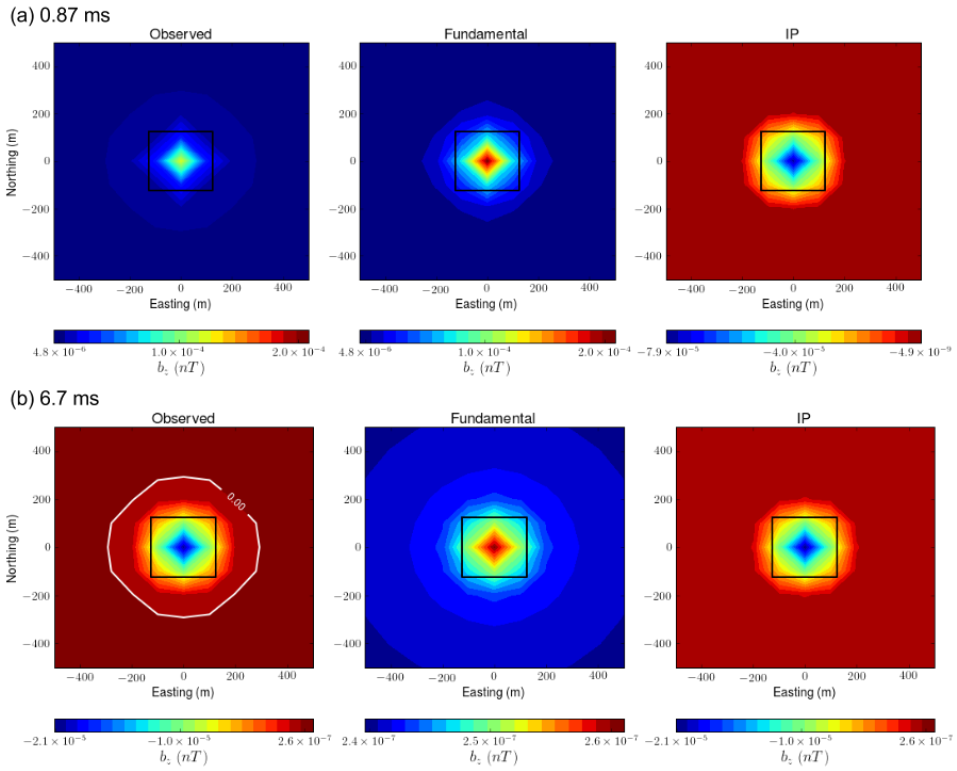

Figure 2.6: Interpolated maps of observed (left panel), fundamental (middle panel) and IP (right panel) responses. Two time channels at (a) 0.86 ms and (b) 6.7 ms are presented. The white line contours a zero-crossing in the observed response.

2.3.2 Polarization Currents

To evaluate the polarization current shown in eq. (2.14) for the linear functional, I assumed $\vec{e}(t) \approx \vec{e}^{\,ref} w^e(t)$ and defined our reference current as $\vec{j}^{ref} = \sigma_\infty \vec{e}^{\,ref}$. That yielded the polarization current to be $\vec{j}^{pol}(t) \approx -\vec{j}^{\,ref} \tilde{\eta}(t)$. This requires that the polarization current has a direction antiparallel to the reference current, and the direction is the same for all times. With this approximation the time dependence for the polarization currents only occurs through the scalar $\tilde{\eta}(t)$. The validity of the approximation is investigated by evaluating both reference and polarization currents numerically. From eq. (2.17), a reference current can be considered as the maximum fundamental current that occurred throughout the time history. To evaluate polarization currents I rearrange eq. (2.13) as $\vec{j}^{pol} = \vec{j}^{IP} - \sigma_\infty \vec{e}^{\,IP}$.

Here canonical and conductive blocks are used to compute $\vec{j}^{pol}$. Figs 2.7(a) and (b) show reference currents for the canonical and conductive blocks, respectively. A source is located at (-200 m, 0 m, 30 m) and marked as a white solid circle in the figure, where $(\cdot,\cdot,\cdot)$ refers to a point at (easting, northing, depth). Reference currents, $\vec{j}^{\,ref}$ for the canonical block are circular, centered on the source location, and decay with distance. For the conductive block, additional vortex currents are induced. These reference currents are compared with the polarization currents. Fig. 2.8 shows the plan and section view maps of the polarization currents at 0.86 ms. Comparisons of Figs 2.7 and 2.8 clearly show that polarization currents for both canonical and conductive blocks are oppositely aligned with respect to their reference current. This was the hypothesized outcome. Fig. 2.9 shows that the direction of $\vec{j}^{pol}$ at 6.7 ms is similar to those at 0.86 ms. Thus both for the canonical and conductive blocks, the direction of $\vec{j}^{pol}$ after 0.86 ms is constant in time.

Of particular interest is the difference in character of the $\vec{j}^{pol}$ for the canonical and conductive bodies. For the canonical body the $\vec{j}^{pol}$ look like anomalous galvanic currents that would be expected from an DC-IP survey. The resultant magnetic fields will be similar to the magnetic fields obtained from an electric dipole. For the conductive case however, the currents are circular and they reflect the vortex nature of the induced currents. The resultant magnetic fields are those associated with a magnetic dipole. The $\vec{j}^{pol}$ inside a body are therefore complicated by the fact that they are a mixture of galvanic (charge buildup) and inductive

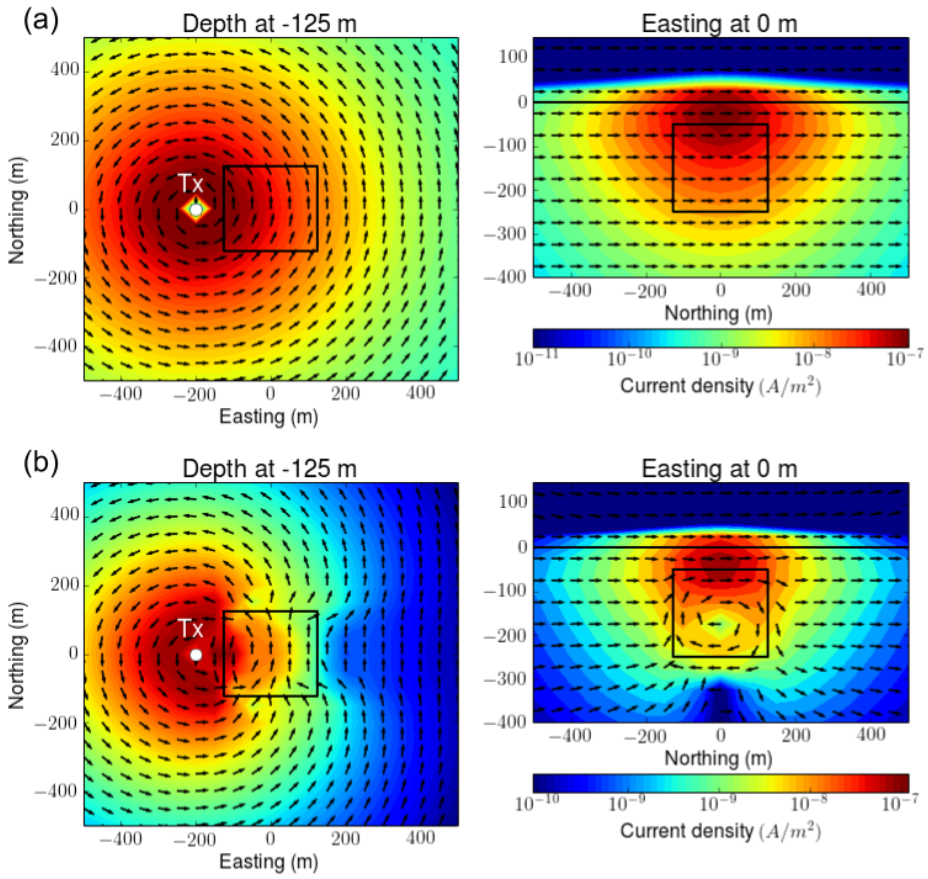

Figure 2.7: Maps of reference currents: (a) canonical and (b) conductive models. Left and right panels show plan and section views at -125 m-depth and 0 m-easting, respectively. A source is located at (-200 m, 0 m, 30 m). Black arrows and colored background respectively indicate the direction and amplitude of the current. Black solid lines outline the boundary of the chargeable body.

processes. Our choice of $\vec{j}^{\,ref}$ effectively incorporates this complexity.

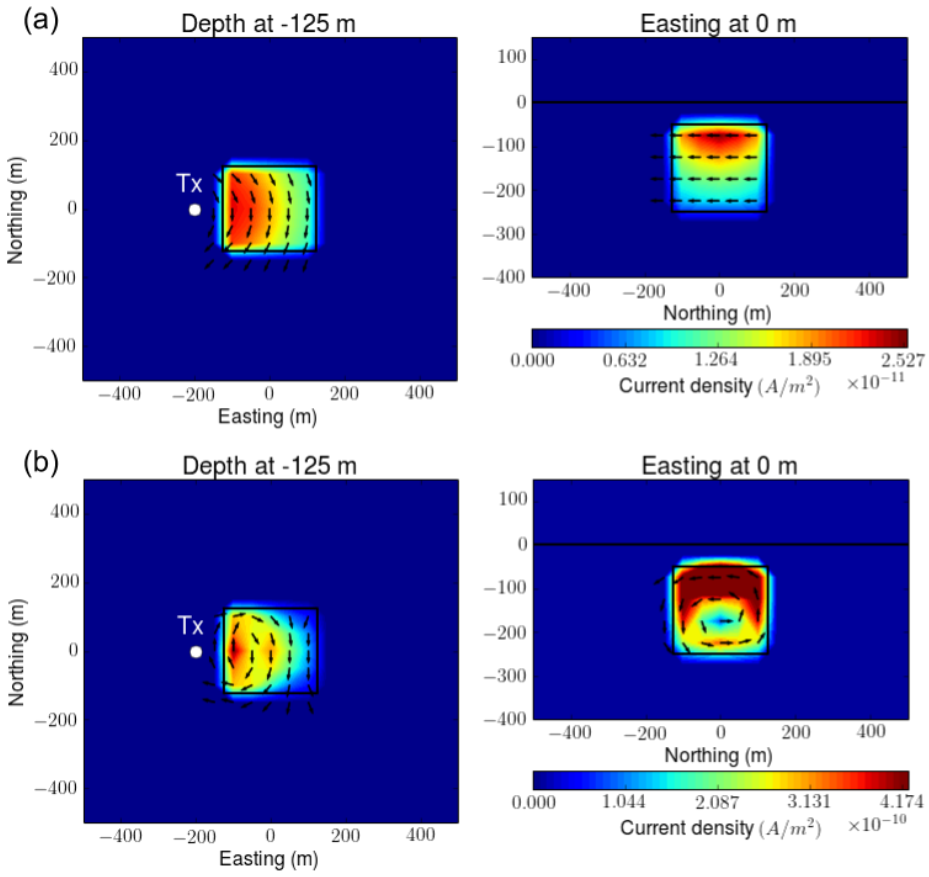

Figure 2.8: Maps of polarization currents: (a) canonical and (b) conductive models at 0.86 ms. Left and right panels show plan and section views at -125 m-depth and 0 m-easting, respectively. A source is located at (-200 m, 0 m, 30 m). Black arrows and shaded values respectively indicate the direction and amplitude of the current. Black solid lines outlin boundary of the surface or the chargeable body.

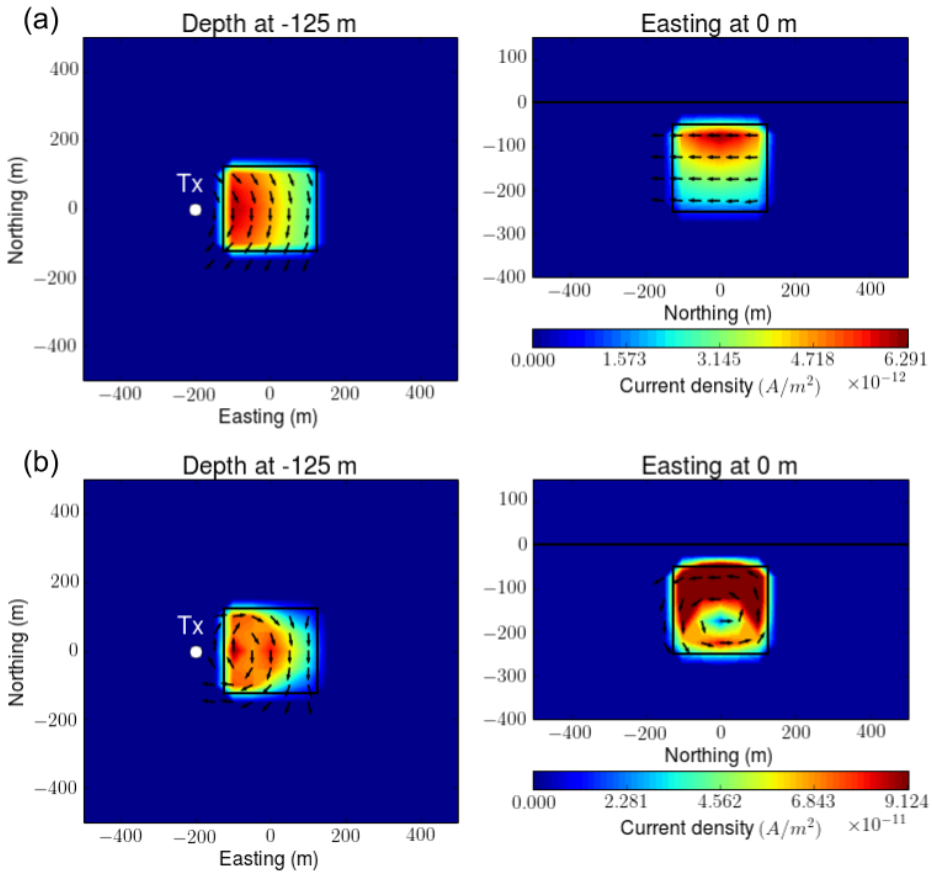

Figure 2.9: Maps of polarization currents: (a) canonical and (b) conductive models at 6.7 ms. Left and right panels show plan and section views at -125 m-depth and 0 m-easting, respectively. A source is located at (-200 m, 0 m, 30 m). Black arrows and shaded values indicate the direction and amplitude of the current, respectively. Black solid outlines boundary of the surface or the chargeable body.

2.3.3 IP Currents

The IP currents, as provided in eq. (2.13), are given as

$$\vec{j}^{IP} = \sigma_\infty \vec{e}^{\,IP} + \vec{j}^{pol}. \tag{2.40}$$

In most analyses, (e.g. Smith et al. [1988]), the term $\sigma_\infty \vec{e}^{\,IP}$ is neglected. I have included this term but with an approximation that $\vec{e}^{\,IP} \approx -\nabla\phi^{IP}$ (eq. 2.27). Here I investigate these approximations, and under what circumstances they hold.

The electric field, $\vec{e}^{IP}$, can be evaluated with forward modelling. It can be broken into galvanic galvanic and inductive parts using the Helmholtz decomposition. So $\vec{e}^{IP} = -\vec{\nabla}\phi^{IP} - \vec{a}^{IP}$. Taking the divergence and making use of the fact that $\nabla \cdot \vec{a}^{IP} = 0$ (vector potential is divergence free). I obtain

$$\nabla \cdot \vec{e}^{IP} = -\nabla \cdot \vec{\nabla}\phi^{IP}. \tag{2.41}$$

Then $\vec{a}^{IP} = -\vec{e}^{IP} + \vec{\nabla}\phi^{IP}$. The effects from the scalar potential are included, but in my approximate formulation (justified below) I have neglected any contribution from the vector potential. I look at the contributions of each of these terms for the three cases of canonical, conductive and resistive bodies. Fig. 2.10 respectively shows plan view maps of $\vec{j}^{pol}$, $-\sigma_\infty\vec{\nabla}\phi^{IP}$, and $-\sigma_\infty\vec{a}^{IP}$for (a) canonical, (b) conductive, and (c) resistive models at 0.86 ms.

Inside the body, the $\vec{j}^{pol}$ has the greatest strength and the strength of these currents is largest in the conductive body and smallest in the resistive body. In all cases, $\vec{j}^{pol}$ is the largest contribution to $\vec{j}^{IP}$. The second column in Fig. 2.10 is related to the scalar potential for the electric field, or effectively to the galvanic currents, $-\sigma_\infty\vec{\nabla}\phi^{IP}$. These exist both inside and outside the chargeable body. Again, these are largest for the conductive body. Note that inside the body, $-\sigma_\infty\vec{\nabla}\phi^{IP}$ has a direction that is opposite to the $\vec{j}^{pol}$. The third column is associated with the vector potential and is associated with vortex currents: $-\sigma_\infty\vec{a}^{IP}$. The effects of these currents have not been included in our linearized approximations. These currents are quite small for the canonical and resistive models but their amplitude starts to be comparable to the galvanic portion for the conductive model.

I evaluate $\vec{j}^{IP}$ and its components at two locations in the body for the conductive

Table 2.1: Amplitudes of decomposed IP currents at two marked points (white stars) shown in Fig. 2.10(b). Units in A/m^2

Division	$\lvert\vec{j}^{IP}\rvert$	$\lvert\vec{j}^{pol}\rvert$	$\lvert-\sigma_\infty\vec{\nabla}\phi^{IP}\rvert$	$\lvert-\sigma_\infty\vec{a}^{IP}\rvert$
Left	1.5×10^{-10}	2.5×10^{-10}	7.6×10^{-11}	1.9×10^{-12}
Right	5.4×10^{-11}	1.2×10^{-10}	3.5×10^{-11}	3.3×10^{-11}

model. These are denoted by white stars in the figures. For both locations, $\vec{j}^{pol}$ has the greatest strength and $-\sigma_\infty\vec{a}^{IP}$ is smaller than $-\sigma_\infty\vec{\nabla}\phi^{IP}$. The $\vec{j}^{IP}$ is smaller than $\vec{j}^{pol}$ mostly because the $-\sigma_\infty\vec{\nabla}\phi^{IP}$ is in the opposite direction compared to the $\vec{j}^{pol}$. The results are tabulated in Table 2.1.

The above figures provide insight about the three contributions to $\vec{j}^{IP}$ but of ultimate interest is the effect of these currents on the measured data. Therefore the Biot-Savart law is applied to each current. It suffices to work with the conductive case. Fig. 2.11 shows d^{IP} computed from the polarization current (stars), galvanic (rectangles) and inductive portions (circles) of the IP current. Here solid and empty markers show negative and positive signs, respectively. The polarization current has the major contribution to the IP response although it is larger than the true value. This overshoot is primarily negated by the galvanic portion of IP responses and further reduced because of the vortex currents. I notice that the contribution of the galvanic currents is generally larger than those due to the vortex currents except near 0.4 ms. At 6.7 ms, the amplitude of the IP response due to the polarization current is about 130 percent of the true polarization current, while the galvanic portion is 30 percent. These results show that the assumption by Smith et al. [1988] is reasonable, but incorporation of the galvanic portion to the IP datum is significant at later times. The inductive portion of the IP responses is small compared to the galvanic portion except for the time before 0.2 ms, and hence ignoring this is justified for the three cases we examined.

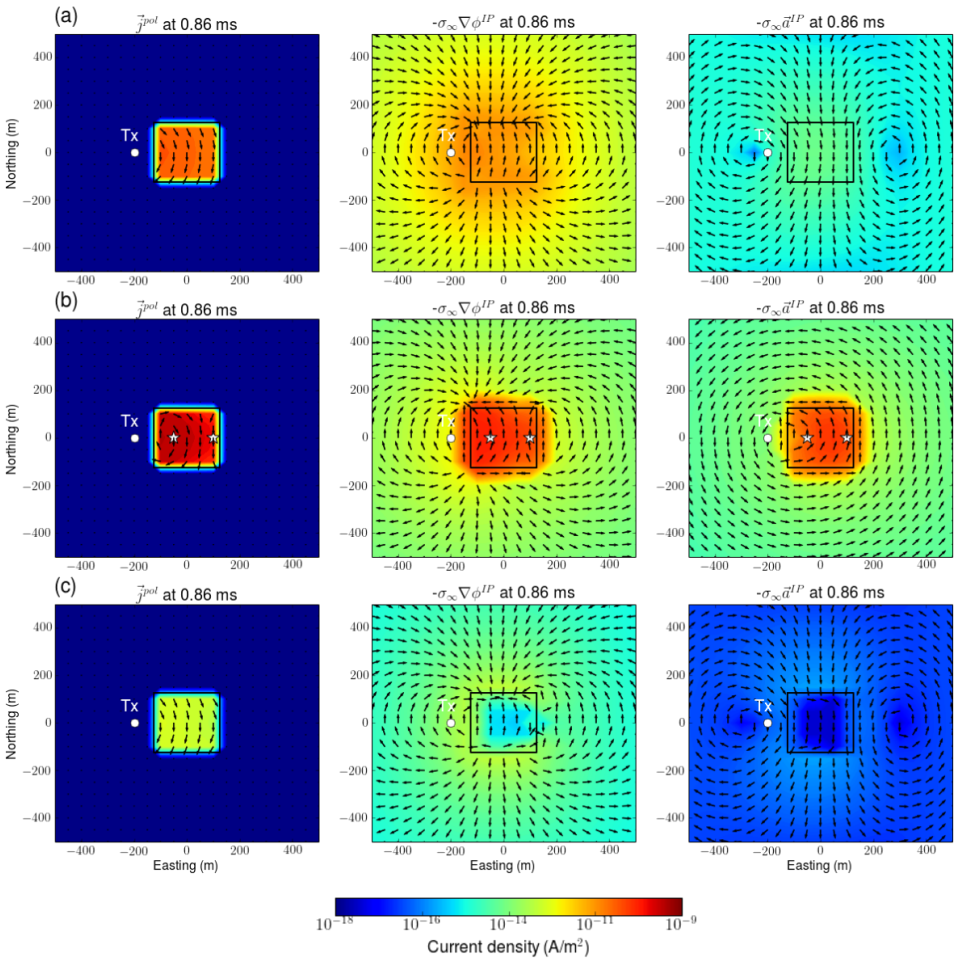

Figure 2.10: Decomposition of the IP currents as $\vec{j}^{pol}$ (left panel), $-\sigma_\infty \vec{\nabla} \phi^{IP}$ (middle panel), and $-\sigma_\infty \vec{a}^{IP}$ (right panel) at 0.86 ms. Plan view maps of the currents at -125 m-depth are shown: (a) canonical, (b) conductive, and (c) resistive cases.

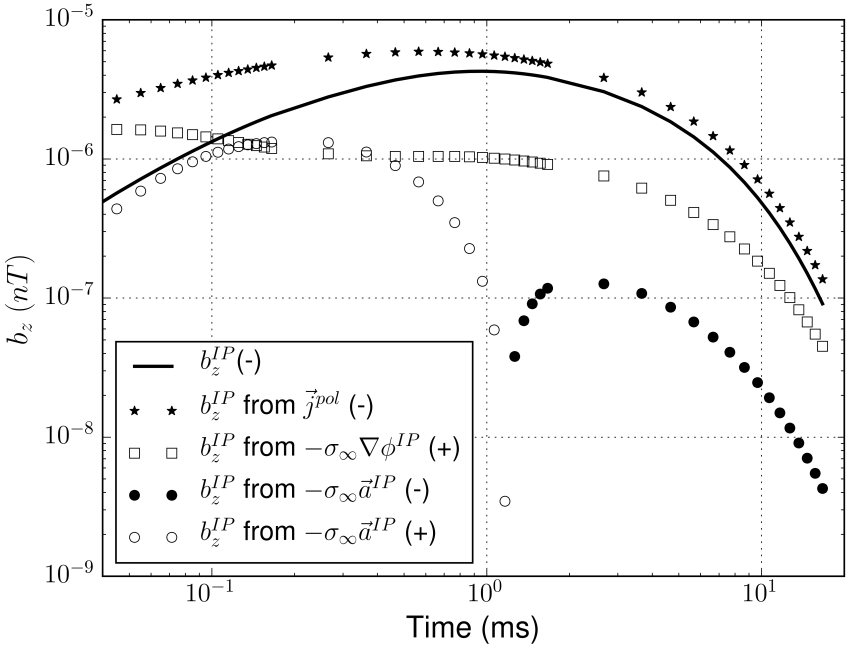

Figure 2.11: Comparisons of contributions of $\vec{j}^{pol}$, $-\sigma_\infty \vec{\nabla}\phi^{IP}$, and $-\sigma_\infty \vec{a}^{IP}$ to the observed IP magnetic field. Solid line indicates true b_z^{IP} responses. Stars, rectangles, and circles correspondingly indicate each IP response generated by applying the Biot-Savart law to $\vec{j}^{pol}$, $-\sigma_\infty \vec{\nabla}\phi^{IP}$, and $-\sigma_\infty \vec{a}^{IP}$. Empty and solid markers represent positive and negative values, respectively.

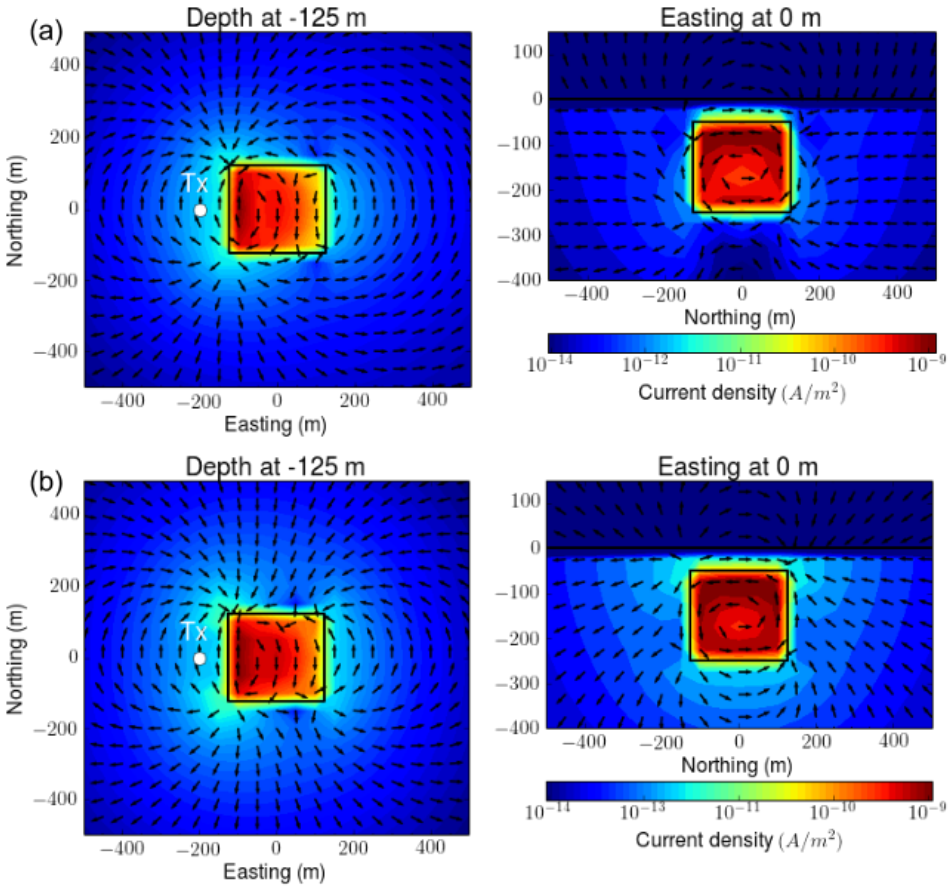

Figure 2.12: Interpolated maps of (a) true and (b) approximate IP currents at 0.86 ms. Left and right columns respectively show plan and section view maps at -125 m-depth and 0 m-easting.

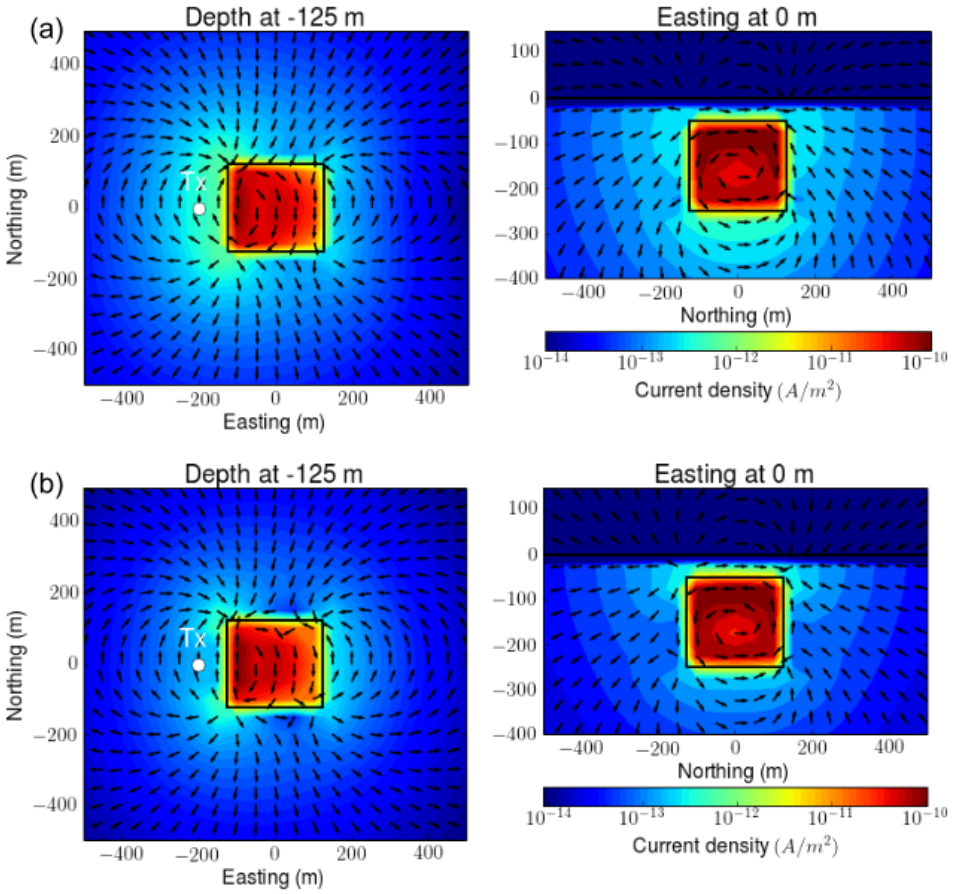

Figure 2.13: Interpolated maps of (a) true and (b) approximate IP currents at 6.7 ms. Left and right columns respectively show plan and section view maps at -125 m-depth and 0 m-easting.

2.3.4 Validations of Linearization

Recall that the linearization of the IP function shown in eqs. (2.38) and (2.39) basically requires obtaining approximate IP currents and then applying the Biot-Savart law. I validate this linearization procedure by numerically comparing both the approximate currents and d^{IP} with true ones. First, for the comparison of IP currents, only the conductive model is considered since this is the most challenging case for linearization. Fig. 2.12 compares the true and approximate IP currents at 0.86 ms. The approximate IP currents match well, both in direction and amplitude, with the true IP currents both inside and outside the body. As shown in Fig. 2.13 the agreement improves as time increases (see the directions of the true and approximate IP currents at (0,0,-350) on the right panels of Figs 2.12 and 2.13). Second, the validity of computing linear d^{IP} is tested. True d^{IP} is obtained by subtracting the d^{F} from d. Approximate d^{IP} is obtained by applying the Biot-Savart law to approximate IP currents shown in Fig. 2.13(b). In Fig. 2.14, comparison of true (blue solid line) and approximate (blue empty circles) d^{IP} are presented. Approximate d^{IP} show lower amplitude after 0.2 ms and differ by 33 percent at the extreme. The difference decreases with increasing time. Overall the two curves are in reasonable agreement, thus validating our linearized forward modeling (eq. 2.38). Also, the discrete Biot-Savart operator is tested by applying it to true IP currents and evaluating d^{IP}. As shown in Fig. 2.14 this d^{IP} (blue stars) is almost coincident with the true one except before 0.01 ms.

In addition, the same analysis of comparing true and approximate d^{IP} data was carried out for the canonical and resistive models, and presented in Fig. 2.14. The true and approximate d^{IP} for both cases show good agreements. Note however, that despite the fact that the linear IP function reasonably explains d^{IP} for the resistive case, the amplitude of d^{IP} is very small compared to EM signal, and this IP signal likely cannot be identified in practice.

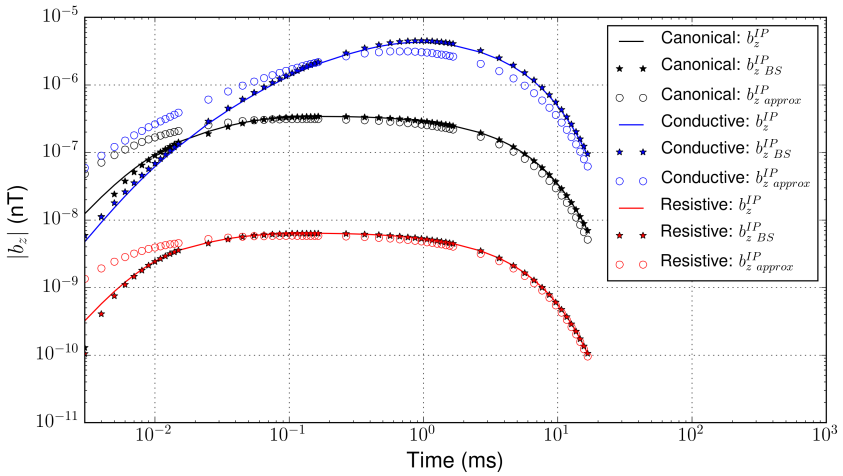

Figure 2.14: Comparison of true and approximate IP responses (b_z^{IP}). Black, blue, and red colors respectively indicate canonical, conductive, and resistive cases. Solid lines indicate true b_z^{IP}, computed by subtracting the fundamental response from the observation. The stars are the application of Biot-Savart to true IP current and generate $b_{z\ BS}^{IP}$. Empty circles show our approximate $b_{z\ approx}^{IP}$ response.

2.4 Effective Pseudo-chargeability

The IP datum is linearized as a function of the pseudo-chargeability, eq. (2.38), and this was developed for a single source. The pseudo-chargeability was defined as a convolution between the impulse pseudo-chargeability, $\tilde{\eta}^I$ and the time history of electric field, $\hat{w}$, as shown in eq. (2.23). Considering a TEM survey including multiple sources, $\hat{w}$ is different for each source resulting in different pseudo-chargeabilities. This is problematic especially when IP inversion is considered, since only a single pseudo-chargeability model is desired to be restored from the d^{IP} data. This important issue should be handled, and it requires combining the pseudo-chargeabilites that arise from individual sources into a source-independent effective pseudo-chargeability. Hence, a desired result is that a d^{IP} datum for any source takes the form:

$$\begin{bmatrix} \mathbf{d}_1^{IP}(t) \\ \mathbf{d}_2^{IP}(t) \\ \vdots \\ \mathbf{d}_{nTx}^{IP}(t) \end{bmatrix} = \begin{bmatrix} \mathbf{J}_1 \\ \mathbf{J}_2 \\ \vdots \\ \mathbf{J}_{nTx} \end{bmatrix} \begin{bmatrix} \tilde{\eta}(t) \end{bmatrix}, \tag{2.42}$$

where $\mathbf{d}_k^{IP}(t)$ and $\mathbf{J}_k$ indicates the IP datum and sensitivity matrix at k-th source. Here $\tilde{\eta}(t)$ stands for an effective pseudo-chargeability, which represents pseudo-chargeability from all sources. Hence, for a given effective pseudo-chargeability I can compute IP responses at all sources.

How to obtain this effective pseudo-chargeability will differ for different types of TEM surveys. I consider three types of TEM surveys:

- Large ground loop survey: a single loop source with multiple receivers
- Airborne survey: a number of a source and receiver loop pairs
- Grounded source survey: multiple current (source) and potential (receiver) electrodes connected by current wires

The first case poses no problem, since the survey includes a single loop source resulting in only a single pseudo-chargeability. The second case is the most problematic since it includes many sources. This issue is addressed in Appendix A.

This requires computing and combining the individual time histories of the electric fields due to each source into an effective time history. The survey geometry of third case is the same as a DC-IP survey, but the effects of EM induction induced from current wire paths is not ignored, but considered. Similar to the DC-IP survey, however, steady-state can be achieved for polarization charge buildup at the late on-time, then the polarization simply decays in the off-time (see red d^{IP} curve in Fig. 1.13). That is, for the grounded sources, a steady-state electric field can be established, and hence assuming that $\hat{w}$ is equivalent to the input current waveform is reasonable. This makes pseudo-chargeabilities of all sources in the survey equivalent. For the above three surveys types, IP data which are linearly related to effective pseudo-chargeability (eq. 2.42) has been obtained. Now for a given $\tilde{\eta}$, d^{IP} can simply be computed as a matrix-vector product when the sensitivity matrix, $\mathbf{J}$ is formed.

2.5 Positivity on Time History of Electric Field

The time history of the electric field, w^{ref}, was defined in eq. (2.22), and there I ignored negative values of w^{ref} by using a positive projection, $P_0[\cdot]$, as shown in eq. (2.20). Here, I discuss why negative portions of w^{ref} can be ignored and discuss potential errors on the assumption. The first motivation for using the positive projection was to enforce the sign of the pseudo-chargeability, $\tilde{\eta}$, to be positive. Intrinsic chargeability is positive and, as in the case of grounded IP, pseudo-chargeability is also a positive quantity. For the inverse problem, forcing positivity on $\tilde{\eta}$ is an important constraint. I show this in Chapter 3.

Because of the complexities of earth structure and the inductive source field, I recognize that there can be situations where w^{ref} is negative. For instance, consider a vertical conductor offset from a transmitter loop as shown in Fig. 2.15. After the transmitter current is turned off, the currents induced due to the half-space (smoke ring) result in a current that is into the page at all depths, but the vortex current induced in the conductor is positive (into the page) at the top and negative (out of the page) at the bottom as shown in Fig. 2.15. So, at the top (yellow voxel) the half-space channeled current and the vortex current are in the same direction, but at the bottom (green voxel) the two currents are in opposite directions. Hence, the bottom voxel has a potential to have negative w^{ref} values based upon eq. (2.22).

In order to address this potential problem, I first carry out a TEM simulation using SIMPEG-EM package [Heagy et al., 2017]. A thin vertical conductor (0.005 S/m) is embedded in a homogeneous half-space earth (0.001 S/m) as shown in Fig. 2.16. A transmitter loop with radius 13 m is located 30 m above the surface, and 150 m away from the conductor (marked as a green solid dot in Fig. 2.16); step-off waveform is used. A receiver which measures the vertical magnetic field is co-located with the transmitter. Fig. 2.17 shows the current density at three different times after the transmitter current is turned off. At 0.01 ms, the half-space channeled currents and the vortex currents are both evident. At the top part of the conductor (see yellow cross mark), the two currents are in the same direction, which increases the net current. However, at the bottom of the conductor (see yellow cross mark), the two currents are in opposition so the net current is decreased. As time passes, the vortex currents decay away (Fig. 2.17b) and eventually only

the channeled currents (Fig. 2.17c) remain. The direction of the currents in the conductor changes with time, and hence w^{ref} can have negative value at some voxels.

Now, suppose the vertical conductor is chargeable and its Cole-Cole parameters are η=0.5, τ=10^{-4} s, and c=1. The question arises regarding how much impact those negative w^{ref} have on the IP data. To answer the question I carry out following procedures:

- Step 1: Compute the reference electric field, e^{ref}:

$$\vec{e}^{ref} = \vec{e} \otimes \vec{t}^{ref}.$$

  Here t^{ref} is the time when the electic field, $\vec{e}$, has a peak amplitude in time.

- Step 2: Evaluate w^{ref} using eq. (2.22) and $P_0[w^{ref}]$.

$$w^{ref}(t) = \frac{\vec{e}(t) \cdot \vec{e}^{ref}}{\vec{e}^{ref} \cdot \vec{e}^{ref}}.$$

- Step 3: Compute $\tilde{\eta}$ (eq. 2.23) with w^{ref} and $P_0[w^{ref}]$:

$$\tilde{\eta} = \tilde{\eta}^I \otimes w^{ref}$$

  and

$$\tilde{\eta}_0 = \tilde{\eta}^I \otimes P_0[w^{ref}],$$

  respectively.

- Step 4: Calculate IP data, d^{IP}, with $\tilde{\eta}$ by using the linear IP function:

$$d^{IP} = J\tilde{\eta},$$

  and d_0^{IP} with $\tilde{\eta}_0$:

$$d_0^{IP} = J\tilde{\eta}_0.$$

  As long as d^{IP} and d_0^{IP} are close enough, my assumption is valid in spite of negative w^{ref} values.

Fig. 2.18 shows the peak current computed from the time history of the currents shown in Fig. 2.17, and it effectively captures both the channeled currents and the vortex currents. The time history of the electric field (w^{ref}) for two voxels is presented in Fig. 2.19(a); the time is in log scale. Here I also provided $P_0[w^{ref}]$ for comparison (cross marks). At the top voxel (yellow line), w^{ref} is always positive, so there is no problem. However, at the bottom voxel (green line), w^{ref} changes from positive to negative around 0.15 ms. These negative values are clearly shown in Fig. 2.20(b) where they are plotted with a linear scale in time. The resultant pseudo-chargeability (eq. 2.23) shows negative values after 0.4 ms.

IP data (d^{IP}) at the receiver location (evaluated with $d^{IP} = J\tilde{\eta}$) is presented in Fig. 2.21(a). The same forward modelling is carried out using $\tilde{\eta}_0$ and the resultant d_0^{IP} is provided (red cross marks). Note that d^{IP} and d_0^{IP} are almost coincident. Thus even though some pixels will be modelled incorrectly, the fact that an IP datum is the cumulative response due to all of the pixels, most of which are correctly modelled, means that our assumption is likely quite robust. An additional reason to give confidence in my assumption is that an AEM survey uses multiple transmitters. Each transmitter will excite the earth differently. The pixel at the bottom of the plate, while having a negative w^{ref} when the transmitter was displaced from the plate, may have a positive w^{ref} when the transmitter moves location. The effective pseudo-chargeability derived from all transmitters used in an AEM survey, basically averages $\tilde{\eta}$s from different transmitters and this may ameliorate negative effects caused by specific coupling geometries (See Appendix 2.4).

Lastly, I comment on the effects of neglecting negative w^{ref} in the inverse problem. Our basic equation is $d^{IP} = J\tilde{\eta}$. Negative values of $\tilde{\eta}$ will reduce the value of d^{IP} compared to that obtained with our assumption (*although the plot show barely no change*). After the inverse problem is solved the recovered $\tilde{\eta}$ will therefore have values lower than they should; that is the recovered pseudo-chargeability will be underestimated.

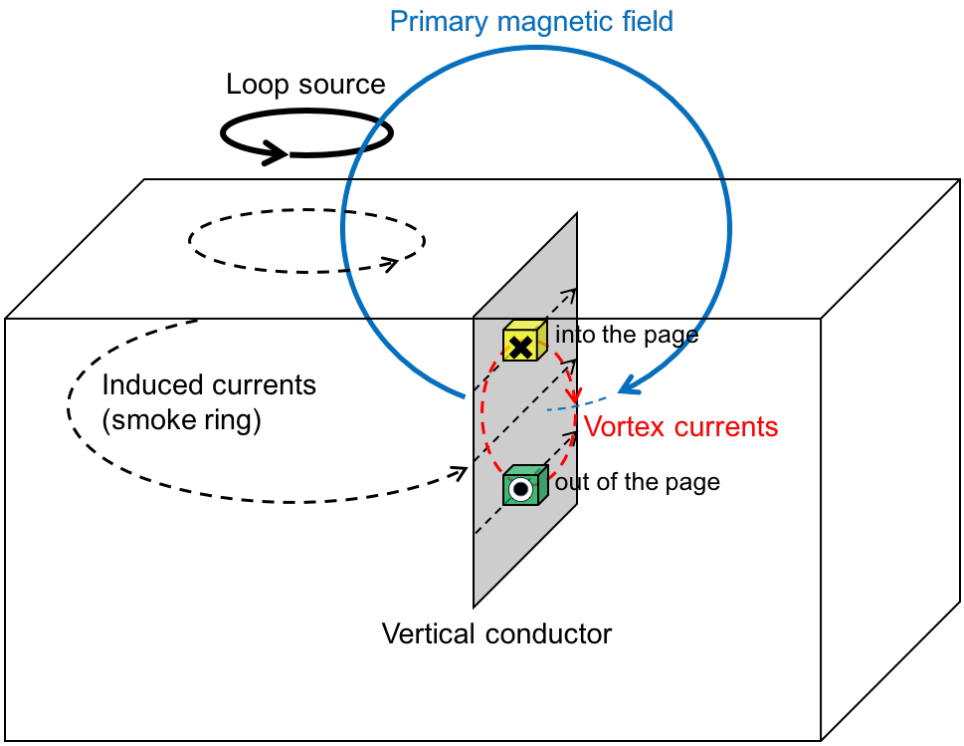

Figure 2.15: Conceptual diagram of EM induction process from a loop transmitter when a vertical conductor is embedded in a homogeneous half-space. After the transmitter current is turned-off from the loop, currents are induced in the subsurface and diffuse away like a smoke ring. This smoke ring currents will be channeled into the vertical conductor (dashed lines), and there will be vortex currents rotating (red dashed circle) in the conductor due to the time-varying magnetic field. In the conductor, at the top voxel (yellow) the half-space channeled current and the vortex current are in the same direction (in to the page), whereas at the bottom voxel they are in the opposite direction.

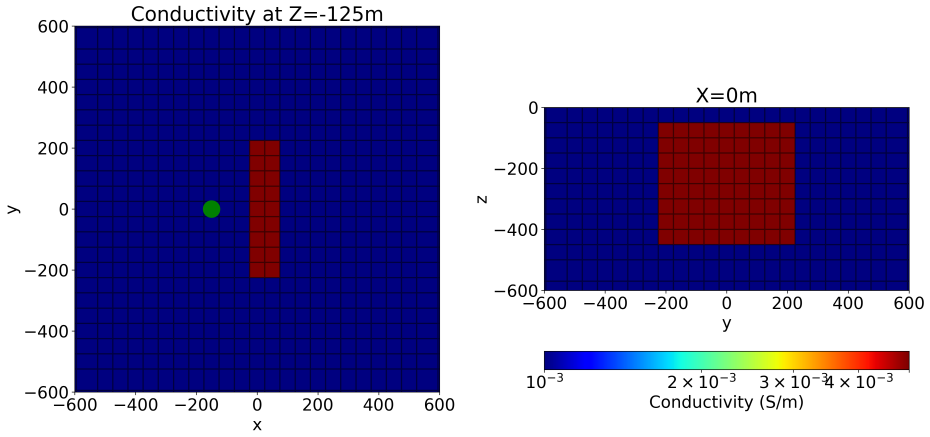

Figure 2.16: Plan and section views of a 3D conductivity model is shown in right and left panels, respectively. A vertical conductor (0.005 S/m) is embedded in a homogeneous half-space (0.001 S/m). Green solid circle indicates the horizontal location of the transmitter loop having 13 m-radius, and located 30 m above the surface.

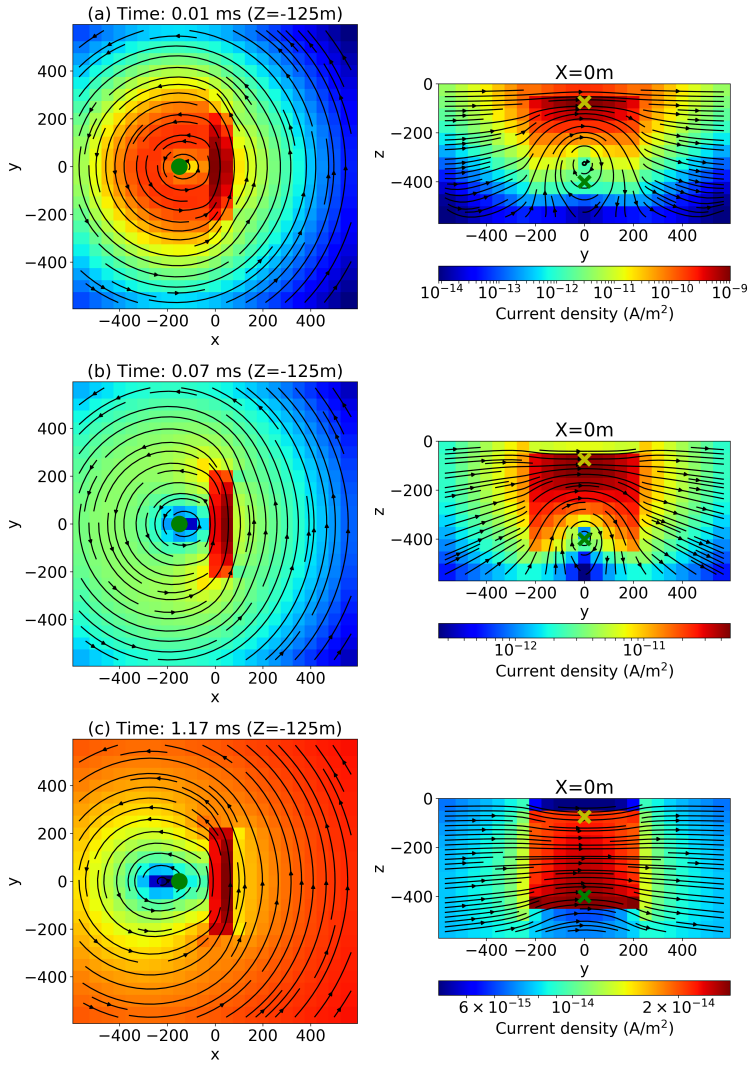

Figure 2.17: The current densities at three different times due to a 13 m-radius loop located 30 m above the surface (marked as green solid circle) with a conductivity model having a vertical conductor shown in Fig. 2.16. Plan and section views of the current density at three different times after the current is off: (a) 0.01 ms, (b) 0.07 ms, and (c) 1.17 ms. The time history of the electric field at the top and bottom voxels in the conductor (yellow and green crosses, respectively) are presented in Fig. 2.19.

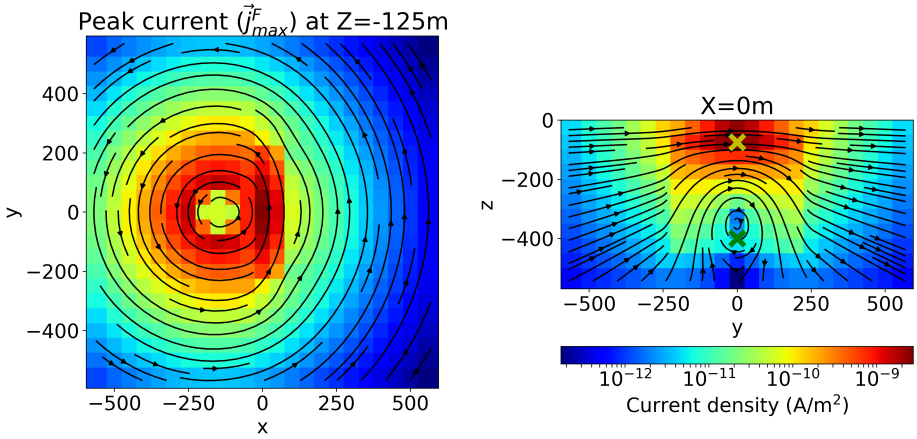

Figure 2.18: The peak current (or reference current) selected from the time history of the current density shown in Fig. 2.17. Plan and sections views are shown in right and left panels, respectively. The time history of the electric field at the top and bottom voxels in the conductor (yellow and green crosses, respectively) are presented in Fig. 2.19.

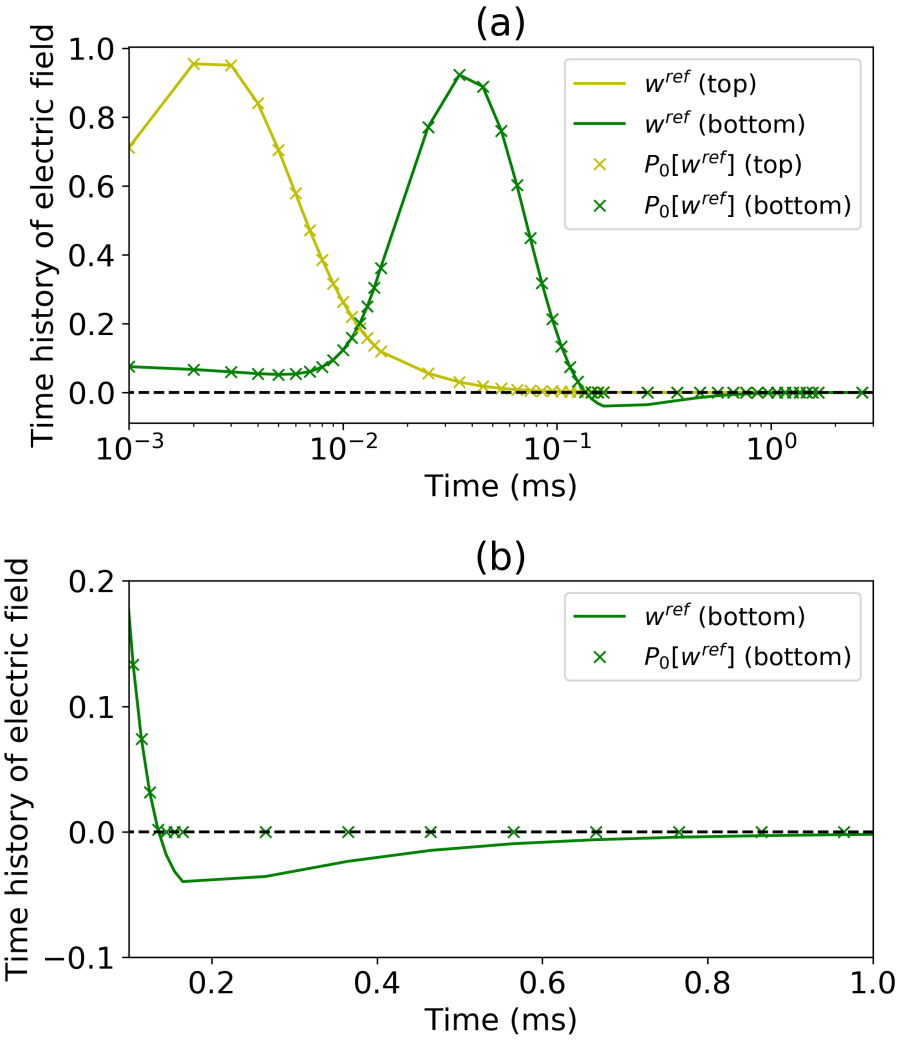

Figure 2.19: The time history of the electric field, w^{ref}, at the two voxels shown in Figs. 2.17 and 2.18. Yellow and green distinguish w^{ref} for the top and bottom voxels, respectively. (a) w^{ref} at the both voxels in semi-log scale ($log(t) - w^{ref}$). (b) w^{ref} at the top voxel only showing later times after 0.1 ms with linear scale in time. The negative values of w^{ref} exist at the very late-time for the bottom voxel (green) as shown in (b).

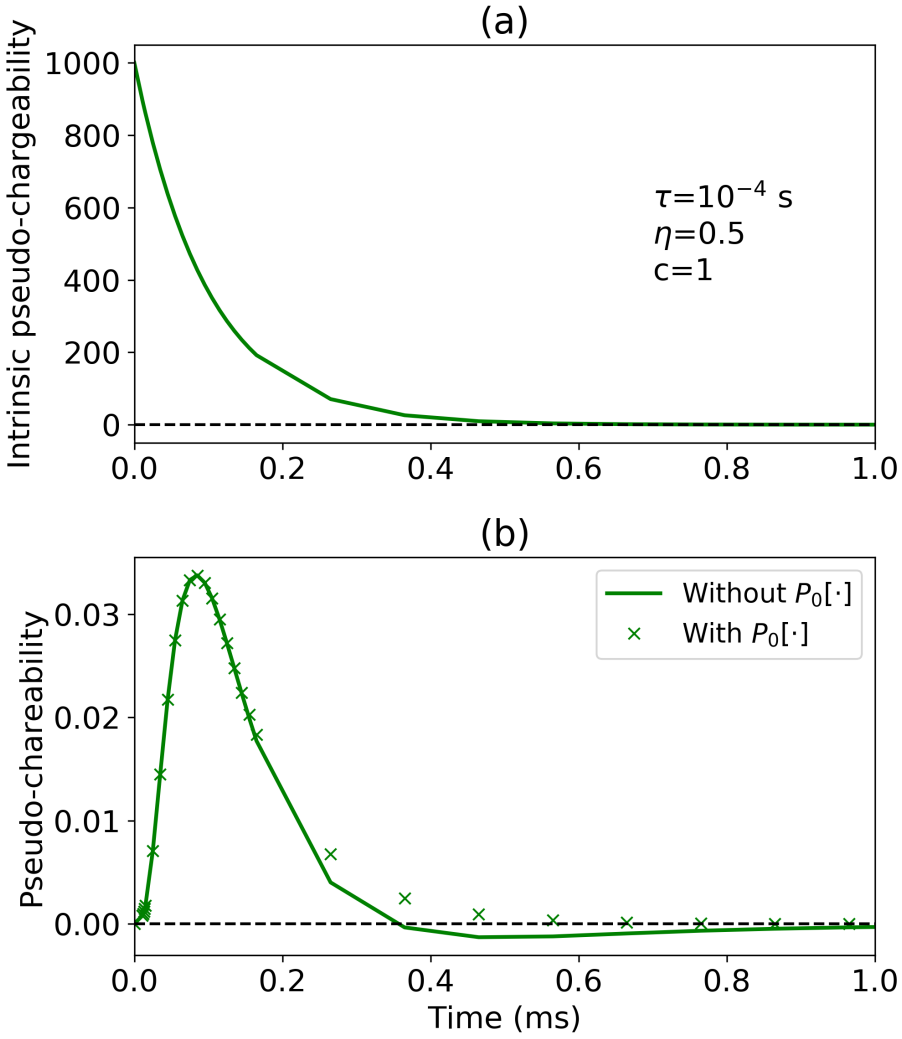

Figure 2.20: (a) Intrinsic pseudo-chargeability, $\tilde{\eta}^I$ as a function of time. Used Cole-Cole parameters are denoted in (a). (b) Pseudo-chargeability, $\tilde{\eta}$, calculated by convolving $\tilde{\eta}^I$ and w^{ref} at the bottom voxel shown in Fig. 2.19. Solid line and cross marks distinguish $\tilde{\eta}$ computed with and without positive projection on w^{ref}, $P_0[w^{ref}]$.

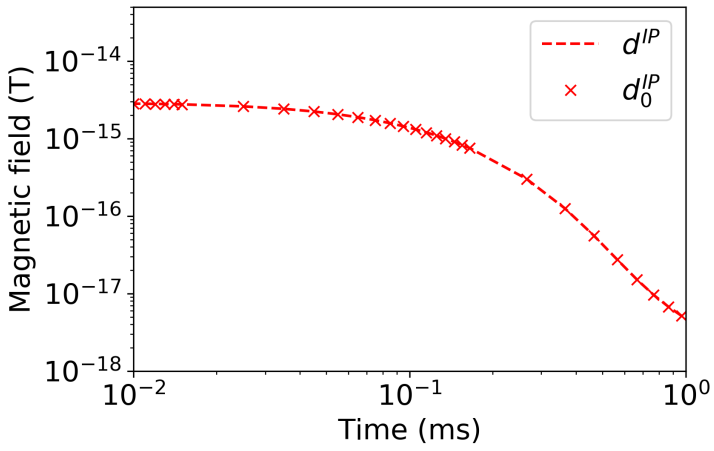

Figure 2.21: Computed IP data, d^{IP}, using linear IP function. IP data are computed with and without positive projection on w^{ref} and denoted as d^{IP} and d_0^{IP}, respectively; red dashed line and red crosses are distinguishing d^{IP} and d_0^{IP}, respectively.

2.6 Conclusions

The linearization of d^{IP} with respect to a pseudo-chargeability is derived for the ISIP data. Pseudo-chargeability is defined as the ratio of the polarization current to a reference current. Unlike the DC-IP case, the electric fields for an inductive source do not achieve steady-state and hence neither do the polarization currents. To address this important difference I evaluate the fundamental electric field at each location in the earth and generate a reference electric field that has the direction and magnitude of the field at the time when the fundamental field reaches its maximum value. The pseudo-chargeability at a point in the earth thus depends upon the polarization parameters (e.g. Cole-Cole: η, τ, and c), the reference electric field, and the time history of the electric field. The situation becomes more complicated when data from many sources such as an AEM survey are to be inverted simultaneously because the time history of the electric field at a point in the earth is different for each source. This is handled by defining an effective pseudo-chargeability and an associated reference electric field that accommodates, in a least squares fashion, the effects of all sources acting on a single cell.

To have confidence in when, and under what circumstances, the approximations are sufficiently valid, a number of rigorous tests are carried out as a synthetic example of an AEM survey. First, three test models consisting of a chargeable block in a non-chargeable halfspace are introduced. The block can be conductive, canonical, or resistive with respect to the halfspace conductivity. The evaluations show that: (a) the choice of reference electric field and its time history produces a good estimate of the $\vec{j}^{pol}$; (b) the $\vec{j}^{IP}$ is dominated by the $\vec{j}^{pol}$, which is an assumption that has been made. However, the galvanic and vortex currents arising from the scalar and vector potentials in the Helmholtz decomposition of $\vec{e}^{\,IP}$ can be significant in some circumstances. The galvanic currents are the second most important contribution to the IP currents and, in the body, they have a direction that opposes the direction of the polarization currents. For the linear IP function, I have included the galvanic currents and neglected the vortex currents which are almost always smaller than the galvanic currents; (c) the d^{IP} data can be evaluated using the Biot-Savart law which provides quite accurate results; (d) with the approximate $\vec{j}^{IP}$, the predicted responses are in reasonably good agreement with true values al-

though they are underestimated at early times for the highly conductive example. These results lead us to infer that our linearized formulation $\mathbf{d}^{IP}(t) = \mathbf{J}\tilde{\boldsymbol{\eta}}(t)$ is a viable representation for the forward modelling at late times when the IP effects are substantial compared to the EM effects. (e) For the multi-source case I derived an effective pseudo-chargeability which is a linear combination of the pseudo-chargeability of each source. These were forward modelled with the linearized formulation and compared to the true responses. The values were underestimated by 33 percent at the extreme for the conductive model but were almost identical for the canonical and resistive models.

Although the numerical experiments shown here focuses on the ISIP method, the linearization itself is general enough to handle d^{IP} from various TEM surveys. This is a valuable contribution in two main perspectives:

- The linearized formulation will be an effective forward simulator to compute IP effects in various TEM surveys.
- The linearized formulation will be used as a forward engine to invert d^{IP} to recover the distribution of $\tilde{\eta}$.

Chapter 3

3D IP Inversion

3.1 Introduction

From the previous chapter, d^{IP} is linearized with respect to the pseudo-chargeability: $\mathbf{d}^{IP}(t) = \mathbf{J}\tilde{\eta}(t)$ for various TEM surveys. Using this linear equation, I develop a 3D IP inversion algorithm, which separately inverts each time channel of d^{IP}. Solving this linear inverse problem is common in applied geophysics so only an essential summary is provided in Section 3.2. After $\tilde{\eta}$ at multiple time channels are obtained, a small inverse problem is solved to extract intrinsic polarization parameters for each cell. The 3D IP inversion algorithm is tested with synthetic examples using an AEM survey geometry with a simple conductive and chargeable block embedded in a halfspace (Section 3.3).

3.2 3D IP Inversion with a Linear Equation

The linear inverse problem to recover chargeability is straightforward and is described in Oldenburg and Li [1994]. I rewrite eq. (2.38) as

$$\mathbf{d}^{pred} = \mathbf{J}\mathbf{m}, \tag{3.1}$$

where $\mathbf{J}$ is the sensitivity matrix of the linear problem, which corresponds to the $\mathbf{J}$ shown in eq. (2.38). Here, $\mathbf{d}^{pred}$ represents IP responses at a single time channel, $\mathbf{m}$ denotes model parameters, which can be either $\tilde{\eta}$ or $-\frac{\partial \tilde{\eta}}{\partial t}$. The important positivity

constraint results because the intrinsic chargeability η is restricted to the range [0,1).

The solution to the inverse problem is the model $\mathbf{m}$ that solves the optimization problem

$$minimize\ \phi = \phi_d(\mathbf{m}) + \beta\phi_m(\mathbf{m}) \tag{3.2}$$

$$s.t.\mathbf{m} \geq\ 0,$$

where ϕ_d is a measure of data misfit, ϕ_m is a model objective function and the β is a regularization or trade-off parameter.

I use the sum of the squares to measure data misfit

$$\phi_d = \|\mathbf{W_d}(\mathbf{Am} - \mathbf{d}^{obs}|)\|_2^2 = \sum_{j=1}^{N}(\frac{d_j^{pred} - \mathbf{d}_j^{obs}}{\varepsilon_j})^2, \tag{3.3}$$

where N is the number of the observed data and $\mathbf{W_d}$ is a diagonal data weighting matrix which contains the reciprocal of the estimated uncertainty of each datum (ε_j) on the main diagonal, $\mathbf{d}^{obs}$ is a vector containing the observed data, $\mathbf{d}^{pred}$ is a vector containing calculated data from a linear equation given in eq. (3.1). The model objective function, ϕ_m, is a measure of the amount of structure in the model and upon minimization this will generate a smooth model which is close to a reference model, $\mathbf{m}_{ref}$. I define ϕ_m as

$$\phi_m = \sum_{i=s,x,y,z} \alpha_i \|\mathbf{W}_i\mathbf{W}(\mathbf{m} - \mathbf{m}_{ref})\|_2^2, \tag{3.4}$$

where $\mathbf{W}$ is a model weighting matrix, which will be defined below, $\mathbf{W}_s$ is a diagonal matrix containing volumetric information of prisms, and $\mathbf{W}_x$, $\mathbf{W}_y$ and $\mathbf{W}_z$ are discrete approximations of the first derivative operator in x, y and z directions, respectively. The α's are weighting parameters that balance the relative importance of producing small or smooth models [Tikhonov and Arsenin, 1977].

Depending on the geometry of TEM surveys, additional weighting could be necessary. For instance in an AEM survey, because only a single datum for each source is available, intrinsic depth resolution is lacking. A similar lack of depth resolution occurs when a gradient array (a single grounded source and multiple re-

ceivers) is used for a DC-IP survey. These are also the same circumstances encountered when inverting magnetic data [Li and Oldenburg, 1996]. Correspondingly I apply a depth weighting through the model weighting matrix ($\mathbf{W}$):

$$\mathbf{W} = \mathbf{diag}(\mathbf{z} - \mathbf{z_0})^{1.5}, \tag{3.5}$$

where $\mathbf{z}$ and $\mathbf{z_0}$ are discretized depth locations and reference depth in the 3D domain. Here the expnent 1.5 arises from the geometric decay of magnetic field $\sim \frac{1}{r^3}$.

Although I use the linear form of d^{IP} data (eq. 2.38), the inverse problem is nonlinear because of imposed positivity on $\mathbf{m}$. An initial model, $\mathbf{m}_0$ is required to start the inversion. This constrained optimization problem is solved by using a projected Gauss-Newton (GN) method [Kelley, 1999]. The trade-off parameter, β, is determined using a cooling technique where β is progressively reduced from some high value. The inversion is stopped when the tolerance is reached; the most obvious stopping criteria is a target misfit, ϕ_d and it is set to the number of data (cf. Oldenburg and Li [2005]). For the implementation of the IP inversion algorithm, I use an open source python package for simulation and gradient-based parameter estimation in geophysics called SIMPEG [Cockett et al., 2015].

3.3 Numerical Experiments

Using the 3D IP inversion algorithm, which uses the linear IP equation as a forward engine (eq. 2.38), I now invert d^{IP}, and recover pseudo-chargeability. As a test, the same model and the AEM survey setup used in the previous section are used except that only the conductive and chargeable block model is used here. Conductivity of the block is σ_2=0.1 S/m, and the halfspace conductivity is σ_1=0.001 S/m. The survey, consisting of 11 soundings along each of 11 lines, is shown in Fig. 2.4(a). Data are from a coincident-loop system and the flight height is 30 m above the surface; the radius of the loop is 10 m. A step-off source waveform is used and the range of the observed time channels is 0.01-60 ms. The observed responses are the vertical component of $\vec{b}$.

When computing the sensitivity matrix, a 3D distribution of $\sigma_\infty(x,y,z)$ is required, and an estimate of this distribution can be achieved in the first step of the TEM-IP workflow: inverting TEM data to recover conductivity. This estimated

conductivity, σ_{est} will always include some errors, and hence this will have some impact on the sensitivity computation. To start, I use the true σ_∞ to calculate the sensitivity matrix, but the issue of incorrect conductivity is addressed in Section 3.3.1. Using the true σ_∞, the sensitivity is computed, d^{IP} data at successive time channels are inverted, and 3D pseudo-changeability at multiple times are recovered. The 3D IP inversion is based upon Oldenburg and Li [1994] and Li and Oldenburg [2000], and it requires some choices for inversion parameters.

For data uncertainties, I use one percent of the maximum amplitude of the observed data ($0.01max(|\mathbf{d}^{obs}|)$). Coefficients for smallness and smoothness are set to $\alpha_s = 10^{-5}$ and $\alpha_x = \alpha_y = \alpha_z = 1$, respectively. The reference model is zero, which means the pseudo-chargeability of every cell is zero, and I applied a depth weighting. The need for a depth weighting arises because the sensitivity function J is primarily controlled by a $1/r^3$ decay associated with the Biot-Savart kernels and IP data map at a single time is inverted to recover a 3D distribution of the pseudo-chargeability. Thus an AEM data set is like a magnetic data set where it is well established that a depth weighting is required to image objects at depth. The following example illustrates this.

I first generate IP responses at a single time using the linear function and specifying that the pseudo-chargeability is unity inside the body and zero outside, as shown in Fig. 3.1(a). Fig. 3.1(b) shows the recovered pseudo-chargeability without depth weighting. The recovered anomalous pseudo-chargeability is concentrated near the surface and the magnitude of the pseudo-chargeability is underestimated; it is $\sim$0.2 rather than unity. By using the depth weighting shown in eq. (3.5), the IP body is imaged closer to its true depth (Fig. 3.1b). Also, the magnitude of the recovered pseudo-chargeability ($\sim$0.6) is closer to the true value than the result without depth weighting. Based on this analysis, I use the same depth weighting for following examples.

3.3.1 Incorrect Conductivity

The 3D distribution of $\sigma_\infty(x,y,z)$ plays a central role in the TEM-IP inversion workflow. It is used in the EM-decoupling process to obtain the IP data: $d^{IP} = d - F[\sigma_\infty]$ and it is also needed to compute the linearized sensitivity, $J[\sigma_\infty]$, for the IP inver-

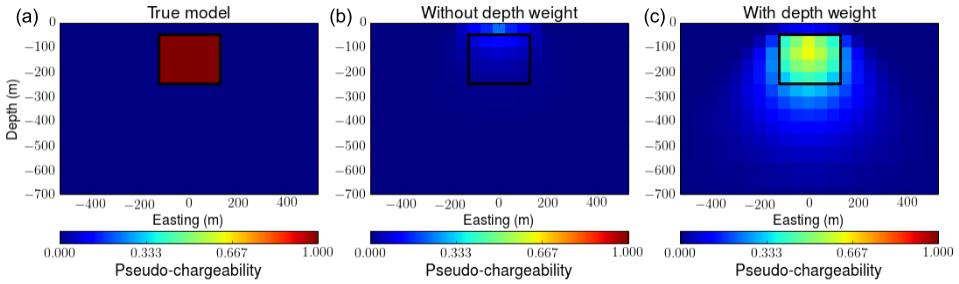

Figure 3.1: Effect of depth weighting in 3D IP inversion. (a) True pseudo-chargeability model on vertical section at 0 m-northing. Recovered pseudo-chargeability models (b) without depth weighting and (c) with depth weighting.

sion. Therefore, estimating the 3D distribution of σ_∞ is an essential step, and inverting early TEM signals having minor IP effects can be an effective option. In this section I do not focus on estimating σ_∞. I do however appreciated that this will never be known exactly. This issue is addressed in more detail with both synthetic and field AEM examples in Chapter 4, but here some consequences of having an incorrect σ_{est} are addressed, in particular with regard to the sensitivity function. I return to the conductive block in a halfspace and evaluate the d^{IP} data when the halfspace conductivity is the true value ($\sigma_1 = 10^{-3}$ S/m) as well as a factor of two too large (2×10^{-3} S/m) and a factor of two too small (5×10^{-4} S/m). Here the conductivity of the chargeable block is fixed to σ_2 = 0.1 S/m. The data along a survey line are plotted in Fig. 3.2.

I invert these three IP responses, and provide sections of the recovered pseudo-chargeability at 0 m-northing. Fig. 3.3(a), (b) and (c) correspondingly show the recovered pseudo-chargeability when the conductivity is: the true value, too high, or too low. With the correct conductivity the geometry of the IP body is reasonably recovered. When the halfspace conductivity is too high, the d^{IP} have a negative bias that results in larger pseudo-chargeabilities and positive-valued artifacts near the IP body (Fig. 3.3b). When the halfspace conductivity is too small, the IP data have a positive bias and this produces negative-valued pseudo-chargeability artifacts either side of the IP body (Fig. 3.3c). White dotted contours shown in Fig. 3.3(c) show zero-crossing lines, which delineate those negative-valued artifacts.

However, based on the definition of the pseudo-chargeability shown in eq. (2.23), the sign of the pseudo-chargeability should be positive. By incorporating positivity as a constraint in the inversion, and re-inverting the IP data that have a positive bias, I obtain the result in Fig. 3.3(d). Considering there are no negative values in the recovered pseudo-chargeability, this is a better result than Fig. 3.3(c). This results shows that the positive constraints prevent fitting positive residual fields. I shall use this positivity constraint for following 3D IP inversion examples.

A distribution of $\sigma_\infty(x,y,z)$ is required when computing the sensitivity function. An incorrect conductivity will affect the sensitivity function. In order to test this, the sensitivity matrix is computed using a halfspace conductivity model ($\sigma_1 = \sigma_2 = 0.001$ S/m). Fig. 3.4 compares the recovered pseudo-chargeability from the 3D IP inversion of the IP datum at 0.86 ms with the true and incorrect sensitivity function using the halfspace conductivity. There is not a large difference between the two inversions and this suggests that an approximate conductivity for the chargeable and conductive body may still provide sensitivities that are adequate for inversion. This parallels results from inverting DC-IP data where even an approximate conductivity can still yield good results when inverting the data. Thus there is robustness in our sensitivity function with respect to an incorrect conductivity. These results suggest that even if one cannot generate a good estimate of σ_∞, a halfspace conductivity might produce an adequate sensitivity function, and hence an inversion can provide some indication of a chargeable body.

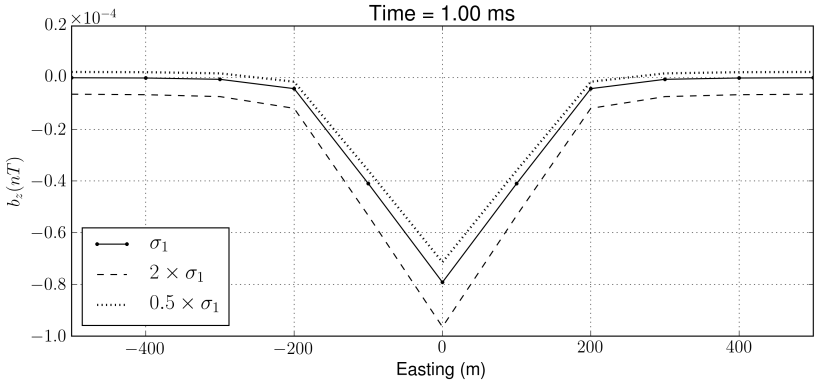

Figure 3.2: IP responses on a profile line at 0 m-northing. IP responses are computed from perturbed σ_∞ models. Halfspace conductivity (σ_1) is perturbed: $2\times\sigma_1$ and $0.5\times\sigma_1$, which respectively resulting in overestimated (dotted line) and underestimated (dashed line) IP responses. The solid line shows the true IP response.

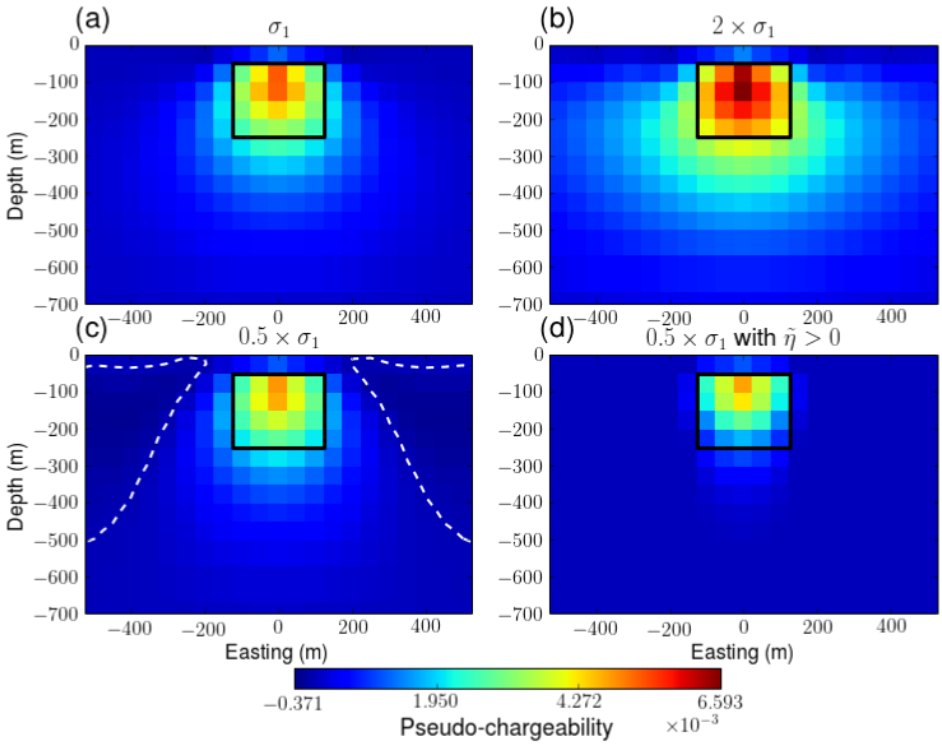

Figure 3.3: Recovered pseudo-chargeability sections from 3D IP inversions at 0 m-northing. (a) d^{IP} with true σ_1. (b) d^{IP} with $2\times\sigma_1$. (c) d^{IP} with $0.5\times\sigma_1$. (d) d^{IP} with $0.5\times\sigma_1$ and the positivity constraint on the pseudo-chargeability. White dashed lines contour zero-crossing lines.

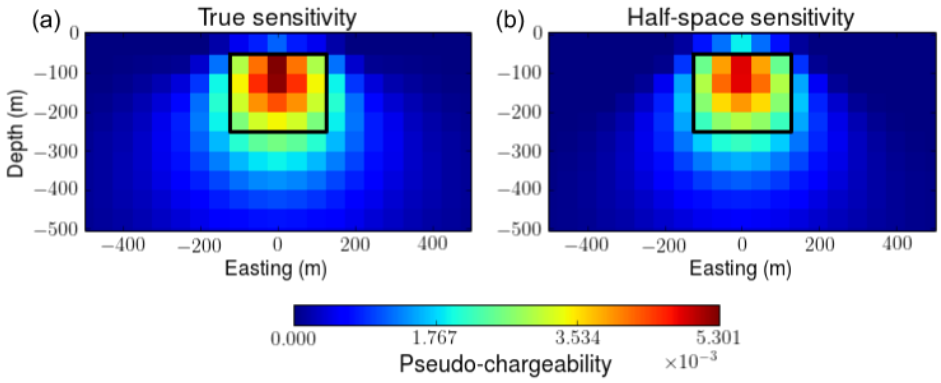

Figure 3.4: Recovered pseudo-chargeability sections from the 3D IP inversions at 0 m-northing. (a) True and (b) incorrect σ_∞ is used to compute sensitivity function. For the incorrect sensitivity I used a halfspace conductivity σ_1.

3.3.2 Extracting Intrinsic IP Parameters

By applying the 3D inversion to each time channel of d^{IP} data separately, 3D distributions of pseudo-chargeability at multiple times can be recovered. The pseudo-chargeability at each time carries different information about the state of polarization and these can be used to recover information about intrinsic IP parameters such as Cole-Cole parameters. Diverse time-dependent conductivity models such as the Cole-Cole model and the Stretched-exponential can be used for this interpretation [Kohlrausch, 1854, Cole and Cole, 1941, Pelton et al., 1978, Tarasov and Titov, 2013].

The Cole-Cole model with $c = 1$ is used here. Pseudo-chargeability at a single pixel is parameterized in terms of chargeability and time constant, and recovered by solving a small inverse problem (see Appendix B for further details). In previous works about this task for the DC-IP problem [Yuval and Oldenburg, 1997, Hördt et al., 2006], the convolution shown in eq. (B.1) was not explicitly mentioned because $\hat{w}(t)$ is a step-off or step-on function and it does not change for different cells and transmitters. This allowed an explicit equation for a step-off or step-on response of the pseudo-chargeability to be derived. However, in our work, convolution plays a fundamental role and needs to be explicitly addressed when extracting intrinsic IP parameters. Also, the details regarding how I defined the effective pseudo-chargeability (eq. A.8) need to be included. Except for this additional complexity related to the convolution, our approach parallels that of Yuval and Oldenburg [1997] and Hördt et al. [2006].

As an example, I use the conductive and chargeable block presented in the previous section and invert 14 time channels of data ranging from 1-10 ms. The EM data are forward modelled using EMTDIP code and the true σ_∞ model is used to evaluate the IP datum and compute the sensitivity function. The recovered pseudo-chargeability from one of the 14 inversions is shown in Fig. 3.4(a). In that pseudo-chargeability model, I select cells that have a pseudo-chargeability value greater than 0.001, and then use the data from all 14 inversions to carry out the nonlinear inversion to estimate the time constant, τ, and chargeability, η, for each cell separately. The forward modelling for this inversion is shown in eq. (A.8), which requires $w^e(t)$ (eq. A.9). The $w^e(t)$ for a pixel in the block is shown in Fig. A.2.

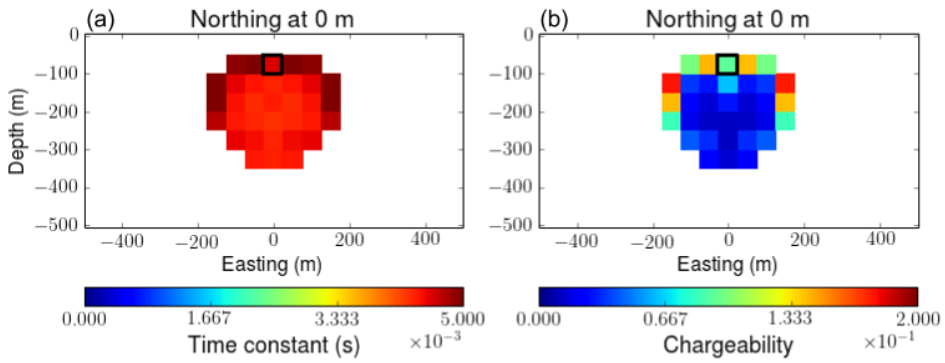

Figure 3.5: Section views of recovered: (a) time constant and (b) chargeability. Any region where the pseudo-chargeability shown in Fig. 3.4a is smaller that 0.001 is ignored in this analysis, and blanked.

Fig. 3.5(a) and (b) correspondingly show the estimated time constants and chargeability as section maps. The estimated time constants show good agreement with the true value τ= 0.005 s. There is less agreement about chargeability for which the true value is $\eta = 0.2$. Recovered values range from about 0.04-0.2 so most values are significantly underestimated. In Fig. 3.6, I also provide time decays of the observed and predicted pseudo-chargeabilities at a single pixel marked as a black rectangle in Fig. 3.5. The estimated time constant, τ_{est}, and chargeability, η_{est}, for this pixel are 0.0046 and 0.09, respectively. These results imply there is greater stability in recovering the time constant than in recovering chargeability with our approach. Again, similar experiments were carried out for the canonical and resistive bodies and the conclusions were also that the time constant was adequately recovered with better fidelity than was the chargeability.

3.4 Conclusions

The 3D inversion algorithm to invert time-domain IP data using the linearized formulation is developed and tested for the synthetic AEM survey example. IP data for the AEM survey have only one receiver for each transmitter and a data map at a single time channel is essentially a potential field. The data do not have intrinsic depth resolving power and hence, as in magnetics or gravity inversions, I

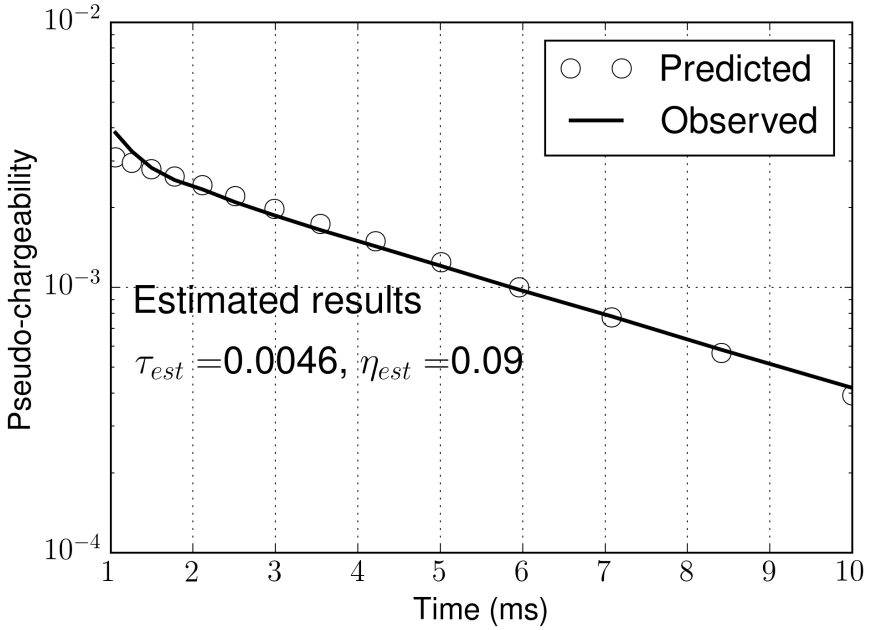

Figure 3.6: Comparisons of the observed pseudo-chargeability at a single pixel in a chargeable body from the 14 inversions at 14 time channels, and the predicted pseudo-chargeability. The empty circles and solid line respectively indicate predicted and observed pseudo-chargeability. The estimated time constant and chargeability are respectively expressed as τ_{est} and η_{est}. The true values for τ and η are respectively 0.005 s and 0.2.

attempt to counteract this by introducing a depth weighting. When this is done, the 3D IP inversion recovers a reasonable geometric shape and location of the chargeable body but the amplitude is underestimated. For the inversion it is assumed that a good estimate of σ_∞ is available. An incorrect σ_∞ has two effects in the inversion. Firstly it can generates errors in the d^{IP} because the estimated fundamental field, which is subtracted from the observations, is incorrect. To obtain insight I looked at the effects when σ_{est} was too low or two high. This respectively yielded positive or negative residual fields in the IP response. A positivity constraint on the pseudo-chargeability (similar to that used in DC-IP surveys) greatly

ameliorated the effects of the positive residuals. The other avenue by which an incorrect σ_∞ can affect the inversion is through the sensitivity matrix $\mathbf{J}$. I showed that, even with an approximate conductivity, I recovered important information about the chargeable body such as geometric shape and location. An inversion of the data at a particular time channel provides information about the effective pseudo-chargeability for each pixel. Inversions carried out at multiple time channels therefore generates a pseudo-chargeability as a function of time for each pixel. The pseudo-chargeability for pixels that had significant chargeability were subsequently fit to a Cole-Cole model to estimate τ and η by assuming $c = 1$. The estimated τ was close to the true value whereas η was underestimated and less robust. This suggests that there is a possibility to extract intrinsic IP parameters from the recovered pseudo-chargeability from AEM surveys if the c values are known or assummed

Chapter 4

Airborne Examples

Most airborne EM (AEM) surveys use wire loops for the source and receiver. This pair of source and receiver loops is attached to either a helicopter or a plane, and can cover a large area quickly. Fig. 4.1 illustrates the geometry of an example AEM system. In particular for time-domain systems, current in the source loop is abruptly turned off after the on-time. This changing current generates a time-varying magnetic field, which induces electrical fields in the earth. These electric fields in the earth diffuse away. Recalling that there will always be polarization effects whenever an electric field is applied to a chargeable medium, induced polarization (IP) effects can occur due to a changing current induced by an airborne system, and IP responses could be measured in the air as well. These IP effects are often observed to have negative transients for late-time channels. Weidelt [1982] showed that for a coincident-loop system, negative transients can be obtained only if the earth medium is chargeable. Historically, negatives have been measured from a number of field AEM surveys [Smith and Klein, 1996, Kratzer and Macnae, 2012, Kaminski and Viezzoli, 2017], and today it is common to measure negatives especially because of the recent developments in instrumentation; specifically low transmitter and receiver heights, large inducing currents and low noise levels. For instance, Fig. 4.2(a) shows a profile line of data obtained from a VTEM survey (2007) over the Mt Milligan porphyry deposit. Around the easting of 433800 m, negatives are observed (red lines). The time decay at a sounding around that location are provided in Fig. 4.2(b), and this shows negative transients at time channels

(> 1 ms).

To illustrate the physics behind negative transients, a simple forward simulation is carried out using EMTDIP code. Fig. 4.3 shows a cylindrical chargeable body embedded in a halfspace earth. The conductivity of the halfspace is 0.001 S/m, and the conductivity of the chargeable medium is 0.01 S/m. TEM simulation is conducted with a loop source with a step-off current waveform; the radius of the loop is 13 m, and it is located 30 m above the surface. Voltage data is measured at the receiver loop when the current is turned off. I first present the electrical field in the subsurface, then show the measured voltages as a function of time. Fig. 4.4 shows the x-z section of the electrical field in the y-direction at three different times. At 0.1 ms, large electric fields are induced in a chargeable medium. Note that the electric field is rotating in the counter-clock-wise direction. As time proceeds, these induced electric fields in the conductor diffuse away (0.5 ms), and at later time (7.9 ms), the electric field is reversed (clock-wise direction); this is due to the polarization current. Fig. 4.5(a) shows the observation at the receiver loop, and negatives are apparent after 0.9 ms. Clearly, these negatives are due to polarization currents flowing in the reverse direction. Another simulation is performed without IP effects ($d^F = F[\sigma_\infty]$), and d^{IP} is obtained by subtracting d^F from d. Time decays of all three data: d, d^F and d^{IP} are plotted in Fig. 4.5(b). In the early-time (< 0.03 ms) EM is dominant ($d \simeq d^F$), whereas in the late-time ($>$ 3 ms) IP is dominant ($d \simeq d^{IP}$). Intermediate time exists when both EM and IP are significant. Thus, AEM data can include IP effects and an effective methodology to handle these effects is necessary.

There can be two perspectives on the IP effects in AEM data: (a) They are noise, which disturbs conductivity signals and (b) IP effects are signals, and they include chargeability information of the subsurface. Both perspectives are valid, and depend upon the goal of an AEM survey and the sources of IP. For mining applications such as seeking kimberlites, IP effects due to permafrost can be considered as geologic noise, which contaminates the conductivity signals from the kimberlites. On the other hand, if kimberlites are chargeable, then IP effects in the data may be considered as signal. The main interest of this Chapter is in the latter, and hence I use the TEM-IP inversion workflow to recover distributed polarization information. This workflow is based upon natural separation of EM and IP effects

in time (Fig. 4.5b), and includes three main steps:

- Step 1: Conductivity inversion. Here I need to invert data that are not contaminated with IP effects to recover the conductivity distribution, $\sigma_{est}(x,y,z)$. Negatives are obvious, and those can be removed. However positive data could include significant IP effects (see 0.1 ms in Fig. 4.5b), and hence determining the latest time at which EM is dominant is a challenge. For the work here I ignored all negative data, and also the first few positive data before the sign reversal.

- Step 2: EM-decoupling. In this step, EM effects are considered as the noise. The fundamental response is estimated by evaluating $F[\sigma_{est}]$, and subtracting it from the observation to yield

$$d^{IP}[\sigma_{est}] = d - F[\sigma_{est}] \tag{4.1}$$

  The obtained IP data, $d^{IP}[\sigma_{est}]$ will always have some errors because σ_{est} is not the same as the true $\sigma_{\infty}(x,y,z)$. EM-decoupling will be effective in the intermediate time when both EM and IP effects are significant. For the EM-dominant time it will not be effective, since the IP is too small; EM-decoupling is not required for the late-time.

- Step 3: IP inversion. Each time channel of the obtained d^{IP} is separately inverted, and pseudo-chargeability: $\tilde{\eta}(x,y,z;t)$ is recovered. Pseudo-chargeability itself can provide some qualitative information about the distributed chargeability. Further, intrinsic polarization information such as Cole-Cole parameters, can be estimated by solving a small inverse problem using pseudo-chargeability of a single cell at multiple times.

I now apply this TEM-IP inversion workflow to three examples. The first is a synthetic example (Section 4.1), and here I test the capability of the workflow to handle airborne IP data. The second example shows an application of the workflow to field AEM data over the Mt Milligan porphyry deposit (Section 4.2), which showed clear negative transients. A 3D distribution of chargeability information is recovered, and this reveals highly altered zones surrounding a resistive stock.

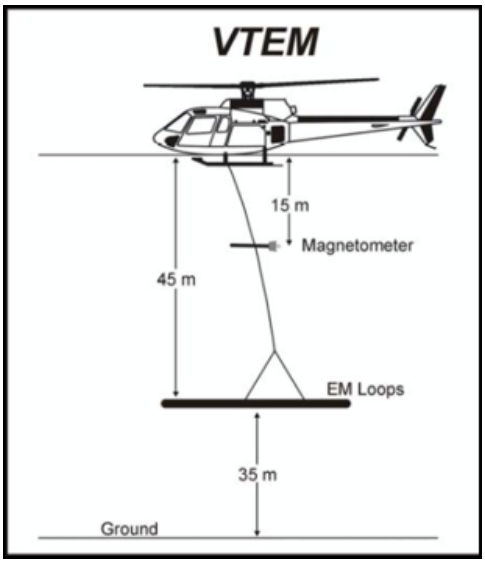

Figure 4.1: Geometry of the VTEM system (Geotech).

The third example presents much stronger negatives obtained over a kimberlite complex at Tli Kwi Cho (TKC) region, and here I show how both conductivity and chargeability information obtained from AEM data can help distinguishing different kimberlites in the ground.

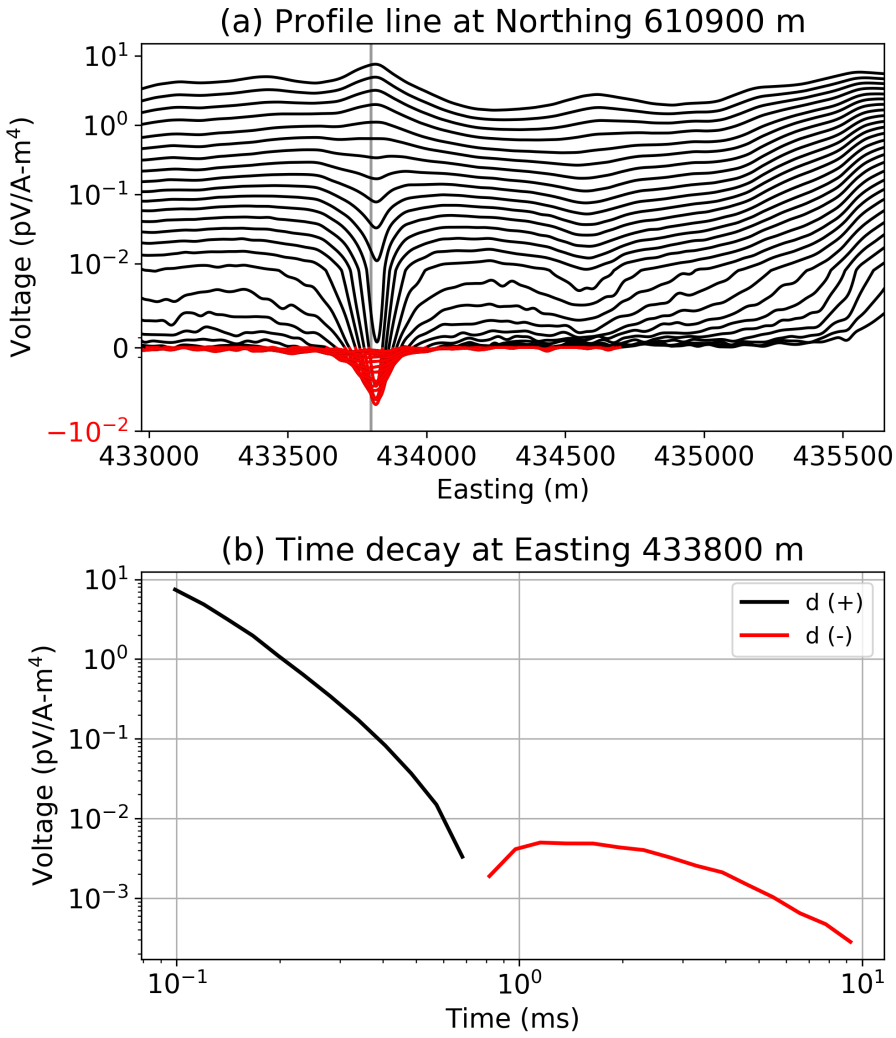

Figure 4.2: Observed VTEM data over the Mt Milligan porphyry deposit, BC, Canada. (a) Profile line at Northing 6109000 m, which crosses Harris fault and Rainbow faults. (b) Time decay at Northing 6109000 m and Easting 433800 m. Here black and red lines distinguish positive and negative values.

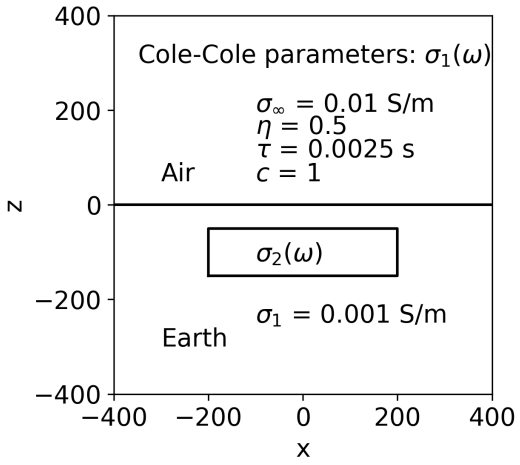

Figure 4.3: Section of a chargeable cylinder embedded in a halfspace. Conductivity of the halfspace is σ_1=0.001 S/m. The conductive chargeable cylinder is parameterized with a Cole-Cole model and has higher conductivity than that of halfspace: σ_∞=0.01 S/m. Other parameters are given in the diagram.

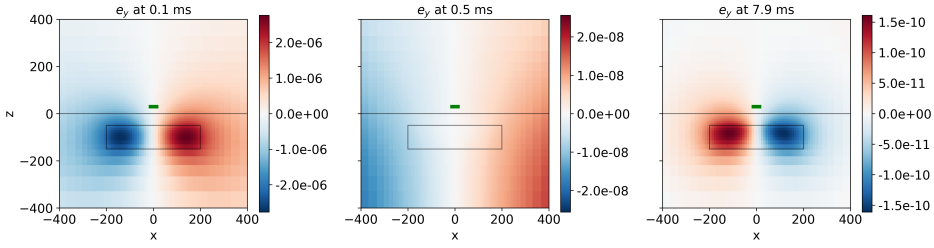

Figure 4.4: Propagation of electric fields in time: 0.1 ms (left), 0.5 ms (middle), and 7.9 ms (right). e_y is plotted in the x-z plane, and fundamental electric field is rotating in counter-clock-wise-direction. In the late-time, the reversed direction of e_y is observed due to strong polarization effects. Boundaries of the air-earth interface and chargeable cylinder are shown as black lines.

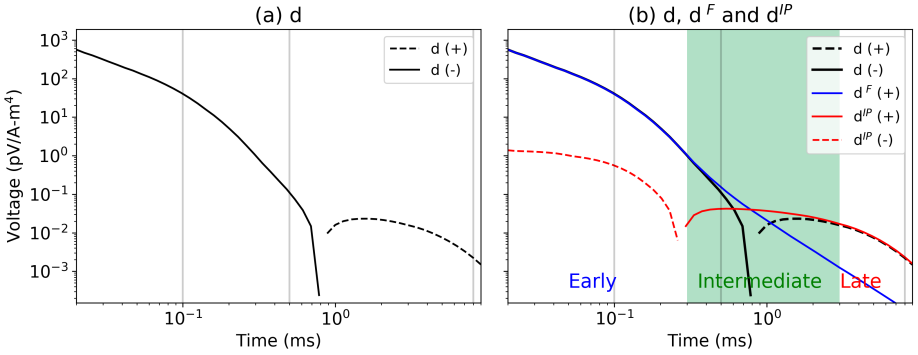

Figure 4.5: Time decays of observed (d), fundamental (d^F), and IP (d^{IP}) voltages over a chargeable cylinder. Solid and dashed lines distinguish positive and negative values. (a) Only observed voltage. (b) All three voltages with distinction of early, intermediate, and late times. Vertical grey lines indicate three times (0.1, 0.5, and 7.9 ms) when electric fields are plotted in Fig. 4.4.

4.1 Synthetic Example

4.1.1 Setup

To interrogate how the workflow could be applied to airborne IP data, a synthetic Cole-Cole model is composed assuming c=1. The $\sigma_\infty(x,y,z)$ model is shown in Fig. 4.6. Conductivities of the resistive host rock and conductive overburden on the west side are 10^{-3} and 10^{-2} S/m, respectively. Four IP blocks, which named A1-A4 are embedded in the subsurface. IP blocks have different σ_∞ and η values as shown in Table 4.1. A3 and A4 are conductors, but A4 is buried at a greater depth. A1 has the same conductivity value as the overburden, and A2 is a resistor. Except for the four IP blocks, η values are set to zero, and τ is set to a constant value, 0.005 s. To compute synthetic AEM data from this Cole-Cole model, the EMTDIP code is used [Marchant et al., 2014]. The survey geometry includes 21 lines as shown in the top-left panel of Fig. 4.6 as black dots. We use a coincident-loop system and the loop is located 30 m above the surface; the radius of the loop is 13 m. A step-off current waveform is used and the range of measured time channels is 0.01-10 ms. The measured responses is voltage, which is proportional to the vertical component of $-\frac{\partial \vec{b}}{\partial t}$. To test the capability of the TEM-IP inversion workflow for airborne IP data, I generate synthetic airborne IP data using the above setup, and apply the workflow to them. The following section presents the synthetic airborne IP data.

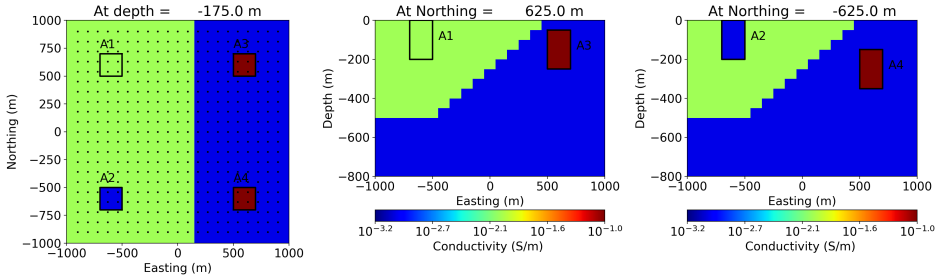

Figure 4.6: Sectional views of $\sigma_\infty(x,y,z)$ model. Solid lines delineate boundaries of four IP blocks.

Table 4.1: Cole-Cole parameters of four anomalous bodies (A1-A4).

Division	A1	A2	A3	A4
σ_∞ (S/m)	0.01	0.001	0.1	0.1
η	0.5	0.5	0.4	0.8
τ (s)	0.005	0.005	0.005	0.005

4.1.2 Data

A forward simulation is performed using the setup described in Section 4.1.1, and here I visualize this synthetic data in three different forms:

- 2D map (at a single time, but all stations)
- Profile line (at multiple times)
- Time decay (at a station)

Fig. 4.7 shows the 2D map of the observed voltage at 0.2 ms, 1.8 ms and 5.6 ms. Here, negative values are presented as white on the color map. At 0.2 ms, EM induction is dominant. The boundary of the conductive overburden and resistive earth clearly show up around easting 250 m. Both conductive and resistive anomalies appears near A3 and A2, respectively. The deep conductor, A4 does not show a high anomaly at this time. At later time, the effect of polarization increases, and the first negatives are shown at 1.8 ms near A3; at 5.6 ms, stations around all four blocks show negatives, hence IP is dominant. For visualizing airborne IP data, often a profile line of data at multiple times are plotted in double-log plot for better representation of negative IP signatures. Fig. 4.8 shows the observed data at two profile lines, which cross the four IP blocks. Near A1 and A3, negatives are clearly shown at late-time channels (marked as red lines in Fig. 4.8 a). Early-time responses of A1 and A3 are different due to their different conductivity structures; A3 shows a high anomaly, whereas A1 is flat. This trend changes with time: both A1 and A3 show low or negative anomaly data as time passes. Profile line data around A2 and A4 are shown in Fig. 4.8(b). Compared to A1 and A3, much smaller negatives are shown near A2 and A4, because A2 and A4 are correspondingly a resistor and a deep conductor; they generate only small polarization effects. Resistors do not have enough induction, and the deep conductor has weaker polarization effects by geometric decay ($1/r^3$). Effects of conductive overburden are much clearer on this line ($\sim$ 400 m easting). Fig. 4.9 shows four time decays over the four A1-A4 blocks. All four decays show negative transients at later times, but the sign reversals occur at different times due to different conductivity and chargeability structures. In the following sections, I apply the workflow to these synthetic airborne IP data.

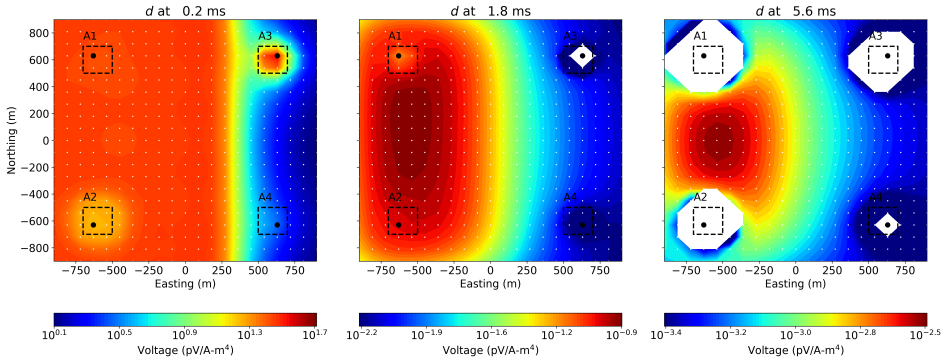

Figure 4.7: 2D map of the simulated data including both EM and IP effects (d). A1-A4 indicate corresponding anomalies due to four IP bodies. Black dotted lines indicate boundaries of the four IP bodies. Negative responses are shaded as white regions. Black dots are locations of Fig. 4.9. Black dots are locations of Fig. 4.9.

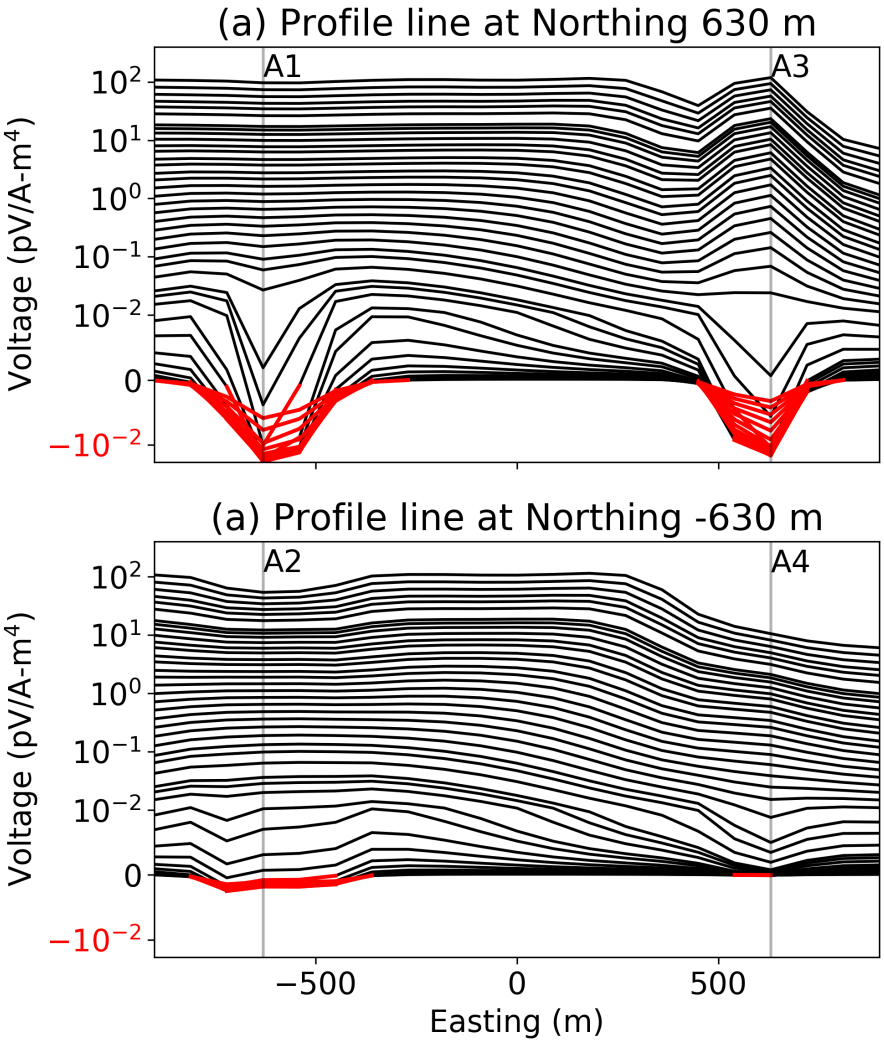

Figure 4.8: Profile line of the observed data, d at Northing (a) 630 m and (b) -630 m. Black and red lines distinguish positive and negative data.

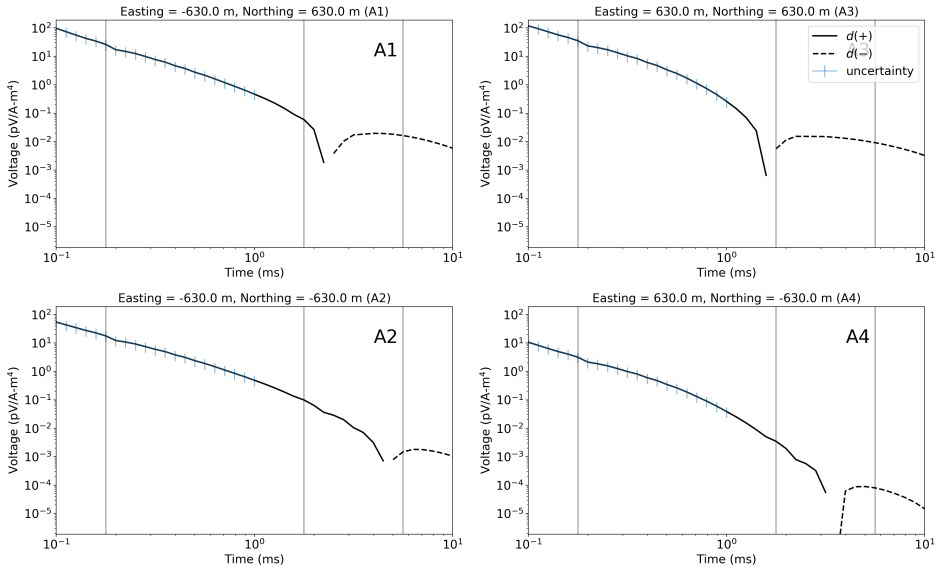

Figure 4.9: Time decays of the observed data, d at four sounding locations close to A1-A4. Here solid and dashed lines distinguish positive and negative data. Error bars are shown from 0.1 to 1 ms, which indicate the uncertainty used in conductivity inversion. Three grey vertical liens indicate time channels shown in Fig. 4.7.

4.1.3 Conductivity Inversion

Conductivity inversion is the first step of the TEM-IP inversion workflow. The main question in this step is: how do I ignore any IP effects when inverting the observed data to obtain a conductivity model. Here, I simply choose time channels from 0.1 to 1 ms (20 channels) for all sounding locations, which do not show any negatives. Using UBC TDoctree code [Haber and Schwarzbach, 2014], these early 20 channels of the observations are inverted, and a 3D conductivity model is recovered. Parameters of the conductivity inversion are summarized in Table 4.2. The estimated conductivity model, $\sigma_{est}(x,y,z)$, is shown in Fig. 4.10. The conductive overburden, resistor (A1), and conductor (A2) are all recovered, but not a deep conductor (A4). This poor conductivity recovery of the deep conductor shows a general challenge of handling late-time conductivity signals when the observation is significantly contaminated by IP. Overall, the estimated conductivity is reasonable enough, and this will be used in the following steps: EM-decoupling and IP inversion.

Table 4.2: Parameters of conductivity inversion.

Parameters	Values
$\alpha_x = \alpha_y = \alpha_z$	1
α_s	10^{-5}
ϕ_d^*	$441 \times 20 = 8820$
Uncertainty(ε_j)	$10^{-1}\ \lvert d_j^{obs} \rvert$
$\mathbf{m}_0$	$log(10^{-3})$
$\mathbf{m}_{ref}$	$log(10^{-3})$
Model weighting	N/A
Bounds constraint	N/A

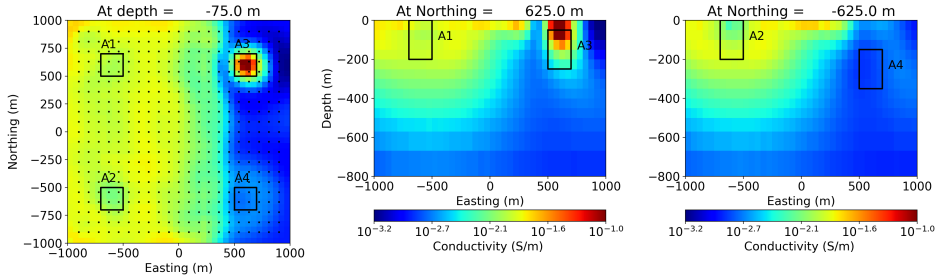

Figure 4.10: Sectional views of the recovered conductivity model (σ_{est}). Solid lines delineate boundaries of the four IP blocks.

4.1.4 EM-decoupling

The conductivity model (σ_{est}) in Fig. 4.10 is used to estimate the fundamental responses, $F[\sigma_{est}]$. 2D maps of $F[\sigma_\infty]$ and $F[\sigma_{est}]$ at three different times: 0.2 ms, 1.8 ms, and 5.6 ms are shown in Fig. 4.11. At 0.2 ms, $F[\sigma_{est}]$ effectively estimated a linear edge of from the conductive overburden, and both anomalies at A2 (resistor) and A3 (conductor). Even at later times: 1.8 and 5.6 ms, $F[\sigma_\infty]$ and $F[\sigma_{est}]$ show reasonable agreements. Note that the range of time used for the TEM inversion is 0.1-1 ms, that is 1.8 and 5.6 ms are not included in the conductivity inversion. Fig. 4.12 presents time decays of $F[\sigma_\infty]$ and $F[\sigma_{est}]$ at four sounding locations close to A1-A4. The overall fit is good not only for times used in the inversion, but also at later times: 1-10 ms. All four stations close to A1-A4 show a good match between $F[\sigma_\infty]$ and $F[\sigma_{est}]$, and this will ensure effective EM-decoupling.

The sought data $d^{IP}[\sigma_{est}]$ can be obtained can be obtained by

$$d^{IP}[\sigma_{est}] = d - F[\sigma_{est}] \tag{4.2}$$

The obtained IP data however, will include some errors since $F[\sigma_{est}]$ is not same as $F[\sigma_\infty]$. To examine these more closely we write

$$d^{IP}[\sigma_{est}] = d - F[\sigma_{est}] = d^{IP}[\sigma_\infty] + \triangle d + n, \tag{4.3}$$

where n is additive noise, and $\triangle d$ ($= F[\sigma_\infty] - F[\sigma_{est}]$) is the error caused because of poor estimate of σ_∞. Undoubtedly there are situations where the errors on the right hand side can become larger than d^{IP}. This will always occur at early-time channels where the IP response is small and EM induction response is large. Thus there is an earliest time channel that can be used for this analysis. The second issue concerns $\triangle d$. This is more difficult to quantify and needs to be treated on a case-by-case basis. I postpone this discussion until later in this section.

I now proceed with EM-decoupling. As this is a synthetic example, both $F[\sigma_{est}]$ and $F[\sigma_\infty]$ will be used, and the obtained $d^{IP}[\sigma_{est}]$ and $d^{IP}[\sigma_\infty]$ are shown in Fig. 4.13(a) and (b), respectively. A comparison shows that the relative strength of $\triangle d$ get smaller as time increases (e.g. 1.8 and 5.6 ms), whereas this error is large at earlier time (0.2 ms). Although there are significant errors, the IP anomaly at A3

is recognized even at 0.2 ms, and this was not shown as a negative anomaly in d (see Fig. 4.7a). At 1.8 ms d did not show negatives except for A3, but with the EM-decoupling all four IP anomalies are recognized. At 5.6 ms $d^{IP}[\sigma_\infty]$ and $d^{IP}[\sigma_\infty]$ are almost identical. Fig. 4.14 compares time decays of $d^{IP}[\sigma_\infty]$ and $d^{IP}[\sigma_{est}]$; they have converged by 2 ms. To summarize, the EM-decoupling shows good performance at the intermediate and late-times (see Fig. 4.5) when the IP signal is significant, whereas it shows poor performance at early times when EM induction is dominant.

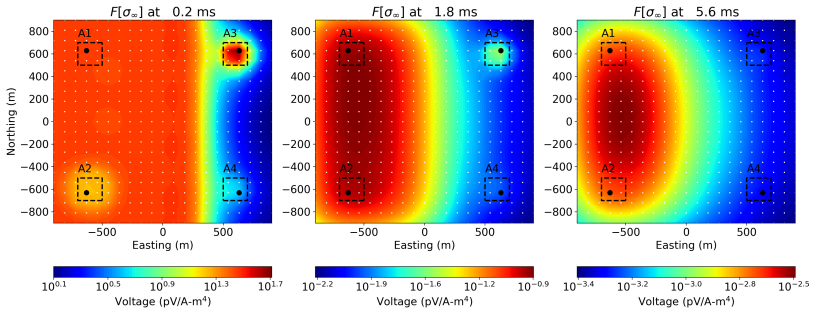

(a) True

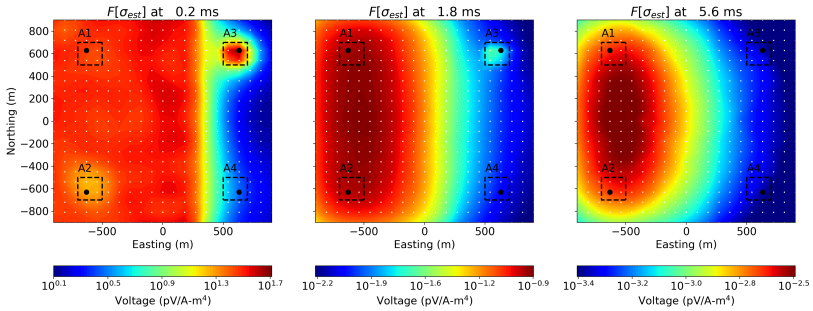

(b) Estimated

Figure 4.11: Comparison of true and estimated fundamental responses at 0.2, 1.8 and 5.6 ms. (a) true fundamental response: $F[\sigma_\infty]$ and (b) estimated fundamental response: $F[\sigma_{est}]$.

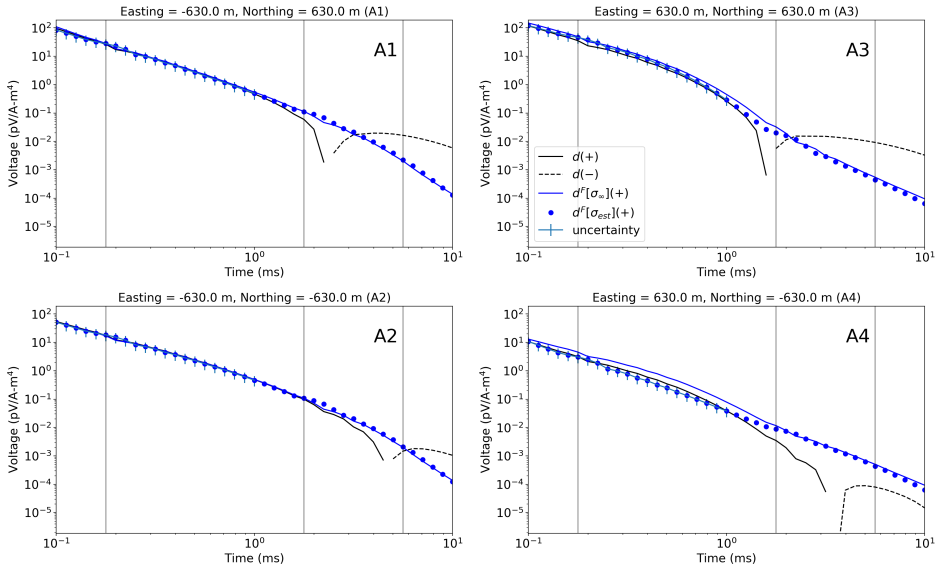

Figure 4.12: Time decays of the d, $F[\sigma_\infty]$, and $F[\sigma_{est}]$ at four sounding locations close to A1-A4. Here solid and dashed lines distinguish positive and negative datum. Error bars are shown from 0.1 to 1 ms, which indicate uncertainty used in conductivity inversion.

Ideas for Contending with $\triangle d$

Although $d^{IP}[\sigma_{est}] = F[\sigma_\infty] - F[\sigma_{est}]$ data are obtained, still they include errors: $\triangle d$. Here I comment about $\triangle d$, and suggest an idea that can reduce its impact of $\triangle d$. It is least important when dealing with resistive bodies and hosts, and most problematic as the bodies and hosts become more conductive. There are a few items of note. Firstly, if σ_{est} is incorrect by a scale factor then this shifts the d^{IP} data. Away from chargeable bodies the d^{IP} response should be zero. Assuming these locations can be recognized, then the regional shift can be estimated and applied to $d^{IP}[\sigma_{est}]$. The same idea is applicable to long wavelength spatial components of regional fields ($\triangle d$). Any corrective procedure, which is akin to removal of regional fields in potential fields processing, relies on identification of areas in the model believed to be free of IP responses.

For example, I choose $d^{IP}[\sigma_{est}]$ at 1.8 ms shown in Fig. 4.15a, and apply a regional removal. Based on identified IP anomalies at A1-A4, some stations

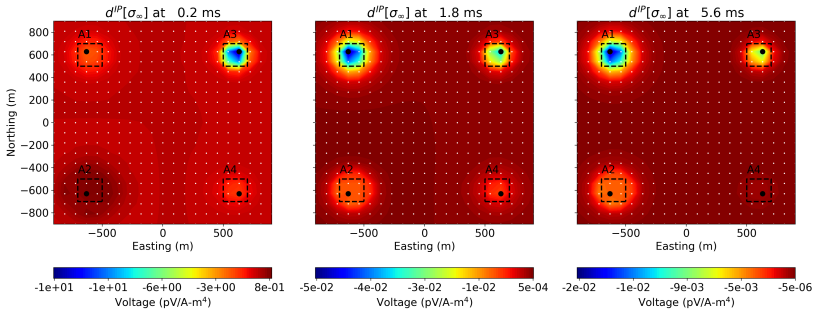

(a) True

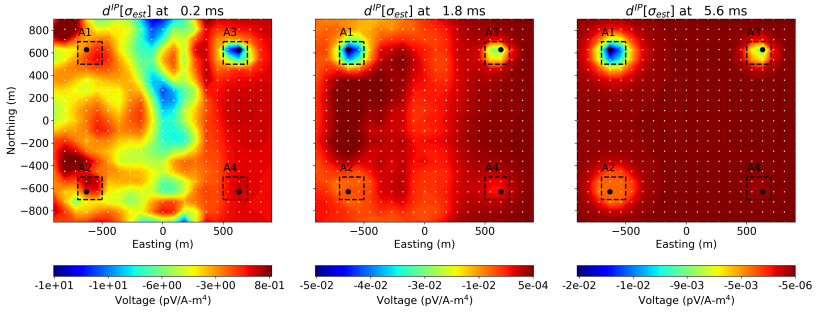

(b) Estimated

Figure 4.13: Comparison of true and estimated IP responses at 0.2, 1.8 and 5.6 ms. (a) true IP response: $d^{IP}[\sigma_\infty]$ and (b) estimated IP response: $d^{IP}[\sigma_{est}]$.

away from those area are selected to estimate regional fields. Selected locations are marked as empty white circles in Fig. 4.15(a). A polynomial function was used to fit $d^{IP}[\sigma_{est}]$ at selected locations, and Fig. 4.15(b) shows the estimated regional field. This is subtracted from $d^{IP}[\sigma_{est}]$ to produce $d^{IP}_{RM}[\sigma_{est}]$ as shown in Fig. 4.15(c). The $d^{IP}_{RM}[\sigma_{est}]$ shows a better match with $d^{IP}[\sigma_\infty]$. Hence, a proper regional removal could improve the quality of $d^{IP}[\sigma_{est}]$. Importantly, however extra care should be put on this step in practice since one could remove IP signals in $d^{IP}[\sigma_{est}]$ data. These are preliminary ideas at this stage, but the example shows promise and this is worthwhile pursuing.

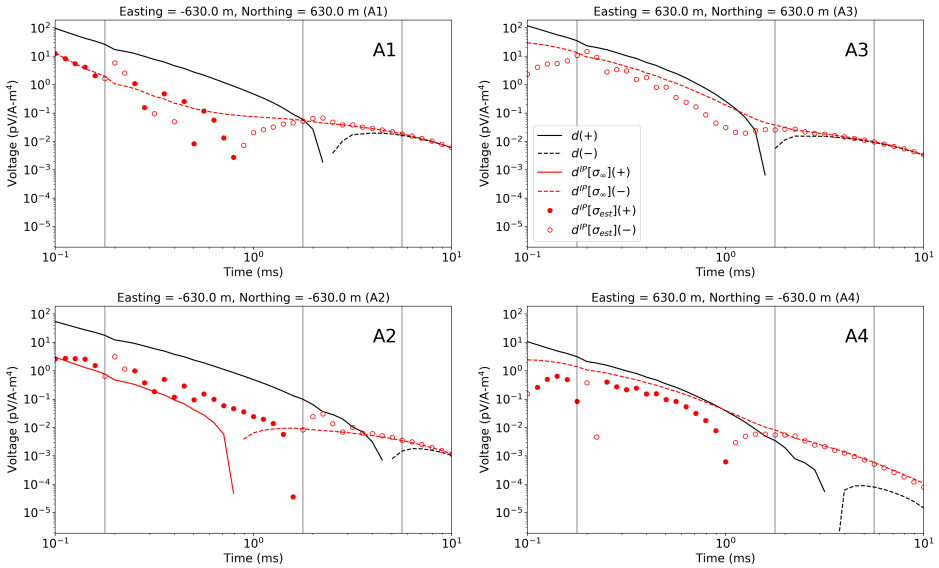

Figure 4.14: Time decays of the d, $d^{IP}[\sigma_\infty]$, and $d^{IP}[\sigma_{est}]$ at four sounding locations close to A1-A4. Here solid and dashed lines or solid and empty circles distinguish positive and negative datum.

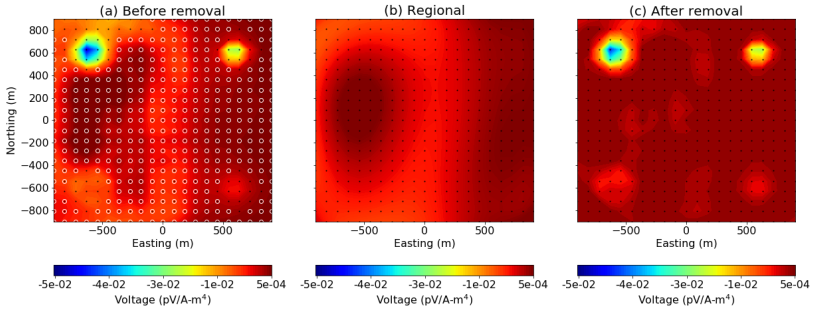

Figure 4.15: Regional removal procedure. Left, middle and right panels correspondingly indicate before removal, estimated regional fields, and after removal of $d^{IP}[\sigma_{est}]$ at 1.8 ms. Black dots and empty white circles indicate all stations and selected stations to estimate regional field.

4.1.5 IP Inversion

The EM-decoupling method in the previous subsection has been used to generate IP responses, d^{IP}. The next step inverts these data to recover a 3D distribution of pseudo-chargeability. 3D IP inversions applied to the $d^{IP}[\sigma_{est}]$ (before regional removal) and the $d^{IP}_{RM}[\sigma_{est}]$ (after regional removal) at 1.8 ms are shown in Fig. 4.15(a) and (c). Parameters of the IP inversion used are shown in Table 4.3.

The recovered pseudo-chargeability models are shown in Fig. 4.16(a) and (b). Without the regional removal, the four chargeable blocks are reasonably imaged, but there is a large-scale rectangular artefact contaminating the image. This is due to errors in the EM-decoupling caused by an inaccurate σ_{est}. These artifacts are effectively removed when the $d^{IP}[\sigma_{est}]$ are processed to remove a regional field. This result indicates that the recovered pseudo-chargeability can provide useful distributed IP information of the subsurface. The inversion results in Fig. 4.16 provide insight about the existence and the geometry of the chargeable rocks. However, there are two important aspects that should be remembered when interpreting the resultant images:

- **Relative magnitude of $\tilde{\eta}$**. The recovered $\tilde{\eta}$ is different from η, and higher $\tilde{\eta}$ does not necessarily indicate higher chargeability.

- **Depth resolution of the IP inversion**. A depth weighting is used to compensate for lack of intrinsic depth resolution. As shown in Fig. 4.16, relative depth information can be extracted from the IP inversion. This is the same issue as in magnetic inversion, and numerous successes of magnetic inversion supports that the inversion with depth weighting still provides relative depth information.

Extracting intrinsic IP parameters

In the above section I have concentrated upon IP inversion at a single time channel. The same IP inversion is now applied to each time channel of $d^{IP}[\sigma_{est}]$, separately, to recover pseudo-chargeability at multiple times. Here pseudo-chargeability is $-\frac{\partial\tilde{\eta}}{\partial t}$ because the data are voltages, which is similar to $-\frac{\partial\vec{b}}{\partial t}$ and hence its dimension is $1/s$. From this pseudo-chargeability: $-\frac{\partial\tilde{\eta}}{\partial t}(x,y,z;t)$, I extract Cole-Cole pa-

rameters by solving a small inverse problem as described in Appendix B. Pseudo-chargeability at a single cell is parameterized in terms of η and τ by assuming c is known and is set to c=1. A representative cell, which has a maximum pseudo-chargeability value, for each of the four anomalies is selected, and corresponding decays are shown in Fig. 4.17. Those four time decays of the pseudo-chargeability are data for a parametric inversion to recover η and τ for each decay. Comparison of observed and predicted pseudo-chargeability at the four cells are shown in Fig. 4.17. Recovered values and selected locations are summarized in Table 4.4. The recovered τ's for cells corresponding to A1-A3 are in fair agreement with true values but A4 differs by a factor of four. Poor recovery of τ for the A4 may be caused by poor estimation of conductivity for this deep conductor. The η values however are all underestimated (see Table 4.1). This result is consistent with the example shown in Section 3.3.2. I conclude that there is the potential to extract intrinsic Cole-Cole parameters from AEM data but the time constant seems to be the most robust parameter to be extracted.

Table 4.3: Parameters of IP inversion.

Parameters	Values
$\alpha_x = \alpha_y = \alpha_z$	1
α_s	10^{-5}
Uncertainty(ε_j)	$10^{-2}\ max(\mathbf{d}^{obs})$
$\mathbf{m}_0$	0
$\mathbf{m}_{ref}$	0
Model weighting	$1/z^3$
Bounds constraint	$\mathbf{m} > 0$

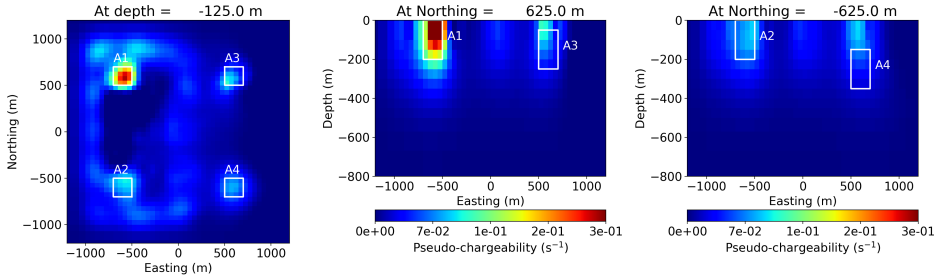

(a)

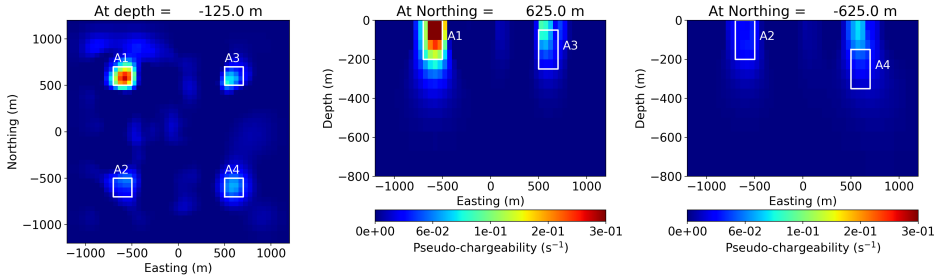

(b)

Figure 4.16: Sectional views of the recovered $-d\tilde{\eta}/dt$ models at 1.8 ms. (a) Without regional removal. (b) With regional removal.

Table 4.4: Recovered Cole-Cole parameters of four chargeable blocks (A1-A4). Values in parenthesis indicates true values.

Division	A1	A2	A3	A4
Cell location	(-575, 625, -25)	(-575, -525, -25)	(625, 575, -75)	(-625, -575, -25)
η	0.39 (0.5)	0.033 (0.5)	0.006 (0.4)	0.01 (0.8)
τ	0.006 (0.005)	0.0035 (0.005)	0.0036 (0.005)	0.0019 (0.005)

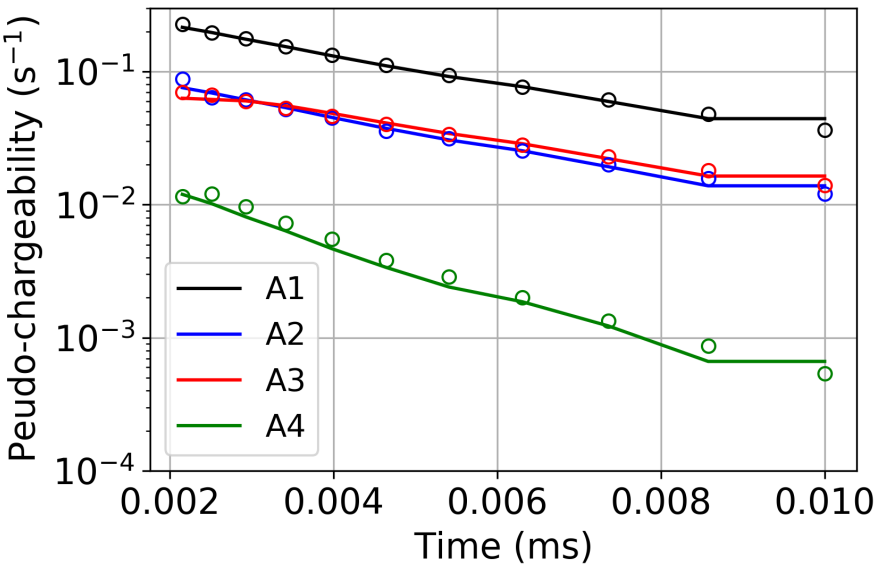

Figure 4.17: Comparison of observed and predicted pseudo-chargeability for four chargeable anomalies: A1-A4. Solid lines and empty circles distinguish observed and predicted pseudo-chargeability.

4.1.6 Conclusions

The TEM-IP workflow is applied to a synthetic AEM example, and each of three steps is carefully analyzed and tested. The first step is conductivity inversion, and early-time channels which do not have negative values are used to recover 3D conductivity, σ_{est}. Overall the conductivity structures are imaged well, except for the deep conductor, A4. Using the obtained conductivity, the second step is EM-decoupling. By subtracting $F[\sigma_{est}]$ from d, I obtain $d^{IP}[\sigma_{est}]$. The EM-decoupling shows great performance in the intermediate and late-times, but as expected it gives poor results in the early-time. Four IP anomalies are obtained, even at 1.8 ms when the observational data are positive for some blocks. To illustrate an approach to reduce the error of EM-decoupling characterized at early times, a regional removal is applied by assuming the error is a long-wavelength spatial component of a regional field. This regional removal procedure helped and it may be worthy of follow up research. The third step is IP inversion. Each time channel of the obtained $d^{IP}[\sigma_{est}]$ is inverted to generate 3D pseudo-chargeability models at multiple times; they provide useful information about the distributed polarization of the subsurface. Furthermore, by interpreting the recovered pseudo-chargeability, Cole-Cole parameters: η and τ are extracted for the four anomalies: A1-A4. Recovery of τ was reasonable, but η is mostly underestimated. To conclude, this synthetic example demonstrates the capability of the TEM-IP inversion workflow to handle airborne IP data, and recover distributed polarization information in 3D.

4.2 Field Example: Mt Milligan

4.2.1 Setup

Mt Milligan is located in BC, Canada (Fig. 4.18). It is a copper and gold porphyry deposit within the Early Mesozoic Quesnel Terrane, a Late Triassic to Early Jurassic magmatic arc complex that lies along the western North American continental margin. Previous geologic and geophysical work has illuminated that the mineralization is associated with monzonite stocks that intruded into basaltic volcaniclastic rocks Oldenburg et al. [1997], Yang and Oldenburg [2012][Reference]. A VTEM survey (2007) was flown over the Mt Milligan porphyry deposit, and it uses a helicopter-borne system with co-located source loop and receiver loop, which is similar to the coincident-loop system. This VTEM survey is a part of the QUEST project, which covers a much broader region; roughly 514 km in length by 124 km in width as shown in Fig. 4.18. The Mt Milligan VTEM survey has 13 lines, each 2.7 km in length resulting in a total of 37.5 line-km. Voltages are measured at 27 time channels ranging from 0.099 to 9.3 ms; the current waveform is shown in Fig. 4.20. Survey lines of the VTEM survey are shown in Fig. 4.19 as grey lines. That figure also presents the geology of the region and structural features. The topography of the area is shown in Fig. 4.21 and it ranges from 1044 to 1419 m. The flight height of the EM loops was about 30 m.

An effective 3D TEM inversion was developed by Yang et al. [2014], and they inverted the VTEM data, and recovered a 3D conductivity model. The most prominent intrusive monzonite stock, MBX, was successfully recovered as a resistive target. A conductive alteration zone surrounding this resistive stock, often called a halo structure, was recovered. This was an important example for the industry because it showed the necessity of 3D AEM inversion. 1D inversion could not recover this 3D conductivity structure, and it generated a misleading conductive feature at the location of the MBX stock [Yang and Oldenburg, 2012]. Negative transients were observed at some stations (see Fig. 4.2), and these stations were not included in the 3D AEM inversion. These negative transients suggest the existence of chargeable materials in the Mt Milligan area, and this was also supported by DC-IP inversion conducted by Oldenburg et al. [1997]. Based upon the TEM

inversion done by Yang et al. [2014], I apply the TEM-IP inversion workflow to the VTEM data over the Mt Milligan area. This is the first application of the TEM-IP inversion workflow to a field example, and an attempt to recover 3D chargeability information. The focus of this field AEM example will be EM-decoupling and the IP inversion since the 3D conductivity model has already been obtained by Yang et al. [2014].

Figure 4.18: Location of Mt Milligan and QUEST survey area.

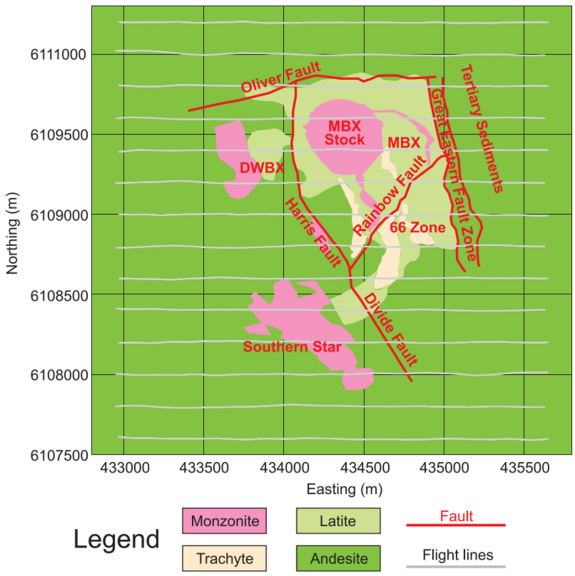

Figure 4.19: Geology and VTEM survey at Mt Milligan porphyry deposit in British Columbia, Canada [Yang and Oldenburg, 2012].

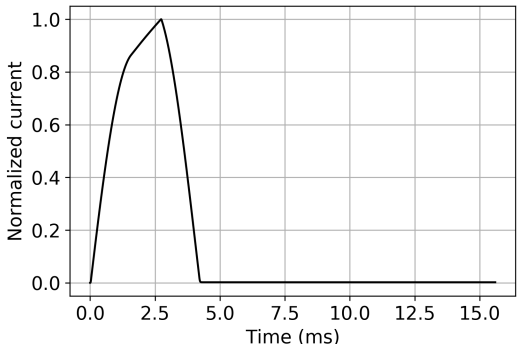

Figure 4.20: Normalized current waveform of the VTEM survey (2007) at Mt Milligan deposit.

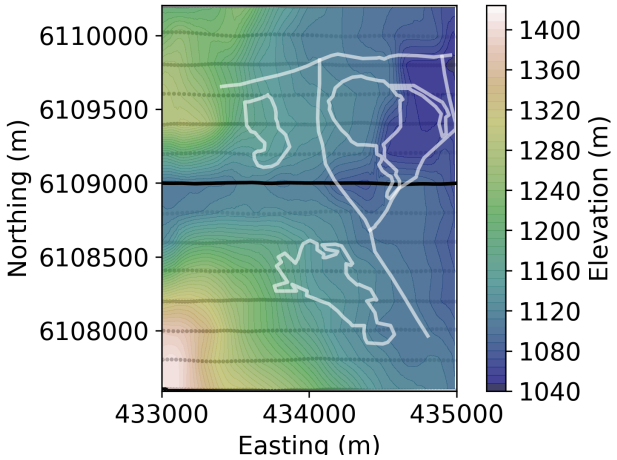

Figure 4.21: Topography of the VTEM survey of the Mt Milligan region. Geology indicated with white lines.

4.2.2 Data

From the VTEM survey 14,760 stations of the TEM data are collected and each station has 27 time channels. Fig. 4.22 shows a 2D map of the observed data at eight time channels ranging from 0.2 to 2.7 ms. At 0.2 ms, high anomalies are shown in the central western side and the north east side of the map. High voltages at the east side of the region are due to highly conductive Tertiary sediments. The central anomaly may be due to a conductive alteration zone around the resistive MBX stock. At later times, this high positive anomaly changes to negative values at 1 ms. Other negative anomalies are shown at later times. In the left panel of Fig. 4.23, three negative anomalies are marked as white dashed circles and named A1-A3. A2 is the main negative anomaly, which is the positive high anomaly in the central west discussed above. Corresponding time decays are shown on the right panel of Fig. 4.23. Decays at A2 show the greatest negative values indicating strong IP effects. Both A1 and A3 show negatives, whereas their amplitudes are quite small: $\sim 10^{-4}$ pV/A-m^2, which is about the noise level for this survey; and hence it may be questionable to consider them as negative anomalies due to chargeable materials. However, the A2 anomaly is definitely strong enough to be considered as an IP signal. We will test this by applying the TEM-IP workflow to this VTEM data set, and recover 3D chargeability information over the Mt Milligan deposit.

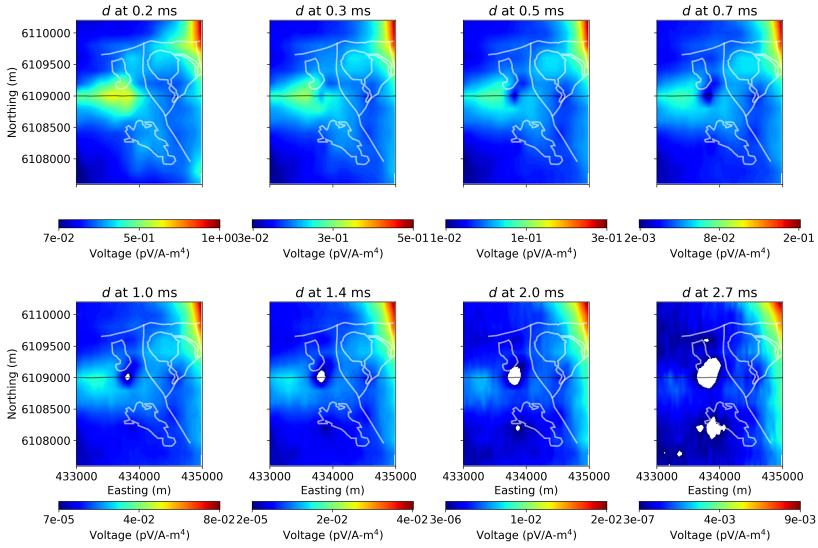

Figure 4.22: 2D map of the observed VTEM data at eight different times ranging from 4.6-7.1 ms. Solid white lines show boundaries of different gelogical units and the white areas indicate where the response has gone negative.

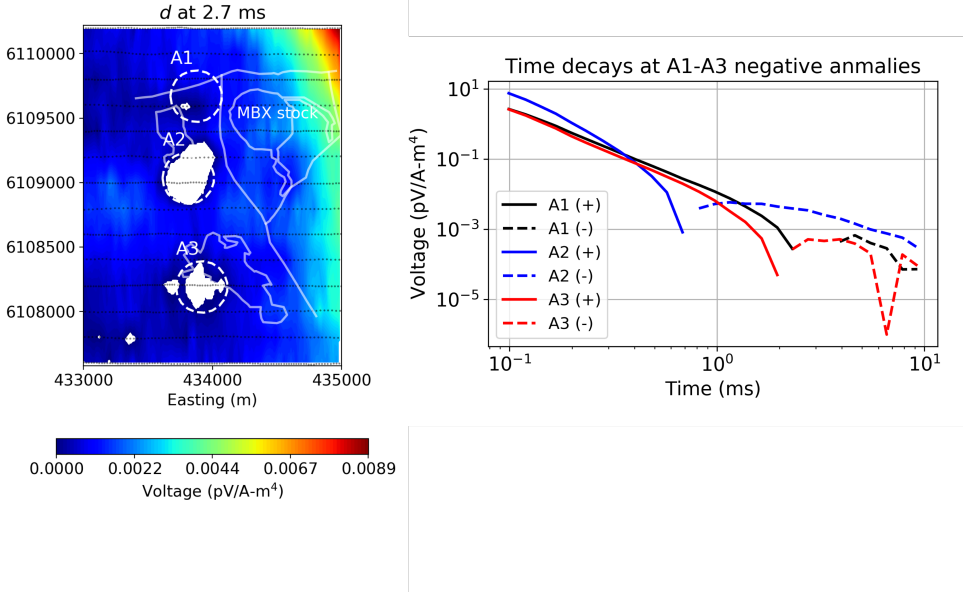

Figure 4.23: 2D map of the VTEM data at 2.7 ms (left panel) and time decays at three stations close the negative anomalies at A1-A3 (right panel). Solid white lines on the right panel show boundaries of different geological units, and white dashed lines indicate the approximate locations of where there are.

4.2.3 Conductivity Inversion

Because detailed information about the 3D conductivity inversion of the VTEM is described in Yang et al. [2014], only a brief summary of the inversion is provided here. In the total 14,362 soundings (except for some soundings showing negatives (around A1)), and 8 time channels ranging from 0.2 to 2.7 ms are used in the 3D TEM inversion. Five earlier time channels are ignored due to lack of knowledge about the exact current waveform; after 2.7 ms the signals are noisy. For data uncertainty, 10 percent of the data and a floor of 10^{-13} (V/A) floor are used. Fig. 4.24 shows plan and sections views of the estimated conductivity, σ_{est}. The resistive MBX stock and the surrounding conductive halo structure are successfully recovered. Note that the region where the conductive halo structure is recovered is where negatives are observed: A1-A3 anomalies. Using the obtained σ_{est}, EM-decoupling will be applied to obtain IP data.

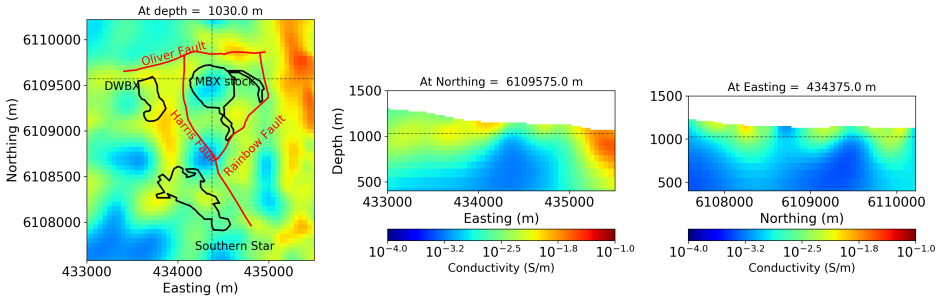

Figure 4.24: 3D Conductivity model of Mt Milligan porphyry deposit obtained by Yang et al. [2014].

4.2.4 EM-decoupling

Although negatives are measured at later time channels (¿ 1 ms), the observations still include EM effects, and these need to be removed to recognize IP signals in the data. For this, the EM portion is estimated by forward modelling TEM data using σ_{est}. The $d^{IP}[\sigma_{est}] = d - F[\sigma_{est}]$.

Fig. 4.25 illustrates the EM-decoupling applied to the observed data, d at three different time channels: 2.7 ms, 0.7 ms, and 0.2 ms. In the figure, left, middle and right panels respectively show d, $F[\sigma_{est}]$, and $d^{IP}[\sigma_{est}]$. At 2.7 ms, $F[\sigma_{est}]$ reasonably estimates d except for the region where negatives are shown. The $d^{IP}[\sigma_{est}]$ plotted in the right panel of Fig. 4.25(a) show five anomalies named A1-A5. Note that A4-A5 did not show any negatives in the observations, whereas A1-A3 did. The EM-decoupling shows good performance even at earlier times (0.7 ms and 0.2 ms), as shown in Fig. 4.25(b) and (c). Fig. 4.26 shows time decays at A1-A5. Overall, d and $F[\sigma_{est}]$ show reasonable agreements at early times, but the discrepancy between them increases with time (see A2 in Fig. 4.26). The EM-decoupling converts this to an IP signal. However, the obtained $d^{IP}[\sigma_{est}]$ can include errors originating from discrepancies between $\sigma_{\infty}(x,y,z)$ and σ_{est}, and hence some caution is necessary; I postpone this issue to the following section.

To summarize, the EM-decoupling process is effectively applied to the Mt Milligan VTEM data, and $d^{IP}[\sigma_{est}]$ are obtained, which illuminated five IP anomalies: A1-A5. In the following section, the obtained $d^{IP}[\sigma_{est}]$ will be inverted to recover a 3D pseudo-chargeability in the Mt Milligan area.

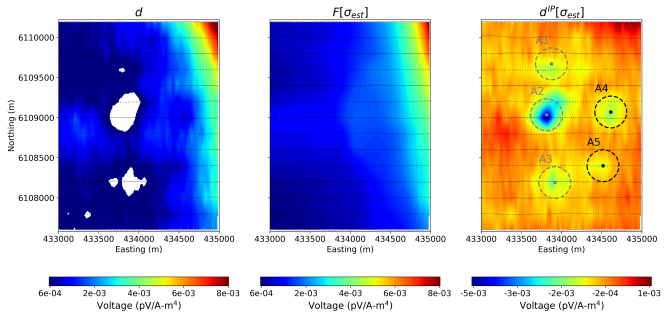

(a) 2.7 ms

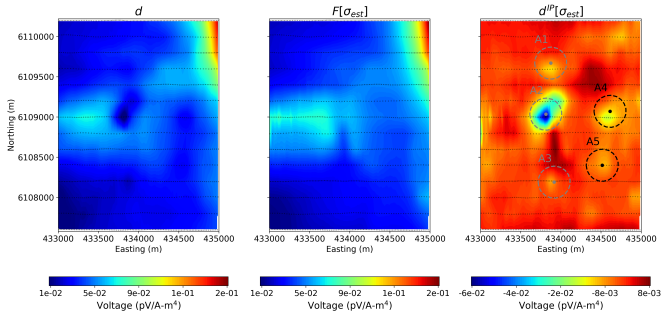

(b) 0.7 ms

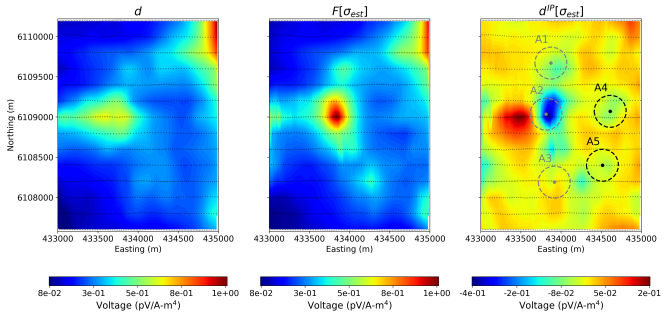

(c) 0.2 ms

Figure 4.25: EM-decoupling of the VTEM data over Mt Milligan region. 2D maps of d, $F[\sigma_{est}]$, $d^{IP}[\sigma_{est}]$ are shown at (a) 2.7, (b) 0.7 and (c) 0.2 ms. $F[\sigma_{est}]$ is subtracted from d to obtain $d^{IP}[\sigma_{est}]$. A4-A5 are IP anomalies recognized by EM-decoupling, whereas A1-A3 were shown as negatives in d. A1-A3 and A4-A5 are marked as grey and black dashed circles, respectively.

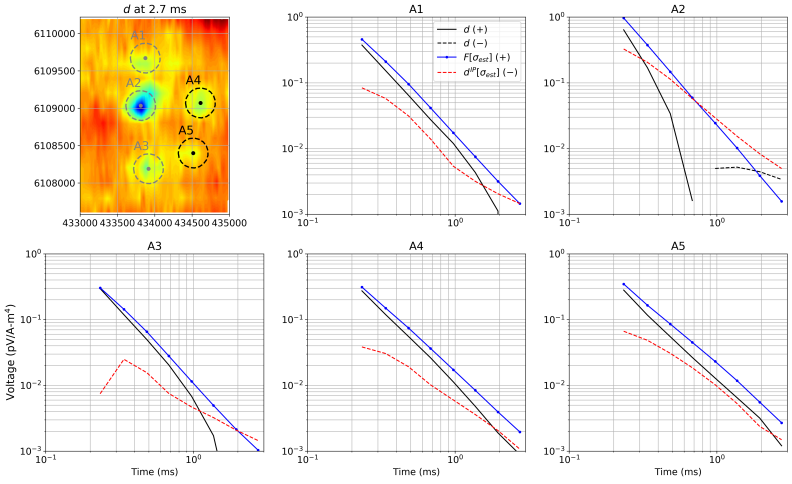

Figure 4.26: Time decays of d, $F[\sigma_{est}]$, $d^{IP}[\sigma_{est}]$ at the five IP anomalies: A1-A5. Top left panel showed 2D map of $d^{IP}[\sigma_{est}]$ at 2.7 ms.

4.2.5 IP Inversion

From the EM-decoupling, eight time channels of the $d^{IP}[\sigma_{est}]$ (from 0.2 ms-2.7 ms) are obtained. Each time channel of the $d^{IP}[\sigma_{est}]$ is inverted separately, and a 3D distribution of pseudo-chargeability is recovered at each of eight channels. Parameters of the inversion used here are the same as those used in Section 4.1.5 as described in Table 4.3. Fig. 4.27(a)-(c) shows plan and section views of the recovered pseudo-chargeability at three different time channels: 2.7 ms, 0.7 ms, and 0.2 ms, respectively. At 2.7 ms anomalous pseudo-chargeability volumes are recovered around A1-A5, and in particular the pseudo-chargeability around A2 and A3 show strong amplitude. Most anomalies are imaged 100 m below surface. Regional removal can be applied (as described in Section 4.1.4), and it could enhance the quality of the obtained $d^{IP}[\sigma_{est}]$. In contrast, it could remove the IP signals, which indicates that extra care is necessary for the regional removal. Hence, I omitted this step, and to prevent fitting those errors in the $d^{IP}[\sigma_{est}]$, I imposed the positivity constraint on the IP inversion. This positivity constraint effectively ignores most of positive bias in the $d^{IP}[\sigma_{est}]$ as shown in Fig. 4.28. In this figure, the observed and predicted data of the IP inversion are compared at three time channels. Earlier time shows greater misfits, which is a consequence of the greater the errors in the EM-decoupling process.

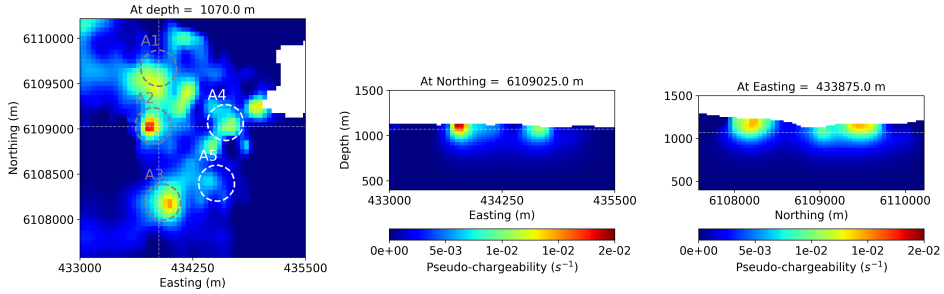

(a) 2.7 ms

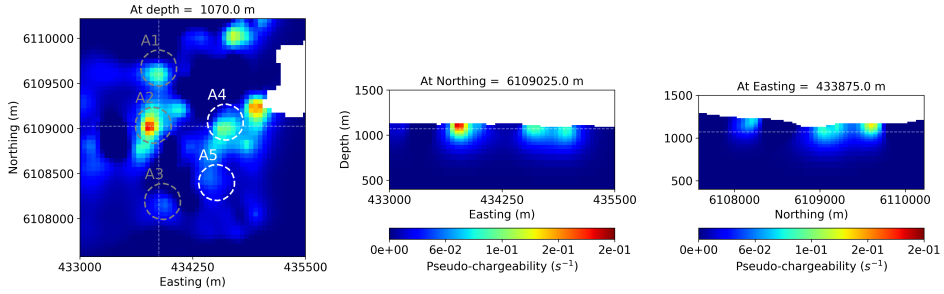

(b) 0.7 ms

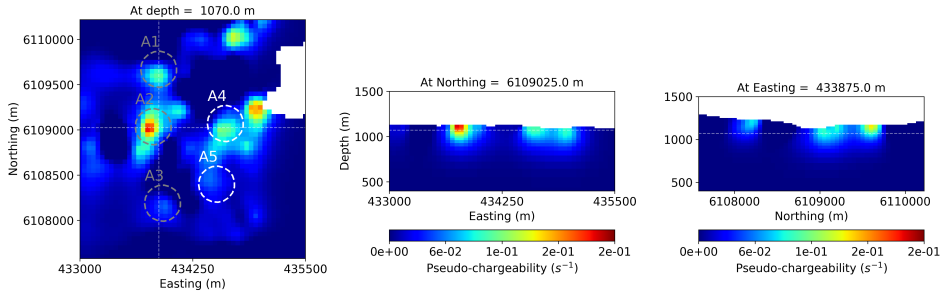

(c) 0.2 ms

Figure 4.27: Plan and section views of the recovered pseudo-chargeability: (a) 2.7, (b) 0.7, and (c) 0.2 ms. Five anomalies recognized from $d^{IP}[\sigma_{est}]$ are marked as dashed circles on plan view (left panels).

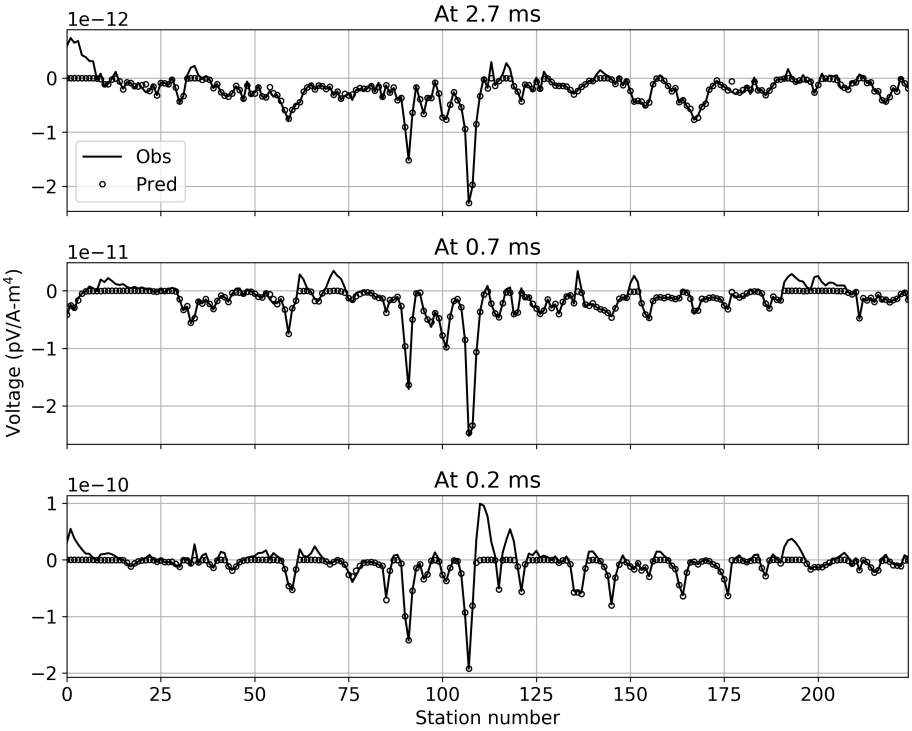

Figure 4.28: Comparison of observed and predicted IP data for the IP inversion at three time channels: 2.7, 0.7 and 0.2 ms.

4.2.6 Interpretation

Using the obtained conductivity and chargeability, in this section, 3D rock models will be constructed. A pseudo-chargeability at 2.7 ms is used for this interpretation; it is the latest time that has the greatest quality of $d^{IP}[\sigma_{est}]$. Fig. 4.29 shows plan and section views of the 3D conductivity and pseudo-chargeability with some geological references (e.g., MBX stock and Rainbow fault). The MBX stock is imaged as an isolated resistor, and conductive halo structures are recovered around the MBX stock . Tertiary sediments on the eastside of the inversion are well imaged as a highly conductive medium. High pseudo-chargeability anomalies, A1-A5, are imaged on the edges of three mineralized zones: MBX, DWBX, and Southerne Star. In particular around the Rainbow fault, high pseudo-chargeability anomalies are imaged and they show good alignment with the Rainbow fault. Note that a higher degree of alteration is expected around faults surrounding the stocks, and they could potentially have strong polarization effects.

With the conductivity and pseudo-chargeability models, a 3D rock model having three units: R1-R3 is constructed and presented in Fig. 4.30. Each of rock units can be interpreted as:

- R1: Highly conductive medium, which correspond to both alteration zones and Tertiary sediments
- R2: Isolated resistive volumes at depth, which indicates resistive monzonite stocks (e.g MBX stock)
- R3: Highly chargeable medium, which may corresponds to highly altered zones especially near the surface.

The above rock model is reasonable, but there can be multiple ways to construct a rock model. For instance, if the emphasis is on the resistive stock and alteration zone, one could obtain a different rock model that looks like Fig. 4.30. Here R1 corresponds to the resistive monzonite stock, and R2 is the alteration zone coming from the obtained chargeability information.

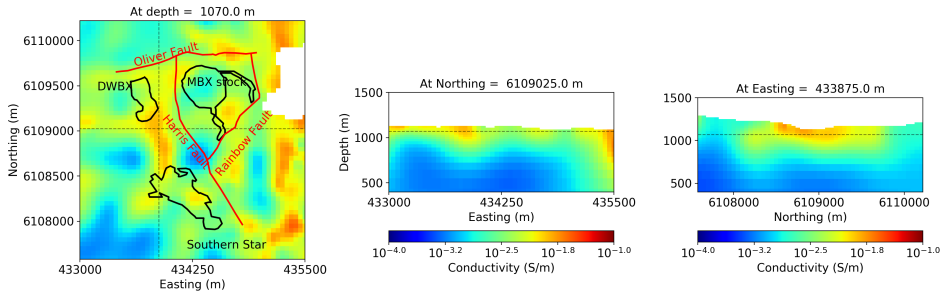

(a) Conductivity

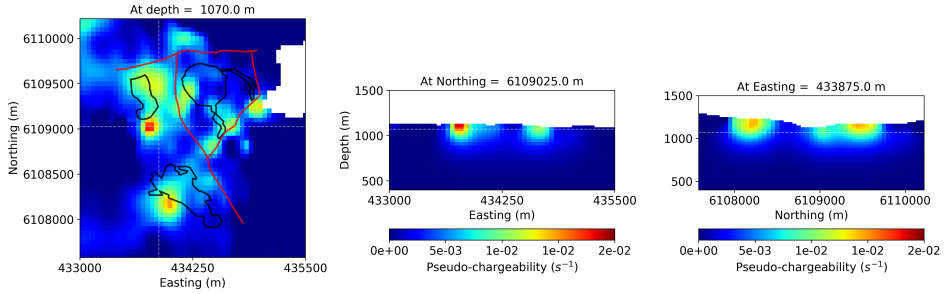

(b) Pseudo-chargeability

Figure 4.29: Plan and section views of 3D conductivity and pseudo-chargeability over Mt Milligan area.

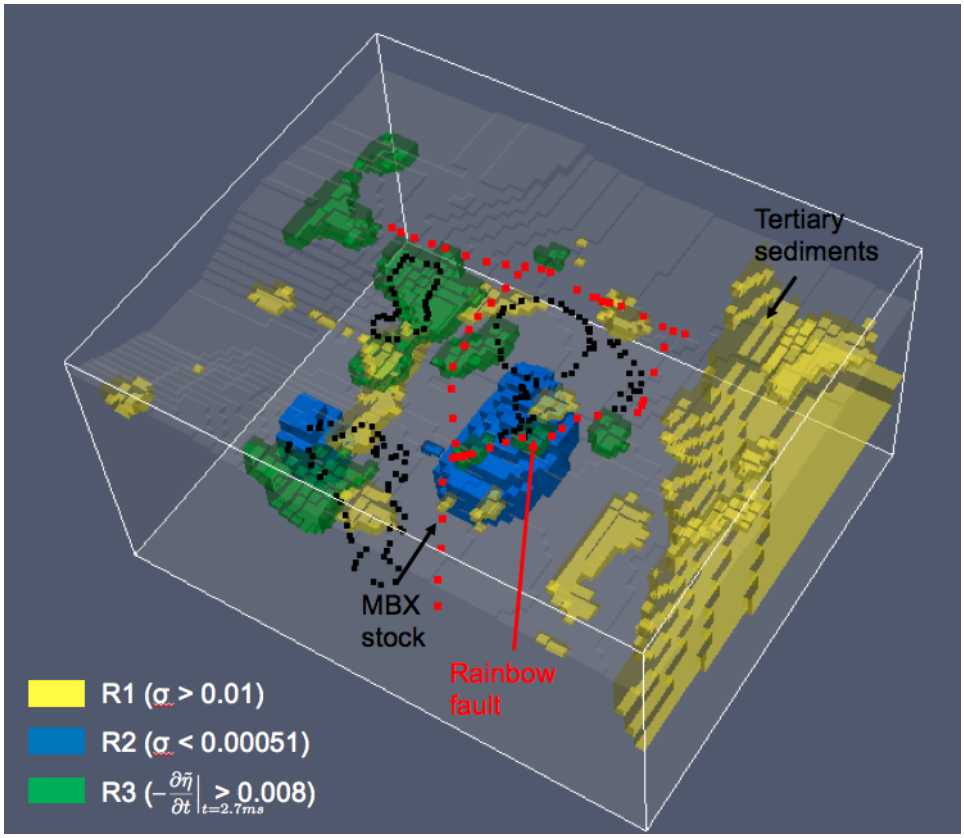

Figure 4.30: The 3D rock model obtained from both conductivity and pseudo-chargeability models. Red and black dots indicates fault structures, and three mineralized zones, respectively. R3 shows the rock units obtained from the airborne IP data.

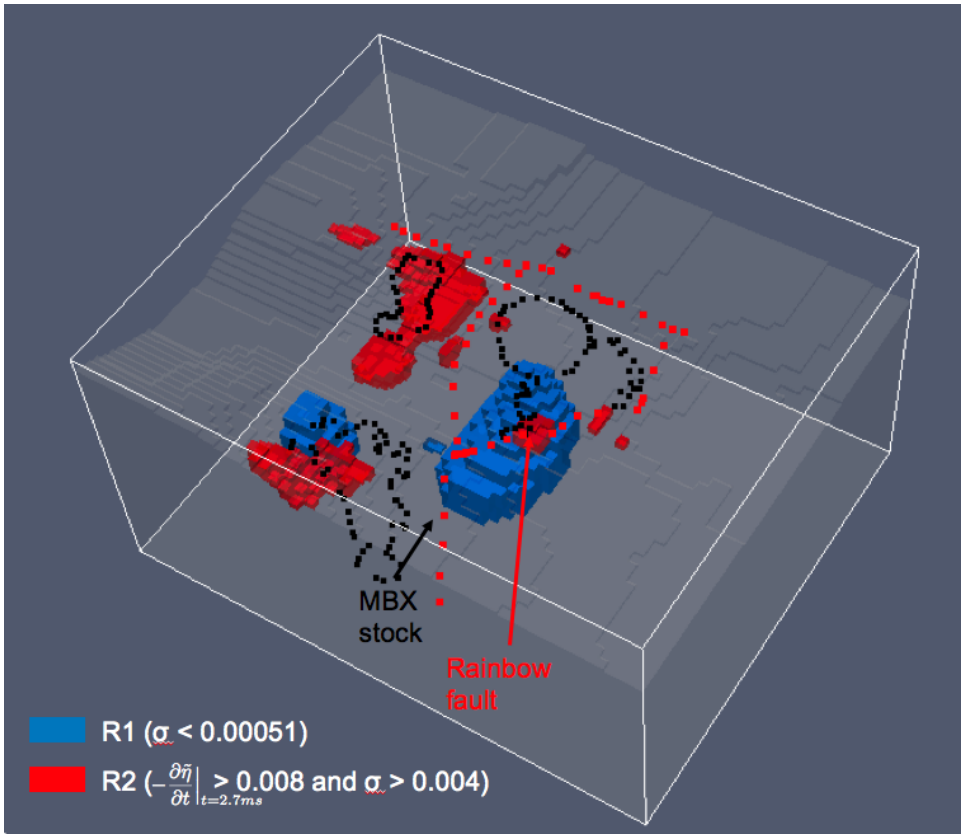

Figure 4.31: The 3D rock model obtained from both conductivity and pseudo-chargeability models. Red and black dots indicates fault structures, and three mineralized zones, respectively. R2 shows the rock units obtained from the airborne IP data.

4.2.7 Conclusions

The VTEM data over the Mt Milligan porphyry deposit have negative anomalies at late-times, which are due to chargeable materials. Three negative anomalies: A1-A3 are recognized in the observations. By applying the TEM-IP inversion workflow, 3D distributions of both conductivity and pseudo-chargeability are obtained. Negatives in the observations are ignored when inverting observations to recover 3D conductivity distribution. The obtained 3D conductivity, σ_{est} is used to carry out EM decoupling to yield $d^{IP}[\sigma_{est}]$ at eight time channels. Two more IP anomalies: A4-A5 around the Rainbow fault are recognized in the obtained $d^{IP}[\sigma_{est}]$; these were not identified in the observations. Using the IP inversion, each time channel of the $d^{IP}[\sigma_{est}]$ is separately inverted, and pseudo-chargeability is recovered at eight time channels. Highly chargeable volumes are successfully imaged on the edges of three mineralized zones, and in particular three of anomlies showed good alignment with the Rainbow fault. These chargeable volumes are interpreted as highly altered zones. Using the conductivity and pseudo-chargeability model at 2.7 ms, 3D rock models are constructed. Importantly, the pseudo-chargeability provided valuable information to characterize highly altered zones of the monzonite stock.

To conclude, the TEM-IP inversion workflow is successfully applied to the VTEM data over Mt Milligan resulting in both conductivity and chargeability models in 3D. This result demonstrates the capability of the workflow to handle field data. Moreover, I believe this was the first time that a 3D chargeability distribution was recovered from field AEM data using a 3D voxel inversion, and the resultant polarization information is promising to be used for characterizing a porphyry deposit. The final step of the workflow, extracting intrinsic IP information, has not been applied here yet but will be applied in the near future.

4.3 Field Example: DO-27/18 kimberlites

4.3.1 Setup

The Tli Kwi Cho (TKC) kimberlites were identified from a DIGHEM survey in 1992 (Fig. 4.32). The kimberlites are located 28 km southeast of the Diavik mine in the Lac de Gras region, Northwest Territories, Canada. The initial discovery targeted two anomalies, named DO-18 and DO-27. Following the initial discovery, several generations of EM systems have been deployed over the TKC area in an effort to characterize the kimberlites. In 1999, the first TEM survey was carried out using the AeroTEM I system [Boyko et al., 2001]. Negative transients were measured, in particular at DO-18, although it was not clear whether these were true signals from the earth or instrumental noise. Surveys with new generations of equipment, AeroTEM II (2003) and VTEM (2004), reaffirmed the negatives. In addition, a ground loop NanoTEM (1993) survey showed negatives at the DO-18 pipe [Jansen and Doyle, 2000]. Airborne TEM systems and NanoTEM have similar geometry and can be considered to be coincident loop systems and hence the negatives are indicative of chargeable material [Weidelt, 1982]. From the perspective of kimberlite exploration however, the existence of an IP signal is not necessarily significant. Ice and near surface clays are known to be chargeable. Their presence distorts EM signals and impede interpretation [Smith and Klein, 1996, Kozhevnikov and Antonov, 2012]. As such, the existence of negative transients is usually considered to be "noise" and it is commonly referred to as IP contamination. Recent studies however, have suggested that negative transients could be attributed to more interesting geological features and thus the negative transients are "signal" [ElKaliouby and Eldiwany, 2004, Flores and Peralta-Ortega, 2009, Kang et al., 2014]. It is this potential that I wish to pursue in this example.

Kimberlite pipes in the Lac de Gras region are generally excellent geophysical targets as they exhibit high physical property contrasts with the granitic host rocks: higher magnetic susceptibility (with high remanence), lower density and higher conductivity [Power and Hildes, 2007]. The standard geological model adopted here for kimberlites consists of three different kimberlitic rocks: hypabyssal kimberlite (HK), volcaniclastic kimberlite (VK), and pyroclastic kimberlite (PK) as

shown in Fig. 4.33 and summarized in Table 4.5. Since each kimberlite unit shows different physical property character, recovering 3D distributions of density, susceptibility, and conductivity will help characterize different kimberlites. In addition, adding chargeability could help this characterization in the TKC region, and this is the motivation to recover 3D chargeability information from the AEM data. For instance, PK and VK are very similar in terms of density, susceptibility, and conductivity. Hence, if chargeability could help distinguish PK and VK, that will be valuable information for diamond exploration.

In this example, I concentrate upon extracting both conductivity and chargeability information from the VTEM data set. The TEM-IP inversion workflow has the three steps: (1) Conductivity inversion, (2) EM-decoupling, (3) 3D IP inversion. In a final stage I compare our petrophysical interpretation, based solely on AEM data, to the extensive drilling data available over the deposit.

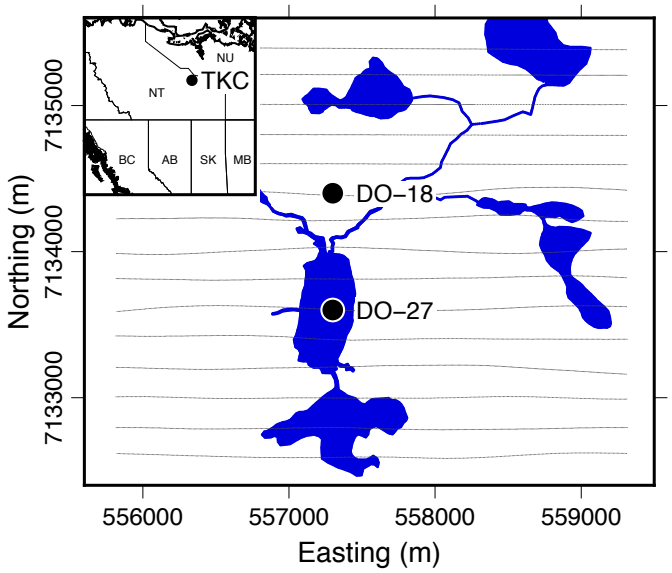

Figure 4.32: Location map for the Tli Kwi Cho (TKC) kimberlites, NWT. DO-18 and DO-27 are two main kimberlite pipes at TKC region. PK, VK, and HK correspondingly indicate pyroclastic kimberlite (PK), volcaniclastic kimberlite (VK), and hypabyssal kimberlite (HK).

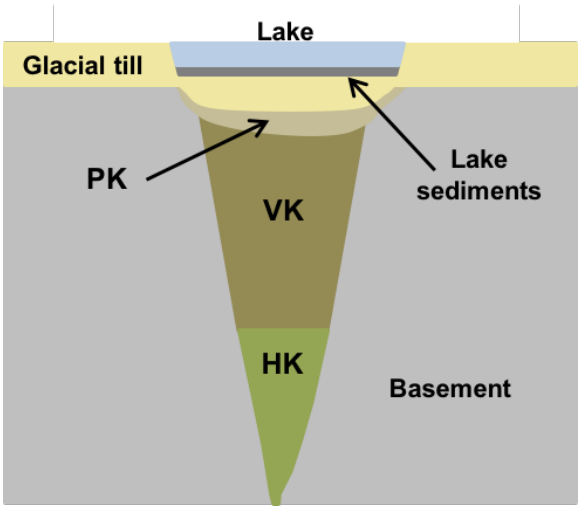

Figure 4.33: Schematic diagram of a kimberlite pipe in the Lac de Gras region (Modified from Devriese et al. [2017]). A lake may be present after glaciation and is often used as a first indicator of a possible kimberlite. Transverse lines are from the DIGHEM survey (1992).

Table 4.5: Expected physical property contrast for kimberlite deposits in the Lac de Gras region [Power and Hildes, 2007].

Rock type	Density	Susceptibility	Conductivity
Glacial till	moderate	none	moderate-high
Host rock	moderate	none	low
Hypabyssal kimberlite (HK)	low-moderate	high	low-moderate
Volcaniclastic kimberlite (VK)	low	low-moderate	moderate-high
Pyroclastic kimberlite (PK)	low	low-moderate	moderate-high

4.3.2 Data

Notable features about the TKC kimberlites can be identified, by simple visual inspection of the EM data. From the DIGHEM data at 7200 Hz, shown in Fig. 4.35(a), positive anomaly highs are observed over the location of DO-18 and DO-27; this indicates that both pipes are more conductive than the host granitic rocks. Fig. 4.34 (b), (c), and (d) correspondingly show NanoTEM (77 μs), AeroTEM II (26 μs), and VTEM (90 μs) data. Here, all three TEM surveys show a positive anomaly near DO-27. I also identify three important anomalies that were not captured by the DIGHEM system and where the data are negative: A1 near DO-18, A2 between DO-18 and DO-27, and A3 near DO-27. Fig. 4.35 (b)-(d) shows all three TEM data sets at later times. Both NanoTEM (603 μs) and AeroTEM II data (534 μs) are significantly noisy. In the VTEM data (680 μs) however the area that was previously positive at early times within DO-27 has switched to negative. This is referred as the A4 anomaly and it suggests that DO-27 has chargeable material.

Data quality, and the time range for which data are sampled, vary across EM systems, hence the EM data sets should show some differences. Fig. 4.36 (a) and (b) respectively provide transients of NanoTEM and VTEM data at several sounding locations at DO-18. Soundings taken away from the pipe are referred to as 'background'. In NanoTEM data, all transients show negative values, but the negative transients from the background decay faster than those over the DO-18 pipe. The IP signal in the background soundings is likely due to surface glacial sediments (including ice and clays). These background negative transients were not identifiable in the VTEM data, likely because the VTEM system does not extend as early in time and also the survey equipment is higher off of the ground.

Since the VTEM data set includes most of the important IP features observed at TKC, while showing less noise at later time channels than other TEM data, I focus our analysis on the VTEM data. From those data, four negative anomalies of interest (A1-A4) are identified, and they appear to have different decaying rates as shown in Fig. 4.36 (b).

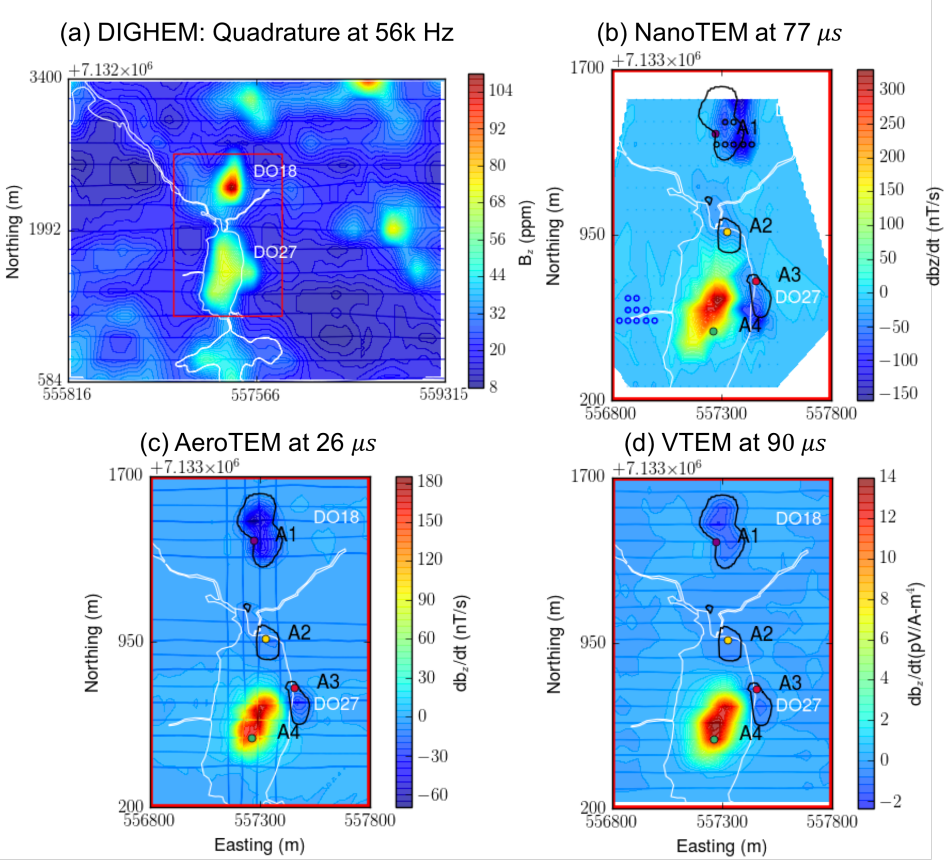

Figure 4.34: Plan maps of four EM data sets at TKC: (a) DIGHEM (56000 Hz), (b) NanoTEM (77 μs), (c) AeroTEM II (26 μs), (d) VTEM (90 μs). For TEM data sets, a smaller region (red box) close to DO-18 and -27 is presented. The black line is a contour line of the negative anomaly (-8 nT/s) from AeroTEM data at 26 μs. The white line shows the boundary of the lakes. Negative anomalies: A1-A4 are correspondingly marked as purple, yellow, red, and green solid circles; A1-A3 showed strong negatives for all TEM data at an early-time as shown in Fig. 4.35.

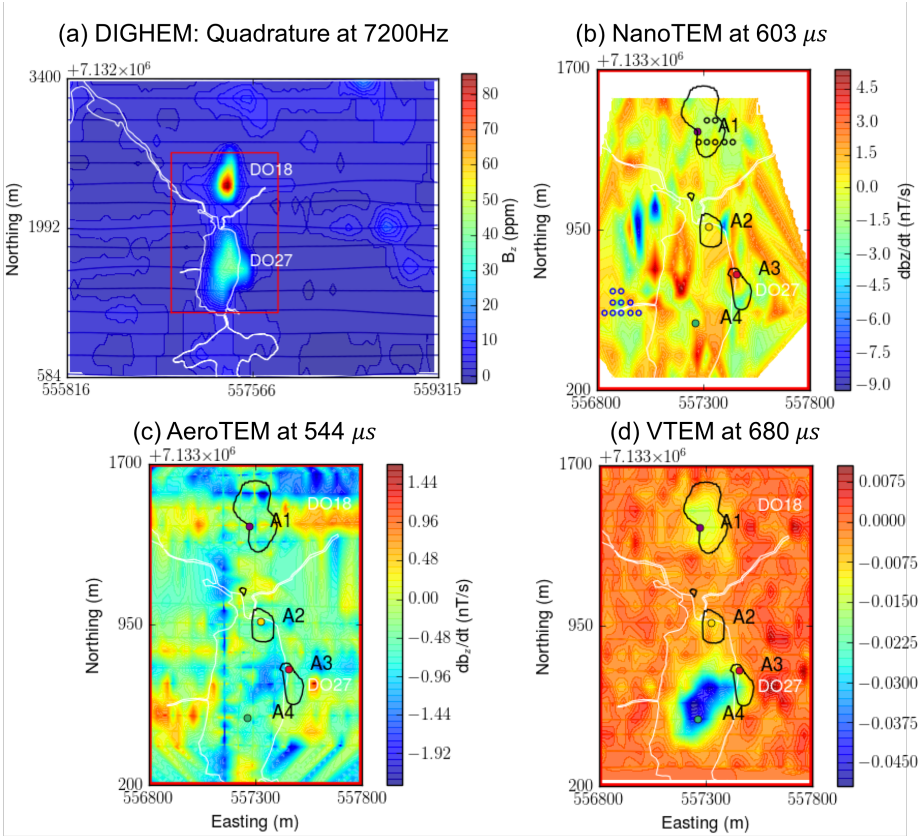

Figure 4.35: Plan maps of four EM data sets at TKC: (a) DIGHEM (7200 Hz), (b) NanoTEM (603 μs), (c) AeroTEM II (534 μs), (d) VTEM (680 μs). For TEM data sets, a smaller region (red box) close to DO-18 and -27 is presented. The black line is a contour line of the negative anomaly (-8 nT/s) from AeroTEM data at 26 μs. The white line shows the boundary of the lakes. Negative anomalies: A1-A4 are correspondingly marked as purple, yellow, red, and green solid circles; A1-A3 showed strong negatives for all TEM data at an early-time as shown in Fig. 4.35.

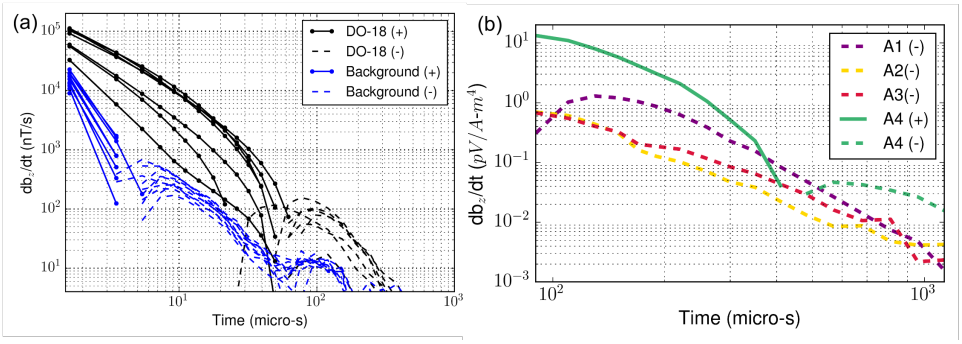

Figure 4.36: Transient curves of NanoTEM and VTEM data. (a) NanoTEM soundings away from the pipe and representative of background (blue lines) and over the DO-18 pipe (black lines). They are marked as blue and black solid circles in Fig. 4.34(b). (b) VTEM soundings at A1-A4 (correspondingly purple, yellow, red, and green lines). They are marked as purple, yellow, red, and green solid circles in Fig. 4.34 (d) and Fig. 4.35(d). Solid and dashed lines distinguish positive and negative observations.

4.3.3 Conductivity Inversion

The first step in the workflow is to estimate the background conductivity, σ_∞ from the TEM data. Detailed information about this step is described in Fournier et al. [2017] and hence only brief summary is provided here. All of the DIGHEM data, and VTEM data that were positive, were cooperatively inverted. In some areas near DO-18, even the earliest time channel was negative so only DIGHEM data could be used there. The neglect of potential IP contamination in the DIGHEM data, and the likelihood of IP contamination in VTEM time channels that were positive, probably contributed to the difficulty we had in obtaining a single conductivity distribution that fit both data sets. Nevertheless, the two models found through the cooperative inversion were very similar. For my purposes here, where I concentrate on extracting information from the VTEM data, I use the inversion model obtained from the last step of the cooperative inversion where the starting and reference model was from the DIGHEM data but the data to be fit were the VTEM data.

Fig. 4.37(a) and (b) shows the estimated conductivity model from the VTEM and the DIGHEM data, respectively. The two conductive pipes are imaged at depth. The conductive pipe for DO-27 extends deeper than the pipe for DO-18. Fig. 4.38 shows plan maps of the observed (d) and estimated fundamental responses ($F[\sigma_{est}]$) at 130 μs. Regions in white correspond to negative data and these soundings were not used in the cooperative inversion. Therefore, the conductivity structure near A1-A3 shown in Fig. 4.37 is mostly coming from the DIGHEM data. The major region where both the VTEM and DIGHEM data contributed to the final conductivity is near A4; d and $F[\sigma_{est}]$ in Fig. 4.38 show a good match there.

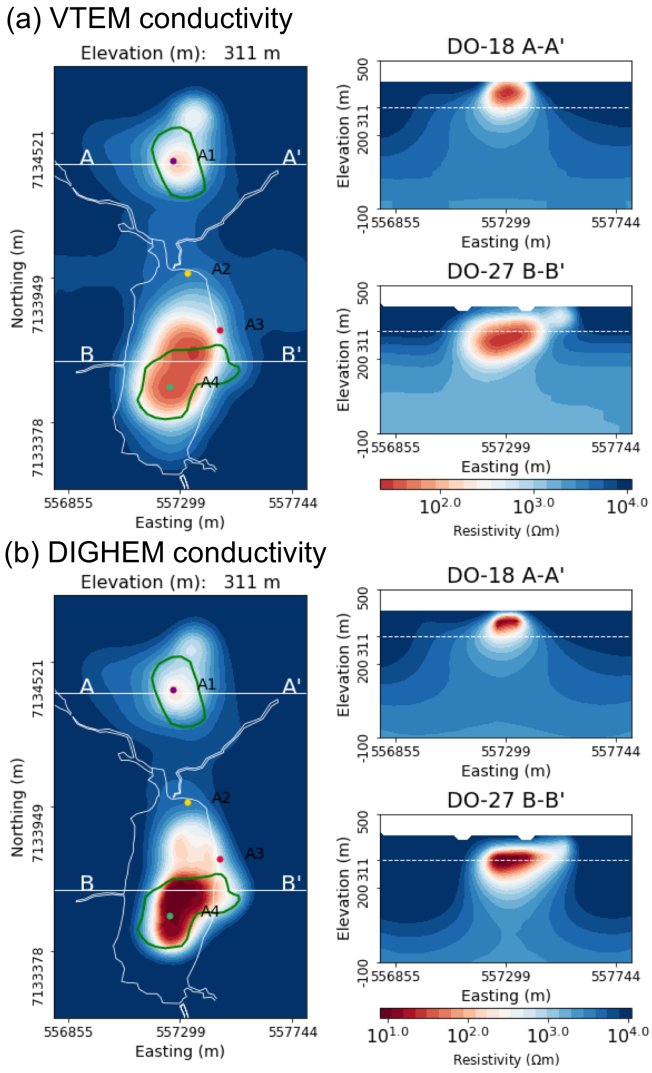

Figure 4.37: Plan and section views of the recovered conductivity model from the cooperative inversion of the VTEM and DIGHEM data sets: (a) VTEM and (b) DIGHEM. The white outlines delineate boundaries of the lake. The green outlines show the extent of DO-27 and DO-18 at the surface, based on drilling.

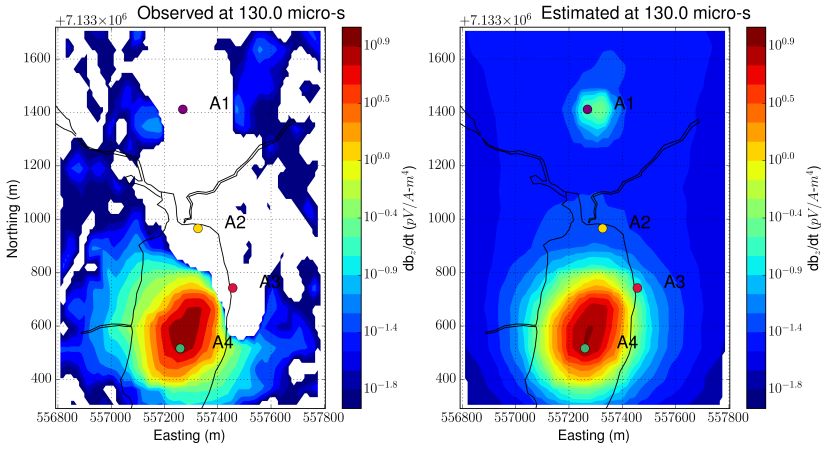

Figure 4.38: Observed and estimated fundamental responses at TKC. Four sounding locations at A1-A4 are marked as solid circles. Regions having negative values are shown as white.

4.3.4 EM-decoupling

Based upon the estimated conductivity, σ_{est} from the previous conductivity inversion (Fig. 4.37a), EM-decoupling is applied: $d^{IP}[\sigma_{est}] = d - F[\sigma_{est}]$. I expect that the EM-decoupling step will only be effective at intermediate times when both EM and IP effects are considerable (see Fig. 4.5). Note that at early times (EM-dominant; positive data), d^{IP} is too small to be obtained, and at late-times (IP-dominant; negative datum) EM-decoupling will have a minor impact. Fig. 4.39 shows time decaying curves of d (black), $F[\sigma_{est}]$ (blue), and $d^{IP}[\sigma_{est}]$ (red) at A1-A4. For A1-A3, as shown in Fig. 4.39 (a)-(c), even the earliest observation has a negative sign (IP-dominant time). The magnitude of $F[\sigma_{est}]$ is much smaller than $d^{IP}[\sigma_{est}]$ except for the few earliest times, hence the EM-decoupling is not necessary. However, at A4 as shown in Fig. 4.39 (d), a full suite of EM-dominant, intermediate, and IP-dominant times are captured. The EM-decoupling is most effective in the intermediate time (200-1000 μs).

To illustrate performance of the EM decoupling I focus on two time channels: 130 and 410 μs. Plan view maps of d, $F[\sigma_{est}]$, and $d^{IP}[\sigma_{est}]$ for the times are shown in Fig. 4.40 (a) and (b). At 130 μs, near A4 the positive high anomaly (from the conductive DO-27 pipe) is effectively removed resulting in some small low amplitude IP features. Near A1-A3 the EM-decoupling results in stronger negatives. At 410 μs, around A4, the EM-decoupling makes a greater impact, and it converts a small area with positive observations within negatives to a larger negative amplitude area. Having separated the EM and IP signals in the VTEM data, the obtained $d^{IP}[\sigma_{est}]$ at each time channel can now be inverted to recover a 3D pseudo-chargeability. The inversion will be carried out for all time channels.

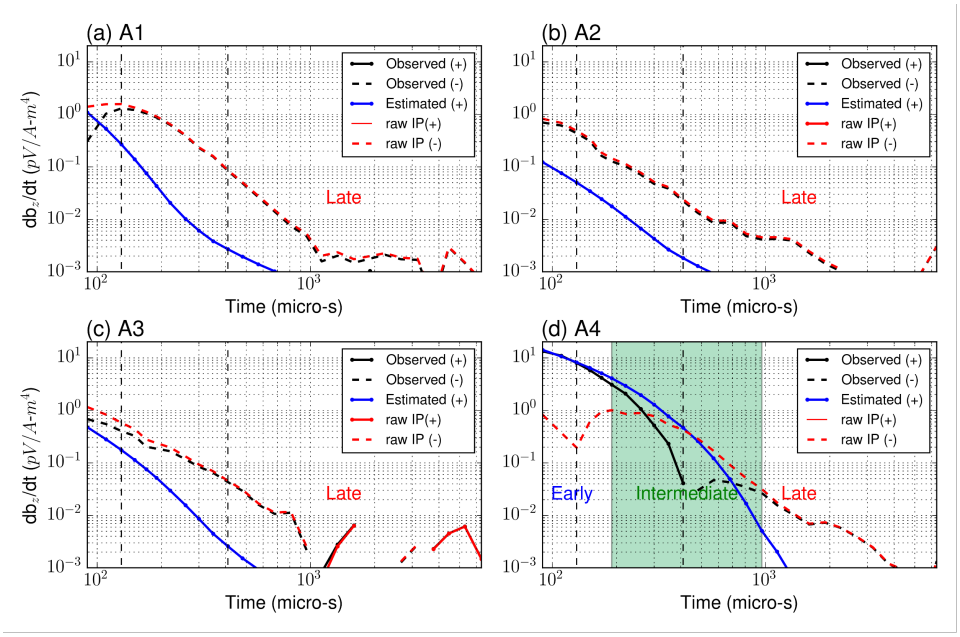

Figure 4.39: Time decaying curves of the d (black line), $F[\sigma_{est}]$ (blue line), and $d^{IP}[\sigma_{est}]$ (red line) data at (a) A1, (b) A2, (c) A3, and (d) A4. Solid and dashed lines distinguish positive and negative values. Vertical black dashed line indicate 130 and 410 μs, respectively.

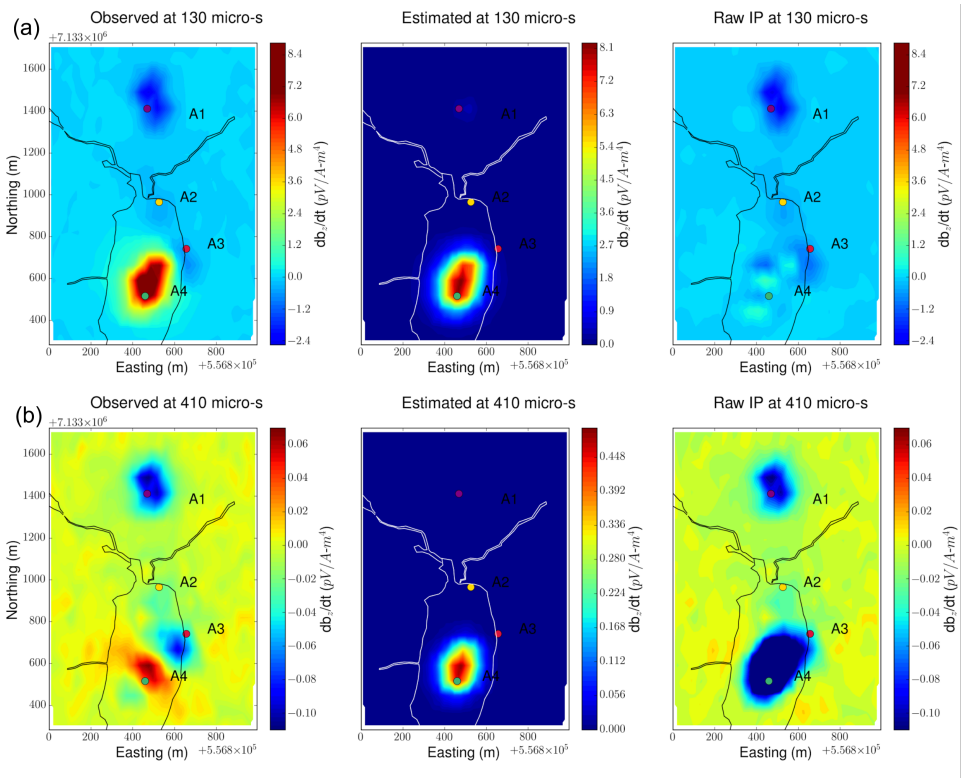

Figure 4.40: Plan maps of d, $F[\sigma_{est}]$ and $d^{IP}[\sigma_{est}]$ at (a) 130 and (b) 410 μs. Left, middle, and right panels correspondingly show the d, $F[\sigma_{est}]$ and $d^{IP}[\sigma_{est}]$.

4.3.5 IP Inversion

Each time channel of $d^{IP}[\sigma_{est}]$ is separately inverted to recover a pseudo-chargeability model. The recovered pseudo-chargeabilities at two time channels: 130 μs and 410 μs are shown in Figs 4.41(a) and (b), respectively. At 130 μs three chargeable bodies are recovered: A1-A3; A1 and A3 are imaged at DO-18 and the north-eastern part of DO-27, respectively. Dashed contours (red) shown in Fig. 4.41(a) delineate three chargeable bodies. No chargeable volume is recovered around the southern part of the DO-27 (see green lines at DO-27 shown in Fig. 4.41a). At 410 μs however, a chargeable body is imaged at this southern part of the DO-27 (A4); solid contour (red) indicates this chargeable volume. Other chargeable structures are imaged at 410 μs around A1 and A2, but their amplitudes are much smaller than A4. This reflects the different time decaying features of the IP signals: A1-A3 decay faster than A4 (see Fig. 4.36).

The recovered pseudo-chargeability at 130 μs and 410 μs provides some important information about the different kimberlites in the region. However, that IP information is still qualitative and hence it motivates the following quantitative analysis.

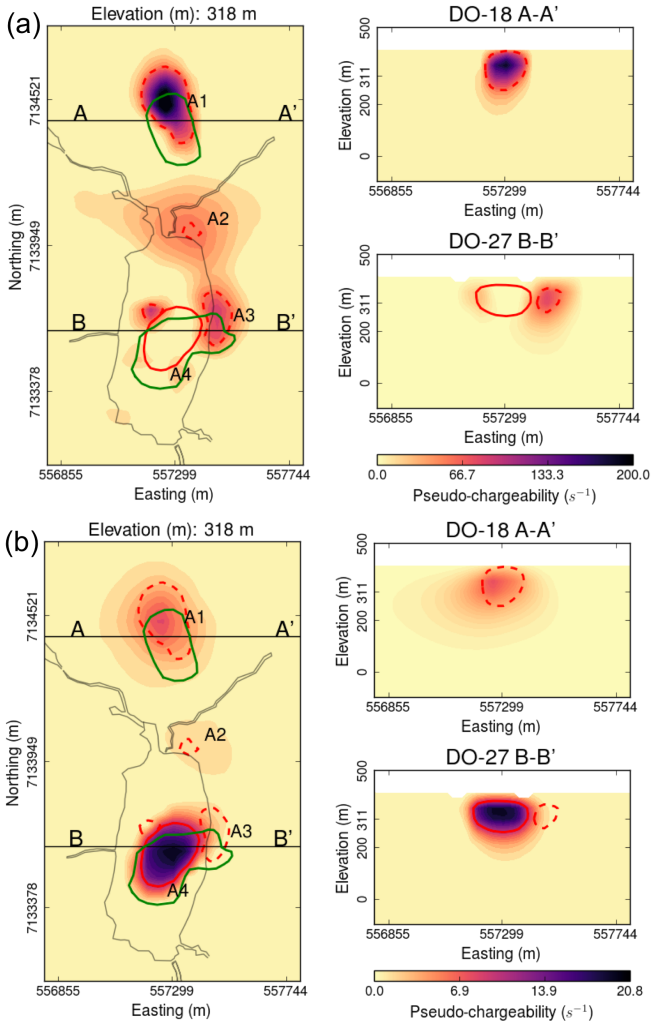

Figure 4.41: Plan and section views of the recovered pseudo-chargeability model from the 3D IP inversion of the raw IP at (a) 130 μs and (b) 410 μs, respectively. Left panel shows plan map at 99 m below surface. Top and bottom of right panels show A-A' and B-B' sections, respectively. Solid and dashed red lines delineate contours of the recovered pseudo-chargeability at 50 s^{-1} (130 μs) and 10 s^{-1} (410 μs). The black outlines delineate boundaries of the lake. The green outlines show the extent of DO-27 and DO-18 at the surface, based on drilling.

Extracting intrinsic IP parameters

A distribution of pseudo-chargeability values at multiple times has been recovered and I now wish to use those results to extract intrinsic information about the polarization parameters of the kimberlites. Pseudo-chargeabilities at representative cells close to A1-A4 anomalies are chosen, and plotted as a function of time in Fig. 4.43 (a). Using the procedure described in Appendix B, I fit $-\frac{\partial \tilde{\eta}}{\partial t}(t)$ using Cole-Cole model, which can be expressed as

$$\sigma(\omega) = \sigma_\infty - \frac{\sigma_\infty \eta}{1 + (1-\eta)(\imath\omega\tau)^c}, \tag{4.4}$$

where ω is angular frequency (rad/s), σ_∞ is the conductivity at infinite frequency (S/m), η is the chargeability, τ is the time constant (s), c is the frequency exponent. Fig. 4.42 shows an example Cole-Cole model as a function of frequency. Each Cole-Cole parameter determine different characters of $\sigma(\omega)$:

- Magnitude of the $\sigma(\omega)$ is dominated by σ_∞ at high frequencies.
- η controls the difference of $\sigma(\omega)$ between low and high frequency asymptote.
- τ mainly controls the peak frequency (see imaginary part in Fig. 4.42), and this effectively controls the characteristic rate of decay in time. For instance, as τ decreases the peak frequency increases and the polarization response decays faster in time.
- c controls the spread in time decays.

In these analyses, two Cole-Cole parameters: σ_∞ and c are assumed to be known, hence I only estimated η and τ in this inversion. For σ_∞, the σ_{est} obtained from the conductivity inversion is used. I empirically used c=1 for cells close to A1-A3 and c=0.5 for those close to A4. Justfication of this was trial and errors. I could not fit A4 using c=1, and vice versa. Solid circles in Fig. 4.43(a), show the predicted pseudo-chargeability; they match well with the observed pseudo-chargeability (lines). Median values of the pseudo-chargeability at each time channel are shown in Fig. 4.43(b), and they demonstrate the different

rates of decay between A1-A3 and A4. A summary of the estimated τ and η at each cell is presented in Table 4.6. Fig. 4.44 (a) shows a cross-plot of the estimated τ and η for A1-A4. Clustering of A1-A4 indicates distinctions between the different kimberlite units based upon the estimated τ and η:

- A4 can easily be distinguished from others on the basis of τ
- A1 and A3 can be differentiated by η and perhaps by τ
- The distinction between A1 and A2 is subtle, but it may be possible based upon τ values

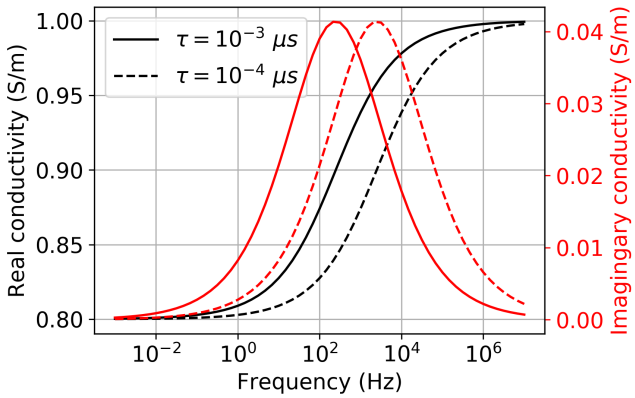

Figure 4.42: Cole-Cole conductivity as a function of frequency [Pelton et al., 1978]. Black and red lines indicate real and imaginary part of the Cole-Cole conductivity. Used Cole-Cole parameters are: σ_∞=1 S/m, η=0.2, and c=0.5; two τ values are considered: 10^{-3} s and 10^{-4} s. Solid and dashed line indicates complex conductivity generated with $\tau = 10^{-3}$ s and $\tau = 10^{-4}$ s, respectively.

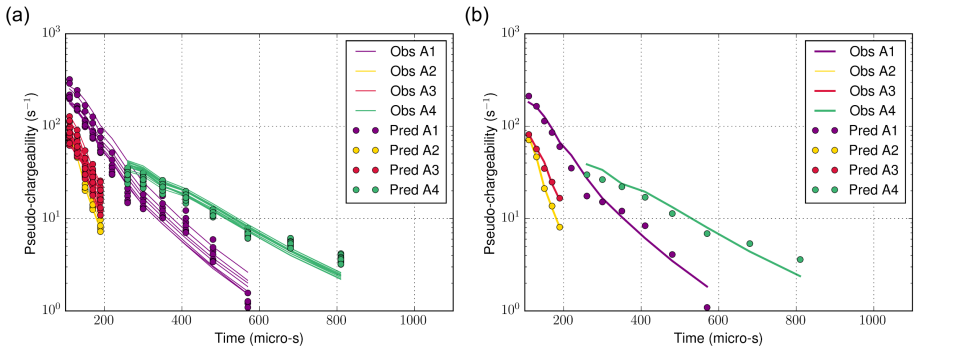

Figure 4.43: Comparison of the observed (lines) and predicted (solid circles) pseudo-chargeability at cells close to A1-A4 (correspondingly purple, yellow, red, and green colors). (a) All time decaying curves of the observed and predicted pseudo-chargeability. (b) Median values of the observed and predicted pseudo-chargeability at each time.

Table 4.6: Mean and standard deviation of estimated τ (μs) and η for A1-A4. Used values of c for fitting are given.

Division	Mean τ	Mean η	Std. τ	Std. η	c
A1	110	0.4	24	0.13	1
A2	50	0.4	9	0.11	1
A3	40	0.12	9	0.07	1
A4	1600	0.15	380	0.1	0.5

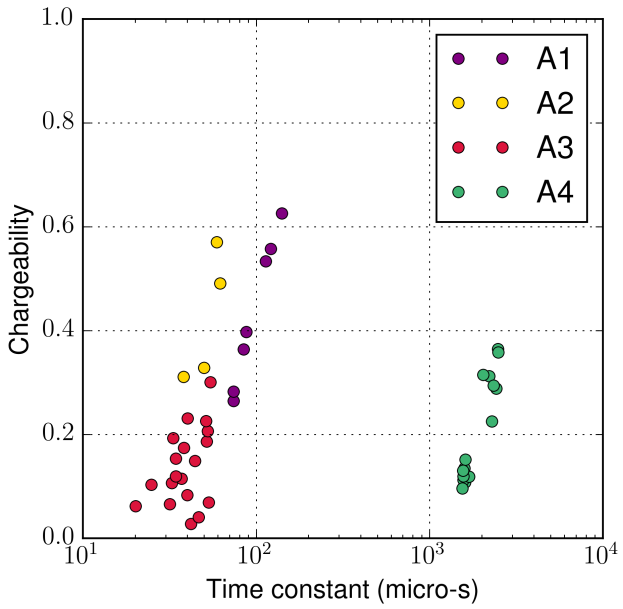

Figure 4.44: A cross plot between the estimated time constant (τ) and chargeability (η) at cells close to A1-A4. Solid circles shaded as purple, yellow, red, and green colors correspondingly indicate A1-A4.

4.3.6 Interpretation

From the application of the TEM-IP inversion workflow to the VTEM data over the TKC region, both conductivity and chargeability information are recovered in 3D. Using these, along with basic geological information given for kimberlites (e.g. Table 4.6), I can build a 3D rock model for the TKC kimberlites. For this, I will use DIGHEM conductivity model shown in Fig. 4.37(b), and the pseudo-chargeability models at 130 and 410 μs (Fig. 4.40). The pseudo-chargeability model for 130 μs and 410 μs are correspondingly referred as the early pseudo-chargeability, $\tilde{\eta}_E$, and the late pseudo-chargeability, $\tilde{\eta}_L$.

Compared to the host rock, kimberlites are supposed to have higher conductivity (Table 4.5), and hence conductivity can provide the volumes of kimberlitic materials; chargeability information about kimberlites is not well-known. From the conductivity model shown in Fig. 4.37(b), I extracted moderately conductive volumes ($<$ 1250 Ω m), and overlaid them in to Fig. 4.45(a) as grey regions; they indicate overall kimberlites at DO-18 and DO-27. From the early pseudo-chargeability ($\tilde{\eta}_E >$55 s^{-1}), I obtained two main chargeable volumes close to A1 and A3 (red regions); they have small time constant ($\tau \simeq 75$ μs). The late pseudo-chargeability ($\tilde{\eta}_L >$8 s^{-1}) provides another chargeable volume at the southern part of the DO-27 (green region); it has a large time constant ($\tau \simeq 1600$ μs). Note that all chargeable anomalies are within the conductive volume (grey region).

By using the above anomalous volumes overlaid in the Fig. 4.45(a), a 3D rock model having four different rocks types (R0-R3) is constructed and presented in Fig. 4.45(b). Each rock unit has different character with regard to conductivity and chargeability.

- R0: Low conductivity and non-chargeable
- R1: Moderate-High conductivity and non-chargeable
- R2: Moderate-High conductivity and chargeable (small τ)
- R3: Moderate-High conductivity and chargeable (large τ)

This 3D rock model provides some important information about the TKC kimberlites. First, the DO-27 pipe is embedded at depth, but the DO-18 pipe is exposed

to the surface. Second, the DO-18 and DO-27 kimberlite pipes are different based upon distinction between R2 and R3; this supports that the two pipes are distinct events. Third, at the DO-27 pipe there are at least two different kimberlites (see R2 and R3 shown in the right-bottom panel of the Fig. 4.45b).

One remaining question here is how do we interpret rock units obtained geophysically as lithological units. From Table 4.5, there are three different kimberlite units: PK, VK, and HK. HK does have good susceptibility contrast, but not conductivity contrast from the host rock, and hence I ignore HK unit in this interpretation. PK and VK have moderate-high conductivity, and hence all rock units except R0 can correspond to them. R2 and R3 can be different kimberlite units, and they have different polarization character: R3 has greater τ than R2. However, both R2 and R3 can be either PK or VK and hence distinction of PK and VK is not clear. PK is a subclass of VK and is deposited after an explosive event. Both units can be highly weathered resulting in significant clay content which is conductive and chargeable. Because of its explosive origin, PK likely has greater pore size than VK; the pore may be filled with water. The pore size of the rock is strongly correlated with the time constant: greater pore size result in larger time constant [Pelton et al., 1978, Revil et al., 2014]. Based upon that, I interpret R2 (small τ) and R3 (large τ) as VK and PK, respectively. Here, polarization mechanisms of PK and VK can be related to both membrane polarization and Maxwell-Wagner polarization. Final interpretation is summarized in Table 4.7.

Table 4.7: Petrophysical domains built from inversions of airborne EM data sets. Here σ, $\tilde{\eta}_E$, and $\tilde{\eta}_L$ correspondingly conductivity, and pseudo-chargeability at 130 and 410μs.

Rock Unit	σ	$\tilde{\eta}_E$	$\tilde{\eta}_L$	τ	Interpretation
R0	Low	Low	Low	N/A	Host Rock
R1	Mod.-High	Low	Low	N/A	Kimberlite
R2	Mod.-High	High	Low	Small	VK
R3	Mod.-High	Low	High	Large	PK

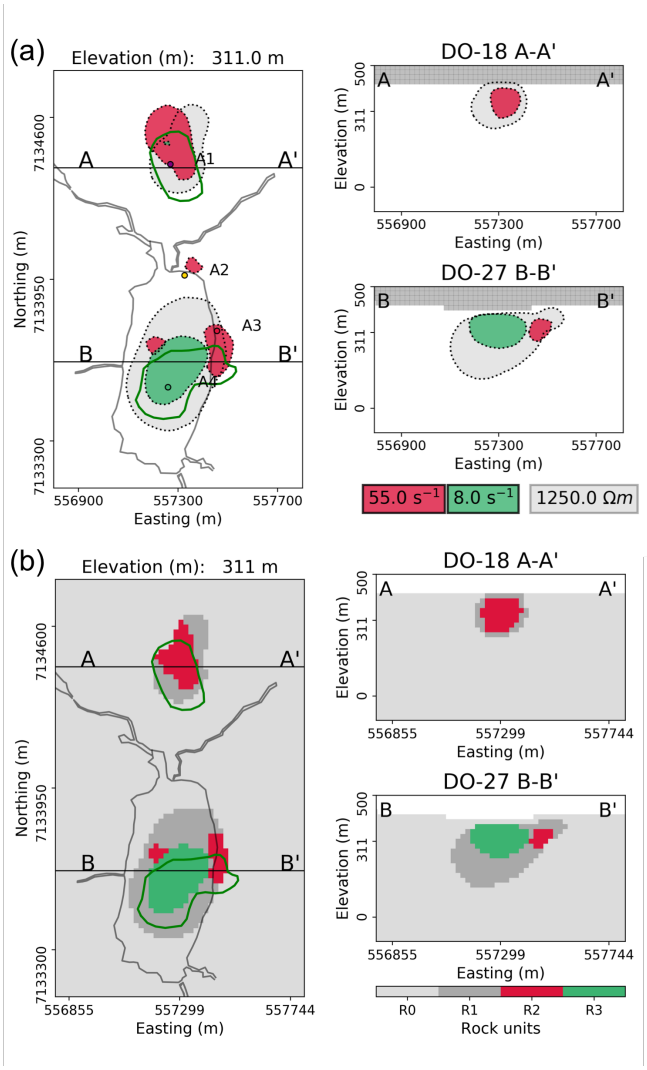

Figure 4.45: Comparative sections through the TKC kimberlites. (a) Overlaid anomalies of three physical property models: conductivity (dark grey), pseudo-chargeability at 130 (red), and 410 μs (green). (b) Generated rock model from three anomalies. The white outlines delineate boundaries of the lake. The green outlines show the extent of DO-27 and DO-18 at the surface, based on drilling.

4.3.7 Synthesis

Extensive drilling programs have been carried out at TKC, from which four different kimberlite units have been identified [Doyle et al., 1999, Eggleston and Brisebois, 2008]:

- Dipping sheets of hypabyssal kimberlite (HK) facies limited to the north-east part of DO-27.
- Shale-rich volcaniclastic kimberlite (VK) crater facies in the northern part of DO-27.
- Resedimented pyroclastic kimberlite (PK) crater facies infilling the core of DO-27; Diamondiferous unit.
- Xenocryst-rich volcaniclastic kimberlite (XVK) crater facies mostly restricted to the core of DO-18.

Fig. 4.46(a) and (b) compares the final petrophysical model obtained from interpretation of the AEM data sets to the geology based upon drilling results from an extensive drilling program. The agreement is quite good, particularly regarding the geometric confinement of the pipes. For the DO-27 pipe, interpretation of R2 and R3 as respectively VK, and PK, agrees with the ground truth. From the comparative sections at DO-27 (B-B'), the upper part of the PK and VK units are well imaged with R2 and R3, respectively. The deeper part of the PK unit is mapped by R1 (obtained from σ), but the bottom boundary is not well distinguished. This may due to lack of resolution for the AEM survey for the bottom boundary of a conductor since the EM field significantly decays in the conductor. In addition, our interpretation that the DO-18 pipe is VK, is reasonable. XVK is a subunit of VK and was identified through drilling. The HK unit is not distinguished since it does not show any anomalous conductivity or chargeability; however, this can be distinguished by susceptibility which is often available through the magnetic survey that are usually flown with an AEM survey. Overall, our analysis has clearly demonstrated impact of the obtained IP information from the AEM surveys to characterize various kimberlite units at the TKC region.

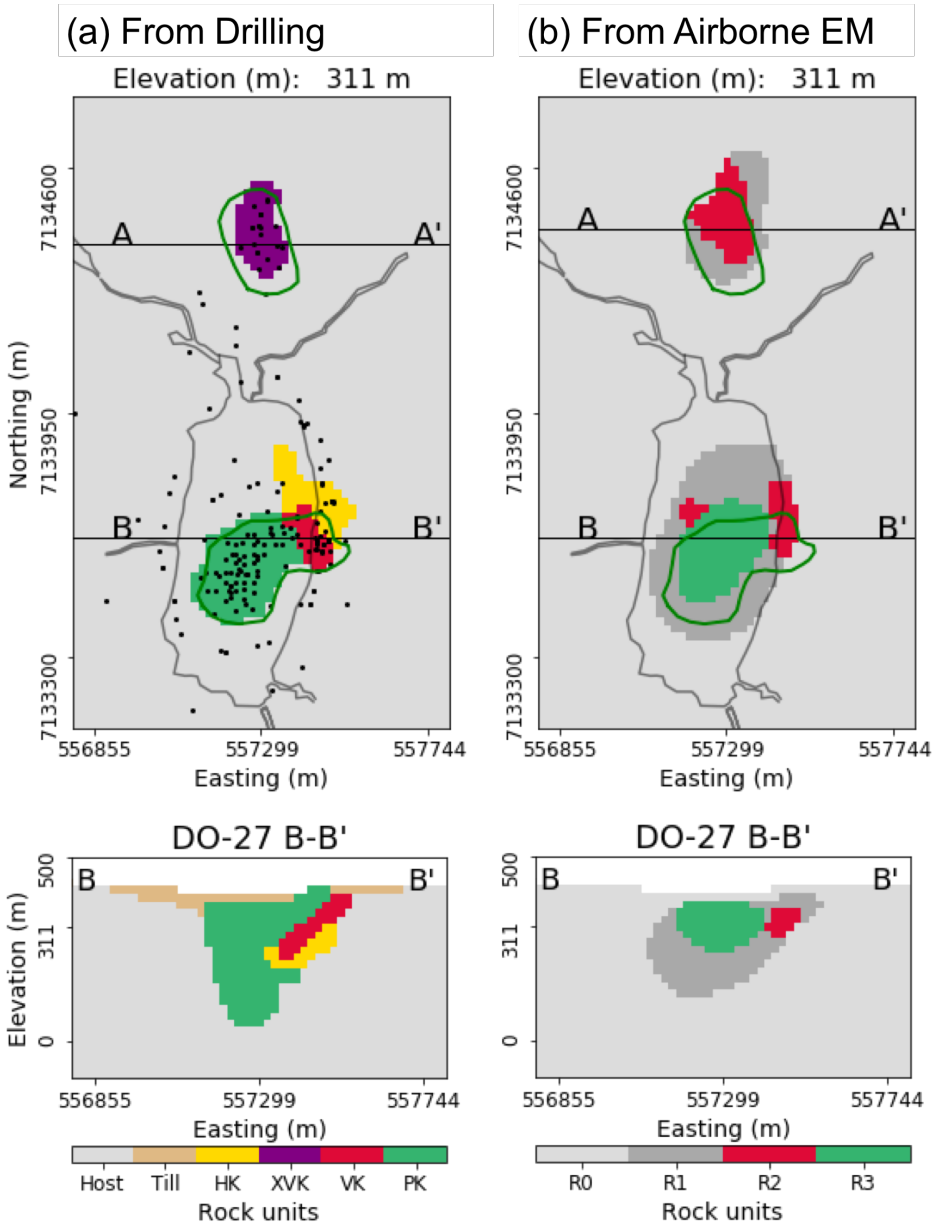

Figure 4.46: Comparison of 3D geology and rock model. (a) 3D geologic model obtained from the known geology and drilling results at the TKC area (b) 3D petrophysical model obtained from airborne EM. The black outlines delineate boundaries of the lake. The green outlines show the extent of DO-27 and DO-18 at the surface, based on drilling.

4.3.8 Conclusions

Consistent negative transients have been observed at TKC with various TEM surveys: NanoTEM, AeroTEM II, and VTEM. These are due to chargeable materials. Focusing on the most recent VTEM data, four distinct IP anomalies showing different decaying features all delineated. The TEM-IP inversion workflow is applied to the VTEM data. Even the earliest time channel of the VTEM data showed negatives and this presented a significant challenge to undertake conductivity inversion. This was overcome by cooperatively inverting the VTEM and DIGHEM data, and generated a 3D distribution of σ_{est}. $d^{IP}[\sigma_{est}]$ are obtained by implementing the EM-decoupling procedure. The $d^{IP}[\sigma_{est}]$ were inverted to recover the 3D pseudo-chargeability at multiple time channels. Then by using representative cells from the four chargeable bodies, pseudo-chargeabilities were fitted using a Cole-Cole model to recover η and τ. Four chargeable bodies are imaged at depth, but in different time channels: chargeable bodies near A1-A3 are seen at 130 μs; chargeability near A4 is seen at 410 μs. The estimated τ for cells close to A4 is 1160 μs and this is much greater than τ ($\sim$70 μs) for A1-A3. The DO-18 pipe (A1) can thus be differentiated from the southern part of DO-27 (A4), which supports the geologic hypothesis that the two pipes are distinct intrusive events.

Finally, using both conductivity and chargeability information, a 3D rock model is constructed, which includes four different rocks: R0-R3. Three of them were related to the kimberlites: R1-R3. The moderate conductivity at the upper part of the two pipes suggested that this was a highly weathered kimberlitic rock that might be PK or VK, but we were not able to differentiate between those units. The addition of IP information however, enabled us to make this distinction because the two rocks have significantly different τ values. Our final rock model was compared to the 3D geological model built up from an extensive drilling program; the two models are quite similar. No explicit information regarding the known geology has been used to constrain both conductivity and IP inversions. Only the general kimberlite model, the component rock types and their relative physical property contrasts were used. Despite that, a rock model is obtained whose major features were representative of the geologic model from drilling. The AEM data used in the analysis were obtained from airborne which are far easier, and less costly, to

collect than ground data.

Chapter 5

Grounded Source Example

5.1 Introduction

Controlled-source electromagnetic (EM) methods excite the earth using either a grounded source (a generator attached to two grounded electrodes) or an inductive source (currents flowing in a wire loop). For both cases, an electric field will be generated in the earth, and polarization charges will be accumulated if chargeable material exists. Effectively, the rock is electrically polarizable, and this is understood by allowing the electrical conductivity to be frequency- or time-dependent [Pelton et al., 1978, Tarasov and Titov, 2013, Revil et al., 2015]. A typical electrical induced polarization (EIP; often called DC-IP) survey [Seigel, 1974] using a grounded source is shown in Fig. 5.1. It consists of grounded electrodes carrying a current waveform (like the square wave with half-duty cycle shown) and electrodes to measure voltage differences. When the ground is chargeable the received voltage looks like that in Fig. 5.2. The decay in the current off-time is the IP effect. To interpret the observed IP data, a two-stage inversion is usually deployed [Oldenburg and Li, 1994]. The first step is to invert late on-time data (V_0) using a DC inversion to obtain the background conductivity. The second step is to use the obtained conductivity to generate a sensitivity function, and then invert late off-time data (V_s); this is often called DC-IP inversion.

Although application of this method has been successful, especially for mining applications [Fink et al., 1990, Oldenburg et al., 1997, Wait and Gruszka, 1986], a

main concern is the second step. The time-decaying fields are assumed to be purely the result of IP phenomena and any EM induction effects in the data are ignored. This assumption can be violated when the earth has a significant conductivity and EM effects remain stable and flat even in the late off-time [Veeken et al., 2009a,b] Removing EM induction responses from the measured data is referred to as EM-decoupling and it has been a focus of attention for many years. Most analyses have used simple earth structures, a half-space or a layered earth, to ameliorate its effects [Routh and Oldenburg, 2001, Wynn and Zonge, 1975, Kratzer and Macnae, 2012]. However, with recent capability to handle 3D TEM forward modelling and inversion [Commer et al., 2011, Haber, 2014, Oldenburg et al., 2013], I can use more complicated conductivity models. In addition, full 3D TEM forward modelling using a complex conductivity model is currently available. Results can be obtained directly in the time-domain [Marchant et al., 2014] or by transforming frequency domain responses to the time-domain [Hohmann and Newman, 1990, Flis et al., 1989]. With these advances I can revisit the challenge of decoupling EM effects and extracting better information about conductivity and chargeability.

A TEM-IP workflow illustrated in Section 1.6 has successfully been applied to airborne IP data using inductive sources (Chapter 4). The workflow includes three main steps: 1) inverting early-time TEM data (those not affected by IP) to recover a 3D conductivity model, 2) EM-decoupling (forward modelling the EM response and then subtracting it from the observations), and 3) IP inversion to recover pseudo-chargeability distribution at each time channel. The problem of inverting IP data using grounded sources follows the same workflow, but some aspects are greatly simplified because DC-IP measures data when electric fields, and charge accumulations, have reached a steady state. This provides another data set from which information about the electrical conductivity can be extracted. A major difference between a conventional DC-IP inversion and our approach is the use made of early-time channels in the DC-IP data. In conventional work these have been considered as "noise" being corrupted by EM coupling effects and hence thrown away. However, I consider these as "signal" to recover conductivity. In this study, the TEM-IP inversion workflow is applied to a synthetic example using a gradient array with a grounded source. I illustrate the steps in the workflow listed above but the first step is altered so that one can optionally invert the DC data

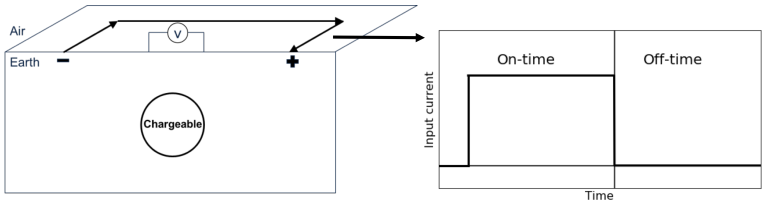

Figure 5.1: Conceptual diagram of a ground-based grounded source with half-duty cycle current waveform.

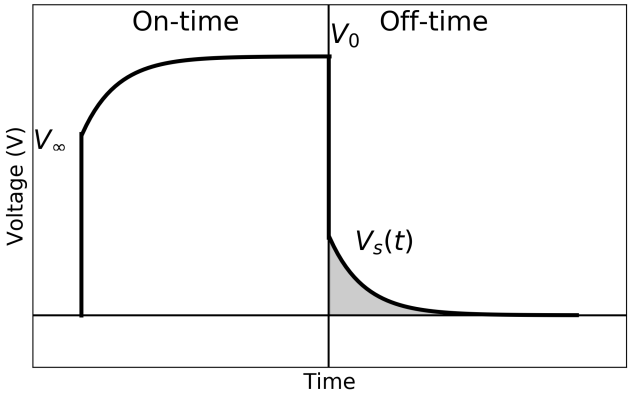

Figure 5.2: A typical example of overvoltage effects in electric IP data.

and use that for decoupling. This allows me to compare the effects of different estimates of the conductivity model on the final chargeability models.

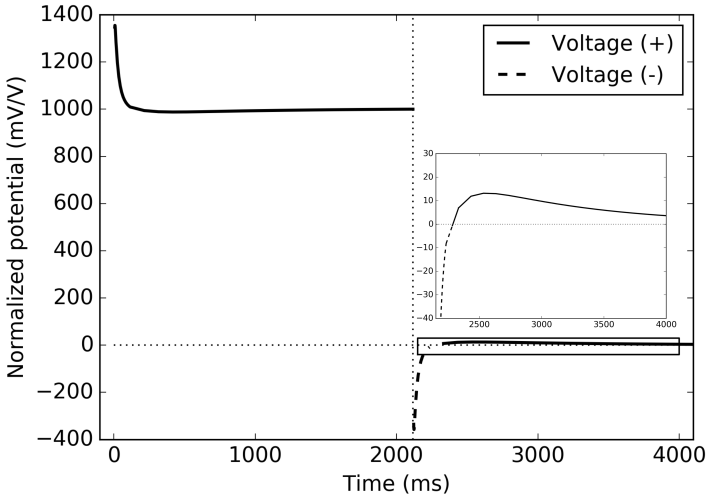

Figure 5.3: Observed voltage with EM induction effects. EM effects dominate the early on and off-time data. Inset figure shows the enlarged off-time voltage and it demonstrates early EM induction effects (negative) and late-time IP effects (positive). Dashed and solid lines distinguish positive and negative voltages.

5.2 TEM-IP Inversion Workflow for Grounded Source

The TEM-IP inversion workflow has applied to airborne EM examples in Chapter 4, and it is applicable here for the grounded sources, but there are some differences to be taken care of. The workflow has three steps. The first step is to invert the TEM data to recover the 3D conductivity model. As in the inductive source work, I use only early-time data, which are not IP-contaminated. Note that these early-time data have previously been considered as "noise in conventional DC-IP analyses and hence have been thrown away. However, here I consider these as "signal" and use them to recover a better conductivity model. Another possibility for obtaining a background conductivity is to use the steady-state fields (stable plateau level) just prior to switching the current off. These are the potentials that are traditionally used in DC-IP inversion. Inversion of these data yields a conductivity that is $\sigma_0 = \sigma_\infty(1-\eta)$ (when on-time pulse is long enough to be fully charged up) but if η is small then this will be a reasonable approximation to σ_∞. The inversion of DC data is analogous to inverting only one frequency in a frequency-domain data set. Hence it might be expected that inverting data at multi-times (equivalent to multi-frequencies) would produce a better result. Our experience verifies this. Nevertheless, the DC fields are valuable and I wish to use them. The options are to invert the DC and TEM data together, or treat them as two separate data sets. For the present I have chosen the latter since I then do not have to contend with the issue that the DC fields are really σ_0, but TEM data at early off-time are close to σ_∞. To investigate how much information can be extracted from each data set, here I separately invert DC and TEM data and recover both DC and EM conductivities.

The second step of the workflow is EM-decoupling. The estimated conductivity model, σ_{est}, from step 1, is used to generate estimated IP data, $d^{IP}[\sigma_{est}]$, according to

$$d^{IP}[\sigma_{est}] = d - F[\sigma_{est}] \tag{5.1}$$

where $F[\cdot]$ Maxwell's operator taking 3D conductivity as an argument, and $F[\sigma_{est}]$ is the estimated fundamental data. Note that $F[\sigma_{est}]$ might be different from $F[\sigma_\infty]$ because σ_{est} is not identical to σ_∞. The differences will be most pronounced at early times when induction responses are large. Thus potential errors in $d^{IP}[\sigma_{est}]$ will be largest at early times. EM-decoupling will be effective in the intermediate

times when both EM and IP signals are considerable; at late times (IP-dominant), EM-decoupling may not be required.

The final step in the process is to carry out the IP inversion. I adopt the conventional IP inversion approach [Oldenburg and Li, 1994], which uses a linear form of IP responses written as

$$\mathbf{d}_i^{IP} = \mathbf{J}\tilde{\eta}_i \tag{5.2}$$

where $\mathbf{J}$ is the sensitivity matrix, and $\tilde{\eta}_i$ is a column vector for the pseudo-chargeability at the i-th time channel. The conductivity model σ_{est} is required to generate the sensitivity matrix. From eq. (2.23), pseudo-chargeability can be defined as

$$\tilde{\eta}(t) = -\int_{-\infty}^{t} \frac{\triangle\sigma(t-u)}{\sigma_\infty} w^e(u)du \tag{5.3}$$

where $\triangle\sigma(t) = \mathscr{L}^{-1}[\triangle\sigma(s)]$, and $\mathscr{L}^{-1}[\cdot]$ indicates the inverse Laplace transform; $w^e(t)$ is the time history of the electric field. In particular, for the EIP case with the step-off current, I let $w^e(t) \approx 1 - u_{on}(t)$, where $u_{on}(t)$ is a Heaviside step function. For instance, with the Cole-Cole model shown in eq. (1.7), integration in eq. (5.3) can simply be evaluated when c=1,

$$\tilde{\eta}(t) = \eta e^{-\frac{1}{(1-\eta)\tau}t} \tag{5.4}$$

Here $(1-\eta)$ in the power of the denominator arises from the conductivity formulation of Pelton's Cole-Cole model [Pelton et al., 1978], whereas it is absent in the resistivity formulation. I invert each time channel of IP data separately, and recover pseudo-chargeability at multiple times. The recovered pseudo-chargeability will be a 4D property: $\tilde{\eta}(x,y,z;t)$. Interpreting this recovered pseudo-chargeability to extract intrinsic IP information such as η, τ, and c is possible [Yuval and Oldenburg, 1997, Hördt et al., 2006, Fiandaca et al., 2012], but I do not attempt that in this grounded source example.

5.3 Data

As an example, I use a grounded source and multiple receivers which measure voltages as shown in Figure 5.4; this is often called a gradient array. Four blocks (A1-A4) presented in Figure 5.4 have different σ_∞ and η values (see Table 5.1); all blocks have τ=0.5 s and c=1 (Debye model). Only blocks A2 and A3 are chargeable. The length of the source wire is 6 km and the potential differences between two electrodes along easting lines are measured at 625 locations (200-m length for the potential electrodes). Simulations were performed using the EMTDIP code [Marchant et al., 2014] with a step-off waveform. The initial condition of this simulation corresponds to solving a DC problem for on-time data using a DC conductivity, σ_0, then time-stepping proceeds to compute TEM responses at off-times. Two separate simulations are performed calculating $d = F[\sigma(s)]$ and $d^F = F[\sigma_\infty]$. For the latter simulation η was set to zero everywhere. Note that $\sigma(s) = \sigma_\infty$ when $\eta = 0$.

Fig. 5.5 shows the observed DC voltage during the on-time and its conversion to apparent resistivity. Lower apparent resistivity anomalies are reflective of the A1 and A3 bodies. After current switch-off, voltages are measured at sixty logarithmic-based time channels ranging from 1-600 ms. Computed responses at 5, 80, 130, and 500 ms are shown in Figure 5.6. To investigate EM effects at different times, I present the time decaying curves of d and d^F at A1-A4 in Figure 5.7. The four vertical black lines correspond to the times for the data maps shown in Figure 5.6.

At 5 ms EM induction effects are dominant and all data are negative. At 80 ms both EM and IP effects are considerable but still, all data are negative. At 130 ms a sign reversal has occurred at A2 and A3 bodies resulting in positive data. A1 also has smaller positive values. Note that A2 and A3 are chargeable but A1, which is conductive, is not. Therefore it is difficult to differentiate chargeability and conductivity anomalies just by looking at observed data at 80 and 130 ms. At 500 ms however, EM induction effects here significantly decayed and IP signals are dominant; only A2 and A3 show positive anomalies. Thus, depending on the measured time window, background conductivity, and IP parameters of chargeable bodies, data could be dominated by IP effects or not. Hence, whenever our measured time

window is not late enough to be considered as IP-dominant time, EM-decoupling is a crucial step. Note that the A1 anomaly at 80 and 130 ms could have been misinterpreted as a chargeable response.

Table 5.1: Conductivity (σ_∞) and resistivity (ρ_∞) at infinite frequency, and Cole-Cole chargeability (η) values for five units: A1-A4 and half-space.

Division	A1	A2	A3	A4	Half-space
σ_∞ (S/m)	1	0.01	0.1	0.001	0.01
ρ_∞ (Ωm)	1	100	10	1000	100
η	0	0.1	0.1	0	0

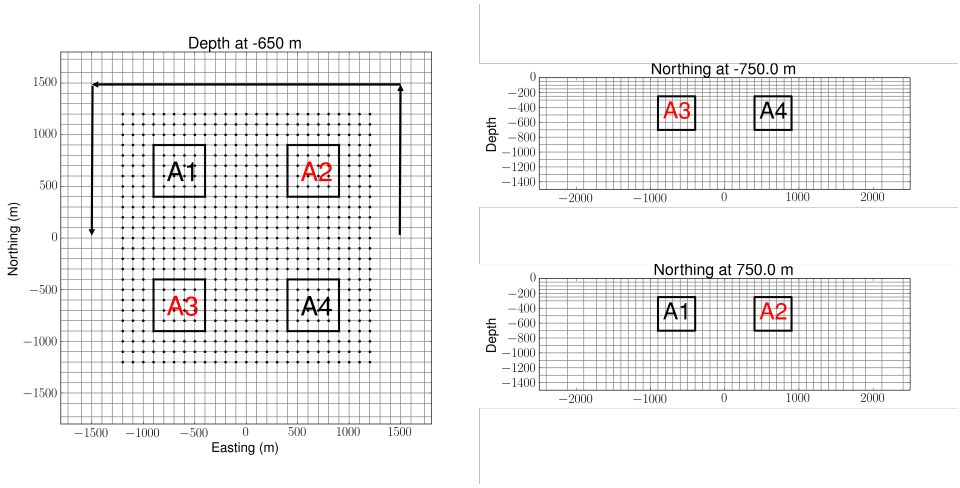

Figure 5.4: Plan and section views of the 3D mesh. Black solid lines show the boundaries of four blocks (A1-A4). Only A2 and A3 (red labels) are chargeable. Arrows indicate a wire path for the grounded source. Black dots indicate potential electrodes.

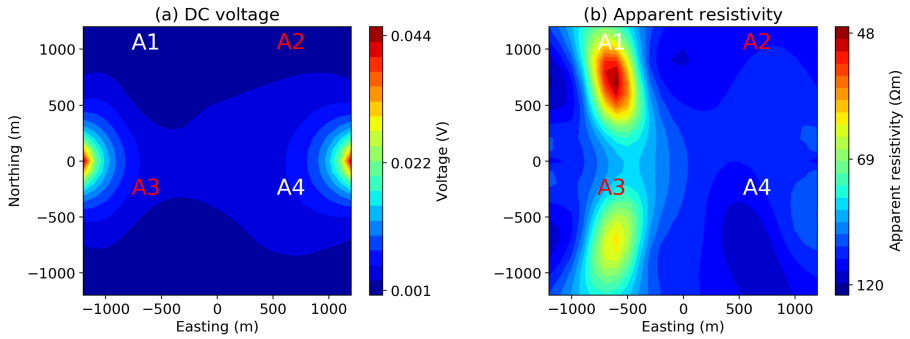

Figure 5.5: Plan maps of the observed DC data: (a) Voltage and (b) Apparent resistivity.

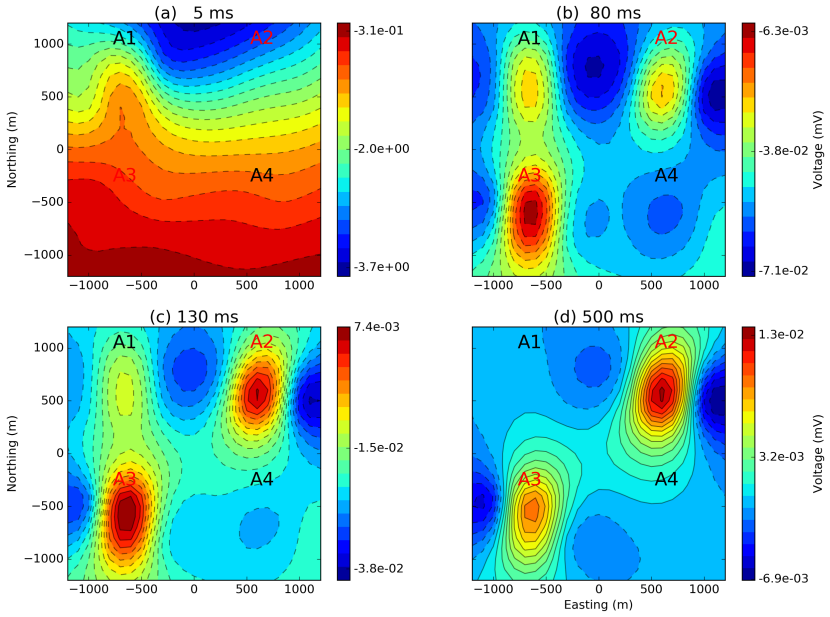

Figure 5.6: Plan maps of the observed TEM data at (a) 5 ms, (b) 80 ms (c) 130, and (d) 500 ms. Dashed and solid contours differentiate negative and positive data.

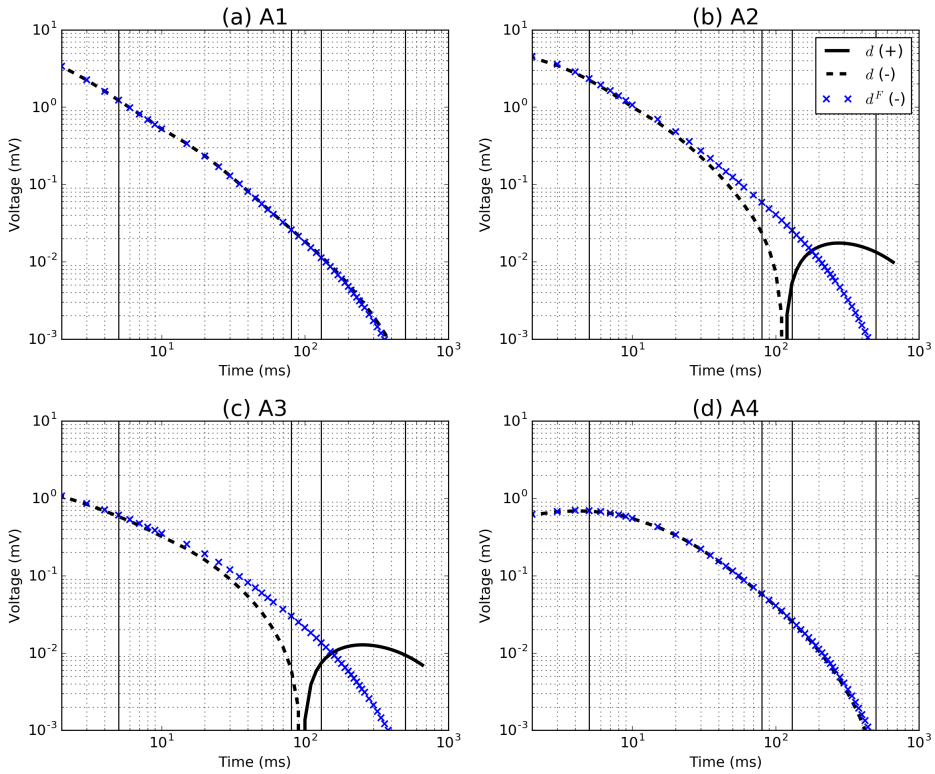

Figure 5.7: Time decaying curves of the observed (d) and fundamental (d^F) data. Four sounding locations close to (a) A1, (b) A2, (c) A3, and (d) A4 are presented. Blue and black color indicates d and d^F.

5.4 Conductivity Inversion

To recover $\sigma_\infty(x,y,z)$, the first six channels of the TEM data (1-6 ms) are used; these have only minor contamination from IP. In addition, DC data which contain IP effects, but have minor EM induction effects can be used. I first invert the DC data and recover the DC conductivity, σ_{est}^{DC}. Note that this theoretically represents σ_0 rather than σ_∞. For DC inversion, the DC-IP package of SIMPEG is used [Cockett et al., 2015]. The gradient array data used here have only a single source and hence they can be represented as a potential field and have no inherent depth resolution. Without a depth weighting the resultant conductivity from the inversion can be a thin layer at the surface. To overcome this, I incorporate a depth weighting similar to that used in magnetic inversion [Li and Oldenburg, 1996]. The TEM data are inverted with our H3DTD code [Oldenburg et al., 2013]. Parameters for both inversions are summarized in Table 5.2 and further details are given in Section 3.2. The recovered conductivity models from the 3D TEM and DC inversions are respectively shown in Figure 5.8(a) and (b). The conductive blocks A1 and A3 are better imaged with the TEM inversion. Note the TEM data have inherent depth resolution and hence no depth weighting was required.

Table 5.2: Parameters for the TEM and DC inversions. See Section 3.2 for explanation of parameters. σ_{half} indicates conductivity of the homogeneous half-space, which has a value of 0.01 S/m.

Parameters	TEM inversion	DC inversion
α_x=α_y=α_x	1	1
α_s	10^{-4}	10^{-4}
ϕ_d^*	$625 \times 6 = 3750$	
Uncertainty(ε_j)	$0.02\|d_j^{obs}\|$	$0.05\|d_j^{obs}\|$+0.01
$\mathbf{m}_0$	$log(\sigma_{half})$	$log(\sigma_{half})$
$\mathbf{m}_{ref}$	$log(\sigma_{half})$	$log(\sigma_{half})$
Model weighting	N/A	$(z-z_0)^{-3}$
Bounds constraint	$\mathbf{m} > 0$	N/A

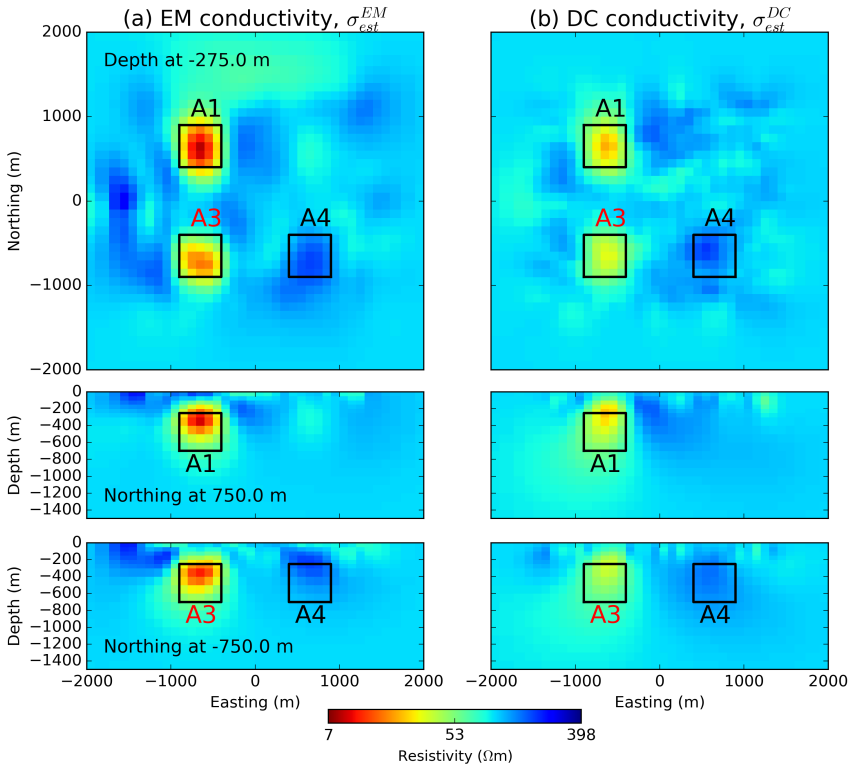

Figure 5.8: Recovered conductivity models from: (a) TEM and (b) DC inversions by inverting off-time (EM) and on-time data (DC), respectively.

5.5 EM-decoupling

The next step is EM-decoupling. Eq. (5.1) is implemented by using σ_{est} from the TEM inversion (Fig. 5.8). In Fig. 5.9, I present d, $F[\sigma_{est}^{EM}]$ and $d^{IP}[\sigma_{est}^{EM}]$ data at 80 ms. At this time, both EM and IP effects are considerable. Our EM-decoupling procedure removes EM effects due to conductivity especially for regions close to A1 (not chargeable) and A3 (chargeable). Removing the conductive anomaly at A1 is especially important, because this could have been misinterpreted as chargeable anomaly.

A crucial aspect of our EM-decoupling procedure is the effect of the background conductivity. To show this I consider three other candidates, namely true σ_∞, σ_{est}^{DC}, and half-space conductivity, σ_{est}^{half}. I compare the performance of the EM-decoupling procedure for all four conductivity models. Fig. 5.10 shows the true and estimated fundamental responses. σ_{est}^{EM} does the best job of predicting the fundamental response followed by σ_{est}^{DC}. The halfspace response is very smooth and is a poor approximation to the fundamental response.

The discrepancies between the true and estimated fundamental responses are directly observed when the true and estimated d^{IP} data are compared as in Fig. 5.11. $d^{IP}[\sigma_{est}^{EM}]$ are the closest representation of d^{IP}, followed by $d^{IP}[\sigma_{est}^{DC}]$. Note that the latter still has some positive response over A1. As expected the $d^{IP}[\sigma_{est}^{half}]$ results in a poor representation of the IP response. It indicates that A1 is chargeable, and that the data at A3 are higher than those at A2. If these data are input to a 3D IP inversion, they produce strong artifacts from which incorrect conclusions can be drawn.

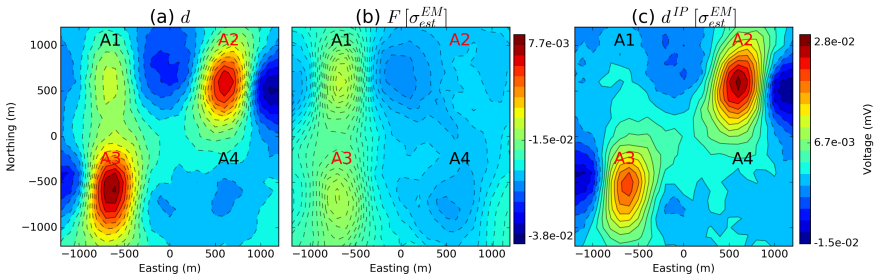

Figure 5.9: Plan maps for 80 ms. (a) observed data, (b) estimated fundamental using σ_{est}^{EM}, and (c) IP.

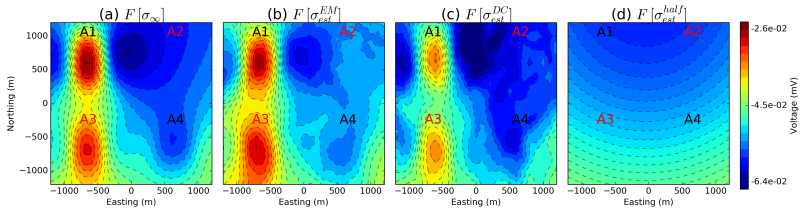

Figure 5.10: True and estimated fundamental responses at 80 ms. (a) True fundamental response; (b), (c), and (d) correspondingly indicate estimated fundamental responses using σ_{est}^{EM}, σ_{est}^{DC}, and σ_{est}^{half}.

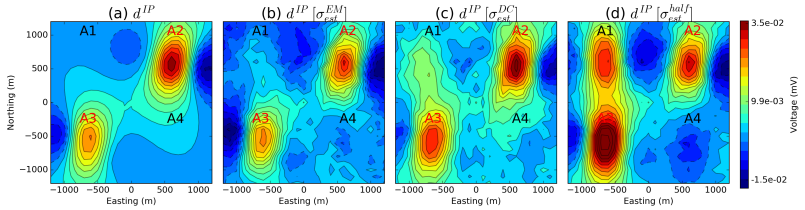

Figure 5.11: True and estimated IP responses at 80 ms. (a) True d^{IP}; (b), (c), and (d) correspondingly indicate estimated IP responses using σ_{est}^{EM}, σ_{est}^{DC}, and σ_{est}^{half}.

5.6 IP Inversion

To recover 3D pseudo-chargeability, I invert the IP data sets at 80 ms obtained using the two estimated conductivity models: σ_{est}^{EM} and σ_{est}^{DC}. These conductivities are used to generate the linearized sensitivities as outlined in Section 2.2. The unit of the pseudo-chargeability is basically dimensionless, but I use mV/V. The linear system is inverted with the added constraint of positivity on the pseudo-chargeability [Oldenburg and Li, 1994]. Inversions are done using a single time channel and a single source so there is no depth resolution for the IP inversion. Thus, similar to the previous DC inversion, a depth weighting needs to be incorporated. For the IP inversion the reference model, $\mathbf{m}_{ref}$ is set to zero, and the uncertainty is set to 5% of the maximum amplitude of IP data (0.05 $max(d^{IP})$) at 80 ms. The recovered 3D pseudo-chargeability models from $d^{IP}[\sigma_{est}^{EM}]$ and $d^{IP}[\sigma_{est}^{DC}]$ are shown in Figure 5.12. The two true chargeable bodies, A2 and A3, are well imaged although the pseudo-chargeability model from $d^{IP}[\sigma_{est}^{EM}]$ is of better quality than that from $d^{IP}[\sigma_{est}^{DC}]$: a) it has fewer artifacts near A1 as expected from $d^{IP}[\sigma_{est}^{DC}]$ and b) the recovered chargeable blocks are more compact. In addition, considering the true pseudo-chargeability value of both A2 and A3 is 83 mV (obtained from the eq. 5.4), the recovered $\tilde{\eta}$ values of A2 and A3 blocks ($\sim$30 mV/V) are in a reasonable range.

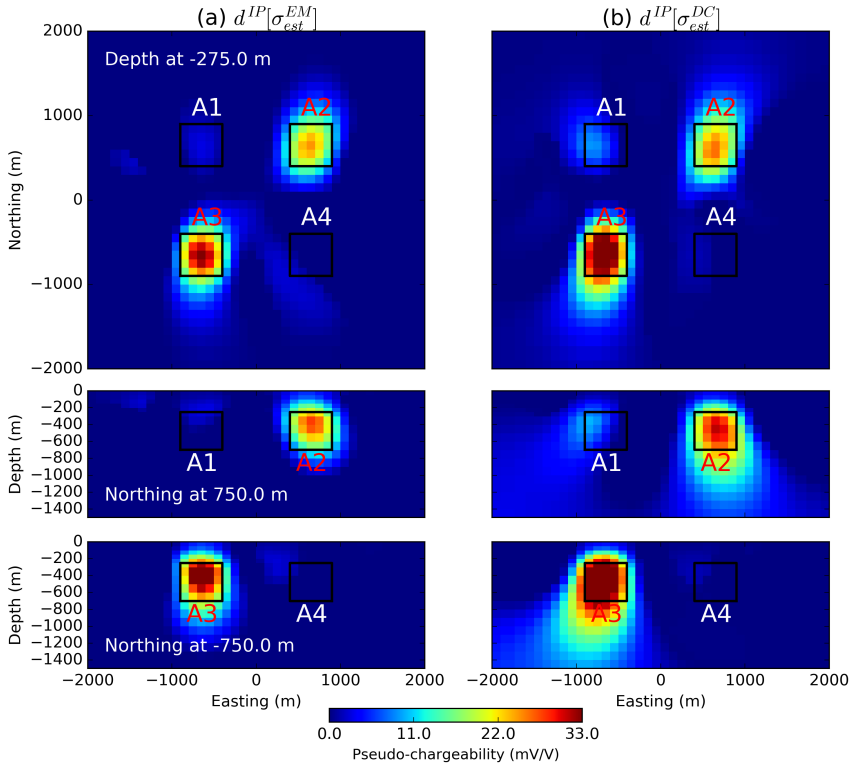

Figure 5.12: Recovered chargeability models from IP inversions. IP data computed using an estimated conductivity model from (a) TEM and (b) DC inversions, respectively.

5.7 Discussion

Conductivity inversion is a crucial part of the TEM-IP inversion workflow, and for the time-domain DC-IP case there are two types of data: a) DC (late on-time) and b) TEM (early off-time). The DC data can be inverted directly to give an estimate of $\sigma_0 = \sigma_\infty(1-\eta)$. Often η is small ($\ll 1$) hence $\sigma_0 \approx \sigma_\infty$. In the example presented here using a gradient array however, it was required to incorporate a depth weighting. With that, the recovered conductivity was sufficiently good to allow a good EM-decoupling and subsequent inversion of the IP data. The recovered chargeability nicely delineated the two chargeable bodies but a weak chargeable artefact was observed at the location of conductor. In the synthetic example the early-time TEM data produced a better conductivity model, without the need for any depth weighting. This illustrated the resolving power that is inherent in working with multiple time channels. The pseudo-chargeability recovered from the inversion was improved compared to that using the DC data. Notwithstanding that result, the challenge with inverting the early-time TEM data is the need to work with data that do not exhibit significant IP effects. IP contamination in the data will bias recovered conductivities towards increased resistivity and thereby generate artefacts. Deciding how to recognize when data are IP-coupled is an area for future research. So too is the need to invert both the DC and early-time TEM data simultaneously. Both issues need to be tested for a more realistic model (e.g. complicated background model) and different arrays of DC-IP surveys (e.g. pole-dipole) to be used in practice.

The accuracy to which σ_∞ needs to be estimated depends upon the information that is ultimately desired. If the goal is for detection of a body then a less resolved conductivity may suffice. As time increases, the d^{IP} data obtained through EM-decoupling is less adversely affected by inaccuracies in σ_{est}. For example, as shown in Fig. 5.13, performance of the EM-decoupling with the σ_{est}^{DC} at 130 ms was good. At 80 ms (Fig. 5.11) the performance is still generally good but artefacts are beginning to be more prominent (for example around A1). For the purpose of detection, both of these results may suffice. But, although the detection of a chargeable body can be accomplished with a moderately good approximation to the true conductivity, the need to obtain a high quality conductivity becomes

more important when spectral information is sought. This may require quality IP data at early times. Fig. 5.14 shows time decaying curves of the observed, estimated fundamental and IP data at A3 (conductive and chargeable). $d^{IP}[\sigma_{est}^{DC}]$ converges to $d^{IP}[\sigma_{\infty}]$ after 130 ms. However, $d^{IP}[\sigma_{est}^{EM}]$ converges to $d^{IP}[\sigma_{\infty}]$ after 20 ms resulting in a broader time band of the IP data compared to $d^{IP}[\sigma_{est}^{DC}]$. This will be a crucial factor for recovering intrinsic IP parameters because capturing IP information in a greater time band will reduce non-uniqueness in the inverse problem for multiple parameters such as $\eta(x,y,z)$, $\tau(x,y,z)$, and $c(x,y,z)$ [Lajaunie et al., 2016].

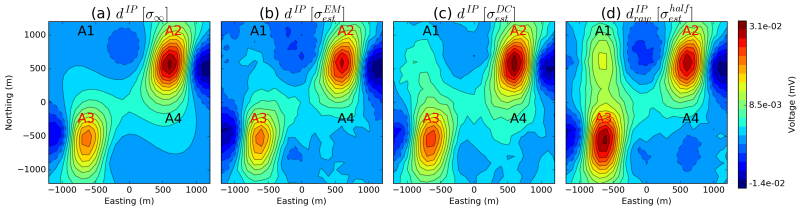

Figure 5.13: True and estimated IP responses at 130 ms. (a) True d^{IP}; (b), (c), and (d) correspondingly indicate estimated IP responses with use of EM, DC, and half-space conductivity.

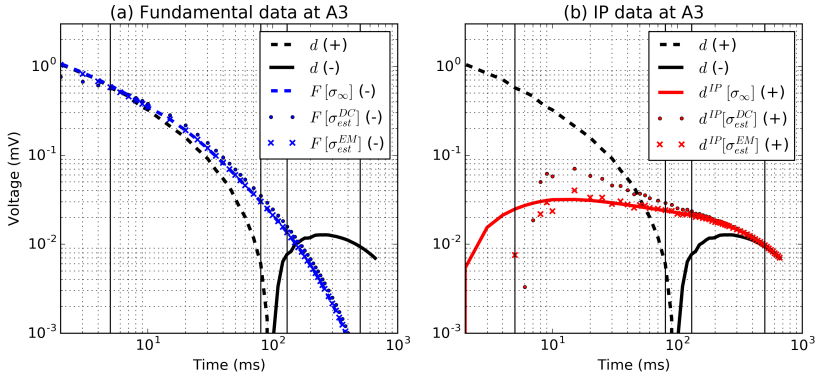

Figure 5.14: Decay curves of the observed, fundamental and IP data at A3. (a) True and estimated fundamental responses with the observed data. (b) True and IP responses with the observed data.

5.8 Conclusions

In this chapter, the TEM-IP inversion workflow has been applied to a synthetic grounded source TEM example. First, I inverted on-time DC data and recovered a 3D conductivity. Then, I inverted six of the earliest time channels of TEM data, which have minor IP-contamination, and recovered an another estiamte of the 3D conductivity. These early TEM data have often been thrown away because they are considered as "noise". However, by considering them as "signal" and inverting them, I recovered a better conductivity model in the sense of depth resolution. Second, the recovered conductivity, σ_{est}^{EM} was used in our EM-decoupling procedure to generate IP data. The procedure was effective for removing EM induction in the observations, especially for regions close to A1 and A3, which had significant conductivity responses. Third, I inverted the IP data set generated from the TEM conductivity model using conventional 3D IP inversion. The recovered pseudo-chargeability successfully imaged two true chargeable anomalies. This demonstrates that our TEM-IP inversion workflow can be effective for recovering a good estimate of electrical conductivity, for removing EM-coupling from IP data, and for obtaining a 3D distribution of pseudo-chargeability.

Chapter 6

Conclusions

Earth materials are chargeable, and hence EM data can include IP effects. The latest developments of instrumentation and processing techniques provide high quality EM data in which small IP signals can be observed. For instance, measuring negative transients in AEM surveys are now commonly observed and regarded as signal whereas that was not the case a decade or more ago. Therefore, developing an effective methodology to handle EM data that includes both EM and IP signals, is timely. My goal is to develop physical understanding and computational procedures to recover 3D conductivity and chargeability from EM data, and to apply the technique to field data sets. This requires separation of the EM and IP portions in the EM data, and thus contending with important aspects of EM-coupling is another essential task. I have designed this thesis to contribute to the scientific community by developing a workflow, which extracts 3D conductivity and chargeability from time-domain EM data. The procedure has been applied to synthetic and field examples. For the development of the workflow, and its application, I focus on answering three important and unsolved questions:

1. How can we understand the fundamentals of inductive source IP, and can the time-domain airborne IP data be linearized similar to DC-IP data?

2. Can distributed IP information be recovered from the airborne data showing IP effects?

3. Can EM effects in DC-IP data be effectively removed to generate high qual-

ity IP data?

The following sections summarize my work on these questions. Of central importance is the development of the workflow to handle TEM-IP data.

6.1 Development of the TEM-IP Inversion Workflow

The TEM-IP inversion workflow includes three main steps: a) Conductivity inversion, b) EM-decoupling, and c) IP inversion. In the first step, TEM data at early-time channels (where IP effects are minor) are used to recover an estimated 3D conductivity model, σ_{est}. In the second step, estimated fundamental data, $F[\sigma_{est}]$, are simulated and subtracted from the observations to generate IP data, d^{IP}; this is the EM-decoupling procedure. In the third step, the obtained IP data are linearized as a function of the pseudo-chargeability: $\mathbf{d}^{IP} = \mathbf{J}\tilde{\eta}$. Then by using that relationship, the IP data can be inverted to generate a 3D distribution of pseudo-chargeability. This inversion can be done for multiple time channels. Lastly the pseudo-chargeability of a cell at different times can be used as data in a parametric model for estimating parameters to characterize the chargeability. Here I estimate Cole-Cole parameters of chargeability and time constant. Linearizing IP data for inductive sources is more challenging than for grounded sources, because of the dynamic polarization buildup that arises from nature of the diffusive electric fields. This polarization character needs to be captured to develop a linear IP function.

Chapter 2 is related to the first question stated at the beginning of this conclusion section. I present linearization of inductive source IP (ISIP) data. A core idea of linearizing ISIP data is based upon the time behavior of the electric field from an inductive source. Consider a single pixel in the earth. When the current is turned off, the electric field at the pixel increases to a peak and then decays. I assumed that the major polarization effect is characterized by the electric field at the time when it reaches the maximum. Based upon that hypothesis, the IP current is expressed as a function of the pseudo-chargeability. This IP current captures both vortex and galvanic currents which contribute to the IP signals. With the application of the Biot-Savart law to the IP current, both the magnetic field and its time derivative are obtained. This provides a desired linear form: $\mathbf{d}^{IP} = \mathbf{J}\tilde{\eta}$ for ISIP data. The assumptions made to linearize the IP function are thoroughly tested with numerical

experiments. Particular emphasis is placed upon the airborne IP case.

Chapter 3 constructs a foundation to answer the second question. By using the linearized IP function, I develop a 3D IP inversion algorithm, and test that with a synthetic airborne IP data. Depth weighting is introduced to compensate for a lack of intrinsic depth resolution in the airborne IP data. With this, the 3D IP inversion recovers a reasonable geometric shape and location of the chargeable body. For the inversion I assumed that the true $\sigma_\infty(x,y,z)$ is available. However, in practice σ_{est} obtained in the first step is always different from σ_∞. This incorrect conductivity has two effects on the IP inversion. First it generates errors in the $d^{IP}[\sigma_{est}]$. A positivity constraint imposed on the pseudo-chargeability greatly ameliorates these errors particularly where errors are positive. The other avenue by which an incorrect conductivity can affect the inversion is through the sensitivity matrix, which is ideally $\mathbf{J}[\sigma_\infty]$. However the impact of an incorrect conductivity in the sensitivity is much less than the errors obtained by an incorrect fundamental response $F[\sigma_{est}]$. A synthetic example is introduced and each time channel of the d^{IP} is inverted, and pseudo-chargeability at multiple times are obtained. The pseudo-chargeabilities at multiple times can be inverted to obtain Cole-Cole parameters η, τ. I have found that the estimated τ was close to the true value, whereas η was poorly estimated.

6.2 Application to Airborne IP Data

Chapter 4 addresses the second question by applying the TEM-IP inversion workflow to airborne EM (AEM) data. This chapter is composed of three sections, which present a synthetic AEM example, and two field airborne examples over mineral deposits: the Mt Milligan porphyry deposit and the Tli Kwi Cho kimberlites.

In Section 4.1, I generate the synthetic AEM data, and apply the workflow. Each of three steps in the workflow is carefully tested. For the conductivity inversion, early-time channels which do not have negative values are used to recover a 3D conductivity, σ_{est}. Overall, the conductivity structures are imaged well. In the second step, $d^{IP}[\sigma_{est}]$ is obtained by subtracting $F[\sigma_{est}]$ from the observations. This EM-decoupling shows good performance in the intermediate and late times. However, the EM-decoupling shows poor performance in the early times, which

is expected. The third step is the IP inversion. By inverting each time channel of the obtained $d^{IP}[\sigma_{est}]$, a pseudo-chargeability at multiple times is recovered. This demonstrates that an IP inversion can provide location and geometric shape of chargeable bodies embedded in the subsurface as long as appropriate depth weighting is applied. By interpreting the recovered pseudo-chargeability, Cole-Cole parameters, η and τ, are extracted at four selected cells, that corresponded spatially to the four chargeable blocks. Recovery of τ is reasonable, whereas η is mostly underestimated. From this result, I conclude that there is the potential to extract intrinsic Cole-Cole parameters from airborne IP data but the time constant seems to be the most robust parameter to be extracted.

Section 4.2 presents application of the workflow to field VTEM data over the Mt Milligan porphyry deposit. Clear negative anomalies are shown in the VTEM data. By applying the workflow, a 3D distribution pseudo-chargeability is recovered. Negative transients are ignored for the conductivity inversion. The obtained 3D conductivity, σ_{est}, is used in an EM-decoupling procedure, and $d^{IP}[\sigma_{est}]$ at eight time channels are obtained. Two IP anomalies, which are not visible as negative voltages in the observation, are detected around the Rainbow fault. Using the IP inversion, each time channel of the $d^{IP}[\sigma_{est}]$ is separately inverted, and a 3D pseudo-chargeability at each of the eight time channels is recovered. Highly chargeable volumes are successfully imaged on the edges of three mineralized zones; they are interpreted as highly altered zones. Using both conductivity and pseudo-chargeability models, 3D rock models are constructed. Importantly, highly altered parts of the monzonite stock is recognized from the pseudo-chargeability, and this may have potential to help characterize a porphyry deposit. I believe that this was the first time that a voxel inversion has been used to recover a 3D chargeability from AEM data.

In Section 4.3, the workflow is applied to the VTEM data over the Tli Kwi Cho kimberlites where consistent negative transients have been observed with various TEM surveys. A main question here is whether observed negatives are geological noise or signal that can be useful for kimberlite exploration. I focus on the latest VTEM data, which shows four distinct IP anomalies, and apply the workflow. Even at the earliest time channel, some of the VTEM data are negatives, and this presents challenges for the conductivity inversion. This is overcome by coopera-

tively inverting the VTEM and DIGHEM data, and a 3D distribution conductivity is recovered. Two conductive pipes are respectively imaged at DO-18 and DO-27 pipes; the conductive pipe at DO-27 is embedded at depth, whereas that at DO-18 extends to the surface. The estimated conductivity is used for EM-decoupling procedure resulting in $d^{IP}[\sigma_{est}]$ at multiple time channels. $d^{IP}[\sigma_{est}]$ at 130 μs shows three IP anomalies at DO-18 and in the north-eastern part of the DO-27. At 410 μs, an IP anomaly at the southern part of the DO-27 is revealed. Hence four IP anomalies are identified in total. By inverting the obtained $d^{IP}[\sigma_{est}]$, 3D pseudo-chargeabilities at multiple time channels are recovered. Four chargeable bodies are imaged at different time channels. By using the recovered pseudo-chargeability at multiple times, η and τ values of representative cells for the four chargeable bodies are extracted. The recovered τ from the chargeable body at southern part of the DO-27 is greater than that from the other three chargeable bodies showing that there is at least two distinct rock units. The pseudo-chargeability at 130 μs and 410 μs along with the conductivity are used to generate a 3D rock model. Three different rock units related to kimberlites are identified. Particularly, two rock units are interpreted as PK and VK units. Distinction between PK and VK is obtained from the different polarization character considering their pore size: PK is characterized by large pore size and hence large τ, and VK is characterized by small pore size and hence small τ. The PK unit is the diamondiferous unit. In conclusion, the 3D rock model that is obtained from the interpretation of the AEM data shows major features that are a representation of the geologic model obtained from drillings. I believe this demonstrates how the obtained polarizable information could help a kimberlite exploration.

6.3 Application to DC-IP Data

Chapter 5 deals with the third question. The workflow is applied to a synthetic grounded source example. Emphasis is on EM-decoupling. This requires an estimate of the background conductivity. This is first obtained by inverting the DC data to generate σ_{est}^{DC}. Then several early-time channels of TEM data are inverted with a 3D TEM inversion is used to recover σ_{est}^{EM}. These early TEM data have often been discarded because they are considered as "noise". However, by consid-

ering them as "signal" and inverting them, a better conductivity model than that from the DC data is recovered The σ_{est}^{EM} is used in the EM-decoupling procedure. This was effective for removing EM induction in the observations, especially for the conductive blocks embedded in the earth. The resultant IP data are inverted to recover a 3D pseudo-chargeability. Chargeable blocks are successfully imaged. These results demonstrate that the TEM-IP workflow can be effective for recovering a good estimate of electrical conductivity, for removing EM signals from IP data, and for obtaining a 3D distribution of pseudo-chargeability from grounded source TEM data.

6.4 Future Research

Notwithstanding the successful recovery of a 3D chargeability from synthetic and field TEM data sets using the developed workflow, there are some potential weaknesses in the workflow, and they require further investigations. Hence, I will elaborate on them and also suggest potential approaches for improvement.

A crucial challenge arises from an incorrect conductivity obtained in the first step, and its impact on subsequent EM-decoupling. Let $\triangle d = F[\sigma_\infty] - F[\sigma_{est}]$. The obtained $d^{IP}[\sigma_{est}]$ always includes residuals, $\triangle d$ as well as other additive noise.

$$d^{IP}[\sigma_{est}] = d^{IP}_{true} + \triangle d + \text{noise}. \tag{6.1}$$

I suggested applying a regional removal technique to reduce the effect of $\triangle d$, and presented a synthetic example. Basically I selected some regions of the data which were felt to have minimal IP effects. So $d^{IP}[\sigma_{est}] \simeq \triangle d$. I fitted those points with a polynomial and used the surface as an estimate of $\triangle d$. This was subtracted from $d^{IP}[\sigma_{est}]$. This procedure is similar to the removal of a regional field in gravity and magnetics. It suffers form the same limitations but as in potential field inversions. However it may be an effective way to handle an unwanted background signal.

An alternative and less subjective approach was to put a positivity constraint on $\tilde{\eta}$ when inverting $d^{IP}[\sigma_{est}]$ to prevent positive bias, since negative $\tilde{\eta}$ usually generate postive IP data for the coincident-loop airborne system. I used the positivity constraint in the field examples to prevent fitting positive $\triangle d$, so negative $\triangle d$ can still make artefacts in a recovered pseudo-chargeability model. When that is the

case, developing an effective regional removal technique to obtain clean IP data might be important, and it is worthy of further investigation.

For the conductivity inversion, data which have minimal IP effects are required. I choose several early-time channels, which do not have negative values. Depending upon how one selects time channels to obtain EM-dominant data, the quality of an estimated conductivity can vary. A more robust approach needs to be developed.

Three options are considered. The first option is using the on-time data [Smith and Klein, 1996] because the on-time data will be dominated by the primary fields and EM induction effects. This is the simplest and effective solution, but in reality obtaining the high quality on-time data for a time-domain AEM system is challenging due to the inaccuarate measure of the primary field. The second option is to modify the TEM-IP inversion workflow. To improve the quality of the conductivity inversion, an additional step is required for the original workflow to remove IP effects in observations when inverting for a conductivity. Accordingly, the original workflow can be altered as (a) Conductivity inversion, (b) EM-decoupling, (c) IP inversion, and (d) IP-decoupling. (a) and (b) can be same as the original workflow, but (c) needs to be modified to estimate d^{IP} for subsequent IP-decoupling procedure. For this, rather than separately inverting for each time channel of d^{IP} to recover a pseudo-chargeability at multiple time channels, I suggest parameterizing the pseudo-chargeability with a representative function such as Cole-Cole or Stretched exponential [Kohlrausch, 1854, Pelton et al., 1978, Tarasov and Titov, 2013], and inverting all time channels of d^{IP} together to recover 3D distributions of the parameters; this can be considered as a spectral IP inversion similar to Fiandaca et al. [2013]. For instance, considering a Cole-Cole model for the parameterization, $\eta(x,y,z)$, $\tau(x,y,z)$, and $c(x,y,z)$ can be recovered and then d^{IP} can be estimated. The estimated d^{IP} can be subtracted from observations to yield cleaner EM data; this is an IP-decoupling step. The four steps of the workflow can be iterated until it reaches to a stopping criteria. This iterative workflow still require the approach to select EM-dominant data when inverting for conductivity, but the impact of this selection is much less than the original workflow since the quality of EM data will be enhanced in the iterative procedure by the IP-decoupling.

The thrid option is inverting both EM and IP signals together. As mentioned previously there are various ways to parameterize a complex conductivity. The

TEM data with a Cole-Cole representation can be written as

$$d[\sigma_\infty, \eta, \tau, c]. \tag{6.2}$$

Four Cole-Cole parameters are defined in 3D space, and hence this increases the number of unknowns compared to the inversion used in the workflow; this increases non-uniqueness of the inversion. Moreover, the problem is now non-linear rather than linear. This makes the solution more complicated to achieve. Lastly, evaluation of the convolution between time-dependent conductivity and the electric field is required for each transmitter to compute forward responses, and this dramatically increases the computational cost of the inversion. However, the possibility exists to make this option robust and computationally efficient, and it is worthwhile to pursue. For the non-uniqueness issue, rather than starting from a homogeneous conductivity, one can invert early-time channels of TEM data to recover a 3D conductivity, then use the recovered conductivity as a starting model for the non-linear inversion.

When linearizing IP response from an inductive source (Section 2.2), I assumed a step-off current waveform, and based upon that an electric field at maximum was selected as the reference electric field to compute the sensitivity function. However in practice, TEM surveys use various types of current waveforms. Although the linearization steps suggested in the thesis are general enough to handle this, more complicated waveforms still needs to be taken into account, and tested; this can be important especially when quantitative polarization information is desired.

Finally, the workflow has been applied to the synthetic grounded source example, but not to field examples. Therefore, the workflow must be applied to field example to demonstrate its capability.

6.5 Concluding comments

Before I finish this thesis, I want to remind readers about why extracting polarization information of the subsurface is important. Most of earth rocks are chargeable, and they have different polarization characteristics. This polarization information will be valuable information to characterize the subsurface in various applications:

mining, oil and gas, groundwater, and geotechnical problems. In addition, IP signals, which have often been acquired from the ground using DC-IP surveys, can now readily be obtained from the air using AEM surveys with the latest improvements in instrumentation, although AEM surveys has limited depth of investigation for chargeable bodies compared to DC-IP surveys. In this perspective, the IP technique is just now starting to be used, and I believe there will be more areas that IP can make impact. I illustrate a few important areas below.

First is airborne IP. This allows polarization information of a broad region to be quickly mapped. It is still controversial about whether measured IP data are geological noise or signals that can be useful for mineral explorations. Nonetheless, there are IP signals in AEM data, and hence some polarization information can be extracted, and this may be useful for various applications. For instance in the thesis, I showed an example when airborne IP can be used to distinguish different kimberlites in the ground. In addition, clays and permafrost are also chargeable, and hence they can be delineated from the airborne IP data. A second application is estimating hydraulic permeability of rocks using grounded IP surveys. A number of lab-scale and some field-scale research, which estimate permeability of rocks from IP data, have been performed and showed promising results [Slater and Lesmes, 2002, Revil and Florsch, 2010, Weller et al., 2010, Hördt et al., 2007]. This can make an impact on groundwater studies, which uses hydraulic permeability as an input for their simulations. A third application is characterizing landfill or waste dumps. Some contaminated materials in the landfills can be chargeable, and hence grounded IP surveys can be used to characterize them, particularly for old landfill areas, which do not have sealing facility to prevent leaking leachate [Gazoty et al., 2012]. Further, depending upon the situation, contaminated ground needs to be remediated, and for this bioremediation can be an option. If this remediation process removes chargeable contaminants, then the chargeability of the ground may decrease, and hence these changes can be monitored by IP.

To conclude, obtaining polarization information of the subsurface is an important task for geoscience applications, and further there will be more applications in which IP can play a crucial role. The workflow, and its application, presented in this thesis provide a general framework that can extract polarization information from EM data. The results obtained in this thesis show that important information

about chargeability can be obtained from EM data and this opens the scope for potential new applications.

Bibliography

W. Boyko, N. R. Paterson, and K. Kwan. AeroTEM: system characteristics and field results. *The Leading Edge*, 20(10):1130–1138, 2001. → pages 136

M. Bücker and A. Hördt. Long and short narrow pore models for membrane polarization. *Geophysics*, 78(6):E299–E314, 2013. → pages 11

Y. Chen and D. Or. Geometrical factors and interfacial processes affecting complex dielectric permittivity of partially saturated porous media. *Water Resources Research*, 42(6):1–9, 2006. → pages xiii, 11, 12, 14

R. Cockett, S. Kang, L. J. Heagy, A. Pidlisecky, and D. W. Oldenburg. SimPEG: An open source framework for simulation and gradient based parameter estimation in geophysical applications. *Computers & Geosciences*, 85, Part A: 142–154, 2015. → pages v, 81, 172, 208

K. S. Cole and R. H. Cole. Dispersion and Absorption in Dielectrics I. Alternating Current Characteristics. *The Journal of Chemical Physics*, 9(4), 1941. → pages 15, 88

M. Commer, G. A. Newman, K. H. Williams, and S. S. Hubbard. 3D induced-polarization data inversion for complex resistivity. *GEOPHYSICS*, 76 (3):F157–F171, 2011. → pages 32, 163

D. Cowan. personal communication, 2015. → pages xiii, 18

S. G. R. Devriese, K. Davis, and D. W. Oldenburg. Inversion of airborne geophysics over the DO-27/DO-18 kimberlites Part 1: Potential fields. *Interpretation*, 5(3):T299–T311, 2017. → pages xxiii, 138

B. J. Doyle, K. Kivi, and B. H. S. Smith. The Tli Kwi Cho (DO27 and DO18) Diamondiferous Kimberlite Complex, Northwest Territories, Canada. In *Proceedings of the VIIth International Kimberlite Conference*, pages 194–204, 1999. → pages 158

T. Eggleston and K. Brisebois. DO-27 Diamond Project, Northwest Territories, Canada. Ni 43-101 report, AMEC, aug 2008. → pages 158

H. ElKaliouby and E. Eldiwany. Transient electromagnetic responses of 3D polarizable body. *GEOPHYSICS*, 69(2):426–430, 2004. → pages 136

R. J. Enkin, D. Cowan, J. Tigner, A. Severide, D. Gilmour, A. Tkachyk, M. Kilduff, and J. Baker. Physical property measurements at the GSC paleomagnetism and petrophysics laboratory, including Electric Impedance Spectrum methodology and analysis. → pages xiii, 16, 17, 19

G. Fiandaca, E. Auken, A. V. Christiansen, and A. Gazoty. Time-domain-induced polarization: Full-decay forward modeling and 1D laterally constrained inversion of Cole-Cole parameters. *Geophysics*, 77(3):E213, 2012. → pages 3, 32, 167

G. Fiandaca, J. Ramm, A. Binley, A. V. Christiansen, and E. Auken. polarization data through 2-D inversion. pages 631–646, 2013. → pages 3, 187

J. Fink, E. McAlister, B. Sternberg, W. Wieduwilt, and S. Ward. *Induced Polarization Applications and Case Histories*. Society of Exploration Geophysicists, 1990. → pages 162

M. Flis, G. Newman, and G. Hohmann. Induced olarization effects in timedomain electromagnetic measurements. *GEOPHYSICS*, 54(4):514–523, 1989. → pages 163

C. Flores and S. A. Peralta-Ortega. Induced polarization with in-loop transient electromagnetic soundings: A case study of mineral discrimination at El Arco porphyry copper, Mexico. *Journal of Applied Geophysics*, 68(3):423–436, 2009. → pages 136

D. Fournier, S. Kang, M. S. McMillan, and D. W. Oldenburg. Inversion of airborne geophysics over the DO-27/DO-18 kimberlites Part 2: Electromagnetics. *Interpretation*, 5(3):T313–T325, 2017. → pages vi, 143

A. Gazoty, G. Fiandaca, J. Pedersen, E. Auken, A. V. Christiansen, and J. K. Pedersen. Application of time domain induced polarization to the mapping of lithotypes in a landfill site. *Hydrology and Earth System Sciences*, 16(6): 1793–1804, 2012. doi:10.5194/hess-16-1793-2012. → pages 189

GPG. Geophysics for practicing geoscientists, 2018. URL https://gpg.geosci.xyz/content/induced_polarization/induced_polarization_physical_properties.html. → pages xii, 10

E. Haber. *Computational Methods in Geophysical Electromagnetics*. Society for Industrial and Applied Mathematics, Philadelphia, PA, 2014. → pages 163, 207, 208

E. Haber and C. Schwarzbach. Parallel inversion of large-scale airborne time-domain electromagnetic data with multiple OcTree meshes. *Inverse Problems*, 30(5):055011, may 2014. → pages 105

L. J. Heagy, R. Cockett, S. Kang, G. K. Rosenkjaer, and D. W. Oldenburg. A framework for simulation and inversion in electromagnetics. *Computers & Geosciences*, 107:1–19, 2017. ISSN 0098-3004. doi:https://doi.org/10.1016/j.cageo.2017.06.018. → pages 67, 209

G. W. Hohmann and G. A. Newman. Transient electromagnetic responses of surficial, polarizable patches. *GEOPHYSICS*, 55(8):1098–1100, 1990. → pages 163

A. Hördt, T. Hanstein, M. Hönig, and F. M. Neubauer. Efficient spectral IP-modelling in the time domain. *Journal of Applied Geophysics*, 59(2): 152–161, jun 2006. → pages 3, 45, 88, 167

A. Hördt, R. Blaschek, A. Kemna, and N. Zisser. Hydraulic conductivity estimation from induced polarisation data at the field scale the Krauthausen case history. *Journal of Applied Geophysics*, 62(1):33–46, 2007. → pages 2, 189

J. Jansen and K. Witherly. *The Tli Kwi Cho kimberlite complex, Northwest Territories, Canada: A geophysical case study*, chapter 289, pages 1147–1150. 2004. → pages 4

J. C. Jansen and B. J. Doyle. The Tli Kwi Cho Kimberlite Complex, Northwest Territories, Canada: A Geophysical Post Mortum. *Northwest Mining Association Practical Geophysics (III)*, 2000. → pages 136

V. Kaminski and A. Viezzoli. Modeling induced polarization effects in helicopter time-domain electromagnetic data: Field case studies. *GEOPHYSICS*, 82(2): B49–B61, 2017. → pages 4, 48, 92

S. Kang and D. Oldenburg. Recovering IP information in airborne-time domain electromagnetic data. *ASEG Extended Abstracts*, (1):1–4, jan 2015. → pages v

S. Kang and D. W. Oldenburg. TEM-IP: Extracting more IP information from galvanic source time domain EM data. *Geophysical propecting*, 2017. → pages vi

S. Kang, D. Oldenburg, D. Yang, and D. Marchant. On recovering induced polarization information from airborne time domain EM data. In *SEG Technical Program Expanded Abstracts 2014*, pages 1785–1789. Society of Exploration Geophysicists, aug 2014. → pages v, 136

S. Kang, D. Fournier, and D. Oldenburg. Inversion of airborne geophysics over the DO-27/DO-18 kimberlites Part 3: Induced polarization. *Interpretation*, pages T327–T340, mar 2017. → pages vi, 4, 5, 48

C. T. Kelley. *Iterative Methods for Optimization*. Society for Industrial and Applied Mathematics, 1999. → pages 81

A. Kemna, A. M. Binley, and L. Slater. Cross-borehole IP imaging for engineering and environmental applications. *Geophysics*, 69(1):97–107, 2004. → pages 3, 32

A. Kemna, A. Binley, G. Cassiani, E. Niederleithinger, A. Revil, L. Slater, K. H. Williams, A. F. Orozco, F. H. Haegel, A. Hördt, S. Kruschwitz, V. Leroux, K. Titov, and E. Zimmermann. An overview of the spectral induced polarization method for near-surface applications. *Near Surface Geophysics*, 10 (6):453–468, 2012. → pages 2, 11

R. Kohlrausch. Theorie des elektrischen Rückstandes in der Leidener Flasche. *Annalen der Physik*, 167(2):179–214, 1854. → pages 88, 187, 206

N. Kozhevnikov and E. Antonov. Fast-decaying inductively induced polarization in frozen ground: A synthesis of results and models. *Journal of Applied Geophysics*, 82:171–183, jul 2012. → pages 136

T. Kratzer and J. Macnae. Induced polarization in airborne EM. *Geophysics*, 77 (5):E317—-E327, 2012. → pages 5, 48, 92, 163

M. Lajaunie, P. Maurya, and G. Fiandaca. Comparison of Cole-Cole and Constant Phase Angle modeling in time-domain induced polarization. *4th IP workshop*, B(4):1192–1202, 2016. → pages 179

Y. Li and D. W. Oldenburg. 3-D inversion of magnetic data. *Geophysics*, 61(2): 394–408, 1996. → pages 81, 172

Y. Li and D. W. Oldenburg. 3-D inversion of induced polarization data. *Geophysics*, 65(6):1931–1945, nov 2000. → pages 37, 82

J. C. Macnae. *Geophysical Prospecting with Electric Fields from an Inductive EM Source: Ph.D dissertation*. PhD thesis, University of Toronto, 1988. → pages 4

D. Marchant, E. Haber, and D. Oldenburg. Recovery of 3D IP distribution from airborne time-domain EM. *ASEG Extended Abstracts*, 144:1–4, 2013. → pages 32

D. Marchant, E. Haber, and D. W. Oldenburg. Three-dimensional modeling of IP effects in time-domain electromagnetic data. *Geophysics*, 79(6):E303–E314, 2014. → pages v, 22, 32, 48, 99, 163, 168

D. J. Marshall and T. R. Madden. INDUCED POLARIZATION, A STUDY OF ITS CAUSES. *GEOPHYSICS*, 24(4):790–816, 1959. → pages 11

D. Oldenburg and Y. Li. Inversion of induced polarization data. *Geophysics*, 59 (9):1327–1341, 1994. → pages 3, 32, 33, 37, 40, 79, 82, 162, 167, 176

D. W. Oldenburg and Y. Li. 5. Inversion for Applied Geophysics: A Tutorial. In *Near-Surface Geophysics*, chapter 5, pages 89–150. 2005. → pages 81

D. W. Oldenburg, Y. Li, and R. G. Ellis. Inversion of geophysical data over a copper gold porphyry deposit: A case history for Mt. Milligan. *Geophysics*, 62 (5):1419–1431, 1997. → pages 117, 162

D. W. Oldenburg, E. Haber, and R. Shekhtman. Three dimensional inversion of multisource time domain electromagnetic data. *GEOPHYSICS*, 78(1): E47–E57, 2013. → pages 163, 172

W. Pelton, S. Ward, P. Hallof, W. Sill, and P. Nelson. MINERAL DISCRIMINATION AND REMOVAL OF INDUCTIVE COUPLING WITH MULTIFREQUENCY IP. *Geophysics*, 43(3):588–609, 1978. → pages xi, xii, xxv, 1, 3, 6, 7, 10, 11, 15, 22, 88, 152, 156, 162, 167, 187

M. Power and D. Hildes. Geophysical strategies for kimberlite exploration in northern Canada. In *Proceedings of Exploration '07: Fifth Decennial International Conference on Mineral Exploration*, pages 1025–1031, 2007. → pages xi, 136, 138

A. Revil. On charge accumulation in heterogeneous porous rocks under the influence of an external electric field. 78(4), 2013. → pages xiii, 11, 13

A. Revil and N. Florsch. Determination of permeability from spectral induced polarization in granular media. *Geophysical Journal International*, 181(3): 1480–1498, 2010. → pages 189

A. Revil, N. Florsch, and C. Camerlynck. Spectral induced polarization porosimetry. *Geophysical Journal International*, 198(2):1016–1033, 2014. → pages 156

A. Revil, G. Z. Abdel Aal, E. A. Atekwana, D. Mao, and N. Florsch. Induced polarization response of porous media with metallic particles Part 2: Comparison with a broad database of experimental data. *Geophysics*, 80(5): D539–D552, 2015. → pages xii, 10, 11, 12, 162

P. S. Routh and D. W. Oldenburg. Electromagnetic coupling in frequency-domain induced polarization data: a method for removal. *Geophysical Journal International*, 145(1):59–76, 2001. → pages 4, 22, 163

H. Seigel. Mathematical formulation and type curves for induced polarization. *Geophysics*, 24(3):547–565, 1959. → pages 3, 37, 40, 41

H. Seigel. The magnetic induced polarization (MIP) method. *Geophysics*, 39(3): 321–339, 1974. → pages 33, 162

L. Slater and D. P. Lesmes. Electrical-hydraulic relationships observed for unconsolidated sediments. *Water Resources Research*, 38(10):33–46, 2002. → pages 189

R. S. Smith and J. Klein. A special circumstance of airborne inducedpolarization measurements. *Geophysics*, 61(1):66–73, jan 1996. → pages 4, 5, 48, 92, 136, 187

R. S. Smith and G. F. West. Field examples of negative coincidentloop transient electromagnetic responses modeled with polarizable halfplanes. *GEOPHYSICS*, 54(11):1491–1498, 1989. → pages 21

R. S. Smith, P. W. Walker, B. D. Polzer, and G. F. West. The time-domain electromagnetic response of polarizable bodies: an approximate convolution algorithm. *Geophysical Prospecting*, 36(April):772–785, 1988. → pages 44, 57, 58

A. Tarasov and K. Titov. On the use of the Cole-Cole equations in spectral induced: Polarization. *i*, 195(1):352–356, 2013. → pages 16, 88, 162, 187

A. N. Tikhonov and V. Y. Arsenin. *Solutions of Ill-Posed Problems*. W.H. Winston and Sons., 1977. → pages 80

P. Veeken, P. Legeydo, I. Pesterev, Y. Davidenko, E. Kudryavceva, and S. Ivanov. Geoelectric modelling with separation between electromagnetic and induced polarization field components. *first break*, 27(12):53–64, 2009a. → pages 2, 163

P. C. Veeken, P. J. Legeydo, Y. A. Davidenko, E. O. Kudryavceva, S. A. Ivanov, and A. Chuvaev. Benefits of the induced polarization geoelectric method to hydrocarbon exploration. *Geophysics*, 74:B47–B59, 2009b. → pages 2, 163

A. Viezzoli, V. Kaminski, and G. Fiandaca. Modeling induced polarization effects in helicopter time domain electromagnetic data: Synthetic case studies. *GEOPHYSICS*, 82(2):E31–E50, 2017. → pages 5

J. R. Wait and T. P. Gruszka. On electromagnetic coupling "removal" from induced polarization surveys. *Geoexploration*, 24(1):21–27, 1986. → pages 162

P. Weidelt. Response characteristics of coincident loop transient electromagnetic systems. *GEOPHYSICS*, 47(September):1325–1330, 1982. → pages 4, 48, 92, 136

A. Weller, S. Nordsiek, and W. Debschutz. Estimating permeability of sandstone samples by nuclear magnetic resonance and spectral-induced polarization. *Geophysics*, 75(6):E215, 2010. → pages 189

J. Wong. An electrochemical model of the induced-polarization phenomenon in disseminated sulfide ores. *Geophysics*, 44(7):1245, 1979. → pages 10, 11

J. C. Wynn and K. L. Zonge. EM coupling, its intrinsic value, its removal and the cultural coupling problem. *Geophysics*, 40(5):831–850, 1975. → pages 4, 163

Z. Xu and M. S. Zhdanov. Three-Dimensional Cole-Cole Model Inversion of Induced Polarization Data Based on Regularized Conjugate Gradient Method. *Geoscience and Remote Sensing Letters, IEEE*, 12(6):1180–1184, jun 2015. → pages 32

D. Yang and D. W. Oldenburg. Three-dimensional inversion of airborne time-domain electromagnetic data with applications to a porphyry deposit. *Geophysics*, 77(2):B23–B34, 2012. → pages xxii, 117, 119

D. Yang, D. W. Oldenburg, and E. Haber. 3-D inversion of airborne electromagnetic data parallelized and accelerated by local mesh and adaptive soundings. *Geophysical Journal International*, 196(3):1492–1507, 2014. → pages vi, xxii, 117, 118, 124

K. Yee. Numerical solution of initial boundary value problems involving maxwell's equations in isotropic media. *IEEE Transactions on Antennas and Propagation*, 14(3):302–307, 1966. → pages 207

Yuval and D. Oldenburg. Computation of ColeCole parameters from IP data. *Geophysics*, 62(2):436–448, 1997. → pages 3, 45, 88, 167, 206

Appendix A

Handling Multiple Sources for AEM Surveys

The linearization for inductive sources in Chapter 2 has been developed for a single source and 3D information about chargeability can be obtained if there are multiple receivers. For ATEM data however, here is only a single receiver location for each source but There are multiple source locations. Our goal is to alter the problem to work with an effective pseudo-chargeability.

In our linearized eq. (2.38), each source has its own sensitivity and pseudo-chargeabilty. For our airborne case the sensitivity for the k-th source is the k-th row of $\mathbf{J}$ and the pseudo-chargeability is $\tilde{\eta}^k$. The corresponding IP datum is

$$d_k^{IP}(t) = \sum_{i=1}^{nC} J_{k,i}\tilde{\eta}_i^k(t), \;\; k = 1,\ldots,nTx, \tag{A.1}$$

where nTx is the number of sources, nC is the number of cells in the domain, and $J_{k,i}$ indicates an element of the Jacobian matrix for the k-th source and the i-th cell. I want to replace $\tilde{\eta}_i^k$ with a single effective pseudo-chargeabilty $\tilde{\eta}_i$ and therefore write the IP datum as

$$d_k^{IP}(t) = \sum_{i=1}^{nC} J_{k,i}\tilde{\eta}_i(t), \;\; k = 1,\ldots,nTx, \tag{A.2}$$

The waveforms are different for each source and hence this representation cannot be exact. To examine the implications of this it suffices to look at the contribution of any volumetric pixel. Each pixel contributes to all of the IP data but in differing amounts. The total contribution of the i-th pixel to the nTx data set at a single time is

$$q_i = \sum_{k=1}^{nTx} J_{k,i}\tilde{\eta}_i^k(t), \;\; i = 1,\ldots,nC. \tag{A.3}$$

Our goal is to find an effective chargeability that produces the same net effect on the measured data. I search for a source-independent $\tilde{\eta}_i$ such that

$$q_i^{est} = \sum_{k=1}^{nTx} J_{k,i}\tilde{\eta}_i(t), \;\; i = 1,\ldots,nC. \tag{A.4}$$

Minimizing the least squares difference between eqs (A.3) and (A.4) yields

$$\tilde{\eta}_i(t) = \frac{\Sigma_{k=1}^{nTx} J_{k,i}^2 \tilde{\eta}_i^k(t)}{\Sigma_{k=1}^{nTx} J_{k,i}^2} = \sum_{k=1}^{nTx} a_i^k \tilde{\eta}_i^k(t), \;\; i = 1,\ldots,nC. \tag{A.5}$$

where the normalized weight (a_i^k) is

$$a_i^k = \frac{J_{k,i}^2}{\Sigma_{k=1}^{nTx} J_{k,i}^2}, \;\; i = 1,\ldots,nC. \tag{A.6}$$

With the above understanding about how $\tilde{\eta}_i$ relates to the $\tilde{\eta}_i^k$ from each source I can proceed as follows. Firstly, from eq. (2.23) I have

$$\tilde{\eta}_i^k(t) = \tilde{\eta}^I \otimes \hat{w}_i^k(t) \tag{A.7}$$

Substituting eqs (A.7) into (A.5) allows us to write

$$\tilde{\eta}_i(t) = \tilde{\eta}^I(t) \otimes w_i^e(t), \tag{A.8}$$

where I define the effective time history of the electric field, $w_i^e(t)$ as

$$w_i^e(t) = \sum_{k=1}^{nTx} a_i^k \hat{w}_i^k(t), \;\; i = 1,\ldots,nC. \tag{A.9}$$

The above equations shows that the pseudo-chargeabilty for any pixel recovered from the inversion is equal to the convolution of the impulse pseudo-chargeability, $\tilde{\eta}^I(t)$, with an effective time history of the electric field $w^e(t)$. Although it is somewhat involved, the $w^e(t)$ associated with each pixel can be evaluated by knowing the electric fields associated with the fundamental EM problem. Ultimately this allows us to estimate the parameters associated with the impulse pseudo-chargeability in the same manner as outlined for the case with a single source. Our ability to evaluate the $w^e(t)$ and test the validity of eq. (A.2) is treated below.

For each pixel I have equation:

$$\tilde{\eta}_i(t) = \tilde{\eta}_i^I(t) \otimes w_i^e(t), \tag{A.10}$$

where $\tilde{\eta}_i^I(t)$ is the impulse pseudo-chargeability associated with an individual pixel. The effective time history of the electric field, $w_i^e(t)$ is a linear combination of the fundamental electric fields due to the individual sources. I can calculate $w_i^e(t)$ and carry out the convolution to evaluate the effective pseudo-chargeability. The IP data can then be forward modelled using eq. (2.38). This allows us to validate eq. (A.2), which demonstrated the linear form of d^{IP} data at all source locations, by comparing results with the true IP data obtained via forward modelling. It is only necessary to apply this to the conductive model.

The evaluation of the effective pseudo-chargeability is carried out on a cell by cell basis. For each cell I first evaluate $w^e(t)$ (eq. A.9). This requires calculating normalized weights shown in eq. (A.6). Fig. A.1 shows these weights at a single pixel located at (0 m,0 m,-75 m). These decay away from the center pixel because of the decay of the sensitivity functions. Because those are weights used to compute $w^e(t)$, I could expect that the computed $w^e(t)$ will be mostly affected by $\hat{w}_k$ from a few stations close to the center. In Fig. A.2, I provide both $\hat{w}_k$ (dashed lines) from all source locations and $w^e(t)$ (eq. A.9; solid line). The $w^e(t)$ is dominantly affected by the $\hat{w}(t)$ at the center source location (solid circles)). Considering that the sources are 50 m apart, the decay of the sensitivity from center source location to others is substantial ($\sim 1/r^3$). This results in the greatest normalized weight at the center source location, and the observed result about $w^e(t)$ is caused by this. $w^e(t)$ is convolved with $\tilde{\eta}^I(t)$ to compute the effective $\tilde{\eta}(t)$ for that cell. When

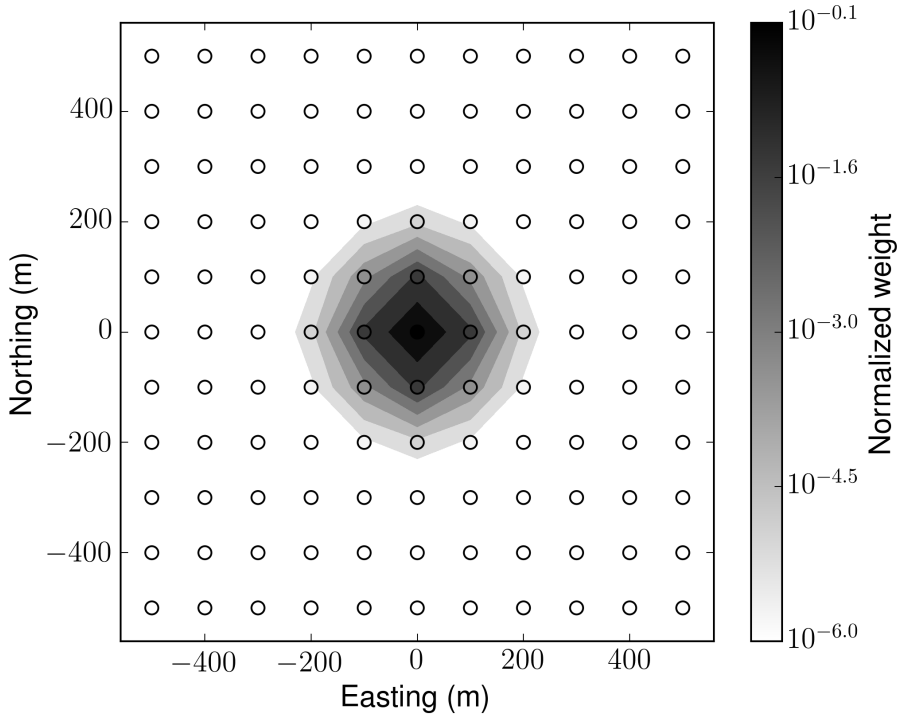

Figure A.1: Normalized weights for the conductive case for all source locations. A single pixel located at (0 m, 0 m, -75 m) is used.

this is carried out for each cell then the approximate IP responses can be computed using eq. (2.38). These can be compared with the true IP responses. Fig. A.3 shows the comparisons at 0.86 ms. The images are nearly identical in shape but the approximate IP responses are nearly a factor of two lower than the true values. This is not entirely unexpected. A similar effect was observed for IP responses for a single source shown in Fig. 2.14. At 0.86 ms, the approximate value was about 70 percent of the true d^{IP}. These results seem to be a worst case scenario. The discrepancy for a conductive body lessens as time increases and analyses for the canonical and resistive bodies shows that the approximate and true IP data are in very good agreement (Section 2.3.4).

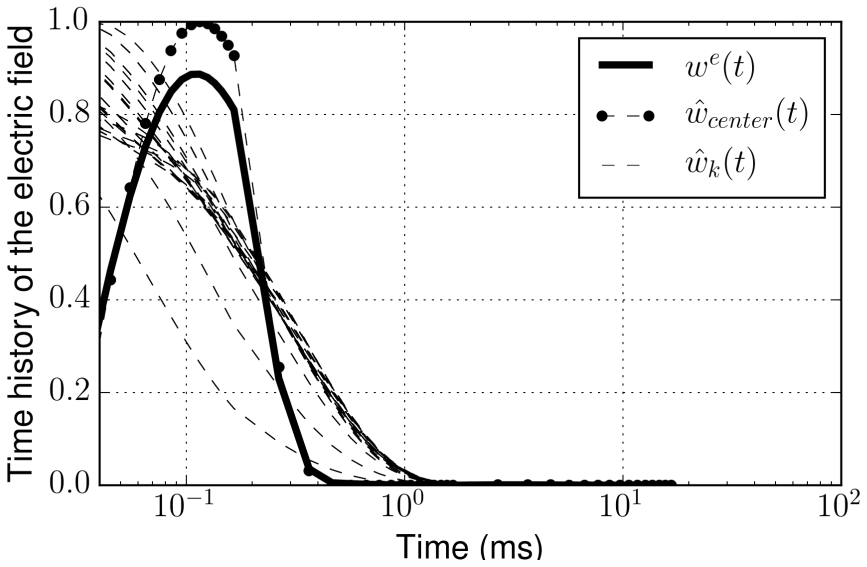

Figure A.2: Time decays of $w^e(t)$ and $\hat{w}(t)$ for the conductive case. A single pixel located at (0 m, 0 m, -75 m) is used. Solid line and dashed lines correspond to $w^e(t)$ and $\hat{w}_k(t)$ for all sources ($k = 1, \ldots, nTx$); $\hat{w}_k$ at the center source located at (0 m, 0 m, 30 m) is marked as solid circles. A number of $w^e(t)$ curves are overlaid due to the symmetric position of source locations to the conductive block.

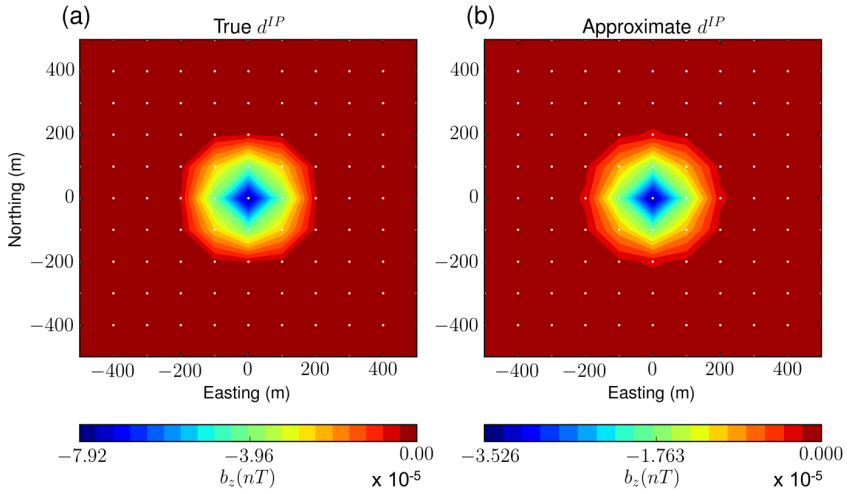

Figure A.3: Comparison of true and approximate b_z^{IP} responses at 0.86 ms on a plan view map.

Appendix B

Extracting Intrinsic IP Parameters

The output of our IP inversion is a 3D distribution of the pseudo-chargeability at multiple time channels. As its name suggests, pseudo-chargeability is not an intrinsic IP parameter like chargeability, but it is a convolution of $\tilde{\eta}^I(t)$ and $\hat{w}(t)$:

$$\tilde{\eta}(t) = \tilde{\eta}^I(t) \otimes \hat{w}(t), \tag{B.1}$$

using the definition of impulse pseudo-chargeability (eq. 2.7). We now use the $\tilde{\eta}(t)$ as the data and recover intrinsic parameters such as η, τ, c in a Cole-Cole model. Assuming a Debye model (c=1), we obtain

$$\tilde{\eta}^I(t) = \frac{\eta}{(1-\eta)\tau} e^{-\frac{t}{(1-\eta)\tau}}, \tag{B.2}$$

Since we have σ_∞ we can compute $\hat{w}(t)$, which is the time history of the electric field. Accordingly, we can unravel the recovered pseudo-chargeability to extract intrinsic IP parameters such as chargeability(η) and time constant (τ). We use a gradient-based optimization and thus we need the sensitivity function for the pseudo-chargeability (eq. B.1) with respect to η and τ. To simplify this procedure, we rewrite impulse pseudo-chargeability as

$$\tilde{\eta}^I(t) = ae^{-bt}, \tag{B.3}$$

where $a = \frac{\eta}{(1-\eta)\tau}$ and $b = \frac{1}{(1-\eta)\tau}$. Then we take the derivative of $\tilde{\eta}(t)$ with regard to a and b:

$$\frac{\partial \tilde{\eta}(t)}{\partial a} = e^{-bt} \otimes \hat{w}(t), \tag{B.4}$$

$$\frac{\partial \tilde{\eta}(t)}{\partial b} = -ate^{-bt} \otimes \hat{w}(t). \tag{B.5}$$

With these sensitivity functions, we can set up an inverse problem, and recover a and b. The chargeability and time constant can be obtained from a and b:

$$\eta = \frac{a}{b}, \tag{B.6}$$

$$\tau = \frac{1}{(1-a/b)b}. \tag{B.7}$$

We apply this inversion separately to each cell in the recovered pseudo-chargeability in a manner similar to Yuval and Oldenburg [1997]. For a better alternative (representation) of time-dependent conductivity, a different parameterization such as stretched-exponential [Kohlrausch, 1854] or Cole-Cole model with variable c can be implemented.

Appendix C

Discretization

C.1 Steady-state Maxwell's Equations

As shown in eq. (2.29), computation of our linearized kernel requires solving steady-state Maxwell's equations. We discretize this system using a mimetic finite volume (FV) method with weak formulation [Yee, 1966, Haber, 2014]. For the discretization, we assume that the electric field $\vec{e}$ is discretized by a grid function **e** on cell edges and the magnetic flux density $\vec{b}$ is discretized by agrid function **b** on cell faces. The electrical potential ϕ is discretized by a grid function ϕ on the cell nodes. For a clear representation of the derivation, recall Maxwell's equations in steady state are

$$\vec{j} = \sigma_\infty \vec{e} = -\sigma_\infty \vec{\nabla}\phi, \tag{C.1}$$

$$-\nabla \cdot \vec{j} = \nabla \cdot \vec{j}_s, \tag{C.2}$$

$$\vec{j}\big|_{\partial\Omega} \cdot \hat{n} = 0, \tag{C.3}$$

where $\partial\Omega$ indicates a boundary surface of the system and $\hat{n}$ is the normal vector of the boundary surface. The weak form of those equations can be written as

$$(\vec{j}, \vec{w}) + (\sigma_\infty \vec{\nabla}\phi, \vec{w}) = 0, \tag{C.4}$$

$$-(\vec{j}, \vec{\nabla}\psi) = (\vec{j}_s, \vec{\nabla}\psi). \tag{C.5}$$

The inner products $(\vec{j},\vec{w})$, $(\sigma_\infty\vec{\nabla}\phi,\vec{w})$, $(\vec{j},\vec{\nabla}\psi)$ and $(\vec{j}_s,\vec{\nabla}\psi)$ are edge-based products. Here we define the inner product as

$$(\vec{a},\vec{b}) = \int_\Omega \vec{a}\cdot\vec{b}dv, \tag{C.6}$$

where Ω is the volume of the system. By discretizing the $\vec{\nabla}$ operator and the inner product in space, we obtain

$$\mathbf{M}^e\mathbf{j} + \mathbf{M}^e_{\sigma_\infty}\mathbf{G}\phi = 0, \tag{C.7}$$

$$-\mathbf{G}^T\mathbf{M}^e\mathbf{j} = \mathbf{G}^T\mathbf{M}^e\mathbf{j}_s, \tag{C.8}$$

where $\mathbf{M}^e$ performs volume averaging, and $\mathbf{M}^e_{\sigma_\infty}$ is the mass matrix of conductivity (σ_∞), which discretizes the edge based inner product. For further details on the formation of this matrix see Haber [2014].

By substituting eq. (C.7) into (C.8), we have

$$\mathbf{A}_{\sigma_\infty}\phi = \mathbf{rhs}^{DC}, \tag{C.9}$$

where $\mathbf{A}_{\sigma_\infty} = \mathbf{G}^T\mathbf{M}^e_{\sigma_\infty}\mathbf{G}$ and $\mathbf{rhs}^{DC} = \mathbf{G}^T\mathbf{M}^e\mathbf{j}_s$. We use the SIMPEG's tensor mesh and solver classes to form and solve above the linear system [Cockett et al., 2015].

C.2 Linearized Kernel for IP Responses

To obtain a linear form of eq. (2.38), we first discretize the Biot-Savart law shown in eqs (2.36) and (2.37). In our discretization $\vec{j}^{IP}$ and $\tilde{\eta}$ are defined at the cell centers, and those for each time channel are constant in a cell volume, whereas $\vec{e}^{\,ref}$ is defined on the cell edges. We define the number of cells and edges in 3D space as nC and nE, respectively. The discretized IP current density, $\mathbf{j}^{IP}_{cc} \in \mathbb{R}^{3nC}_1$, is defined at the cell center. Since $\vec{j}^{IP}$ has three components, we first discretize the integration operator including cross product ($\int_v \frac{\times\hat{r}}{r^2}dv$) as

$$\mathbf{G}_{Biot} = \begin{bmatrix} \mathbf{e}^T & \mathbf{0} & \mathbf{0} \\ \mathbf{0} & \mathbf{e}^T & \mathbf{0} \\ \mathbf{0} & \mathbf{0} & \mathbf{e}^T \end{bmatrix} \begin{bmatrix} \mathbf{0} & \mathbf{S}_z & -\mathbf{S}_y \\ -\mathbf{S}_z & \mathbf{0} & \mathbf{S}_x \\ \mathbf{S}_y & -\mathbf{S}_x & \mathbf{0} \end{bmatrix}, \tag{C.10}$$

where

$$\mathbf{S}_l = \mathbf{diag}(\mathbf{v} \oplus \mathbf{r}_l \oplus \frac{1}{\mathbf{r}^2}),\ l = x,\ y,\ z$$

and the electric field at peak time, $\mathbf{e}^F_{max} \in \mathbb{R}^{nE}_1$ is a column vector, $\mathbf{diag}(\cdot)$ is the diagonal matrix and $\oplus$ is the Hadamard product. Computing the $\mathbf{e}^F_{max}$ requries a forward simulation time-domain electromagnetic problem, and SIMPEG-EM package is used [Heagy et al., 2017]. Then we discretize $\vec{j}^{IP}$ shown in eq. (2.28) as

$$\mathbf{j}^{IP}_{cc}(t) = \mathbf{S}\mathbf{diag}(\mathbf{e}^F_{max})\mathbf{A}^{eT}_c\mathbf{diag}(\mathbf{v})\mathbf{diag}(\sigma_\infty)\tilde{\eta}(t), \tag{C.11}$$

where $\mathbf{A}^e_c$ is a discrete averaging matrix from edge to cell center and

$$\mathbf{S} = \mathbf{A}^e_{ccv}\mathbf{M}^{e-1}[\mathbf{M}^e_{\sigma_\infty}\mathbf{G}\mathbf{A}^{-1}_{\sigma_\infty}\mathbf{G}^T - \mathbf{I}]\mathbf{diag}(\mathbf{e}^F_{max})\mathbf{A}^{eT}_c\mathbf{diag}(\mathbf{v})\mathbf{diag}(\sigma_\infty). \tag{C.12}$$

Here $\mathbf{A}^e_{ccv}$ is a discrete averaging matrix from edge to cell center with consideration of three component vector: $\in \mathbb{R}^{3nC}_{nE}$. Thus, we can have a linear equation for a single time channel as

$$\mathbf{b}^{IP} = \mathbf{G}_{Biot}\mathbf{S}\tilde{\eta},$$

Finally, by letting

$$\mathbf{J} = \mathbf{G}_{Biot}\mathbf{S}, \tag{C.13}$$

we have

$$\mathbf{b}^{IP} = \mathbf{J}\tilde{\eta}, \tag{C.14}$$

where $\mathbf{J}$ is the Jacobian matrix of the linear equation, and since $\mathbf{J}$ is static, we also obtain

$$-\frac{\partial \mathbf{b}^{IP}}{\partial t}\Big| = \mathbf{J}(-\frac{\partial \tilde{\eta}}{\partial t}\Big|). \tag{C.15}$$